NORTHWESTERN UNIVERSITY

Effects of Patterning and Spatial Confinement on Order in Self-Assembling Systems

A DISSERTATION

SUBMITTED TO THE GRADUATE SCHOOL
IN PARTIAL FULFILLMENT OF THE REQUIREMENTS

for the degree

DOCTOR OF PHILOSOPHY

Field of Materials Science and Engineering

By

Albert Melvin Hung

EVANSTON, ILLINOIS

June, 2007

ABSTRACT

Effects of Patterning and Spatial Confinement on Order in Self-Assembling Systems

Albert Melvin Hung

Supramolecular chemistry has proven to be an effective strategy for bottom-up fabrication of monodisperse, functional nanostructures. However, most applications require these nanostructures to be spatially or orientationally ordered. This thesis investigates patterning and spatial confinement as tools for controlling order in self-assembling systems.

We first look to improve the ordering of polar, mushroom-shaped supramolecular aggregates through surface chemistry and addition of small molecule guests. Monolayer and bilayer films are 1 nm/layer thicker on hydrophilic oxide versus hydrophobic surfaces, suggesting more normal orientation and tighter packing of the molecules. By FTIR, 4-cyanobiphenyl incorporated into these films align normal to the surface with an order parameter $f_\theta = 0.38$. f_θ of the host also increases from 0.2 to 0.7, possibly due to occupation of free volume and release of strain about the mushroom "stems" by the guest.

We next develope methods for patterning and aligning 1D, supramolecular peptide-amphiphile (PA) nanofibers. Microcontact printing can directly pattern nanofiber arrays of submicrometer resolution. The features size increases with stamping time and glycerol concentration. Depending on the molecule, PA is deposited by direct contact or fluid transport through a water meniscus. By another method, sonication-assisted solution embossing, we achieve the simultaneous self-assembly, alignment and patterning of nanofibers over large areas. Alignment is due to steric confinement within submicrometer channels and a lyotropic liquid crystalline transition. Nanofibers can also be guided around turns by this technique. FTIR gives

nanofiber orientation parameters of 0.2 to 0.4 and confirms that the nanostructures consist of axially aligned β-sheets. Neural progenitor cells show preferential alignment of cell bodies parallel to these aligned nanofibers, hypothetically due to integrin clustering about the nanofibers leading to a restructuring of the cytoskeleton.

Lastly, we examine the morphology of thin films of an oligothiophene amphiphile that assembles into 2D lamellae. Films thinner than the bulk *d*-spacing of 13.0 nm exhibit regular dotted and striped surface textures of 18 nm periodicity. These monolayer textures depend on the conformation, extended or amorphous, of the poly(ethylene glycol) segments that frustrate the packing of the hydrophobic segments. Friction-transferred Teflon® substrates show promise for controlling the alignment of these textures.

Thesis Advisor: Prof. Samuel I. Stupp

For all who held faith in me

whenever I lost faith in myself

ACKNOWLEDGEMENTS

No worthwhile journey is without its challenges, and no honest traveler can claim to have surmounted all of those challenges by himself. It is with much gratitude that I am able to look back upon how far I've come and recognize those who have helped me along the way. I must first thank my advisor, Prof. Samuel I. Stupp, for granting me not only the opportunity to embark on such a quest but the freedom to explore whatever fascinating paths of research I wished. I also thank the other members of my thesis committee, Prof. Monica Olvera de la Cruz, Prof. Mark Hersam, and Prof. Richard P. Van Duyne, for their patience, their support, and, above all, their commitment to teaching.

Many coworkers have earned my gratitude for contributing to the project and my learning throughout the years. Upon joining the group, Dr. Leiming Li introduced me to the supramolecular mushroom molecule, 3BPOH, and was there to watch over my first awkward steps in an experimental laboratory. Keith Dvorkin was one of the first in our group to really focus on microfabrication and soft lithography techniques and initiated me in a field of research that I would continue to expand upon for my entire tenure. Dr. Hongzhou Jiang has been a patient comrade-in-arms as we both struggled over similar research questions, and the resulting discussions have been invaluable. Dorothea Grieshaber was a masters' student from ETH Zurich who I had the pleasure of working with one summer. She contributed directly to the 3BPOH project, logging so many instrument hours that she drew the concern of our group secretary, Sharon Jacknow. James Hulvat was always around to keep the labs in order, give friendly advice, and help with any X-ray issues.

I am sincerely appreciate the efforts of those with infinitely greater synthetic expertise on whom I've been reliant to provide me with the raw materials I needed to perform my research.

Eugene R. Zubarev, now a professor at Rice University, kindly synthesized all the 3BPOH I could ever wish to use. David Stone meted out precious amounts of his oligothiophene-based amphiphiles that I foolhardily decided to work on my last year despite warnings to avoid picking up new projects so late. Dr. Krista L. Niece provided the batches of peptide amphiphiles that would give me my first positive research results. She also deserves extra gratitude both as my collaborator on the preliminary cell experiments and as a dear friend who has enriched my time here to no end.

Additional contributions were made by Wei-chun Lin, Catherine Czeisler, Benjamin Myers, Robert O'Callahan, Marina Sofos, Lesley Chow, Dr. Eric Spoerke, Dr. Eli Sone, Dr. Mike Arnold, Dr. Josh Goldberger, Melanie Disabb, Ian Tevis, Chung-Yan Koh, Lorraine Hsu, Shuming Zhang, Mark Seniw, and our squad of fantastic group secretaries Laura, Donnie, Sharon, and Chris, whether through scientific work, useful discussions, or simply being a friendly face. I must also thank the Evanston Frisbee guys (and gals) and the Saucony and Avia shoe companies for compelling me to venture outside even in some of the most treacherous weather. After hours in lab hopelessly running in circles and flailing about, there's nothing quite like stepping outdoors just to, well, run in circles and flail about.

Finally, I would like to thank my parents Ching-mao and Pei-jean Hung, my sister Emilie Hung and my brother Jeffrey Hung, my siblings-in-law Ben Tarbell and Leigh Lien, and my nieces Christina and Eileen Hung, all of whom have never failed to offer their love and support.

LIST OF ABBREVIATIONS

3BPOH	See Figure 2.1 for structure
a.u.	Arbitrary units
AFM	Atomic force microscopy
CB	4-cyanobiphenyl (see Figure (2.1)
DC	Direct current
DPN	Dip-pen nanolithography
DR1	Disperse red 1 (see Figure 2.1)
DSC	Differential scanning calorimetry
EUV	Extreme ultraviolet
FFT	Fast Fourier Transform
FRET	Forster resonance energy transfer
FT-IR	Fourier transform infrared (spectroscopy)
HF	Hydrofluoric acid
IR	Infrared
MIMIC	Micromolding in capillaries
Nd:YAG	Neodymium-doped yttrium aluminium garnet; Nd:$Y_3A_{l5}O_{12}$
NLO	Nonlinear optics
NSOM	Near-field scanning optical microscopy
OTS	Octadecytrichorosilane
PA	Peptide amphiphile (see Figure 3.1)
PDMS	Poly(dimethyl siloxane)

(PE)CVD	(Plasma enhanced) chemical vapor deposition
PEG	Poly(ethylene glycol)
PM-IRRAS	Polarization modulated infrared refection absorption spectroscopy
PMMA	Poly(methyl methacryate)
PMT	Photomultiplier tube
POM	Polarized optical microscopy
PS	Poly(styrene)
PTFE	Poly(tetrafluoroethylene) or Teflon
RIE	Reactive ion etching
RMS	Root-mean-squared
SAM	Self-assembled monolayer
SEM	Scanning electron microscopy
SHG	Second harmonic generation
SPM	Scanning probe microsope
TDM	Transition dipole moment
THF	Tetrahydrofuran

TABLE OF CONTENTS

ABSTRACT....2
ACKNOWLEDGEMENTS....5
LIST OF ABBREVIATIONS....7
LIST OF FIGURES....14
LIST OF TABLES....22

Chapter 1: Introduction....24

1.1 Objectives and Significance....24

1.2 Self-Organized Organic Materials....26

1.2.1 Forces Governing Organization Behavior....26
1.2.2 Block Copolymers, Liquid Crystals, and Colloidal Crystals....28
1.2.3 Applications of Self-Organized Systems and the Need for Long Range Order 33

1.3 Supramolecular Self-Assembly....34

1.3.1 Common forces involved in self-assembly....34
1.3.2 Brief introduction to self-assembling systems of interest....35
1.3.3 Difficulties in Aligning Self-Assembled Nanostructures....40

1.4 Alignment and Patterning of Self-Organized and Self-Assembling Systems....41

1.4.1 Alignment by External Fields and Interface Sweeping....41
1.4.2 Surface Patterning and Graphoepitaxy....44
1.4.3 Scanning probe and Soft Lithographic Techniques....48
1.4.4 Other routes to spatial confinement and control of order....51

Chapter 2: Patterning and Molecular Order of Substrate-Supported Thin Films of Supramolecular, Mushroom-Shaped Aggregates....54

2.1 Introduction....54

2.2 Materials and Methods....58

2.2.1 Materials....58
2.2.2 Substrate Preparation....59
2.2.3 Surface Treatments....60
2.2.4 Soft lithography....60
2.2.5 Micropatterned silica substrates....61
2.2.6 SAXS and DSC....62
2.2.7 Near-field scanning and polarized optical microscopy....62
2.2.8 Characterization of the substrate and film morphology....63
2.2.9 Second harmonic generation....64

2.2.10 FTIR 65

2.3 Microscale patterning of 3BPOH 65

2.3.1 Characterization of 3BPOH 65
2.3.2 Solution Embossing of 3BPOH 68
2.3.3 3BPOH films on micropatterned silica substrates 71
2.3.4 Nonlinear optical measurements 71

2.4 Effects of surface treatments on film morphology 76

2.4.1 Substrate characterization 76
2.4.2 Film textures 77
2.4.3 Layer thickness and implied molecular orientation 82

2.5 Supramolecular host-guest system 85

2.5.1 Characterization of the guest molecules 85
2.5.2 Preliminary results with disperse red 1 87
2.5.3 Molecular order of 4-cyanobiphenyl mixed in a supramolecular host 89
2.5.4 Molecular order of supramolecular host mixed with 4-cyanobiphenyl 95
2.5.5 Discussion of validity and errors in the spectroscopic model 99

2.6 Summary and Outlook 100

Chapter 3: Microcontact Printing of Self-Assembling Peptide-Amphiphile Nanofibers 103

3.1 Introduction 103

3.2 Materials and Methods 105

3.2.1 Fabrication of anisotropically etched Si masters. 105
3.2.2 Polymer replica molds 107
3.2.3 PA molecules and microcontact printing 108
3.2.4 SEM and AFM 109
3.2.5 Force-displacement measurements 109

3.3 Anisotropically etched Si masters and polymer replicas 110

3.3.1 Resolution of the etched silicon master 110
3.3.2 Elastic contact mechanics and resolution of the polymer replica molds 111

3.4 Micro-contact printing of PA 1 nanofibers 115

3.4.1 Dot and line features 115
3.4.2 Effect of glycerol concentration and stamping time 118

3.4.3 Nanofiber alignment 120

3.5 Micro-contact printing of PA 2 and PA 3 nanofibers 121

*3.5.1 Printing of PA **2** nanofibers and the effect of hydrophobicity 121*
*3.5.2 Preliminary results of printing of PA **3** nanofibers 124*

3.6 Summary and Outlook 125

Chapter 4: Simultaneous Self-Assembly, Orientation, and Patterning of Peptide-Amphiphile Nanofibers by Soft Lithography 128

4.1 Introduction 128

4.2 Materials and Methods 130

4.2.1 PA molecules 130
4.2.2 PDMS grating stamps 130
4.2.3 Substrate cleaning 131
4.2.4 Micromolding in capillaries 132
4.2.5 Sonication-assisted solution embossing 132
4.2.6 AFM, SEM, and polarized optical microscopy 134
4.2.7 Electron-beam lithography 134

4.3 Patterning nanofibers by MIMIC 135

4.3.1 Characterization of the diffraction grating stamps 135
4.3.2 Effect of channel width 139
4.3.3 Mechanism of patterning 141

4.4 Patterned, aligned nanofibers by sonication-assisted solution embossing 141

4.4.1 AFM of patterned, aligned PA nanofibers 141
4.4.2 Mechanism of patterning 144
4.4.3 Effect of ultrasonication and initial solution concentration 147
4.4.4 Mechanism of alignment and lyotropic liquid crystalline behavior 148
4.4.5 Guiding PA nanofibers through complex paths 151

4.5 Summary and outlook 153

Chapter 5: Infrared Spectroscopy and Preliminary Cell Studies on Peptide-Amphiphile Nanofibers Patterned and Aligned by Solution Embossing 155

5.1 Introduction 155

5.2 Materials and Methods 158

5.2.1 PA molecules 158

5.2.2 Soft lithography ... 159
5.2.3 FTIR and determination of direction cosines and orientation parameters ... 159
5.2.4 Cell studies ... 160

5.3 Characterization of Nanofiber Structure ... 162

5.3.1 Comparison to the previously proposed structure ... 162
5.3.2 Vibrations perpendicular to the nanofiber ... 166

5.4 Determination of Order Parameters and α_{max} ... 168

*5.4.1 Orientation parameter f_{φ} and quantifying the alignment of PA **1** nanofibers 168*
*5.4.2 Effect of patterning on the alignment and structure of PA **2** nanofibers ... 170*
5.4.3 Effect of channel width and ultrasonication on alignment ... 174
5.4.4 f_{φ} derived from AFM images and discussion of the validity of the calculated values 175

5.5 Effect of nanofiber alignment on cellular morphology ... 177

5.5.1 Results with murine neural progenitor cells ... 177
5.5.2 Resilience of the substrate pattern and the alignment effect ... 179

5.6 Summary and Outlook ... 179

Chapter 6: Morphological Study of Thin Films of Thiophene-Based Amphiphiles .. 183

6.1 Introduction ... 183

6.2 Materials and Methods ... 186

6.2.1 Synthesis ... 186
6.2.2 Material characterization ... 187
6.2.3 Film patterning ... 187
6.2.4 Characterization of film thickness and morphology ... 188
6.2.5 Characterization of optical properties ... 188

6.3 Characterization of thiophene-PEG films ... 189

6.3.1 Material characterization ... 189
6.3.2 Thin film morphology ... 190
6.3.3 Theory of thin film structure ... 193
6.3.4 Preliminary examination of hybrid mixtures ... 195

6.4 Patterning of thiophene-PEG films ... 196

6.4.1 Deposition on friction-transferred PTFE ... 196
6.4.2 Preliminary work on soft lithographic embossing of thick films ... 200

6.5 Summary and outlook 204

Appendix A Determination of molecular orientation by polarized IR spectroscopy... 207

A.1 Quantifying alignement and structure of PA nanofibers 207

A.2 Quantifying order in films of supramolecular mushroom-shaped nanostructures..... 211

References and Notes..... 214

Vita..... 242

LIST OF FIGURES

Figure 1.1. (A) Schematic illustrations of possible chemical architectures of block copolymers. (B) Diblock copolymers can organize into different ordered mesophases depending on the relative length and interaction parameter χ of each block (reproduced from ref. 36, copyright American Chemical Society). 29

Figure 1.2. Schematic depiction of different liquid crystalling phases..... 30

Figure 1.3. Chemical structure of a rod-coil molecule that self-assembles into mushroom-shaped nanostructures, and schematic depiction of the stacking of the nanostructures into a polar film (reproduced from ref. 6, copyright AAAS). 36

Figure 1.4. Chemical structure of an oligo(*p*-phenylene vinylene) amphiphile that assembles into a lamellar structure and organizes as a liquid crystalline phase as seen from the polarized optical micrograph (reproduced from ref 113, copyright American Chemical Society)..... 38

Figure 1.5. (A) Chemical structure and (B) space-filling model of a self-assembling peptide-amphiphile molecule consisting of an aliphatic tail (1), cross-linking segment (2), flexible spacer (3), and functional head group (4, 5). (C) Schematic depiction of self-assembly of the molecule into nanofibers, and (D) transmission electron microscopy images of the nanofibers. (Reproduced from ref 81, copyright AAAS) 39

Figure 1.6. Schematic illustrations of nanometer-scale ordering by (A) zone casting of discotic graphene molecules (reproduced from ref. 154, copyright American Chemical Society) and (B) directional solidification of a polyethylene-polystyrene block copolymer (reproduced from ref. 156, copyright Nature Publishing Group)..... 43

Figure 1.7. Tristable liquid crystalline orientation achieved by surface rubbing with a scanning probe tip and imaged by polarized optical microscopy (reproduced from 168, copyright Nature Publishing Group). 45

Figure 1.8. AFM image of a single, large block copolymer domain ordered by graphoepitaxy on a topographically patterned surface (reproduced from ref. 32, copyright Wiley Interscience).... 47

Figure 1.9. Schematics of methods for pattering chemical monolayers by (A) DPN (reproduced from ref. 194, copyright AAAS) and (B) electro-oxidation by a scanning probe tip (reproduced from ref. 195, copyright Wiley Interscience)..... 49

Figure 1.10. Schematic illustration of four different soft lithographic processes (reproduced from ref. 200, copyright Wiley Interscience). 50

Figure 2.1. Chemical structures of molecules of interest..... 58

Figure 2.2. (A) Schematic of SHG setup, and (B) illustration of sample stage with polarization geometry. θ is the incident angle and *p* and *s* are polarizations parallel and perpendicular to the incident plane. 64

Figure 2.3. SAXS diffraction pattern of 2.1 in powder form and scaped off a film cast from chloroform solution (courtesy of Dr. James Hulvat). 66

Figure 2.4. Birefringent optical micrograph of 3BPOH film drop-cast onto clean glass, annealed at 155 °C for 5 hrs, and imaged between crossed polarizers. Non-annealed films are not birefringent. Scale bar is 50 μm. 66

Figure 2.5. Transmission NSOM images of (A) non-annealed and (B) heat annealed 3BPOH films spin-coated onto clean glass. The contrast in B is theoretically due to polarized absorption of 514 nm illumination by randomly oriented liquid crystal grains, each on the order of 300-500 nm in size. The dark spot in the center of A is sample damage due to the idle probe when the laser is turned on before the scan is started. 67

Figure 2.6. Optical micrograph of micromolded 3BPOH film after removal of the stamp. The pattern consists of 10 μm square mounds, each 1-2 μm tall, equal to the depth of wells in the PDMS stamp. A scratch down the center made by a razor blade reveals the presence of an underlying residual film. 69

Figure 2.7. Birefringent micrographs of micromolded 3BPOH films post-annealing: (A) 10μm and (B) 3μm circular features, scale bars are 50 μm. Inset: a closeup of B shows radial birefringence pattern and what appears to be liquid crystal disclinations. The dotted red circle indicates the location of the original circular mound. Scale bar is 6 μm. 70

Figure 2.8. (A) AFM and (B) transmission NSOM of micromolded 3BPOH films with 3 μm feature size. Heights of the pattern are shown to be roughly 175 nm and correspond to areas of increased domain contrast in the NSOM image. Slight indications of shading in the NSOM image may be due z-motion artifacts.[244, 245] 70

Figure 2.9. SEM images of surface features etched by RIE into a CVD SiO_2 layer deposited on glass slides. Square arrays of (A) 10 μm circular wells and (B) 3 μm circular posts. The roughness of the etch surface can be smoothed out by etching through the oxide layer to an etch stop, either (C) an underlying metal film or (D) the original slide glass. 72

Figure 2.10. Birefringent optical micrographs of 3BPOH films spin-coated and annealed on micromachined glass substrates consisting of (A) 3 μm circular wells or (B) posts. Scale bars in A and B are 50 μm, and the scale bar in the inset is 3 μm. (C) Simulaneous height and (D) transmission NSOM images of the sample in A shows partial filling of some of the wells and a strong contrast due to the substrate features. 73

Figure 2.11. (A) POM images of electrically poled films of 2.1 showing uniform birefringence that is extinguished when the sample is rotated 45 °. The scale bars are 250 μm. (B) The electrically poled film shows a strong SHG signal suggesting alignment of the optic axis parallel to the electric field (in the plane of the substrate). For the fit, $r^2 = 0.61$ 74

Figure 2.12. SHG signal from spin-coated films, both annealed and unannealed, taken at a fixed incident angle of 60° over 2000 pulses gives a slight signal above noise for the *p*-polarized

fundamental beam but not the *s*-polarized. Similar data of annealed films, stamped and unstamped, taken on a different day (*) at 45° incident angle shows significant variation in noise, whether due to laser performance or systematic error. 75

Figure 2.13. SIMS spectra of evaporated titanium-gold-titanium substrates (A) with and (B) without OTS treatment (courtesy of Dorothea Greishaber)..... 76

Figure 2.14. AFM image of 1 wt % 3BPOH on OTS. Height differences in line section: (red) 11.84 nm, (green) 10.81 nm, and (black) 9.81 nm (courtesy of Dorothea Greishaber)..... 78

Figure 2.15. AFM height and phase contrast images of 2.1 on piranha-cleaned silicon cast from (A) 1 mM and (B and C) 2 mM solution in chloroform. The striations visible in the phase image in C have a regular period of 10.6 nm as shown by the inset FFT. 80

Figure 2.16. AFM images of 2.1 cast from (A) 1 mM and (B) 2 mM solution onto OTS-coated silicon. Height differences in the line section of A: (red) 8.28 nm, (green) 8.56 nm, (black) 8.17 nm (courtesy of Dorothea Greishaber). 81

Figure 2.17. Schematic representation of the packing of supramolecular mushroom-shaped aggregates near a surface. In the bulk, free space (orange) between the "stems" can be partially filled by interdigitation of coil segments. However, free space (red) between surface-adsorbed nanostructures must be limited by other mechanisms, such as compression of the "caps" or tilting of the rods. 83

Figure 2.18. Molecular tilt angles calculated from equation 2.3 of layers of 2.1 deposited on various surfaces..... 84

Figure 2.19. FTIR spectra of molecules 2.1 – 2.3 with select peaks of interest labeled..... 85

Figure 2.20. (A) SHG of spin-coated films doped with DR1 dye (1:21 dye to host by weight) show signals indicative of a net orientation normal to the substrate in all cases ($r^2 > 0.97$ for both fits). (B) For 1:70 by weight mixtures, the signal for 3BPOH taken at a fixed angle of 45° over 1000 pulses appears to be slightly larger than for other films (label numbers indicate film thicknesses). (C) Thin films of pure disperse red cast from 0.1wt% solution in chloroform onto clean glass show an SHG signal while those cast onto glass treated with OTS show little signal. (D) DSC scans of 1:21 DR1:3BPOH mixtures show a slight shift in the liquid crystal transitions of 3BPOH..... 88

Figure 2.21. Transmission FTIR spectra of a KBr pellet and spin-coated film of DR1. The film shows a molecular orientation normal to the substrate as vibrations parallel to the molecular axis decrease and those perpendicular increase. 89

Figure 2.22. DSC scans of 3BPOH and 1:1, 3:1, and 10:1 molar mixtures of CB to 3BPOH (exotherm up). Depression of the liquid crystal transition temperatures of 3BPOH is observed, although the isotropization temperature, originally 250 °C, was never observed to go below 240 °C. The 10:1 mixture shows significant phase separation, although the melting temperature of CB is also depressed. 90

Figure 2.23. (A) Transmission IR and PMIRRAS spectra of films of 3:1 and 10:1 molar mixtures of CB to 3BPOH. The intensity of ν(C≡N) is observed to decrease in transmission, suggesting orientation of the molecule normal to the substrate. No vibrations attributable to CB are observed above noise in the more dilute mixtures. (B) Transmission IR and PMIRRAS suggest that films of pure CB alone exhibit minimal net molecular orientation. 91

Figure 2.24. (A) Transmission IR and PMIRRAS spectra of films of 0:1 and 10:1 molar mixtures of CB to 3BPOH. The increased intensity in PMIRRAS of the phenyl ring stretching vibrations at 1603 cm^{-1} and 1495 cm^{-1} (note that for CB, the later is shifted to 1483 cm^{-1}), the ester COC antisymmetric stretch at 1273 cm^{-1}, and the phenol CO stretch at 1190 cm^{-1} suggest a more normal orientation not only of the guest but of the host molecule as well. (B) The transmission spectra of the mixed films show a slight increase in the intensity of the phenyl CH out-of-plane deformations, also suggestive of a more normal orientation. 92

Figure 2.25. Schematic of the space coordinate system and relevant angles describing orientation of the rod segment of molecule 2.1. 96

Figure 2.26. Order parameter f_θ of the 3BPOH molecule calculated from the absorption intensities of the ester ν_{as}(COC) using equation 2.4. 96

Figure 3.1. Schematic detailing the geometry of the anisotropically etched silicon masters and the fabrication of polymer replica molds. 106

Figure 3.2. Chemical structures of PA molecules 1, 2, and 3. 108

Figure 3.3. SEM images of (A) a patterned (100) silicon master anisotropically etched with a grid pattern of sharp ridges, (B) a negative relief replica cast in PDMS showing sharp pyramidal tips, and (C) a positive relief replica cast in polyurethane off of the PDMS replica demonstrating that the resolution of the features is mostly retained. SEM images (D) of a negative PDMS replica loaded against a flat surface shows deformation of the pyramidal tip and gives an idea of the contact area. The inset scale bars for B and D are 6 μm and 2 μm, respectively. 110

Figure 3.4. Schematic detailing the geometric parameters involved in the indentation of a wedge and an axisymmetric cone. 112

Figure 3.5. Load versus displacement in compression of PDMS stamps with negative (square pyramids) and positive (wedges) surface reliefs. 113

Figure 3.6. SEM of a negative relief PDMS stamp after 10 sec exposure to oxygen plasma in the RIE showing slight rounding of the feature tip. 114

Figure 3.7. AFM height images of micro-contact printed dots of PA 1 using different ratios of glycerol to PA in the inking solution: (A) 0:1, (B) 1:1, and (C) 3:1 by weight, respectively. ... 116

Figure 3.8. AFM images of micro-contact printed lines of PA 1 using different ratios of glycerol to PA in the inking solution: (A) 1:5, (B) 1:1, and (C) 4:5 by weight, respectively. All images are height profiles except for A which is a phase image. 117

Figure 3.9. Plot of (■) the width of the microcontact printed dots and (○) the height of the deposited material or nanofibers versus the concentration of glycerol in the inking solution of PA 1. The stamping time was 60 sec. 118

Figure 3.10. Plot of the width of the microcontact printed lines measured at the thinnest point versus stamping time for inking solutions of PA 1 with glycerol:PA ratios (w/w) of (■) 4:5 and (○) 1:1. 119

Figure 3.11. AFM height images of micro-contact printed dots of PA 2 using different ratios of glycerol to PA in the inking solution: (A) 1:1 and (B) 2:5 by weight, respectively. 122

Figure 3.12. AFM height images of micro-contact printed lines of PA 2 using different ratios of glycerol to PA in the inking solution: (A) 2:5, (B) 4:5, and (C) 1:1 by weight, respectively. ... 123

Figure 3.13. Plot of the width of the microcontact printed lines measured at the thinnest point versus glycerol:PA ratios (w/w) for (■) PA 1 and (○) PA 2. 124

Figure 3.14. AFM height images of micro-contact printed (A) lines and (B) dots of PA 3 from an aqueous inking solution of 1:1 by weight of glycerol to PA. Scale bar of the inset magnification in (b) is 500 nm. 125

Figure 4.1. (A) Schematic briefly detailing the two patterning methods employed and (B) photographs of the setup used for sonication-assisted solution embossing. 133

Figure 4.2. SEM micrographs and AFM height contrast image of PDMS stamps molded from diffraction grating of (A) 1200 lines/mm, (B) 2400 lines/mm, and (C) 3600 lines/mm. 135

Figure 4.3. (A) SEM and (B) AFM images of a 2400 lines/mm PDMS stamp after being used for sonication-assisted solution embossing of PA 1. While the PA did appear to coat the stamp, the grooves were very rarely seen to be filled with nanofibers. 137

Figure 4.4. (A) AFM images (phase and height contrast, respectively) and (B) SEM images of nanofibers of PA 1 patterned by MIMIC in capillaries of 833 nm period. Inset in B is a magnification of the center of the image. 138

Figure 4.5. (A) SEM and (B) AFM height contrast images of nanofibers of PA 1 patterned by MIMIC in capillaries of 278 nm period. Inset in (A) is a magnification of the center of the image. 140

Figure 4.6. AFM height and phase images of aligned supramolecular nanofibers of PA 1. The fibers were embossed from a 5 wt % solution into lines with periods of (A) 417 nm and (B) 278 nm (height scales 106 nm and 99.8 nm, respectively). In (A), the widths of the nanofiber bundles were *ca*. 200–300 nm, and the average height of the lines was 55.1 ± 0.7 nm. The inset shows a fast Fourier transform (FFT) of the phase image, revealing the periodicity of the grating pattern (brightest spots toward the center) and the nanofibers within each line (diffuse bands to the outside). In (B), the widths were *ca*. 150 nm, and the average height of the lines was 33.3 ±

1.0 nm. The FFT of the phase image shows similar alignment along the channels as well as some off-axis orientation of the underlying residual layer of nanofibers. 142

Figure 4.7. AFM height and phase images of aligned supramolecular nanofibers of PA 2. The fibers were embossed from a 1 wt % solution into lines with periods of (A) 417 nm and (B) 278 nm (height scales 44.7 nm and 25.4nm, respectively). In A, the widths of the nanofiber bundles were *ca*. 150 nm, and the average height of the lines was 23.1 ± 0.7 nm. The inset FFT of the phase image clearly shows the periodicity of the nanofibers within each bundle oriented nearly parallel with that of the overall line pattern. In B, the widths were *ca*. 50-100 nm, and the average height of the lines was 13.4 ± 1.2 nm. Overall, the degree of alignment and uniformity of deposition was poorer for the 278 nm lines than for the 416 nm lines..... 143

Figure 4.8. Schematic of the proposed mechanisms of nanofiber patterning by MIMIC and by solution embossing..... 146

Figure 4.9. Polarized optical microscopy images of concentrated aqueous gels of PA nanofibers. Both scale bars are 100 μm. (A) PA 1 at roughly 15 wt % shows bright birefringence suggestive of a hexagonal liquid crystalline phase and possible phase separation from an isotropic phase. At higher concentrations, fingerprint textures indicative of a cholesteric phase can be seen, similar to those reported previously.[24] (B) PA 2 at roughly 7 wt % is more weakly birefringent but does display a texture that suggests the formation of a nematic phase. 149

Figure 4.10. SAXS of a 20 wt % aqueous gel of PA 1 with peaks fit to a mixed Gaussian-Lorentzian form (courtesy of James Hulvat). 150

Figure 4.11. (A) SEM image of the complex grating pattern master used in the present study. The master was fabricated by electron-beam lithography and dry etching a 100 nm oxide layer on a silicon wafer. The pattern consists of lines *ca* 200 nm wide with a periodicity of 400 nm. The lines turn corners of angles 135º, 90º, and 45º. A magnified image of the 135º corner is shown in (B)..... 151

Figure 4.12. SEM images of nanofibers of PA 1 aligned in capillaries defined by electron-beam lithography. (A) At a 135º corner, the nanofibers were able to turn the corner without breaking. (B) At a 45º corner, most nanofibers broke before continuing in the new direction but otherwise remained aligned within the channels. 152

Figure 5.1. Chemical structures of PA 1 and PA 2 including a schematic of the molecular structure of the nanofibers into which they assemble. 158

Figure 5.2. Schematic of the three treatments used to pattern the nanofibers. 161

Figure 5.3. Polarized transmission FTIR spectra of nanofibers of 1 aligned in gratings of 278 nm period. Spectra are normalized to the intensity of the residual silane Si-CH_3 peak at 1261 cm^{-1}. Transition dipole moments oriented parallel (*) and perpendicular (+) to the fiber structure can be readily identified as the incident polarization is rotated from 0° to 90° relative to the alignment direction. 162

Figure 5.4. Polarized transmission FTIR spectra of nanofibers of 2 aligned in gratings of 416 nm period. Spectra are normalized to the intensity of the residual silane peak at 1261 cm^{-1}. Transition dipole moments oriented parallel (*) and perpendicular (+) to the fiber structure can be readily identified as the incident polarization is rotated from 0° to 90° relative to the alignment direction. 163

Figure 5.5. PM-IRRAS spectra of PAs 1 and 2 patterned in gratings of 416 nm period..... 165

Figure 5.6. Schematic of the space coordinate system and relevant angles describing nanofiber orientation. 168

Figure 5.7. Upper and lower bound values of the orientational order parameter f_{φ} calculated from selected IR bands for nanofibers of (A) PA 1 and (B) PA 2 aligned in grating channels of different periodicities. 171

Figure 5.8. Optical micrographs of NPCs cultured on substrates of (A) aligned and (B) non-aligned nanofibers of PA 1. 177

Figure 5.9. SEM micrograph of a patterned sample of PA 1 recovered and lyophilized after 7 days in cell culture showing persistence of the topographical grating pattern. 178

Figure 5.10. AFM height and phase images of PA nanofibers patterned by sonication-assisted solution embossing, (A) before and (B) after brief immersion in ethanol. 180

Figure 6.1. Synthetic scheme for molecule 6.1 (courtesy of David Stone). 186

Figure 6.2. POM images of thick films of 6.1 showing radial patterns of birefringence suggestive of spherulitic structures. These structures grow larger and more disordered upon annealing at room temperature under saturated solvent atmosphere (right image). 189

Figure 6.3. AFM height and phase contrast images of a film of 6.1 showing a lamellar step of 12.4 ± 1.4 nm and a surface texture possibly indicative of an underlying molecular structure. 190

Figure 6.4. AFM height and phase images of a thin film of 6.1 showing a dotted surface texture. Assuming the "hole" in the middle of the height image reaches the underlying substrate, the thickness of the film is *ca.* 5 nm. FFT (inset) of the phase image shows that the pattern is periodic with a characteristic period of 18 nm..... 191

Figure 6.5. AFM height and phase images of thin films of 6.1 showing a striped surface texture. The film thickness is *ca.* 8 nm. The striped texture appears to evolve from a coalescence of the dotted texture observed earlier. FFT (inset) of the phase image shows that the 18 nm periodicity in the texture remains. 192

Figure 6.6. AFM height and phase images of films of 6.1 mixed with TiO_2 nanorods. 195

Figure 6.7. AFM height and phase images of friction-transferred PTFE fibers on glass. 197

Figure 6.8. Polarized transmission FTIR spectra of friction-transferred PTFE on silicon shows molecular alignment of the polymer chains parallel to the direction of drawing. 197

Figure 6.9. AFM images of 6.1 (A) spin-coated or (B) drop cast on friction-transferred PTFE on glass and annealed under saturated solvent atmosphere. Phase contrast images (all except image on right in A) show weak ordering of the dot texture adjacent to the PTFE fibers. The scale bar in the inset in A is 150 nm. 198

Figure 6.10. AFM height and phase contrast images of 6.1 patterned by solution embossing into diffraction grating lines of 416 nm period. The ridge heights are 74 ± 10 nm. 200

Figure 6.11. (A) AFM height and phase contrast images of 6.1 patterned by hot embossing a 170 nm thick film into diffraction grating lines of 416 nm period. The ridge heights are 105 ± 3 nm. (B) POM of the edge of the embossed area showing that the grating pattern polarizes light, as the transmitted illumation is extinguished when the sample is rotated 45 °..... 201

Figure 6.12. Absorption spectra of 170 nm thick films of 6.1 either unpatterned or patterned with a 2400 lines/mm grating topology. The solution embossed pattern shows an increase in signal due to incoherent scattering over the entire wavelength range. Second derivative fine structure enhancement shows an extra peak in the spectra of the hot embossed sample at 594 nm. 203

Figure 6.13. Fluorescence excitation spectra of unpatterned and grating patterned films of 6.1. The emission intensity at 545 nm differs little between the two samples. 204

LIST OF TABLES

Table 1.1. Typical energies of molecular interactions and how they scale with distance.[5, 9, 16-18] 26

Table 1.2. Predictions of the order parameter and the concentration ϕ of the isotropic and nematic phases relative to the aspect ratio *L/D* at the phase transition in different models of a lyotropic liquid crystal.[41] 32

Table 2.1. RMS roughness of different substrates. 77

Table 2.2. Thicknesses of layers of 2.1 deposited on various surfaces as measured from AFM of sub-monolayer and sub-bilayer films. 82

Table 2.3. IR vibrations of interest and their observed wavenumbers for 2.1 – 2.3.[246, 247] 86

Table 2.4. Possible values of the tilt angle θ for the rod segment of 2.1 calculated from spectroscopic data. 98

Table 4.1. Geometric parameters of diffraction grating masters. 136

Table 5.1. Absorption peaks analyzed and their assignments.[311, 312] 164

Table 5.2. Calculated direction cosines and α_{max} for TDMs of 1 in different channel sizes. 172

Table 5.3. Calculated direction cosines and α_{max} for TDMs of 2 in different channel sizes. 173

Table 5.4. Values of f_{φ} obtained by two methods of image analysis. 176

CHAPTER ONE

Introduction

Chapter 1: Introduction

1.1 Objectives and Significance

Since Feynman first pronounced in 1959 that "there's plenty of room at the bottom," nanotechnology has blossomed into an expansive and promising field of study.[1] The drive to both observe and create material systems on ever shrinking dimensions has been led by the discovery of unique properties that arise specifically as a consequence of confining matter to small volumes.[2] As such, nanotechnology today has been touted to hold the promise of changing everything from the clothes we wear to the computers we use to how we treat diseases. Efficient methods of synthesizing structures on the nanometer scale are crucial to this research effort. Supramolecular chemistry and self-assembly have emerged as promising routes to the bottom-up fabrication of unique nanostructures.[3-7] These strategies rely on tailoring non-covalent interactions through chemistry, leading to the parallel assembly of molecules into tunable, nanometer-scale objects, often with complex structures and low polydispersity.

However, for many of the sophisticated applications that have been envisioned, it is desirable that these functional objects be micro- or macroscopically ordered.[2, 8-10] Nanostructures can be highly anisotropic and, as a result, exhibit unusual and interesting properties. Without intervention, such systems may display short range order, but defects and grain boundaries often result in long range disorder, effectively neutralizing the anisotropic nature of the component objects.[11] Achieving a common orientation over large length scales could result in a net polarity that extends useful properties over the whole of the bulk material. Higher levels of order may also allow for coupling between individual objects, magnifying properties such as in magnetic materials.[12, 13] However, more advanced applications such as high-density data storage requires not only controlled orientations but controlled placement over

large areas. In this case, the need to be able to individually address specific elements requires that each element be registered at a known location. At a more fundamental level, increasing the degree of order in a material also improves the specificity with which their internal structures can be determined and leads to a better understanding of structure-property relations.

The following research is an exploration into the ways that micrometer and nanometer-scale patterning may be employed to alter and potentially enhance properties of selected self-assembling systems synthesized within our laboratory. Lithographically-defined features on these size scales may induce a specific orientation in these systems locally.[8, 14] Repeating the features could extend short range order over large areas, imitating long range order in a manner that may amplify useful anisotropic properties commonly neutralized by local disorder. Of particular interest is whether or not spatial confinement or patterned surface chemistry can improve ordering of the mesogens without the need to apply an external field. Toward this end, a number of lithographic patterning techniques are adapted for use on self-assembling, organic soft matter. We study the effect of these techniques on the degree of order and subsequent properties of selected self-assembling systems. The various ways in which increased order may be achieved and the forces responsible for inducing order are discussed. While other means of controlling alignment exist, a recurring theme of this work is that limiting the spatial freedom of a supramolecular system may alter its behavior in a predictable fashion. It is a philosophy similar to that which drives research on nanotechnology, which is that novelty can arise from simply shrinking the system.

1.2 Self-Organized Organic Materials

1.2.1 Forces Governing Organization Behavior

Self-organization and self-assembly describe the behavior of certain molecules or mesogens to spontaneously arrange themselves under specific conditions into higher order structures through the use of non-covalent interactions.[3, 6, 7, 15] A representative set of these interactions are listed in Table 1.1 along with their characteristic energies. Organic chemists, building on decades of expertise and more recently taking inspiration from biology, are becoming more and more adept at designing synthetic molecules that exploit these forces to exhibit unique behaviors. In general, any one force only acts in one direction, resulting in either precipitation or dispersion of the molecules. In order to achieve organization of a higher level, multiple competing or complementary interactions must be designed into the molecule, such as by stitching together two or more compounds that are otherwise immiscible.[3, 5]

Table 1.1. Typical energies of molecular interactions and how they scale with distance.[5, 9, 16-18]

Interaction or bond	Strength (kJ/mol)	Energy scaling with separation r
Single covalent bond	100-400	Complicated, short range
Coulomb	250	r^{-1}
Hydrogen bond	10-65, sometimes >100	Complicated, roughly r^{-2}
Ion-dipole	50-200	r^{-2} (fixed dipole), r^{-4} (free)
Dipole-dipole	5-50	r^{-3} (fixed dipole), r^{-6} (free)
Cation-π	5-80	Roughly r^{-n}, $n < 2$
π–π	0-50	Dispersion-related, r^{-n}
van der Waals forces	<5	r^{-6}, longer range for large bodies
Hydrophobic effects	Difficult to assess	Empirically, $e^{-r/\lambda}$, $\lambda = 1 - 2$ nm for $r < 10$ nm
Metal-ligand	0-400	Complicated

These forces can act in a hierarchical manner, leading to multiple levels of organized structure. For example, the amino acid chains that form proteins initially fold into secondary structures dictated by hydrogen bonding and hydrophobic collapse, but those structures are further distorted and assemble together into tertiary and quaternary structures to form the final protein.[19] It is not only the strength of a given interaction that determines the length scale at which it is influential but the specificity of the interaction and how the strength scales with size and distance. While strong, selective binding interactions may dictate the shape of an assembled nanostructure, it is often the more general, long-range interactions that determine if the nanostructures arrange themselves in an ordered array.[20-24]

A review of all the forces governing molecular aggregation would extend far beyond the scope of this thesis. However, in discussing control of order in dense arrays of nanostructures on the size scales of 10 nm or greater, two interactions are worth mentioning: van der Waals or dispersion forces and steric hindrance or excluded volume interactions. Dispersion forces arise from induced polarization of an atom's electron cloud by other atoms. While difficult to solve exactly, the interaction energy due to dispersion between two atoms at relatively large separation distances r (greater than the atomic radius) is approximated closely to decay as r^{-6}.[16] However, the effect is compounded as the system increases in size, so the interaction between two larger objects can be stronger and extend much farther, up to r^{-1}. This force can be attractive or repulsive, contributing to separation and other phase behaviors, but it is always attractive among like objects and pushes the system toward a more condensed phase.[16]

The attractive force is balanced by steric repulsion, moving nanostructures to smooth out fluctuations in packing density. Alternately, it may be more instructive to think of sterics in terms of an excluded volume interaction wherein mesogens restrict the motion of other

mesogens.[20, 21] Translational entropy is at a premium in the condensed phase, so the mesogens cooperatively arrange themselves to make the most efficient use of space and maximize freedom of movement. For spherical particles, this usually translates to an ordered, close-packed structure. This model is most applicable to particles that are relatively rigid and interact by "hard" steric repulsion. Some systems may behave as "soft" particles when solvated, in which case Ziherl and Kamien proposed that a minimum area rule such as in the packing of soap bubbles would be more appropriate and lead to non-close-packed architectures.[25] Implicit in this discussion is the fact that, in the absence of any anisotropy in its shape, the mesogen must be monodisperse in size in order to avoid packing defects and realize an ordered structure.

Depending on the system of interest, other long-range forces must be considered. Coulomb interaction energies are very strong and scale as r^{-1}, and electrostatic repulsion is commonly used to control size or dispersion of nanostructures.[3, 5, 23] However, some modeling and experimental work suggests that systems of mixed charge can display ordered phases, balancing charge compensation with mixing and hydrophobic collapse.[26-29] Solvation forces such as hydrophilic/hydrophobic interactions in aqueous solutions appear to decay as an exponential function, acting at even longer ranges and often play a critical role in the assembly of nanostructures.[16, 19] Lastly, interactions at surfaces and interfaces can nucleate order in the vicinity of the interface, offering several possible methods for controlling order.[20, 23, 30-33]

1.2.2 Block Copolymers, Liquid Crystals, and Colloidal Crystals

Three different self-organized systems are useful to review: block copolymers, liquid crystals, and colloidal crystals. Each system tends to exhibit a high degree of short-range order, often out to the micrometer scale. They have been extensively studied, and many attempts have

been made to extend the order observed in these systems over macroscopic distances. For these reasons, they may be useful to consider as analogous to more complex, self-assembled systems.

Block copolymers are polymer chains that consist of two or more segments or blocks of different chemistry covalently linked together.[22, 33-35] The blocks are most commonly linked in series, but they can also be synthesized in comb-like, branched, and radial star-like architectures,

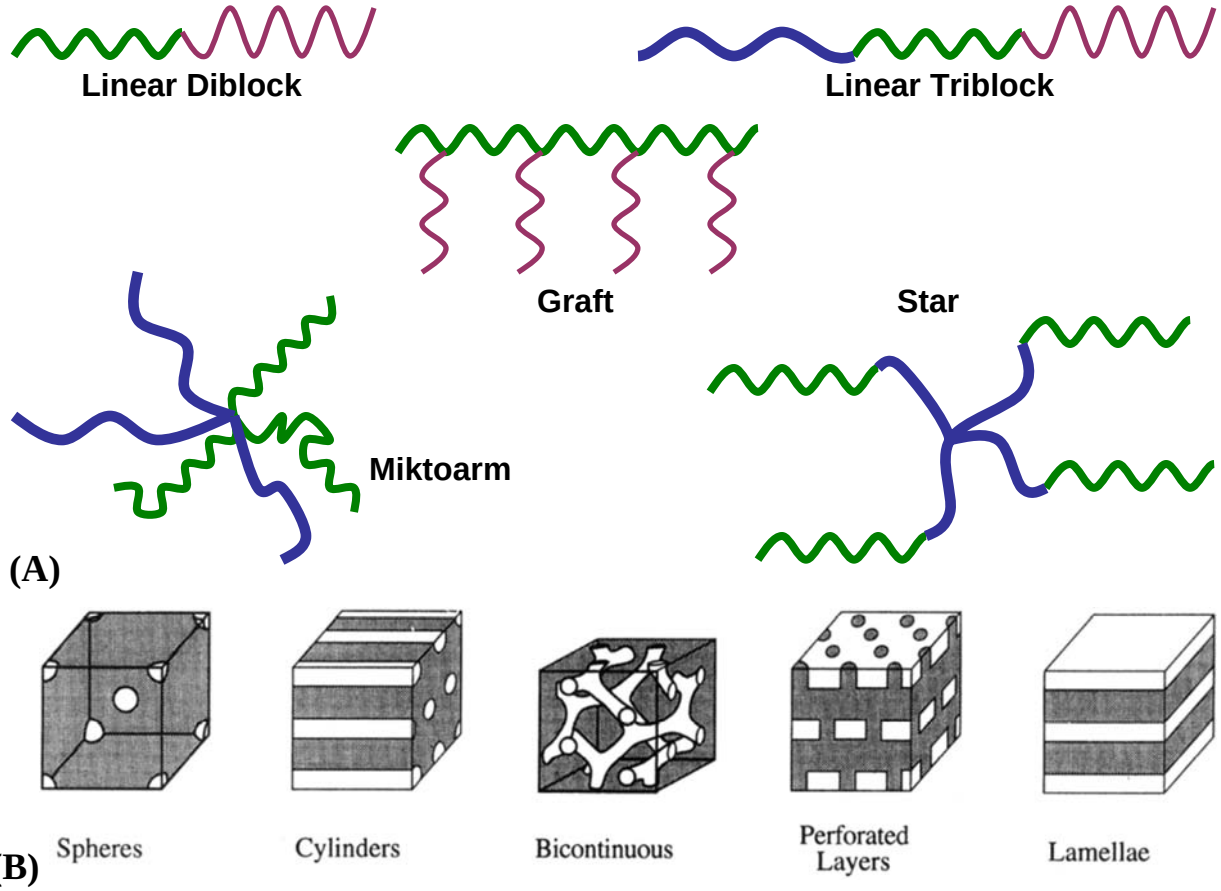

Figure 1.1. (**A**) Schematic illustrations of possible chemical architectures of block copolymers. (**B**) Diblock copolymers can organize into different ordered mesophases depending on the relative length and interaction parameter χ of each block (reproduced from ref. 36, copyright American Chemical Society).

as shown in Figure 1.1. The different blocks tend to phase separate, but because they are convalently attached, they are limited to separating into nanometer scale structures. The balance between surface energy and conformational entropy of the chains determines the size and shape of these micelles.[24] In diblock copolymers, these micelles are most often spheres, cylinders, or lamellae depending on the relative lengths of each block,[24, 36] but triblock copolymers can organize into a plethora of different architectures.[35, 37-39] If the copolymer is monodisperse, then the micelles are monodisperse and tend to arrange in well-ordered, close-packed arrays mediated in part by the entropic elasticity of the chains.

Liquid crystals are materials which, under a certain range of temperatures and concentrations, can exist in a phase that is fluid yet still retains some measure of long range order.[20, 40, 41] Most often, these systems consist of rigid, non-spherical moieties that are not fixed

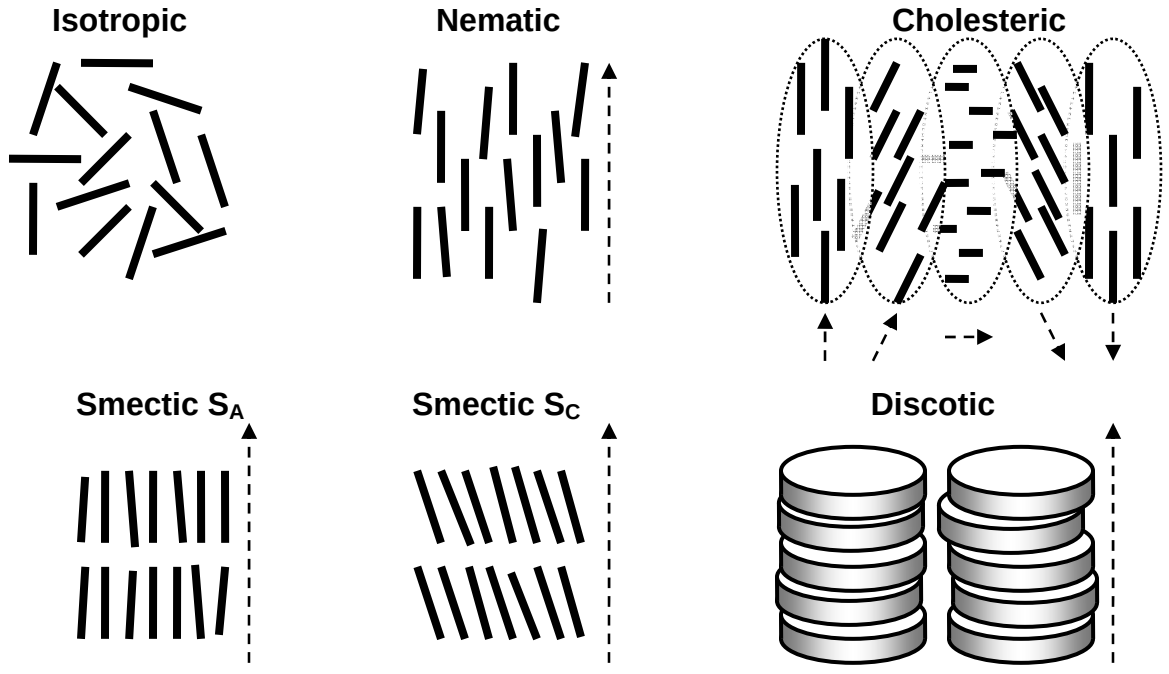

Figure 1.2. Schematic depiction of different liquid crystalling phases.

in place but cooperatively orient with respect to each other, spontaneously aligning in one general direction represented by the liquid crystal director. The mesogens are commonly rod-shaped or disc-shaped and can organize into different types of liquid crystals characterized by their dimensions of ordering as shown schematically in Figure 1.2.

The loss of rotational freedom or entropy due to alignment is compensated for primarily by one of two different factors. For thermotropic liquid crystals in which the liquid crystalline phase is temperature-dependent, this factor is the enthalpic payoff from more intimate intermolecular interactions.[20, 41] For lyotropic liquid crystals wherein the liquid crystalline phase depends on concentration, this factor is greater translational freedom. Thermotropic liquid crystals usually consist of small molecules for which enthalpic interactions such as van der Waals forces between mesogens are comparatively strong. The lyotropic phase is more relevant to this discussion as it most often applies to liquid crystals composed of larger inorganic particles or supramolecular structures in which inter-mesogen forces are relatively weak.[20, 41] Onsager proposed a lyotropic model in the extreme case in which the mesogens were rigid rods that only interacted by repulsive steric forces.[20, 42] This model approximates virial coefficients and is most applicable to dilute solutions. Flory proposed a lattice model on similar principles but which could also include "soft" interactions between the rods and the solvent.[43, 44] This model is more applicable for higher concentration solutions and tends to be more accurate in predicting the concentration at the transition but overestimates the order parameter. One last model proposed by Khokhlov and Semenov is geared more towards semi-flexible polymers and predicts much lower order parameters than the previous two treatments.[41, 45] All three models are based on the same basic principles and predict a first order transition from the isotropic to a more concentrated nematic phase, as well as an increase in the order parameter with increasing

concentration and mesogen aspect ratio. Typical predictions of the models are compared in Table 1.2.

Table 1.2. Predictions of the order parameter and the concentration ϕ of the isotropic and nematic phases relative to the aspect ratio *L/D* at the phase transition in different models of a lyotropic liquid crystal.[41]

Model	Isotropic ϕ_i*L/D	Nematic ϕ_n*L/D	Order parameter S_c
Onsager	3.3	4.2-4.5	0.79-0.84
Flory	7.89	11.57	0.92
Khokhlov, Semenov	10.48	11.39	0.49

Colloids are micrometer or sub-micrometer scale solid particles suspended in a fluid medium.[23, 46] They are usually spherical, and if they are made with sufficiently low polydispersity, they tend to deposit out of solution in well-ordered, close-packed structures analogous to atomic crystals. Colloids are useful to discuss because some similarities can be drawn between them and suspensions of discrete, self-assembled nanostructures. Close-packed order is a result of convective flow, excluded volume effects, and surface tension or capillary forces acting on the particles as they deposit from solution.[21, 47] Colloids and nanoparticles of different shapes, sizes, and materials have been shown to exhibit liquid crystalline behavior[48] or assemble into a wide variety of binary superlattices.[21, 49-51] Other forces such as electrostatics, dipole-dipole interactions, and the surface functionality of the particles may influence the aggregated structure.[52, 53]

1.2.3 Applications of Self-Organized Systems and the Need for Long Range Order

The natural order that arises from these self-organized systems can lead to unique properties and has garnered significant attention as a facile means to template order in other materials or create useful devices. For example, block copolymers have been used to template the growth of arrays of inorganic quantum dots[54, 55] or nanowires[56] that are of interest for applications such as magnetic storage and integrated circuits. Liquid crystals are already used in display technologies as a light polarizing material whose orientation can be easily switched.[40] Their structure and orientational order have also been exploited to template such materials as mesoporous inorganics,[57-59] conducting polymers,[60, 61] and carbon nanotubes.[62] Colloidal crystals are interesting lithographic templates[63, 64] and as photonic band gap materials capable of trapping and guiding light of wavelengths on the same order as the particle diameter.[65] Binary superlattices of inorganic nanoparticles may also exhibit unique behaviors due to electrostatic or magnetic coupling.[13, 53, 66-68]

However, the fact is that ordering is governed by relatively weak, non-specific, non-covalent interactions, so defects in the ordered structure occur frequently and are difficult to eliminate completely. Defects can take several forms, including grain boundaries, point defects, and disclinations, and they are almost always disruptive to material properties. With respect to the examples above, imperfections in block copolymer micelle packing make it more difficult to locate and individually address each feature, a necessary ability for data storage. Packing defects in photonic crystals act as scattering centers and lead to light leakage.[65] Disclinations in liquid crystals disrupt uniaxial alignment and limit the ability of liquid crystals to polarize light. Long-range order in unperturbed films of these materials is commonly limited to micrometer-scale

domains depending on the specific system. This length scale is too small for some applications, so an effective means of extending long range order is highly desirable.

1.3 Supramolecular Self-Assembly

1.3.1 Common forces involved in self-assembly

Self-assembly takes advantage of very specific intermolecular interactions to control aggregation, and thus has proven useful for generating nanostructures of complex shapes, such as three-dimensional networks,[69-71] two-dimensional structured layers,[72-75] one dimensional fibers, helices, ribbons, and tubules,[9, 76-83] and zero-dimensional particles, boxes, and mushroom-shaped aggregates.[6, 84-88] Three commonly used interactions are hydrophobic effects, hydrogen bonding, and π–π stacking. Along with cation-π interactions, these forces are exploited extensively in biology, influencing protein folding, DNA hybridization, receptor-ligand recognition, and other processes.[89] Indeed, many synthetic self-assembly schemes are biologically inspired or directly employ biological compounds.

Hydrophobic interactions are responsible for the assembly character of amphiphilic surfactants or soaps, molecules that have a hydrophobic and hydrophilic segment covalently bonded together. In aqueous solutions, the hydrophobic portions tend to collapse and aggregate together, exposing the hydrophilic components on the surface. In certain non-polar solvents, the reverse may occur. This effect is thought to arise from the complex structure that water molecules adopt around the amphiphile in aqueous solution, making the interaction significant out to a long range and the primary initiator of aggregation.[16] The competition between surface energy, conformational entropy, and hydrophobic collapse determines the size and shape of the assembly.

Hydrogen bonding is a strong but very directional, short-ranged interaction in which a hydrogen proton that is covalently linked to an electronegative "donor" atom, usually oxygen or nitrogen, binds to other electronegative "acceptor" atoms. The highly directional nature of this interaction makes it ideal for molecular recognition, and multiple hydrogen bonds can be used to create very specific linkages and structures.[5, 73, 78, 84] π–π interactions describe the affinity of opposing π orbitals of highly conjugated molecules to associate, resulting in the ordered stacking of molecules. This interaction is attributed to the high polarizability of the electron cloud in the π orbitals and can be loosely thought of as an enhanced dispersion force.[5, 17, 18] While extended π–π stacking primarily results in the formation of one-dimensional objects, the structural diversity of the assemblies discovered so far that utilize this interaction has not been lacking.[9, 90]

Employing these interactions and more, synthetic chemists can create compounds that assemble into nanostructures that have a high degree of molecular order. However, the forces that generate these structures are strong and specific while the forces that dictate how these discrete objects interact and pack can be weaker and long range, so it is often possible to treat each of them independently of each other. A discussion of self-organized systems as well as self-assembling systems is useful because common forces are at work in both cases, and strategies that improve order in one may also be applicable in the other.

1.3.2 Brief introduction to self-assembling systems of interest

Materials that are composed of one or more types of supramolecular units of highly regular shape, size, and chemistry are of technological interest because unique material properties may arise not only from the arrangement and chemical nature of the molecules but of the larger nanostructures as well.[3, 5] As a general strategy, molecules termed "rod-coils" that

consist of one or more rigid rod-like segments covalently bonded to one or more flexible coil-like segments have the potential to assemble into many interesting structures as a result of preferential aggregation and collapse of the rod segments.[6, 91-93] A class of rod-coil molecules synthesized by Stupp, et al. consisting of a rigid biphenyl rod segment and a flexible oligo(isoprene)-co-oligo(styrene) tail are known to self-assemble into mushroom-shaped clusters with the rods crystallizing together as the stem and the coil segments flaring out at one end as the cap.[6, 94] The mushrooms have dimensions of about 10nm and stack head-to-tail to form a polar smectic liquid crystal. This behavior is shown schematically in Figure 1.3 and is proposed to arise from a specific level of competition between van der Waals and dipole-dipole

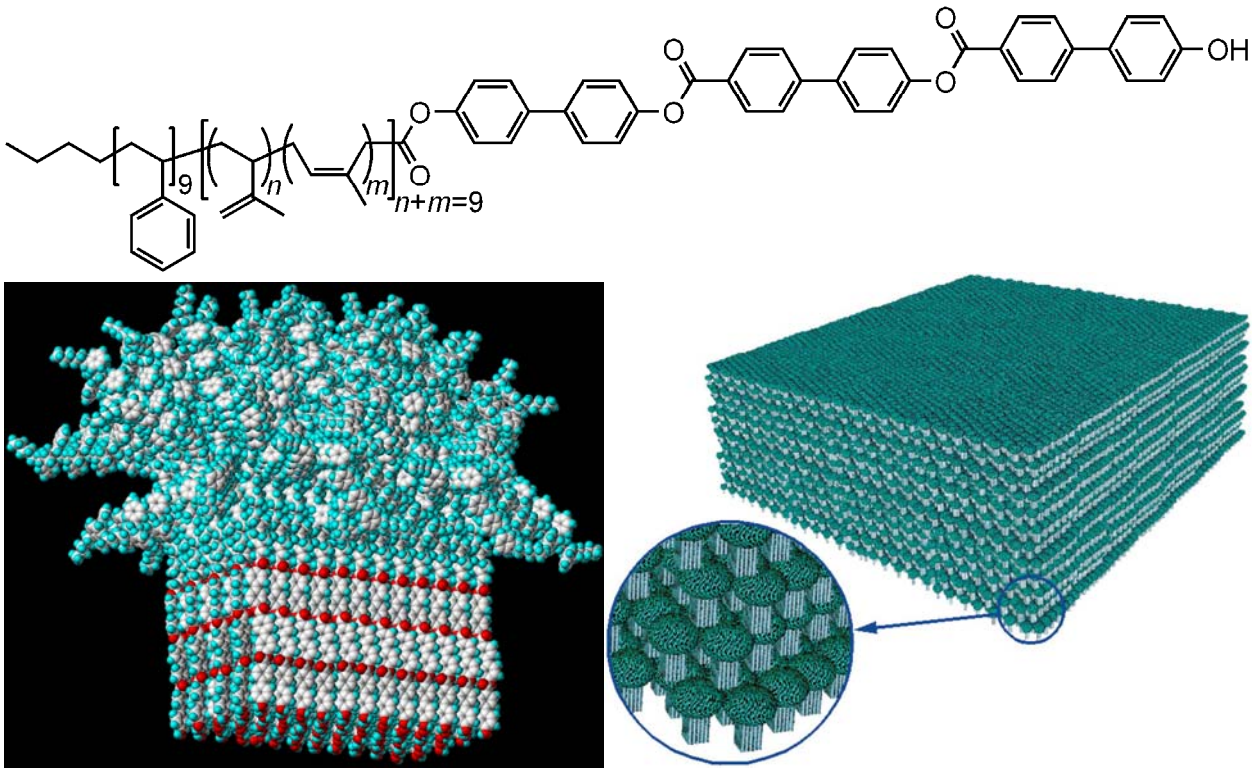

Figure 1.3. Chemical structure of a rod-coil molecule that self-assembles into mushroom-shaped nanostructures, and schematic depiction of the stacking of the nanostructures into a polar film (reproduced from ref. 6, copyright AAAS).

interactions.[95, 96] It was one of the first demonstrations of the ability of supramolecular chemistry to design molecules that can assemble into regular, discrete, nanometer-scale objects with an aggregate mass of 100 kDa or more. These particular structures are interesting because they are non-centrosymmetric, meaning they lack a center of inversion symmetry, and they exhibit a permanent dipole related to their particular architecture. As a result, the material exhibits properties characteristic of polar materials including second harmonic generation (SHG)[6, 97] and piezoelectricity.[98]

Many variations on rod-coil molecules use conjugated oligomers such as oligothiophene and oligo(*p*-phenylene vinylene) as the rigid rod segment because they tend to show a strong affinity to pack regularly with each other due to π–π stacking.[99-107] More importantly, highly conjugated compounds often exhibit useful optical and electrical properties that are of interest for many technological applications including organic electronics, sensors, photovoltaics, and photonics.[108-112] The addition of coil segments serves the dual purpose of introducing competing interactions to drive self-assembly and improving the solubility of the conjugated molecules. Tajima and coworkers[113, 114] reported the synthesis of amphiphiles based on oligophenylene-vinylene such as the one shown in Figure 1.4 that are soluble in polar solvents and self-assembled into lamellar structures. The conjugated rod segments pack together in a mesophase through which energy transfer or charge conduction may occur. In one example, the amphiphile templates the mineralization of silica into a hexagonal phase with the organic confined to cylindrical pores.[114] This material displays remarkable Forster resonance energy transfer (FRET) properties as a result of confinement of the organic within the ordered, nanostructured

environment. Controlling molecular aggregation at this length scale has the potential to greatly improve material performance in optoelectronic devices.

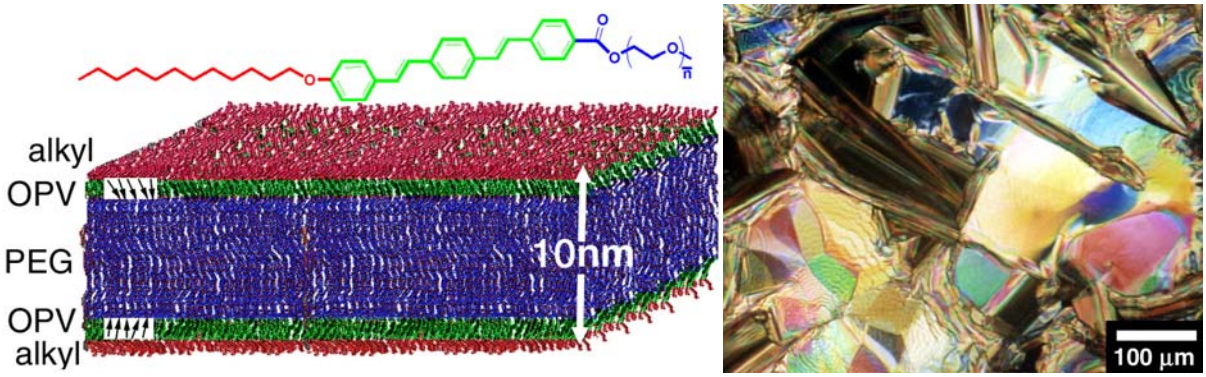

Figure 1.4. Chemical structure of an oligo(*p*-phenylene vinylene) amphiphile that assembles into a lamellar structure and organizes as a liquid crystalline phase as seen from the polarized optical micrograph (reproduced from ref 113, copyright American Chemical Society).

Hydrogen bonding and hydrophobic collapse are also effective means of controlling self assembly and are employed extensively in biology to control the folding of proteins. Peptide-amphiphiles (PAs) are a class of molecules that consist of an aliphatic tail linked to an oligopeptide segment. They have been investigated in recent years and shown to assemble into a wide range of one- and two-dimensional supramolecular structures.[115-118] Hartgerink and coworkers[81] extended this work by synthesizing PAs that were more cone-shaped on the theory that the smaller packing parameter[16] would result in the assembly of one-dimensional nanostructures. These PAs self-assemble into cylindrical nanofibers from aqueous solution by burying their alkyl segments in the core of a nanofiber and displaying their peptide sequences on the surface as shown in Figure 1.5.[81] Self-assembly is mediated by a balance between hydrophobic collapse and electrostatic repulsion. Conditions that limit electrostatic repulsion

such as the addition of salt, changing pH, and increasing concentration tend to induce nanofiber formation.[81, 119-122] The nanofibers intertwine into networks that have been studied in our laboratory as three-dimensional tissue scaffolds for a variety of applications in regenerative medicine, including biomimetic hydroxyapatite mineralization,[81] neural progenitor cell differentiation[120] and blood vessel formation.[123] The peptide segments exposed on the periphery

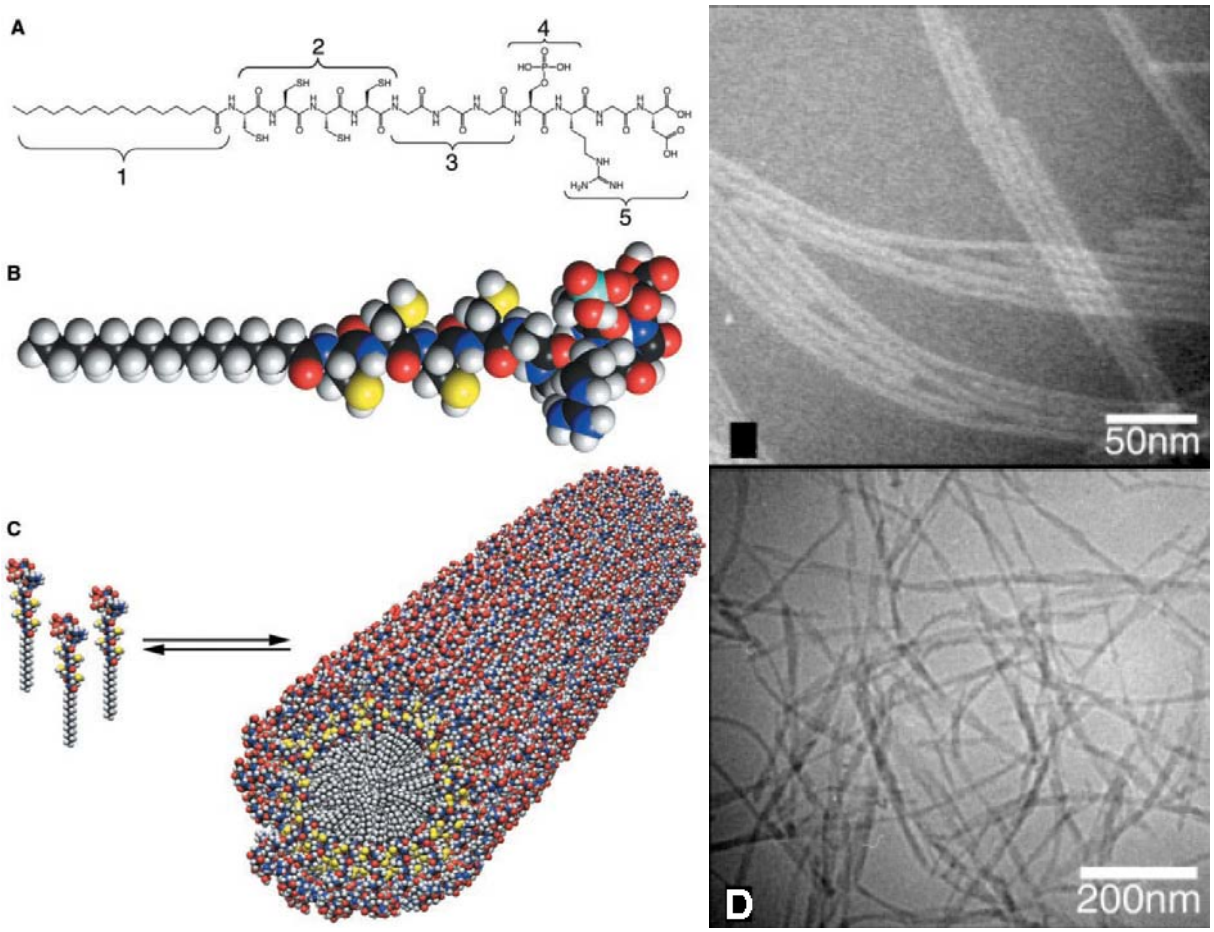

Figure 1.5. (**A**) Chemical structure and (**B**) space-filling model of a self-assembling peptide-amphiphile molecule consisting of an aliphatic tail (1), cross-linking segment (2), flexible spacer (3), and functional head group (4, 5). (**C**) Schematic depiction of self-assembly of the molecule into nanofibers, and (**D**) transmission electron microscopy images of the nanofibers. (Reproduced from ref 81, copyright AAAS)

of the nanofibers can be modified to match known, bioactive sequences, endowing the nanofibers with the potential capacity to provide critical cell signaling. The advantage of such a network is that it mimics many aspects of the extracellular matrix, the complex scaffold that supports cells in normal tissue.

1.3.3 Difficulties in Aligning Self-Assembled Nanostructures

Self-assembled systems are often plagued by the same issues that limit the application of self-organized systems, most notably high defect densities.[11] Thus, controlling the placement and orientation of self-assembling materials over macroscopic distances may dramatically improve function. In addition, the molecular architecture self-assembled nanostructures can be quite complex. Large-scale ordering of these nanostructures would make it easier to study and determine their architecture by X-ray or spectroscopic techniques. This information is useful both for understanding the properties of the supramolecular system and for designing new molecules.

However, alignment of self-assembled materials is not without particular difficulties. The wide variety of supramolecular systems currently known makes any one technique unlikely to be universally successful. Also, methods of alignment generally involve the application of a controlled force on the material. These forces can be weak, such as steric repulsion from a surface, or very strong, as with mechanical shearing. Because the nanostructures are held together by non-covalent bonds, there is a danger of the objects being disassembled by the applied force.[124]

Molecules that self-assemble into discrete, nanometer-scale entities present a unique set of challenges. If the nanostructures are small, thermal energy alone may disrupt any induced

order due to Brownian motion unless the objects are tightly bound. The opposite problem arises if the nanostructures are large, that is, the objects may be difficult to orient in the first place because their mobilites are so low. In the kinetic theory of thermal energy, the velocity of a particle scales as the square root of the mass.[16] Depending on the system, supramolecular nanostructures may reach 1 to 100 MDa or more in mass. Using thermal energy to increase mobility is not often desirable because it is a harsh condition and may lead to unwanted reactions. Solvating the nanostructures is a milder treatment, but it also brings up additional complications associated with the introduction of another component to the system, such as a disruption of the applied forces and disassembly of the aggregates.

1.4 Alignment and Patterning of Self-Organized and Self-Assembling Systems

1.4.1 Alignment by External Fields and Interface Sweeping

One of the easiest ways to induce alignment in self-organized systems is to apply an external field or gradient to the material. Long range order in block copolymers has been achieved to some extent by applying electric,[56, 125-127] magnetic,[128] or mechanical shear[129-131] fields. Similar fields are also used to align liquid crystals, and in fact, the rapid response of liquid crystals to an applied electric field is necessary for proper function in display applications.[40] Supramolecular polymers and liquid crystals have been aligned by external fields,[132-135] but discrete, self-assembled nanostructures tend to be more difficult to align by this method because of the necessary presence of solvent. Some success has been shown in aligning certain one-dimensional, self-assembled nanostructures by the use of an electric field.[136, 137] Because liquid crystal phases are easily aligned by applied forces, another strategy has been to

mix 1-D, supramolecular nanostructures into a liquid crystal host.[138-140] In this manner, alignment of the nanostructure is controlled by the alignment of the liquid crystal.

For this method to be applicable, the material must have an inherent anisotropy defined by a director that will respond to the force field in a manner that reduces the field energy. This condition is satisfied in most self-organized systems of interest, making the technique more materials general than most, even if the mechanism of alignment differs. For example, most liquid crystals have a permanent or easily induced dipole that will orient parallel to the applied potential gradient.[40, 141] But striped phases of block copolymers will align under an electric field only if there is sufficient contrast in the dielectric constant between the two blocks.[126] One-dimensional nanostructures might even align under a third mechanism in which dielectrophoretic motion of the object during deposition out of solution results in parallel alignment due to shear.[136]

Strong forces can also exist at the interface between phases, and controlling the movement of the interface may result in alignment of one of the phases. This concept is commonly applied in Langmuir Blodgett techniques, where the solution-air interface line is carefully dragged across a substrate surface either by slow removal of the substrate or by gradual evaporation of solvent.[142] Material is drawn from solution to the drying front by capillary and convective forces where it deposits onto the substrate. During deposition, the material is acted upon by surface tension forces, resulting in alignment and close-packing. Drying front combing and related techniques such as zone casting have been used to align a variety of one-dimensional nanostructures[143-147] as well as deposit aligned block copolymer films[148] and well-ordered colloidal crystals.[149, 150] While this method has proven effective in aligning some supramolecular liquid crystals and one-dimensional assemblies,[76, 151-155] its applicability to other self-assembling

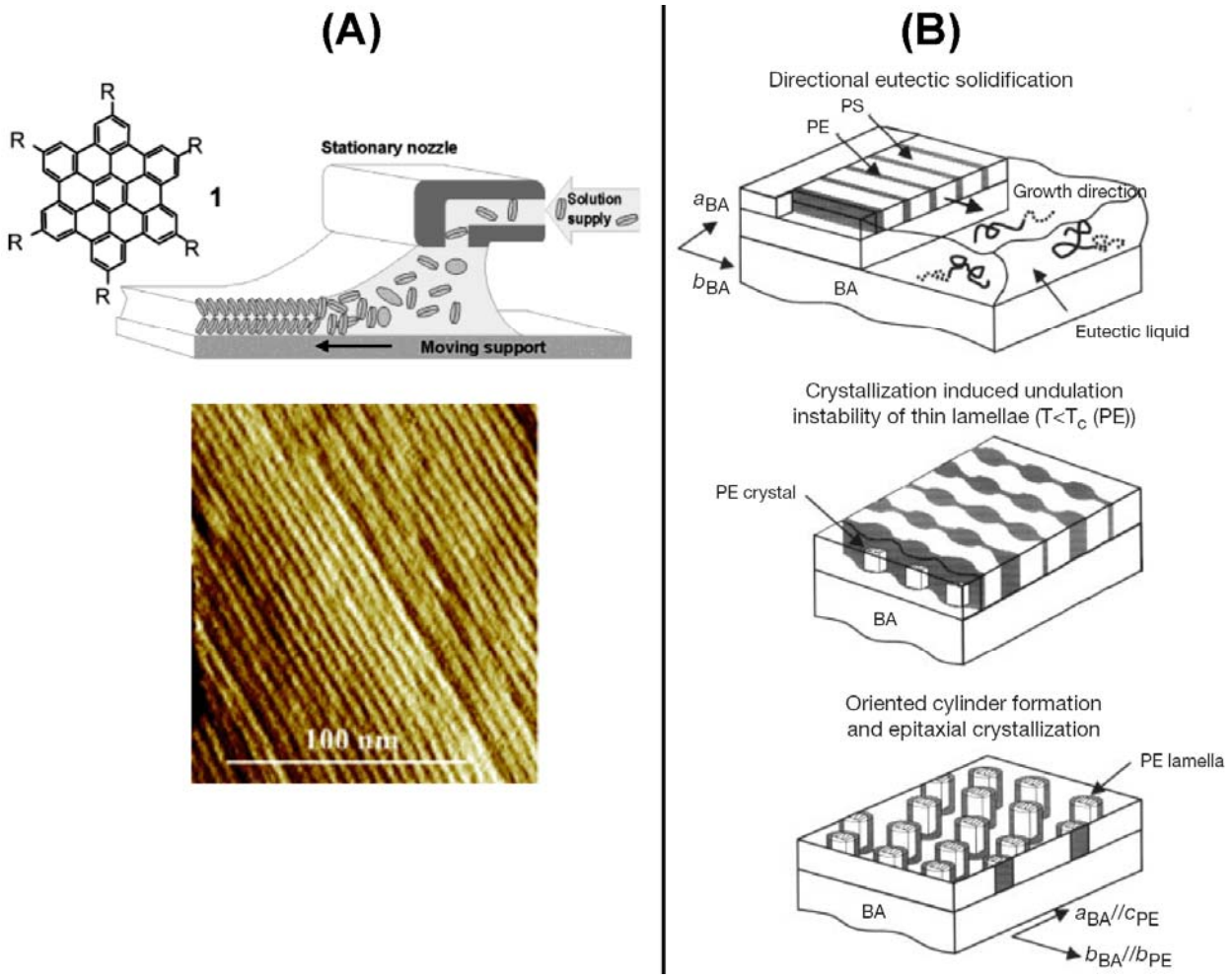

Figure 1.6. Schematic illustrations of nanometer-scale ordering by (A) zone casting of discotic graphene molecules (reproduced from ref. 154, copyright American Chemical Society) and (B) directional solidification of a polyethylene-polystyrene block copolymer (reproduced from ref. 156, copyright Nature Publishing Group).

systems is dependent on the assembly behavior of each system in solution. The concept of interface sweeping can also be applied to a solid-melt interface by carefully controlling the movement of a temperature gradient. De Rosa et al. demonstrated the alignment of the hexagonal phase of a block copolymer by this method of directional solidification, shown schematically in Figure 1.6.[156, 157]

One drawback of these techniques is that while it is easy to align large areas, one is most often limited to uniaxial alignment. Another disadvantage of external fields is the fact that the self-organized and self-assembled components must have sufficient mobility to rearrange themselves in response to the field, but at the same time, if the phase is too fluid, relaxation times are fast and the alignment does not persist after the field is turned off.[158, 159] For block copolymers, the material is often annealed while the field is applied. Most liquid crystals require a different influencing force to achieve persistent alignment. Discrete nanostructures must be deposited out of suspension or solution during patterning, which means that the nature of the material and its response to the applied field may vary with solvent evaporation. Lastly, while the methods discussed above can be very effective in aligning self-organized and self-assembled systems, they generally cannot control the spatial placement and patterning of the material without the aid of additional lithographic steps.

1.4.2 Surface Patterning and Graphoepitaxy

Because of the concerns regarding alignment by external fields, it may be preferable to employ a method of ordering that is permanently defined by the substrate or the material so that the effect is persistent. For systems that are deposited on a substrate, patterned surface interactions[160, 161] or topologies[31, 32, 162-164] show promise in controlling order in this regard. Surface treatments are already employed commercially to induce large-scale, stable alignment of liquid crystals in display technologies.[40] Even without patterning, liquid crystal mesogens inherently orient themselves near a surface at least on a small scale.[165] The interface can be with any other phase of matter including air, and the liquid crystal can orient parallel, perpendicular, or at a tilted angle to the interface depending on the specific nature of the intermolecular forces

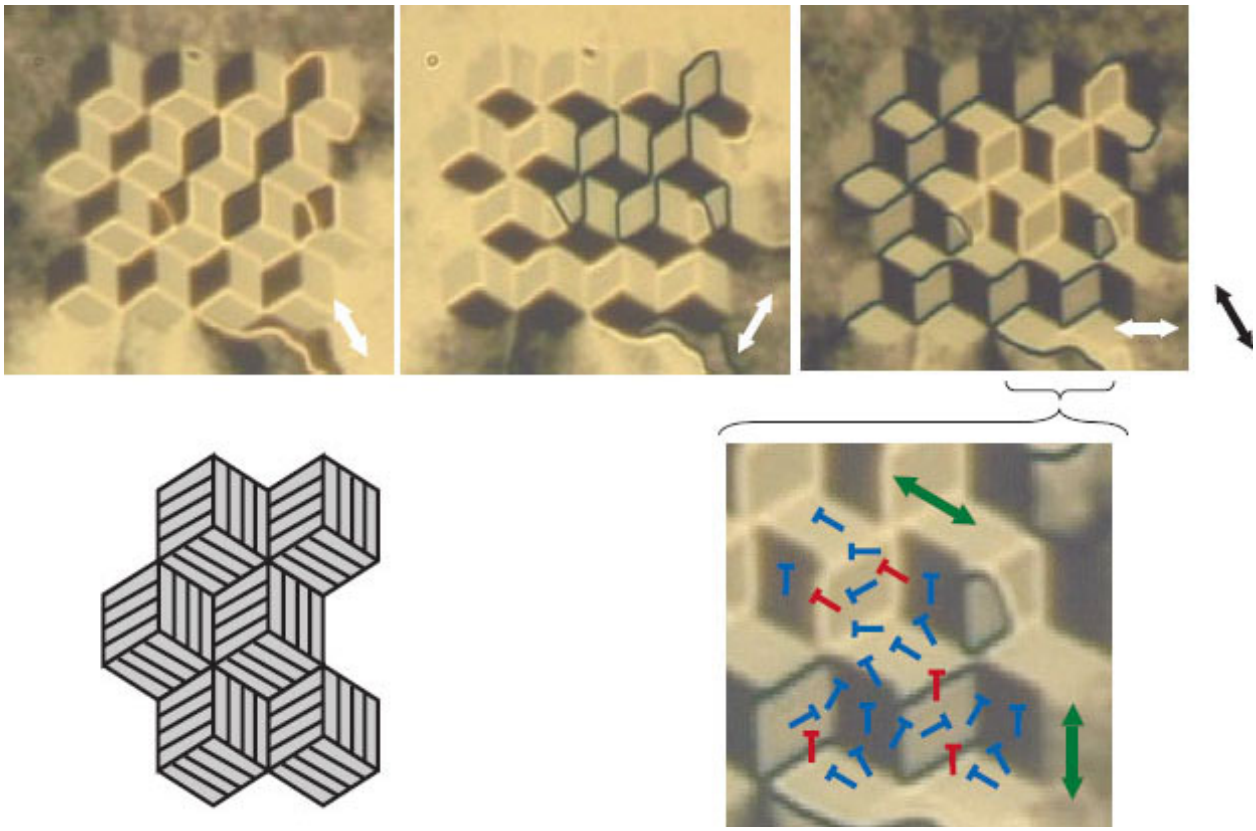

Figure 1.7. Tristable liquid crystalline orientation achieved by surface rubbing with a scanning probe tip and imaged by polarized optical microscopy (reproduced from 168, copyright Nature Publishing Group).

present.[165-167] Rubbed polymer surfaces are known align certain nematics over large areas in the direction of rubbing, theoretically due to grooving of the surface and anchoring of the mesogens to aligned polymer chains.[30, 168-171] Smectic phases can also be aligned in this manner with the mesogens parallel and the lamellae perpendicular to the grooving direction.[167, 172] Rubbing of a polymer surface is most often performed by the controlled application of shear with uniaxial orientation over large areas. But shearing can also be performed at sub-micrometer length scales with arbitrary orientation by the application of a scanning probe tip. Kim et al employed this method to fabricate a substrate that induces tristable liquid crystalline orientations as shown in

Figure 1.7.[168] However, this versatility in orientation comes at the cost of being able to efficiently pattern large areas.

Creating patterns of different surface chemistries on the micrometer scale or smaller has also been employed to influence the order of self-organized systems.[160, 161, 173] Spatial patterning of different chemical functionalities can be achieved by conventional photolithography or electron-beam lithography, although more unconventional methods such as scanning probe lithography and soft lithography are very popular and will be discussed in the following section. A wide variety of chemistries have been studied for this purpose including directionally crystallized aromatic hydrocarbons,[174-176] thiol- and silane-based SAMs,[161, 177, 178] and polyelectrolytes.[179, 180] In the simplest case, different functionalities are deposited that either attract or repel the nanostructures resulting in selective adsorption to the substrate. This method has been used to control the deposition of colloidal particles,[180, 181] block copolymers,[160, 161, 174-176] liquid crystals,[182] and supramolecular mushroom aggregates,[183] to name a few. The surface interactions may also be tailored to favor adsorption of a selected segment or conformation of the molecule of interest. Reinhoudt et al. employed supramolecular interactions to selectively deposit adamantine-functionalized molecules on molecular printboards of cyclodextrin SAMs with controlled orientation relative to the surface normal.[88, 184] Kim et al. patterned stripes of different surface chemistries with a resolution of tens of nanometers by EUV interference lithography and showed that the pattern could effectively control the orientation of block copolymer lamellae.[160] Beyond the latter example, however, demonstrating in-plane ordering of adsorbed, self-organized systems solely by patterned surface chemistry is rare, let alone demonstrating order more complex than uniaxial alignment.

Micrometer-scale topological patterns can be easily fabricated over large areas with arbitrary designs on rigid substrates by conventional photolithograpy and etching techniques. Steric hindrance of nanostructures near surfaces and interfaces can result in close-packing, so while the patterned features may be much larger than the self-organized unit cell, they may act as nucleation sites for the growth of larger domains of controlled orientation. Segalman et al. dubbed this phenomenon "graphoepitaxy" and demonstrated how topological surface patterning even at length scales much longer than the micelle periodicity can induce ordering and orientation in a monolayer of spherical micelles in a block copolymer film.[31, 32] Single grains of preferred orientation nucleate at the vertical sidewalls of microfabricated silicon nitride mesas and extend to span a gap of up to 4.5 μm, at least five times wider than non-patterned grains as shown in Figure 1.8. Topologically patterned substrates have also been used to align liquid crystals[133, 185] and colloidal crystals.[186-189] The geometry of the features can be tailored to induce

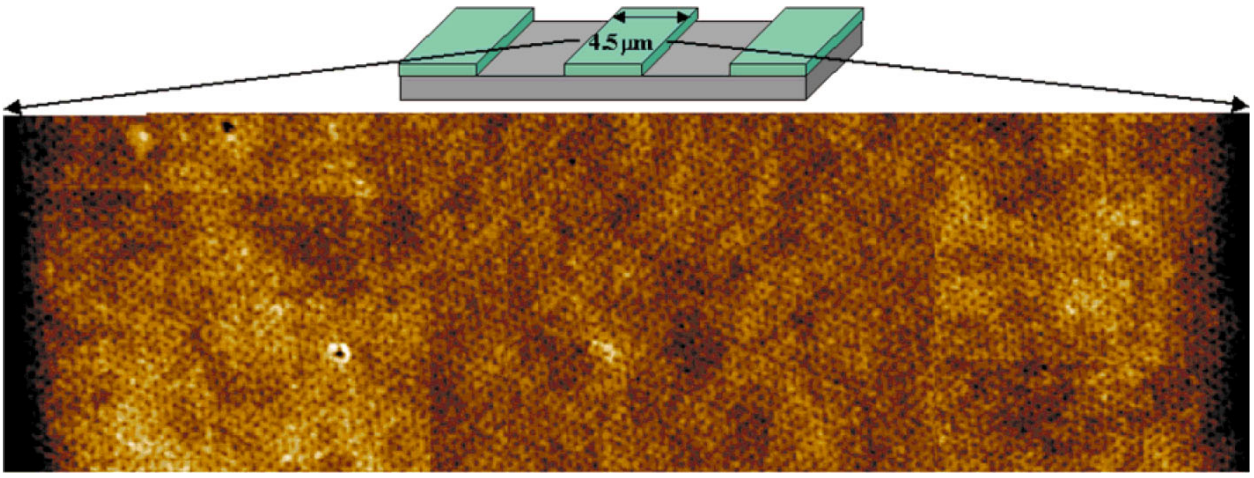

Figure 1.8. AFM image of a single, large block copolymer domain ordered by graphoepitaxy on a topographically patterned surface (reproduced from ref. 32, copyright Wiley Interscience).

the colloidal crystals to display non-close-packed facets or crystal structures,[187-189] an important goal for photonic applications.

Surface patterning is not always the best choice for creating order in some applications as the processing steps may be incompatible with the materials or the surface pattern itself could interfere with other functions. In addition, ordering at the surface may not extend very far into the bulk. However, the latter point becomes less of an issue as devices continue to shrink, and it is still quite attractive to be able to generate persistent order in a material simply by casting it on a prepared substrate. Graphoepitaxy in particular demonstrates how one can manipulate steric forces and free volume effects, the same factors governing order in many self-organized systems, to extend nanometer-scale order over micrometers without the need for high-resolution lithography.

1.4.3 Scanning probe and Soft Lithographic Techniques

Because conventional methods of lithography and etching may not be compatible with many organic soft matter systems or desired substrates, significant attention has been focused in recent years on unconventional lithographic techniques including scanning probe lithography and soft lithography.[190-192] Scanning probe lithography involves the use of a sharp probe tip to pattern a surface either by direct mechanical contact, localized transport of a fluid (as in dip-pen nanolithography, or DPN),[193, 194] or focused application of energy (as in electrical current or light),[195-199] as shown in Figure 1.9. Scanning probe techniques excel at being able to directly write arbitrary patterns with high resolution, but they are serial processes and cannot efficiently pattern large areas. Still, DPN may be an effective means of directly drawing patterns of supramolecular "inks." One limitation is that because the volume of fluid being manipulated is

small, larger supramolecular structures may not be able to assemble properly or to sufficient sizes.

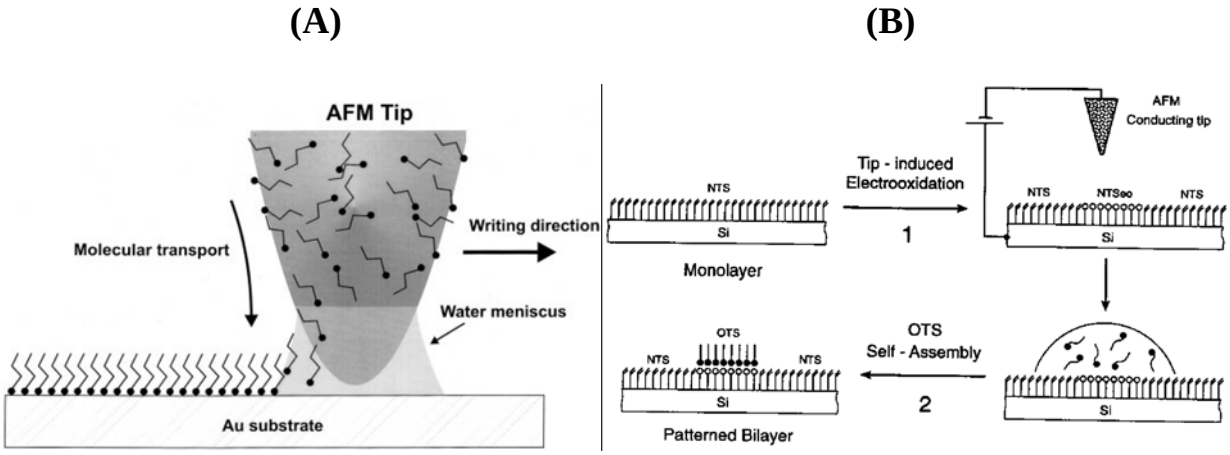

Figure 1.9. Schematics of methods for pattering chemical monolayers by (A) DPN (reproduced from ref. 194, copyright AAAS) and (B) electro-oxidation by a scanning probe tip (reproduced from ref. 195, copyright Wiley Interscience).

Soft lithography is another general term that encompasses the many ways in which a topographically patterned, elastomeric stamp can be used to physically replicate a pattern over a large area.[200] The stamp is most often made of polydimethylsiloxane (PDMS) that is molded from a rigid, patterned master. Although high resolution features may need to be drawn on the master in a time-consuming process such as electron-beam lithography, this step need only be done once. The elastomeric stamp molded from the master is can then used to rapidly replicate the pattern in a parallel fashion. The most commonly employed soft lithographic methods are microcontact printing, micromolding in capillaries (MIMIC), solvent-assisted micromolding, and microtransfer molding.[200] Figure 1.10 gives a schematic outlining the basic steps involved in each technique, although the general idea of all of them is to use the topographically patterned

stamp to define the feature shape and placement of a fluid or granular phase of matter by direct physical contact. The mechanical flexibility of the stamp allows for conformal contact and the patterning of non-planar surfaces.[201] These techniques are attractive as versatile, low-temperature means of patterning a wide variety of soft matter, although their applicability is limited somewhat by the need for the material of interest to be moldable and by the potential for unwanted deformations due to contact stress and adhesion. The latter point is most concerning for supramolecular systems as it means that proper assembly is not guaranteed. However, embossing techniques are attractive as a means of reversibly applying 3-D spatial confinement on a self-assembling system without the need to alter the substrate.

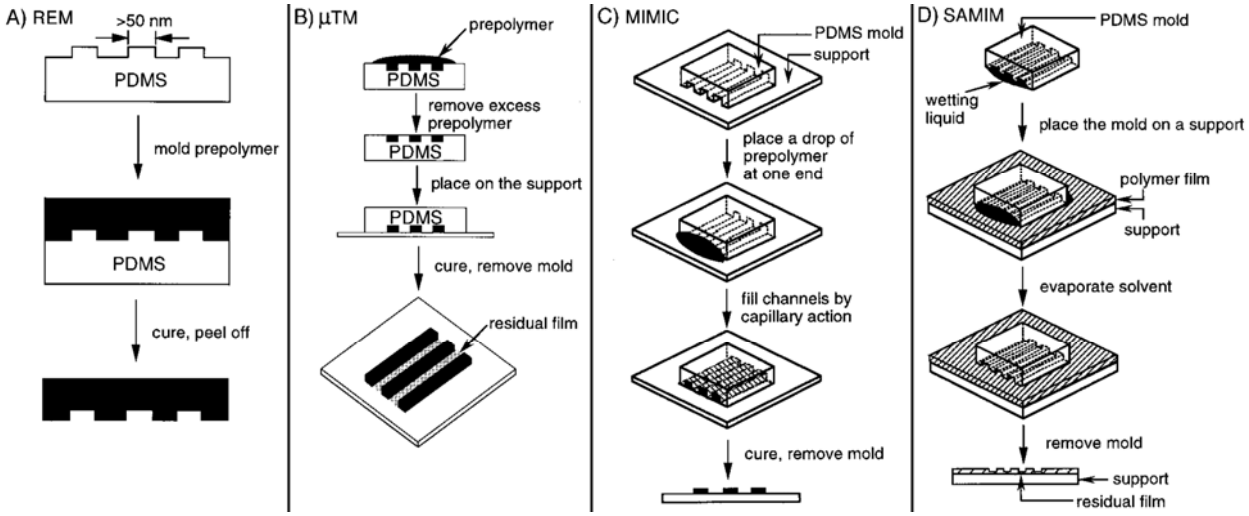

Figure 1.10. Schematic illustration of four different soft lithographic processes (reproduced from ref. 200, copyright Wiley Interscience).

In contrast to the other methods mentioned so far, scanning probe and soft lithographic techniques have the ability to deposit the material of interest directly onto an unmodified substrate with precise control over the spatial pattern and potentially high resolution. The ability

to pattern material from a fluid phase is particularly useful for discrete, nanometer-scale objects. However, application of these techniques to directly deposit self-organized and self-assembled systems is limited, partly because the forces involved may be disruptive to assembly. Direct patterning of a number of self-organized systems by microcontact printing has been reported, including 2-D colloidal particle arrays,[202] polyelectrolytes,[169] layered bionanocomposites,[203] and phase-separating, binary alkanethiol mixtures.[204] MIMIC has been used to pattern arrays of 3-D colloidal crystals.[205] Trau et al. also used MIMIC to align and mineralize the cylindrical phase of a surfactant, although alignment was aided by the application of an electric field.[206] Sgarbi et al. reported the self-assembly of microcontact printed laminin-1 into two-dimensional physiological networks.[207] Lastly, Jiang et al. demonstrated direct patterning of self-assembling peptide-amphiphile nanofibers by DPN and reported limited alignment of the fibers along the scanning direction.[208]

1.4.4 Other routes to spatial confinement and control of order

It is hypothesize that because translational freedom is often a strong driving force for order in self-organized systems, spatial confinement may be an effective means of controlling and enhancing that order. Surface patterning and soft lithography have been reviewed as means of achieving this end, but they are not the only methods available. For instance, block copolymers have been infiltrated into colloidal crystals[209] and pores of anodic alumina,[210, 211] yielding ordered structures of different shapes. Liquid crystals have also been confined in droplets and anodic alumina pores and shown preferential alignment.[212-215] Encapsulation not in rigid templates but in the cores and interstices of other supramolecular systems might also be considered a form of confinement. But the methods need not be so complex, as simply

decreasing the thickness of a film may yield unique behaviors due to the spatial limitation in one dimension.[216] Confinement effects may take on many forms, just as there are many more methods for aligning self-assembled and self-organized materials than the ones presented here. However, the examples given highlight some of the basic principles and considerations of controlling order in supramolecular systems.

CHAPTER TWO

Patterning and Molecular Order of Substrate-Supported Thin Films of Supramolecular Mushroom-Shaped Aggregates

Chapter 2: Patterning and Molecular Order of Substrate-Supported Thin Films of Supramolecular, Mushroom-Shaped Aggregates

2.1 Introduction

Molecular alignment in materials is desirable because it often leads to the enhancement of functional properties along the axis of alignment.[12, 143, 217-219] Materials that are not only macroscopically aligned but possess a permanent dipole are especially interesting because they tend to exhibit unique and useful properties that are otherwise absent in non-polar systems.[141] Our laboratory reported the synthesis of a class of rod-coil molecules that assemble into mushroom-shaped nanostructures with the rod portions crystallizing together as the stem and the coil segments expanding outward as the cap.[6, 94] These nanostructures in turn stack head-to-tail in layers to form a polar smectic liquid crystalline structure. On a local level, films made of these supramolecular constituents exhibit a net polarity, which is expressed in its piezoelectric behavior[98] and nonlinear optical (NLO) properties.[6, 97] This system is also interesting because it is uncommon for polar materials to be achiral, and understanding the nature of assembly in this system may lead to new insights into the development of ferroelectric liquid crystals.[141, 220, 221]

However, it is thermodynamically more feasible for the material to exist as a polycrystalline structure of microscopic grains of different orientations, reducing the anisotropic nature of the bulk material. On clean silica or other oxides, the mushrooms prefer to align stem down because the phenolic groups of the rod segments can hydrogen bond to the surface.[6, 97] As a result, the film still exists in equilibrium as a polydomain structure but with a small net polarization perpendicular to the plane of the glass. It is conceivable that if the material can be divided into a microscopic array of single, isolated domains on silica, the domains may be biased

adopt the same orientation. The resulting material would be macroscopically polar and might demonstrate unique properties. Previous work was done using a focused ion beam to etch glass substrates into an array of shallow, square mesas.[222] Second-harmonic generation measurements performed on films deposited on the patterned glass suggested that patterning might indeed enhance polar orientation normal to the substrate.[222] AFM studies have also shown preferential adsorption to clean, hydrophilic silica surfaces as opposed to silane-functionalized, hydrophobic surfaces.[183] This observation suggests another means of patterning surface interactions or controlling spatial segregation of the material.

One way of patterning the supramolecular material is by solution embossing. This method is a simple and versatile soft lithographic technique for patterning materials from a fluid phase or suspension[200] and involves using an elastomeric stamp with a patterned surface relief to mold the material of interest directly on the substrate with the aid of solvent. Upon removal of the stamp and solvent, the material is imprinted as a negative of the surface relief of the stamp. This technique can be applied to generate an array of isolated mounds of the supramolecular material on many different surfaces. If more rigid spatial confinement is required, another possibility is to etch deep topological features into the substrate itself by conventional microfabrication techniques. The higher aspect ratio of these features compared to those used in the previous study[222] may have a stronger effect upon the orientation of the mushroom-shaped nanostructures when the material is cast onto the substrate.

Polarized optical microscopy (POM) can be used to look for distinctive patterns of birefringence within the film, which would give some indication of the effectiveness of the patterning techniques. However, the resolution of POM is limited by diffraction, and the sample birefringence may be convoluted by the polarizing effect of surface topology. Near-field

scanning optical microscopy (NSOM) can therefore be a useful tool as it obtains optical information below the diffraction limit through the use of a sharpened fiber optic probe tip coupled to a laser.[223, 224] The tip illuminates the sample locally, and a photomultiplier tube (PMT) collects the reflected or transmitted light while the tip is scanned across a selected area. Since the probe tip is brought into tapping contact with the surface, it can also be used as a crude atomic force microscope (AFM) to simultaneously give topographical information, which becomes important when imaging patterned films. In addition, because the light intensity decays exponentially with increasing distance from the tip, the illumination is only sensitive to roughly the top 50 nm of the sample surface.

Second harmonic generation (SHG) measurements are a simple way of probing polar order, either in the bulk or at a surface.[225] Under high intensity laser irradiation, multiple photons can be absorbed by a material and re-released as single photons of higher frequency in a process known as optical parametric generation.[226] This is represented mathematically by expanding the equation for polarization P in the dipole approximation:

$$P_I = \chi^{(1)}_{IJ} E_J + \chi^{(2)}_{IJK} E_J E_K + \chi^{(3)}_{IJKL} E_J E_K E_L + \ldots \qquad (2.1)$$

where E is the applied electric field and $\chi^{(n)}$ is the nth order susceptibility. In the case of SHG wherein two photons are converted to a single photon of double the frequency, $\chi^{(2)}_{IJK}$ is non-zero. Because of symmetry arguments in the equation for polarization potential energy, all even order harmonics can only be seen in materials that are non-centrosymmetric or possessing a permanent dipole.

It is also of interest to ask if the supramolecular system can act as a host phase to align small molecule guests. Controlling the orientation of small molecule dyes is desirable because the dipole moment per molecule in some cases can be quite large, and alignment would enhance

NLO activity.[226, 227] This has been achieved to some degree by stretching polymers[228-231] or liquid crystals[232-234] that are mixed or functionalized with the dye. In comparison, a supramolecular host may be more functional because it would present a more complex and structured environment to the guest molecule. A number of supramolecular structures have been synthesized that exhibit NLO behavior.[235-237] Hulliger and coworkers showed that NLO molecules could form polar inclusion-compounds with perhydrotriphenylene.[238, 239] In the ideal case, both host and guest would contribute to the NLO signal while at the same time cooperatively ordering into a polar structure.

Fourier transform infrared (FTIR) spectroscopy may help elucidate the molecular orientation of each species in a host-guest system. While most commonly used for compositional analysis, this technique can also be used to determine the orientation and degree of order in materials on the molecular level.[240] In transmission IR spectroscopy, only the atomic vibrations or transition dipole moments (TDMs) oriented within the plane of the film are excited. By comparison, polarization modulation-infrared reflection-absorption spectroscopy (PM-IRRAS) only probes the TDMs oriented normal to the substrate due to surface selection rules that govern the reflection of *s* and *p*-polarized light from conductive metal surfaces.[241] Together, the two methods give complementary information on the orientation of molecules on a surface.

In this chapter, we discuss the patterning of the supramolecular film by soft lithographic solution embossing. NSOM and SHG measurements are used to study the polydomain structure of the film and probe the degree of polar order. The results suggest that micrometer-scale features are yet too large to affect the domain morphology of the film. We also study the effect of different surface treatments on the structure of monolayer and bilayer films. AFM images show that the molecule preferentially adsorbs to and may pack more tightly on hydrophilic oxide

surfaces. Films on hydrophobic surfaces appear to be more disordered. Finally, the effectiveness of the supramolecular material as a host phase for aligning small molecule guests is explored by FTIR. The addition of a small molecule guest to thin films appears to result in the molecular alignment of both the guest and the mushroom nanostructures into an orientation more normal to the surface, possibly due to the guest acting to relieve strain associated with packing of the nanostructures.

2.2 Materials and Methods

2.2.1 Materials

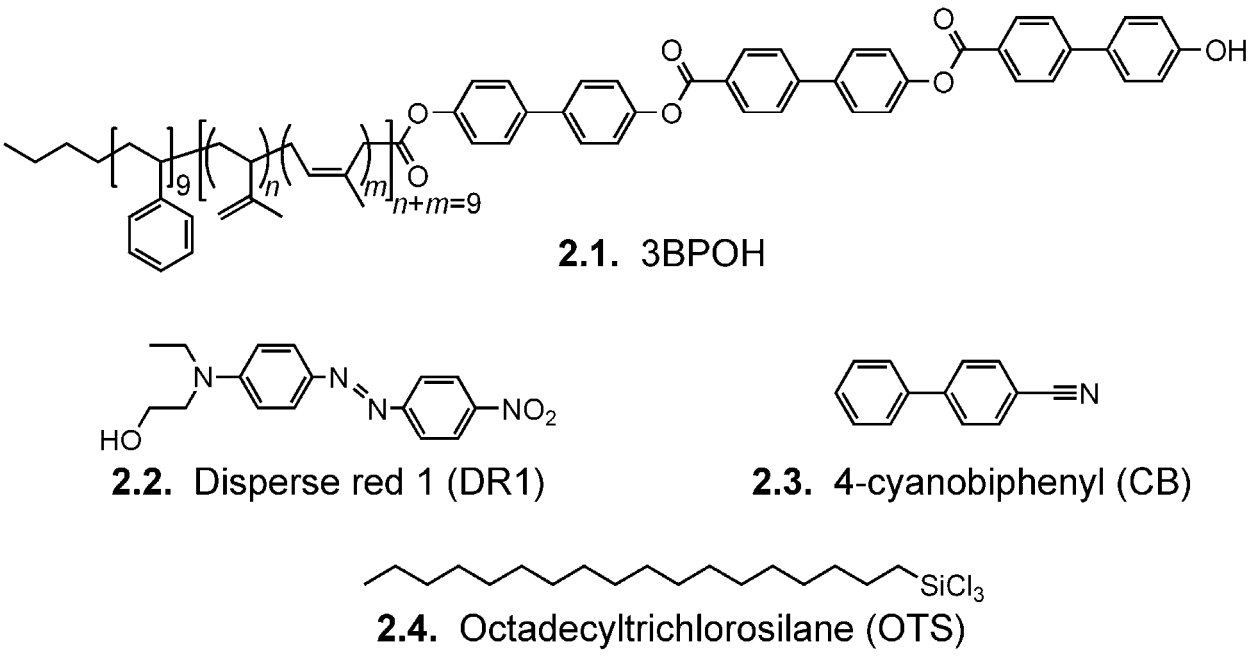

Figure 2.1. Chemical structures of molecules of interest

The structure of molecule **2.1**, or 3BPOH, is given in Figure 2.1, and its synthesis has been previously detailed. Disperse red 1 dye (95 %) and 4-cyanobiphenyl (95 %, 4-bromobiphenyl 5 %) were obtained from Aldrich. The isoprene blocks of **2.1** are capable of

cross-linking over time, so the material is generally stored at –10 °C when not in use. Unless otherwise stated, films of molecule **2.1** and mixtures with the two guest molecules were spin-coated onto substrates from dilute chloroform solution at 3000 rpm for 40 sec.

2.2.2 Substrate Preparation

Undoped (111) silicon (n-type, resistivity: 1500 Ωcm, University Wafer) was used as a substrate for transmission FTIR and AFM studies. Samples for PM-IRRAS measurements were prepared on conductive metal films evaporated onto borosilicate glass slides (Fisherfinest premium plain glass microscope slides, Fisher Scientific). Slide glass was also cleaned for use in fabricating micropatterned substrates. Borosilicate glass or silicon substrates were first cleaned by immersion in a hot piranha mixture of H_2O_2 (30 %) and H_2SO_4 (98 %) at 1:3 by volume (CAUTION: strong oxidizer) for 1 hr at 120 °C. They were then rinsed in deionized (DI) water, immersed in a mixture of H_2O_2 and NH_4OH (29 %) at 1:4 by volume for 15 min at 100 °C, rinsed in DI water a second time, and finally stored in 18.2 Ωcm water (Milli-Q A10, Millipore). Before use, the substrates were blown dry by an industrial grade nitrogen gun and incubated in a dessicator with Drierite dessicant (W. A. Hammond) for 10 hrs to remove adsorbed water.

For PM-IRRAS substrates, a thin metal film was evaporated on clean glass in a BOC Edwards Auto 306 electron-beam evaporator. An adhesion layer of 15 nm of titanium was evaporated first, followed by 35 nm of gold capped with a 1 nm layer of titanium on top of the gold to produce a hydrophilic oxide surface. Evaporated metal substrates were cleaned prior to use by ultrasonication for 10 min each in acetone, isopropanol, and Milli-Q water, followed by exposure to oxygen plasma in a PlasmaLab 80 reactive ion etcher (Oxford Instruments) for 3 min (50 sccm O_2, 150 mtorr, 100 Watts).

2.2.3 Surface Treatments

The cleaning process described above yields substrates with hydrophilic surfaces (contact angles approaching 0 °). To investigate the effects of different surface chemistries, two other surface treatments were applied. In the first treatment, silicon substrates were immersed for 3 min in a solution of hydrofluoric acid (HF, 39 %) diluted 1:50 by volume in water. After rinsing the substrates in DI water and drying under nitrogen, the treatment resulted in weakly hydrophobic (contact angle *ca.* 80 °) silicon surfaces with no native oxide.

Hydrophobic surfaces (contact angle *ca.* 130 °) were obtained by functionalizing the cleaned substrates with octadecyltrichlorosilane (OTS) ($C_{18}H_{37}Cl_3Si$; 95 %, Acros Organics). The substrates were briefly dipped into isopropanol and then into toluene before being immersed in a 1 mM solution of OTS in toluene for 25 min. Addition of a 15 μL drop of DI water to the solution appeared to improve the uniformity of the silane layer by limiting the polymerization of a silane scum at the air-solution interface. After immersion, the substrates were briefly rinsed with toluene, isopropanol, and Milli-Q water (in sequence) and dried with N_2.

2.2.4 Soft lithography

Contact photolithography is used to make square or circular islands of photoresist on a glass substrate for use as a topological master for soft lithography. The piranha-cleaned glass was spin-coated with a layer of positive photoresist (AZ-1518, Clariant Corp.) and soft-baked in a convection oven at 90 °C for 30 min. The substrate was mounted onto a Quintel Q-2000 mask aligner and exposed to 365 nm UV light through a chrome mask on quartz. The mask is patterned with either a square array of circles 3-50 μm in diameter and spaced 3-50 μm apart or an array of squares 10 μm on a side. After development in AZ-400K developer (Clariant Corp.,

1:5 dilution with deionized water), an array of square or circular posts of photoresist remained, 1-2 μm in height.

Sylgard 184 PDMS (Dow Corning) was then prepared by mixing the prepolymer with crosslinker in a 10:1 w/w ratio, and the mixture was cast over the photoresist pattern. The PDMS is cured at 50 °C for at least 2 hrs, after which the stamp was removed. A small drop of 3BPOH in 3 wt % chloroform solution is pipetted onto a clean, hydrophilic glass slide, and the stamp is immediately placed over the drop. The stamp is left in place for up to 1 min as the solvent absorbs into the PDMS or evaporates. Upon removing the stamp, patterned mesas of material 1-2 μm tall remain on the substrate, mimicking the original photolithography pattern. In most cases, the film was annealed in a convection oven at 155 °C under nitrogen for at least 4 hrs.

2.2.5 Micropatterned silica substrates

A layer of SiO_2 roughly 1 μm in thickness is first deposited onto glass slides by plasma-enhanced chemical vapor deposition (PECVD) in a Plasmalab 80 (Oxford Instruments). Photolithography was performed as described in section 2.2.4, followed by electron-beam evaporation of a 20 nm thick nickel film. Liftoff by sonication in acetone yields a metal film with a patterned array of circular holes suitable for use as an etch mask. The substrates are then place in the reactive ion etching (RIE) chamber and exposed to CF_4 plasma to etch the CVD oxide in areas not protected by nickel. One advantage of RIE is that the etching is directional, resulting in features with vertical sidewalls.[242] The borosilicate slide glass itself was used as an etch stop because it was found to be resistant to dry etching, possibly because an oxygen leak in the RIE. The nickel is removed by immersion in nitric acid (70 %) for 5 min, resulting in a glass

substrate with a pattern of wells about 1 μm deep etched into the surface. Posts instead of wells can be obtained evaporating the nickel onto the CVD oxide before photolithography, then using the photoresist as a wet etch mask, etching the exposed metal in nitric acid to yield an array of metal circles. Films of molecule **2.1** were spin-coated at 1000 rpm from 3 wt % solution in chloroform directly onto these substrates and then annealed in a convection oven at 155 °C under nitrogen for at least 4 hrs. These substrates are also quite useful as durable masters for molding PDMS stamps for soft lithography.

2.2.6 SAXS and DSC

Small angle X-ray scattering (SAXS) was performed on a small amount of molecule 2.1 in powder form in a polycarbonate holder. Diffraction was performed in transmission geometry using a Rigaku CuKa source (λ = 1.542 Å, 30 kV, 17 mA) and a 2D Bruker CCD detector. The 2θ scale was calibrated with silver behenate, and the spectrum was collected for 2000 sec. The baseline was substracted and the peaks fit using a mixed Gaussian-Lorentzian fitting algorithm. To examine phase transitions, differential scanning calorimetry (DSC) was done using a TA Instruments 2920 DSC using at least 5 mg of material hermetically sealed in aluminum pans. Mixtures of materials were dropped into the pans as highly concentrated solutions and dried under vacuum. Samples were cycled at 5 °C/min, and transition temperatures were determined from the second or third heating cycle.

2.2.7 Near-field scanning and polarized optical microscopy

Films of **2.1** deposited on transparent substrates were imaged by POM between crossed polarizers on a Leitz Laborlux 12POL polarizing microscope. Birefringence photographs were captured on a 35 mm film camera. To confirm the liquid crystalline phase transitions suggested

by DSC, the samples were imaged while heated on a Linkam THM 600 thermostatic heating stage.

NSOM was performed in illumination transmission mode with a Multiview 1000™ (Nanonics Imaging Ltd.) scanning stage mounted on an optical microscope. Cr/Al-coated cantilevered fiber optic probes (Nanonics) with 100 nm apertures were coupled to an Ar-ion laser emitting at 514.5 nm (10 mW output power). Images in "constant-amplitude" mode were obtained with the normal force feedback loop to maintain constant tip distance from the surface, and the NSOM intensity was collected by a PMT while the tip. The microscope was enclosed in box to limit ambient light and dampen noise, and the entire setup rests on a vibration-isolation table.

2.2.8 Characterization of the substrate and film morphology

The substrate morphology and composition was studied by secondary ion mass spectrometry (SIMS), atomic force microscopy (AFM), and scanning electron microscopy (SEM). To confirm the surface composition of metal substrates for PM-IRRAS, SIMS was performed using a Physical Electronics PHI TRIFT III ToF-SIMS operating in positive ion mode and sputtering with Ga+ ions from a liquid source. The etched silicon masters were sputter coated with 5 nm of gold-palladium alloy (99.99% Au:Pd, 60/40 ratio) in a Desk III sputter coater (Denton Vacuum) and imaged using a Hitachi S4500FE scanning electron microscope. AFM images of the microcontact printed samples were aquired on a JEOL 5200 scanning probe microscope as well as a Park DI SPM, both operating in tapping mode. Applied Nanostructures ACT silicon cantilevers (300 kHz resonant frequency, 40 N/m spring constant) were used for AFM imaging. Film thicknesses were determined using a Tencor P10 profilometer.

2.2.9 Second harmonic generation

SHG measurements are performed using a Q-switched Nd:YAG laser emitting at 1064 nm and a repetition rate of 10 Hz with a 5 ns pulse width. An optics table shown schematically in Figure 2.2 is set up in transmission mode with a rotating sample stage to vary the incident angle θ. Some measurements were done on electrically poled films. Poling electrodes were sputter coated onto clean glass with a 0.6 mm wide strip of electrical tape masking a gap between the electrodes. The material was poled directly from a drop of 1 wt % chloroform solution as it dried under an applied DC voltage of 1.2 kV.

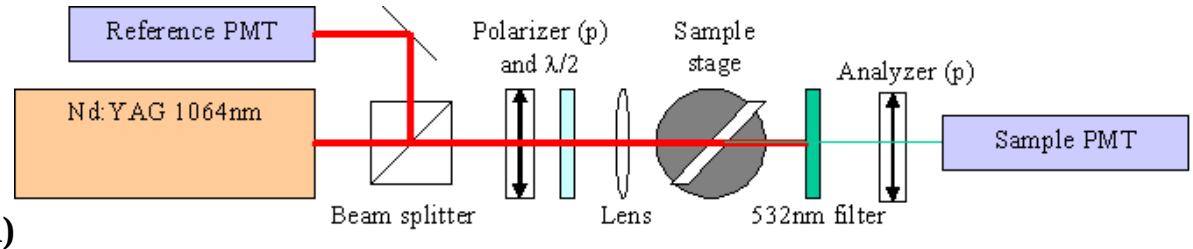

(A)

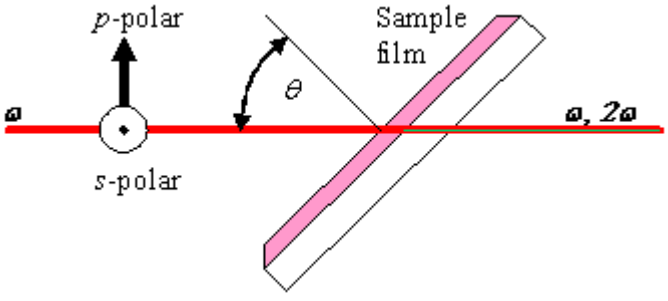

(B)

Figure 2.2. (**A**) Schematic of SHG setup, and (**B**) illustration of sample stage with polarization geometry. θ is the incident angle and *p* and *s* are polarizations parallel and perpendicular to the incident plane.

2.2.10 FTIR

Samples made on undoped silicon substrates were characterized by transmission FTIR using Thermo Nicolet Nexus 870 FTIR spectrometer. Bulk spectra of the materials could also be obtained by performing transmission IR on samples ground with KBr and pressed into pellets. Samples made on thin film metal substrates were studied by PM-IRRAS using the same instrument in grazing-incidence reflection mode with an attached tabletop optics module. Order parameters were calculated from peak areas obtained by integrating the spectra (see Appendix A).

2.3 Microscale patterning of 3BPOH

2.3.1 Characterization of 3BPOH

SAXS spectra of compound **2.1** given in Figure 2.3 show a lamellar peak around 7.4 nm as is expected for the material.[243] Results of DSC measurements of **2.1** are also consistent with previous work,[243] showing shallow, reversible first order peaks at around 125 °C and 150 °C corresponding to smectic liquid crystal transitions. At 250 °C the film becomes isotropic, and shortly above that temperature a broad exothermic peak appears due to polymerization of the isoprene blocks. The transitions are confirmed using a microscope heat stage to observe changes in birefringence with temperature. Films of 3BPOH spin-coated at 1000 rpm from 3 wt % solution in chloroform onto the clean glass are about 400-500 nm thick and are not birefringent, possibly because the solvent evaporates too fast to allow the formation of larger domains. When the film is heated above 125 °C, a fine-grained birefringent structure appears as shown in Figure 2.4 and is persistent on cooling. In subsequent experiments, annealing of the films is generally performed at 155 °C, just above the second liquid crystal transition, for at least 4 hrs in order to

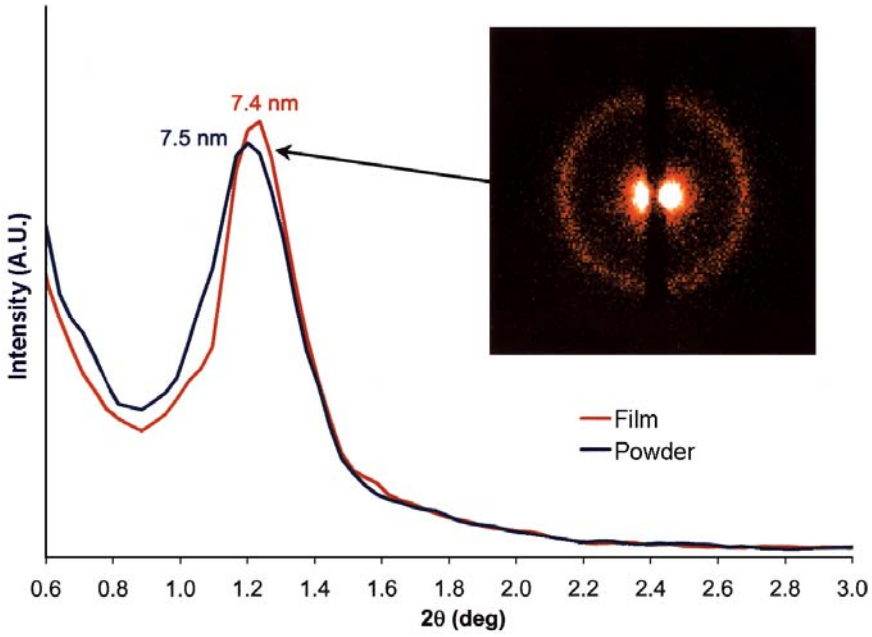

Figure 2.3. SAXS diffraction pattern of **2.1** in powder form and scaped off a film cast from chloroform solution (courtesy of Dr. James Hulvat).

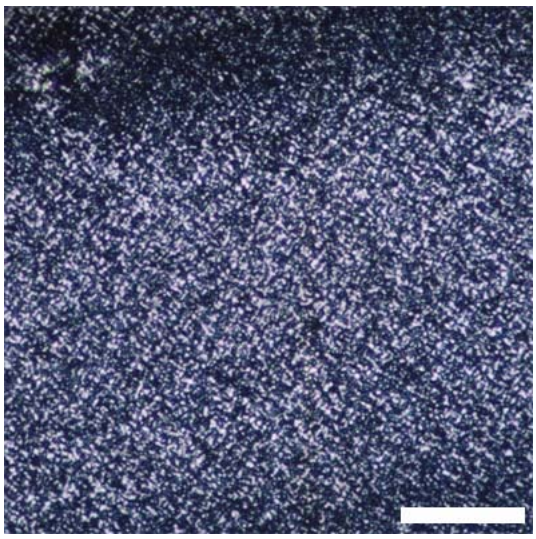

Figure 2.4. Birefringent optical micrograph of 3BPOH film drop-cast onto clean glass, annealed at 155 °C for 5 hrs, and imaged between crossed polarizers. Non-annealed films are not birefringent. Scale bar is 50 μm.

avoid cross-linking of the isoprenes or decomposition of the esters that may occur at higher temperatures.

From the optical micrograph in Figure 2.4, grain sizes appear to be 1-5 μm at most, close to the resolution limit of the microscope. NSOM was employed in an attempt to obtain higher resolution optical images. Figure 2.5 shows NSOM images of non-annealed and annealed spin-coated films illuminated by 514.5 nm polarized light. The non-annealed film is not birefringent and thus shows mostly noise under the NSOM. The annealed film shows light and dark patches that may be due to grains of different orientations, each about 500 nm in size. The topological images show no significant difference between the two samples. However, the fiber optic tip is

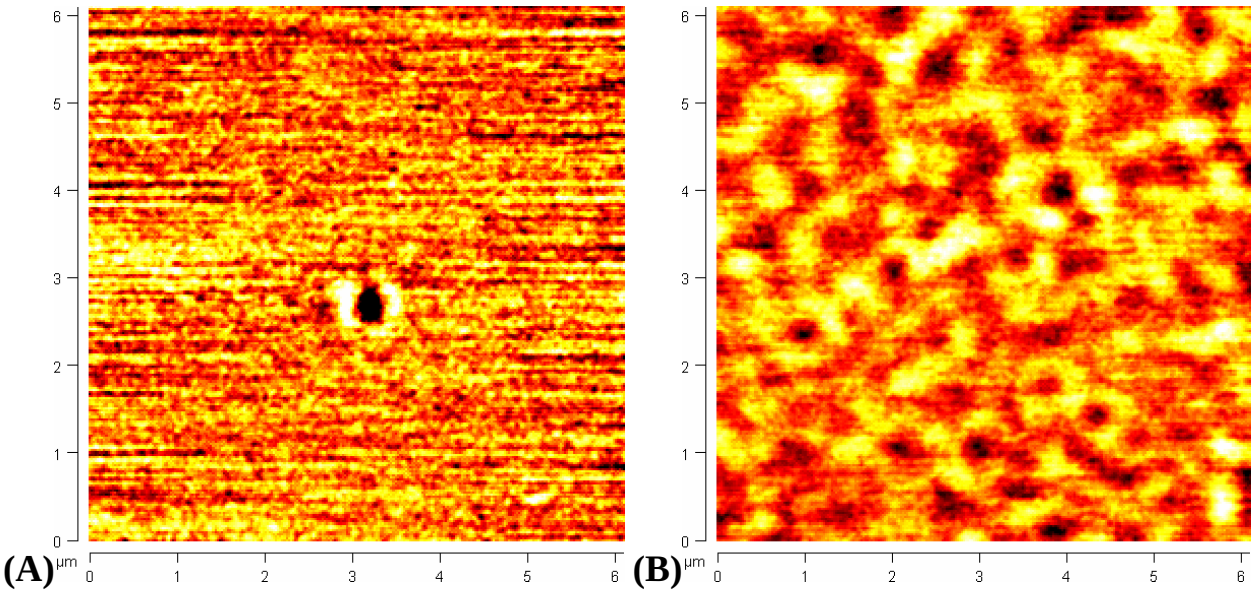

Figure 2.5. Transmission NSOM images of (**A**) non-annealed and (**B**) heat annealed 3BPOH films spin-coated onto clean glass. The contrast in **B** is theoretically due to polarized absorption of 514 nm illumination by randomly oriented liquid crystal grains, each on the order of 300-500 nm in size. The dark spot in the center of **A** is sample damage due to the idle probe when the laser is turned on before the scan is started.

100 nm in width and may miss finer surface features that would also contribute to the optical contrast. Regardless, the images show that thick films of **2.1** exist as a polydomain structure and are likely to have a minimal net polarity. Although the domains appear to be less than one micrometer in size, if the effect of spatial confinement is strong enough, it may not be necessary to lithographically define features that small.

2.3.2 Solution Embossing of 3BPOH

An optical micrograph of a micromolded 3BPOH film is shown in Figure 2.6. A scratch made in the film with a razor blade reveals the presence of a residual film covering the entire substrate surface beneath the patterns ranging in thickness from 50 nm to 1 μm as measured by profilometry. This residual layer is persistent in all samples and is difficult to control due to the speed with which the solvent is absorbed into the PDMS. Upon annealing, the patterned features partially melt, resulting in a decrease in pattern height and definition, particularly for smaller features. While not birefringent initially, the stamped films show periodic birefringent patterns after the heat treatment. Figure 2.7 shows optical micrographs of stamped films (square arrays of circular mounds) that are annealed and imaged through crossed polarizers. In the 10 μm diameter features, individual birefringent grains similar to those seen in a bulk film can be observed within each mound. Around the edge of each island, strong birefringence is also observed indicative of radial orientation of the mesogens due to either surface or flow-induced alignment. In the 3 μm diameter features, this radial orientation seems to dominate resulting in a birefringent pattern similar to what might be seen around a liquid crystal disclination defect of strength 1.

NSOM images of the stamped (3 μm circles), annealed films are given in Figure 2.8. Height images show significant melting of the structures to less than 200 nm tall, and the presence of the underlying residual film can be seen as evidenced by the appearance of domains between the mounds. While the locations of the 3 μm circles can be roughly determined in the NSOM image, there appears to be little change in the domain orientation near the surface. This suggests that the far-field birefringent image in Figure 2.7 is either a result of subsurface domains or an artifact of the optical microscope near its resolution limit.

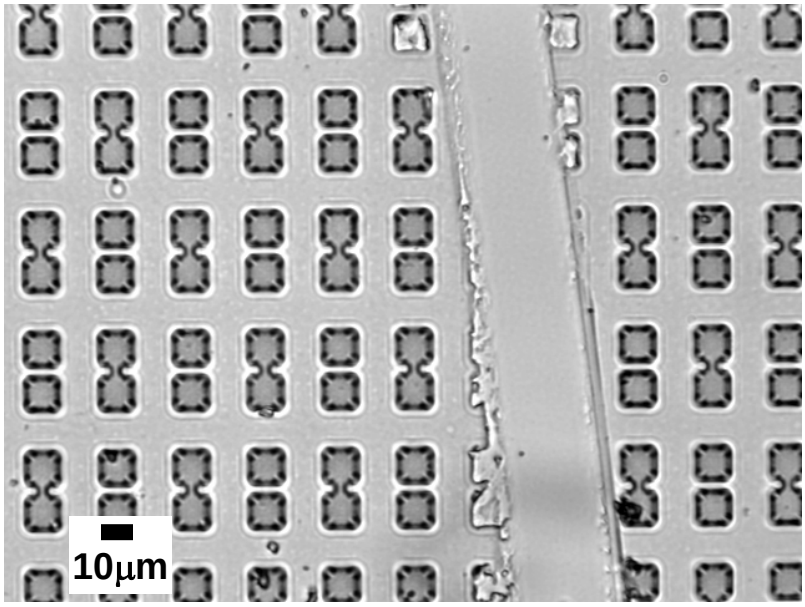

Figure 2.6. Optical micrograph of micromolded 3BPOH film after removal of the stamp. The pattern consists of 10 μm square mounds, each 1-2 μm tall, equal to the depth of wells in the PDMS stamp. A scratch down the center made by a razor blade reveals the presence of an underlying residual film.

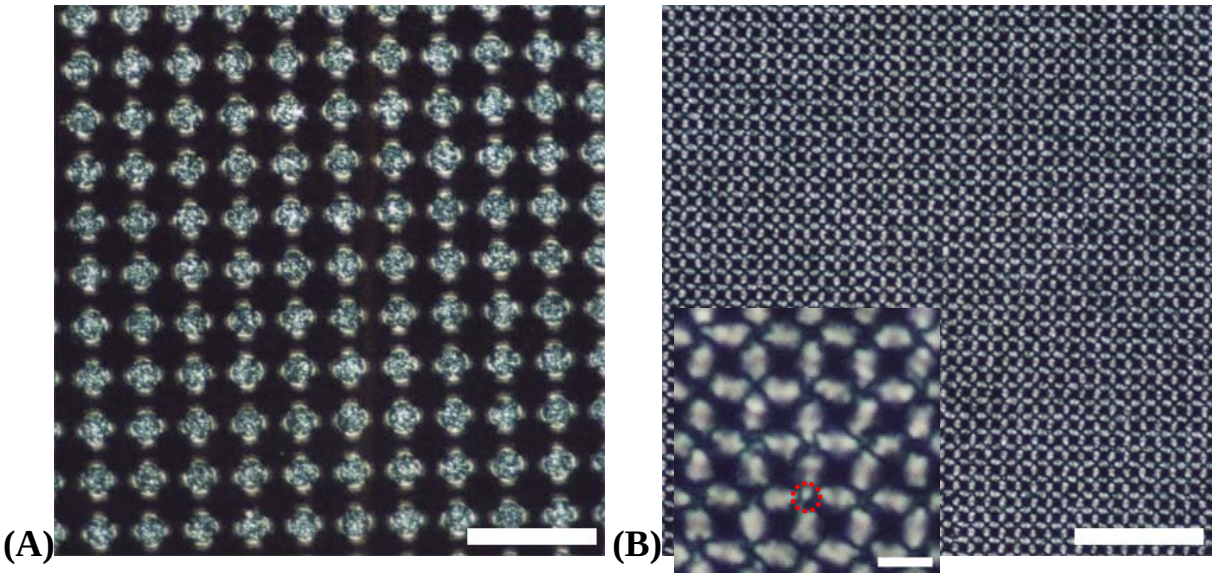

Figure 2.7. Birefringent micrographs of micromolded 3BPOH films post-annealing: (**A**) 10μm and (**B**) 3μm circular features, scale bars are 50 μm. Inset: a closeup of **B** shows radial birefringence pattern and what appears to be liquid crystal disclinations. The dotted red circle indicates the location of the original circular mound. Scale bar is 6 μm.

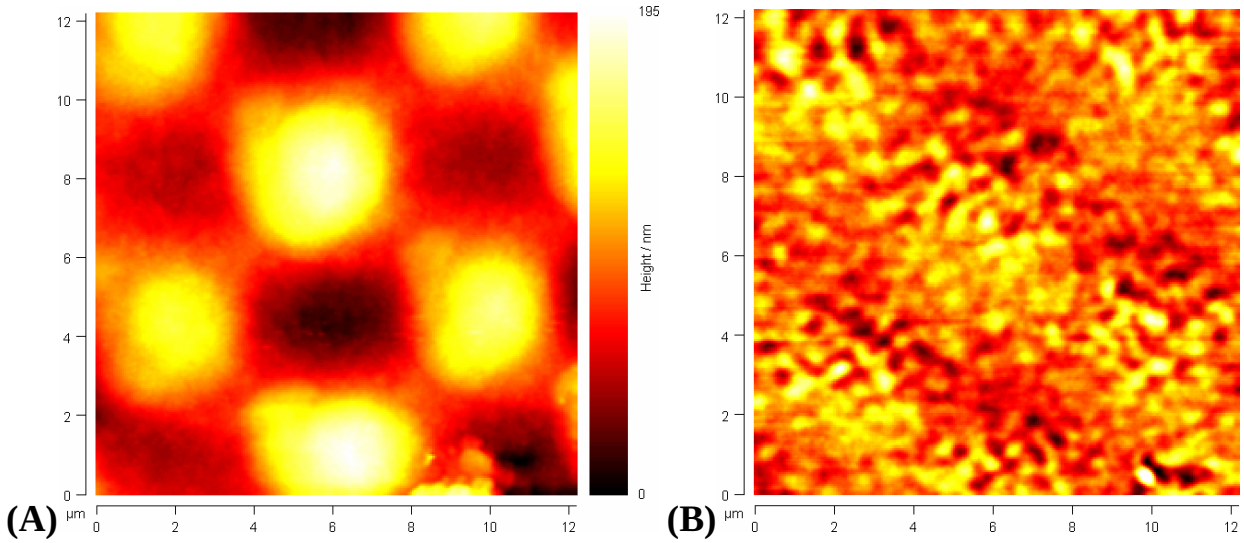

Figure 2.8. (**A**) AFM and (**B**) transmission NSOM of micromolded 3BPOH films with 3 μm feature size. Heights of the pattern are shown to be roughly 175 nm and correspond to areas of increased domain contrast in the NSOM image. Slight indications of shading in the NSOM image may be due z-motion artifacts.[244, 245]

2.3.3 3BPOH films on micropatterned silica substrates

Surface relief patterns can also be etched directly into the substrate itself by conventional micromachining methods. This strategy suffers from the fact that a separate substrate must be fabricated for each desired sample, however it allows for more rigid physical confinement than micromolding by soft lithography. Figure 2.9 shows SEM images of arrays of posts and wells etched into a CVD silica layer and exhibiting vertical side walls. The aspect ratios approach a value of 1 and can be increased by deposition of a thicker silica layer. The top surface of the CVD silica layer appears smooth, and the roughness of the etched surfaces can be reduced by the use of an etch stop such as a layer of nickel underneath the deposited silica.

Birefringent textures and NSOM images of thick films of **2.1** spin-coated and annealed on these pre-patterned surfaces are shown in Figure 2.10. The textures observed are similar to those observed in films of **2.1** patterned by solution embossing. From the NSOM images, it can be seen that the material does fill much of the micrometer-scale wells. However, the domain structure of the film cannot be clearly identified as the contrast from the glass patterns drowns out much of the contrast from the liquid crystal. SHG measurements can't be reliably performed because the array of substrate features tends to diffract the laser beam, reducing the signal to an unacceptable level.

2.3.4 Nonlinear optical measurements

As shown in Figure 2.11, when the film is electrically poled directly from solution between two gold electrodes deposited onto a single glass slide, the film is uniformly birefringent and gives a strong SHG signal suggesting polar alignment of the aggregates parallel to the electric field. The intensity I can be fit to the rough functional form:

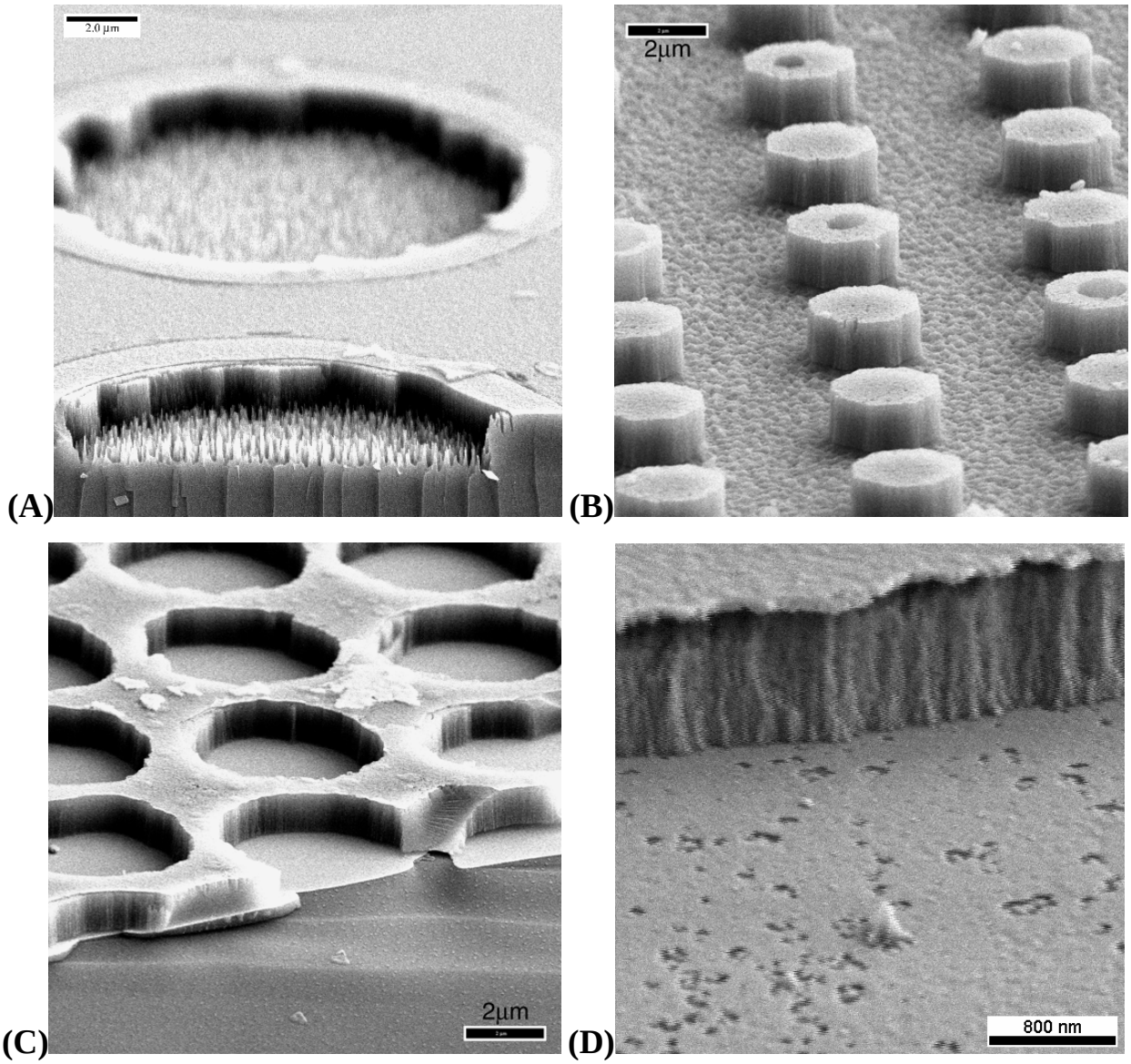

Figure 2.9. SEM images of surface features etched by RIE into a CVD SiO_2 layer deposited on glass slides. Square arrays of (**A**) 10 µm circular wells and (**B**) 3 µm circular posts. The roughness of the etch surface can be smoothed out by etching through the oxide layer to an etch stop, either (**C**) an underlying metal film or (**D**) the original slide glass.

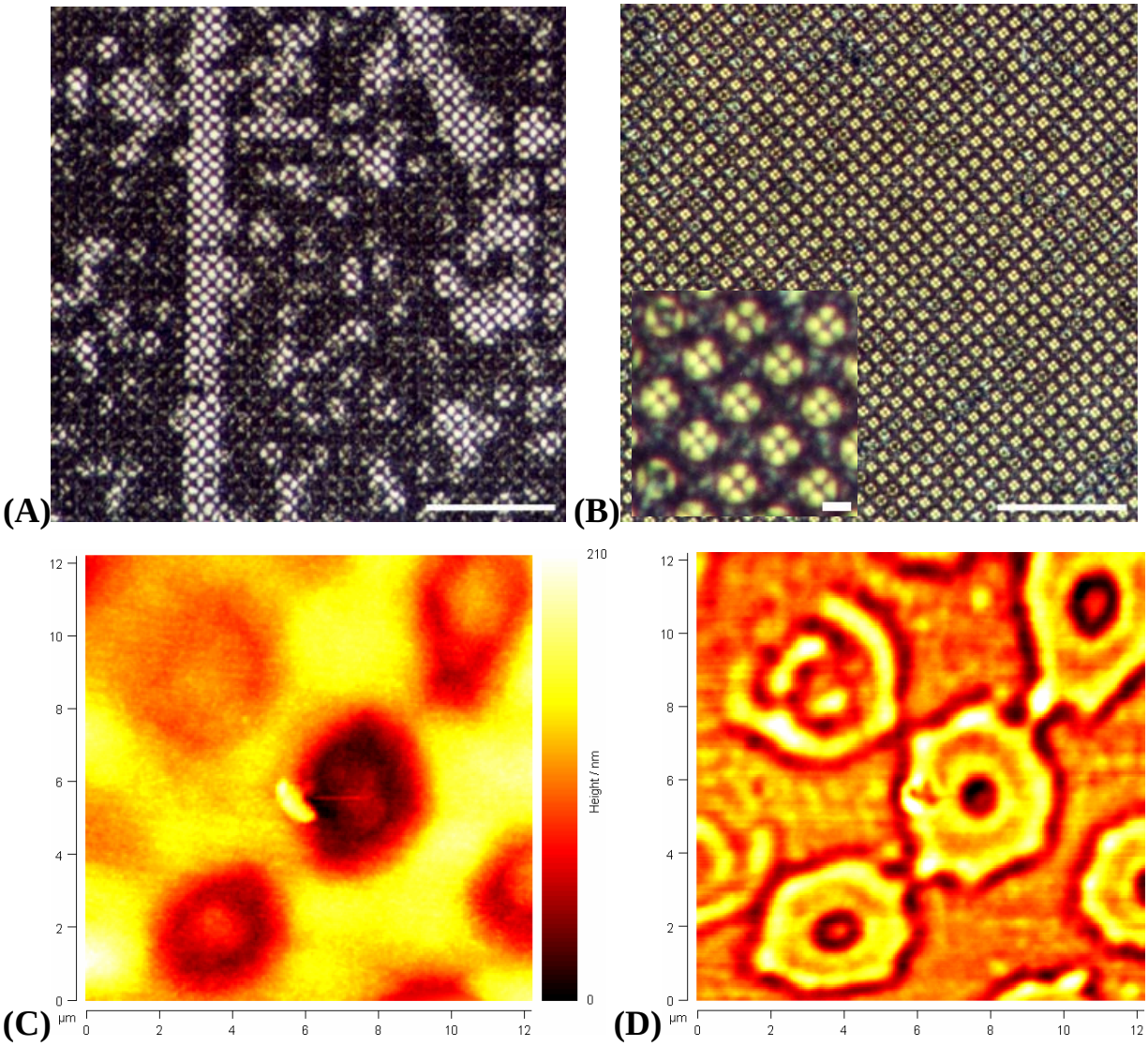

Figure 2.10. Birefringent optical micrographs of 3BPOH films spin-coated and annealed on micromachined glass substrates consisting of (**A**) 3 µm circular wells or (**B**) posts. Scale bars in **A** and **B** are 50 µm, and the scale bar in the inset is 3 µm. (**C**) Simulaneous height and (**D**) transmission NSOM images of the sample in **A** shows partial filling of some of the wells and a strong contrast due to the substrate features.

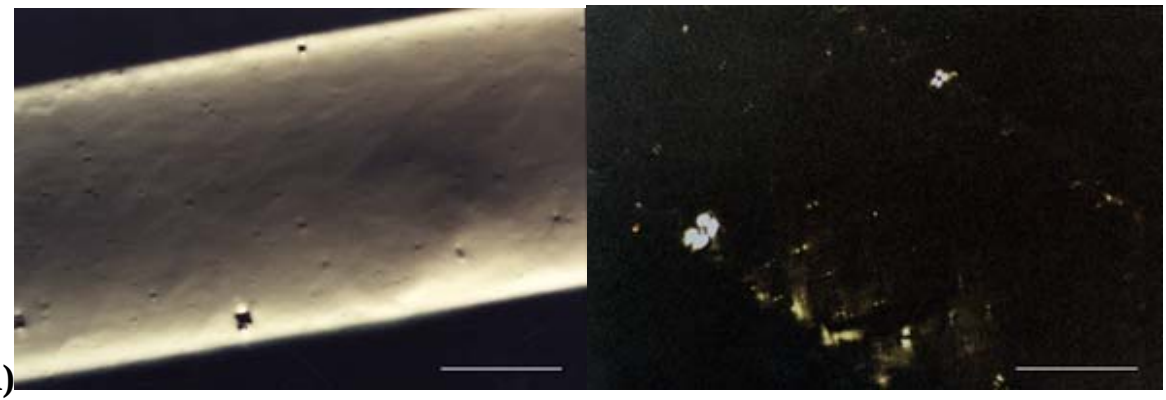

(A)

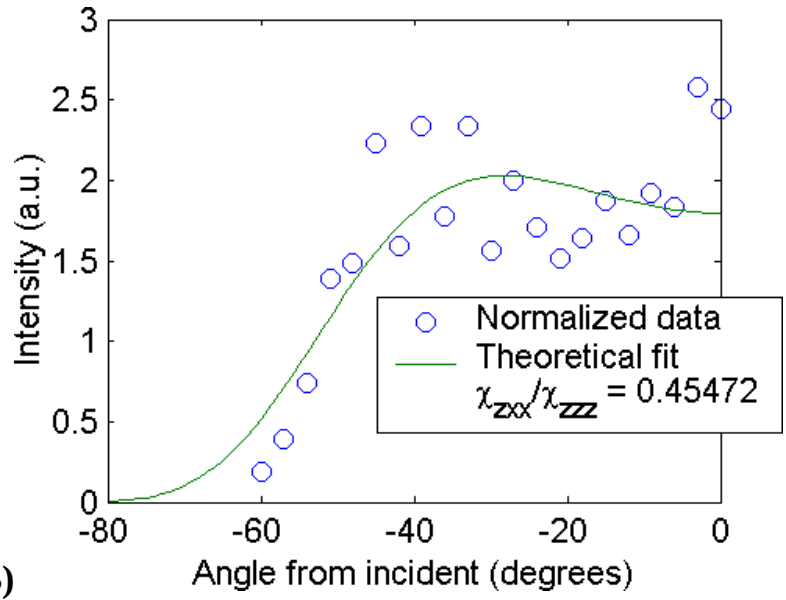

(B)

Figure 2.11. (**A**) POM images of electrically poled films of **2.1** showing uniform birefringence that is extinguished when the sample is rotated 45 °. The scale bars are 250 μm. (**B**) The electrically poled film shows a strong SHG signal suggesting alignment of the optic axis parallel to the electric field (in the plane of the substrate). For the fit, $r^2 = 0.61$.

$$I_p \propto \chi_{eff}^2 T_\omega^2 T_{2\omega} p(\theta)(\sin\Psi)^2 \qquad (2.2)$$

where T_ω and $T_{2\omega}$ are Fresnel transmission factors, $p(\theta)$ is a projection factor compensating for the change in beam spot area with θ, sinΨ is a function dependent on the coherence length and θ that accounts for thickness fringes, and χ_{eff} is the effective second order susceptibility for the

assumed dipole orientation.[226] The film thickness is ca. 20 μm but varies several micrometers as material is drawn into the gap between the electrodes and preferentially deposits nearest to the electrode edges. This fact may account for some of the deviation of the signal from predicted values.

SHG signals from non-poled annealed films are weak, which makes it difficult to draw definitive conclusions due to noise and day-to-day fluctuations in instrument performance, but a non-zero signal is observed the majority of the time. Films patterned by solution embossing didn't appear to give a signal any greater than spin-coated films. Figure 2.12 gives results of SHG measurements on spin-coated and solution embossing patterned films of 3BPOH.

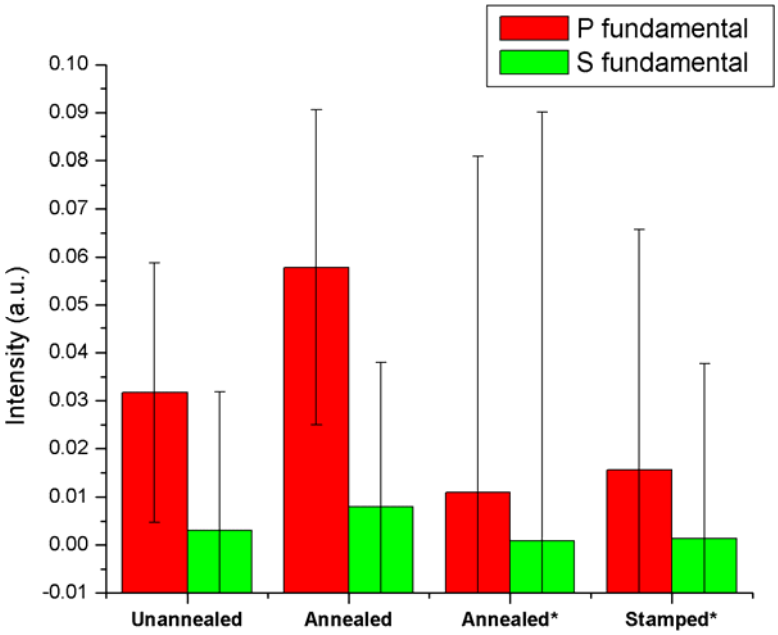

Figure 2.12. SHG signal from spin-coated films, both annealed and unannealed, taken at a fixed incident angle of 60° over 2000 pulses gives a slight signal above noise for the *p*-polarized fundamental beam but not the *s*-polarized. Similar data of annealed films, stamped and unstamped, taken on a different day (*) at 45° incident angle shows significant variation in noise, whether due to laser performance or systematic error.

It is believed that the patterned films are too thick and the features are too large to have a significant impact on the polydomain structure of the film. It may thus be profitable to reduce the patterned feature width to at most 1 μm, closer to the domain sizes observed by optical microscopy. Reducing the film thickness by an order of magnitude may also limit the formation of the polydomain structure. There is a concern that smaller features are more likely to melt away under annealing or diffract light more strongly, limiting the usefulness of spectroscopic measurements. However, reducing the aspect ratio of the features should mitigate both effects.

2.4 Effects of surface treatments on film morphology

2.4.1 Substrate characterization

Figure 2.13 shows SIMS data of the OTS-coated and non-coated metal surfaces on glass. The TiO peak confirms the presence of a thin layer of titania at the substrate surface. The gold peak is very weak, indicating that the 1 nm layer of titanium is not significantly cracked and covers the gold layer with good uniformity. Analysis of the OTS-coated surface reveals both

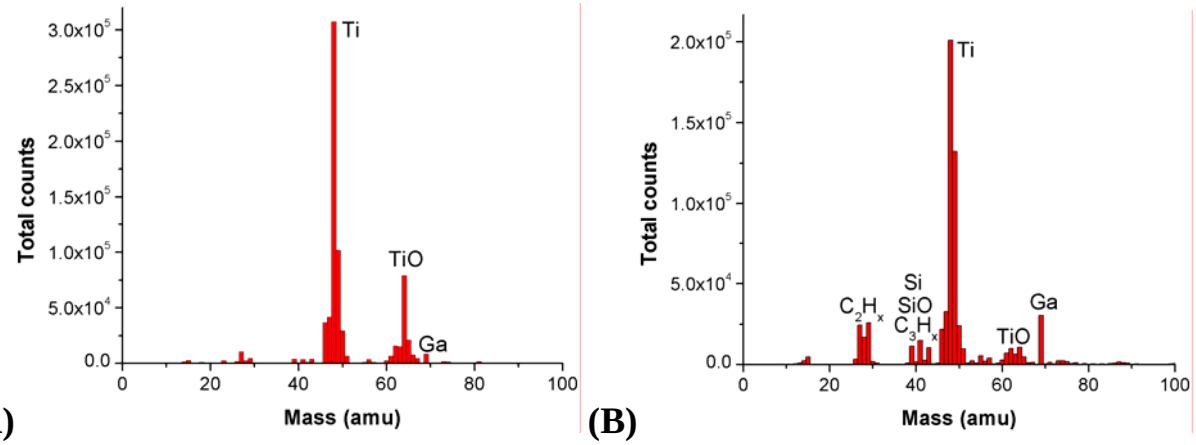

Figure 2.13. SIMS spectra of evaporated titanium-gold-titanium substrates (**A**) with and (**B**) without OTS treatment (courtesy of Dorothea Greishaber).

alkyl and silica fragments, which confirms the presence of the silane on the surface. While this data does not give direct evidence of covalent attachment of the silane to the titania surface, the fact that the silane is still present after vigorous solvent washing indicates that it is at least bound to the surface strongly enough to withstand subsequent sample preparation steps without significant desorption.

Table 2.1 lists the RMS roughness as determined by AFM for each of the different surfaces employed in this study. Both silicon and glass are quite smooth, with roughnesses on the order of 3 Å. The evaporated metal film is rougher due to the grain structure of the metal, but the roughness is still under 1 nm. Silanization of the surfaces with OTS results in a slight increase in roughness for all cases. Generally, all values of roughness are an order of magnitude less than the supramolecular layer spacing and thus are believed to have a minimal impact on the film morphology.

Table 2.1. RMS roughness of different substrates.

Substrate	RMS roughness (Å)
Undoped silicon	3
Borosilicate glass	3
OTS-treated glass or silicon	6
Evaporated metal	7
OTS-treated evaporated metal	9

2.4.2 Film textures

Films obtained from spin-coating a 1 wt % solution of **2.1** at 3000 RPM were 84 ± 8 nm thick. An AFM image of the surface texture of a multilayer film deposited on an OTS-coated

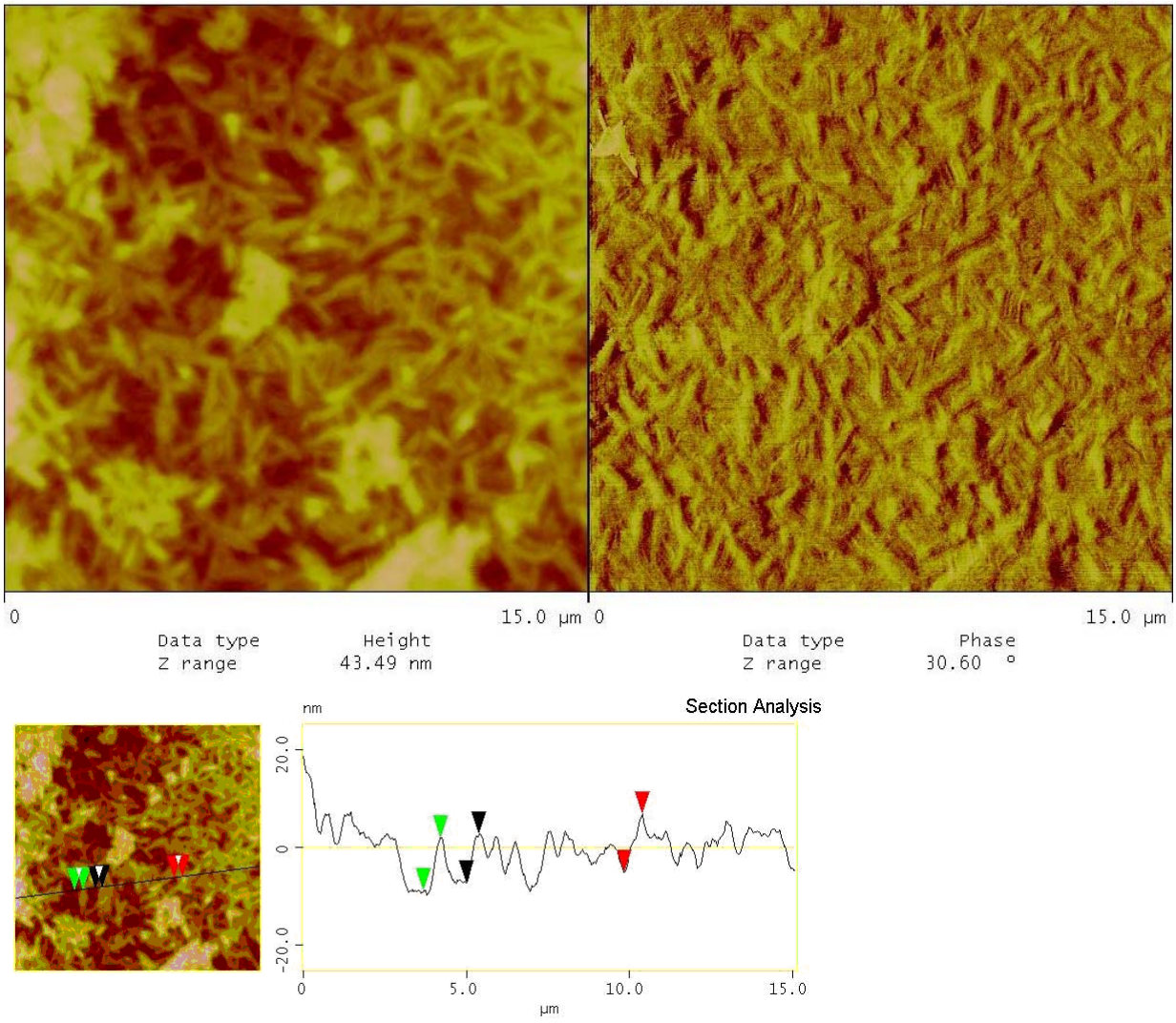

Figure 2.14. AFM image of 1 wt % 3BPOH on OTS. Height differences in line section: (red) 11.84 nm, (green) 10.81 nm, and (black) 9.81 nm (courtesy of Dorothea Greishaber)

substrate is shown in Figure 2.14. The film thickness did not appear to vary with surface treatment, and the surface texture appeared to be only slightly smoother on clean silicon substrates. Even at film thicknesses below 100 nm, a surface morphology can be seen that is suggestive of a polydomain structure. The features on the film surface appear elongated and are *ca.* 500 nm in width, consistent with the earlier NSOM images. The depth of the features is *ca.*

10 nm, suggesting that these are multilayer grains and that disorder is nucleated at some point deeper within the film. The elongated structure and corresponding striations may be due to smectic layering of the mushroom nanostructures.

In order to get a better impression of the effect of surface treatment on film morphology, more dilute solutions were used to achieve monolayer or sub-monolayer films. Figure 2.15 shows AFM images of films of **2.1** spin-coated from 1 mM and 2 mM solutions in chloroform, resulting in sub-monolayer and sub-bilayer coverage, respectively, after annealing. Films deposited on piranha and HF-treated silicon appear to be very smooth with little structure apparent in the height contrast image. However, the phase contrast image sometimes shows a striated texture to the monolayer. The striations have a period of 10.6 nm and are not always observed if the quality of the AFM tip is poor. These images suggest that the mushroom nanostructures in the first layer immediately adsorbed to the substrate may pack into a more one-dimensional structure than as individual mushrooms. A possible explanation for this observation is discussed in the next section.

Films deposited on OTS-coated surfaces are apparently rougher and are likely to be more disordered. Before full monolayer coverage is achieved, bilayer structures can already be seen, demonstrating that the mushroom nanostructures do not prefer to adsorb to the OTS surface. The layers also show a distinct surface texture that is reminiscent of that of thicker films and likely leads to nucleation of the polydomain structure.

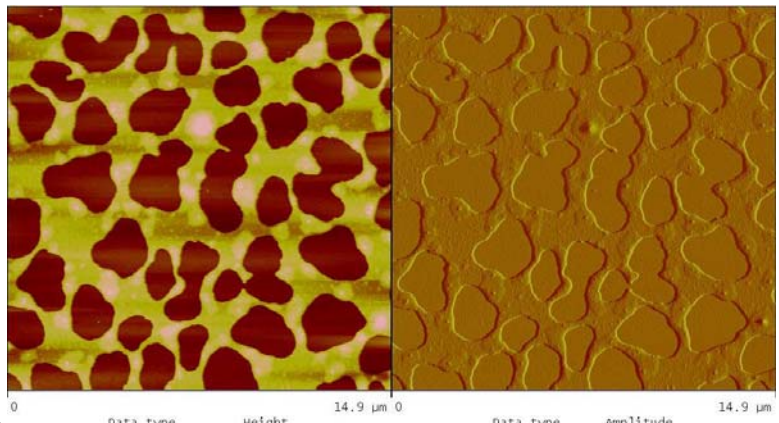

(A)

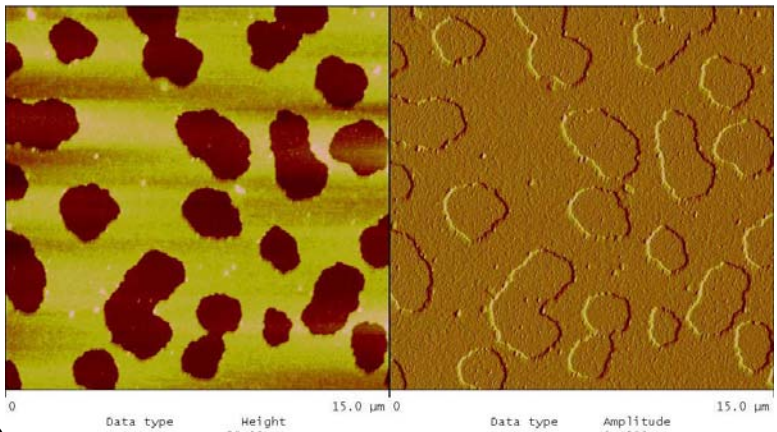

(B)

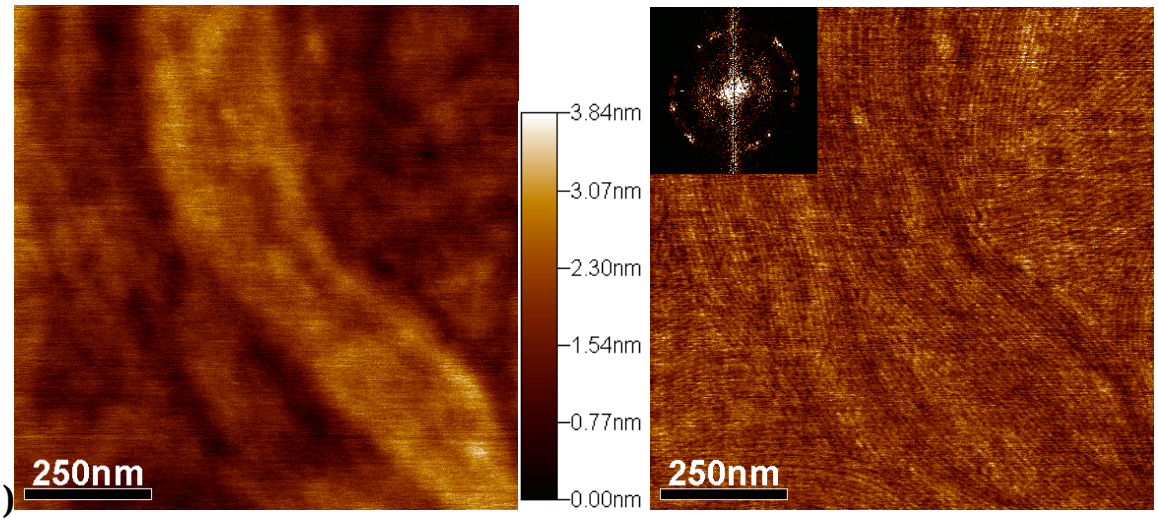

(C)

Figure 2.15. AFM height and phase contrast images of **2.1** on piranha-cleaned silicon cast from (**A**) 1 mM and (**B** and **C**) 2 mM solution in chloroform. The striations visible in the phase image in **C** have a regular period of 10.6 nm as shown by the inset FFT.

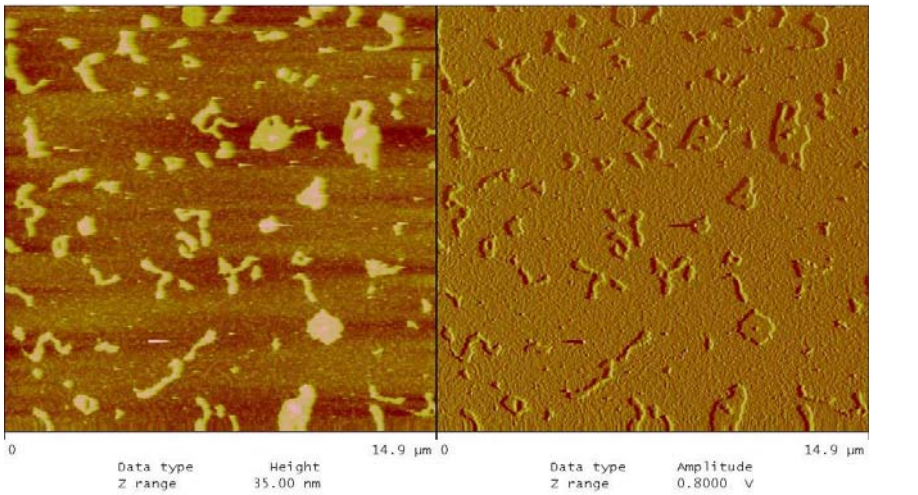

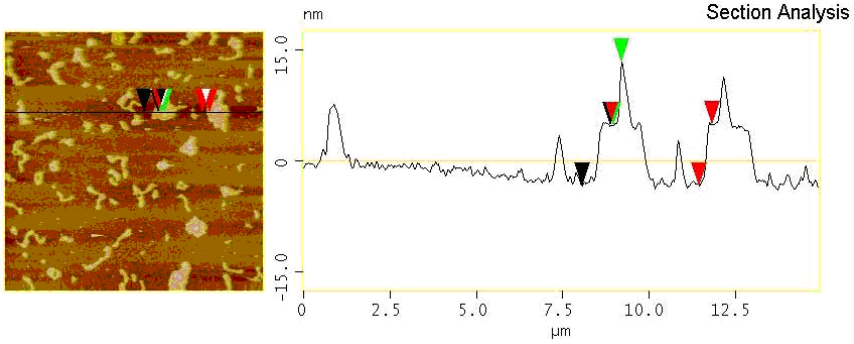

(A)

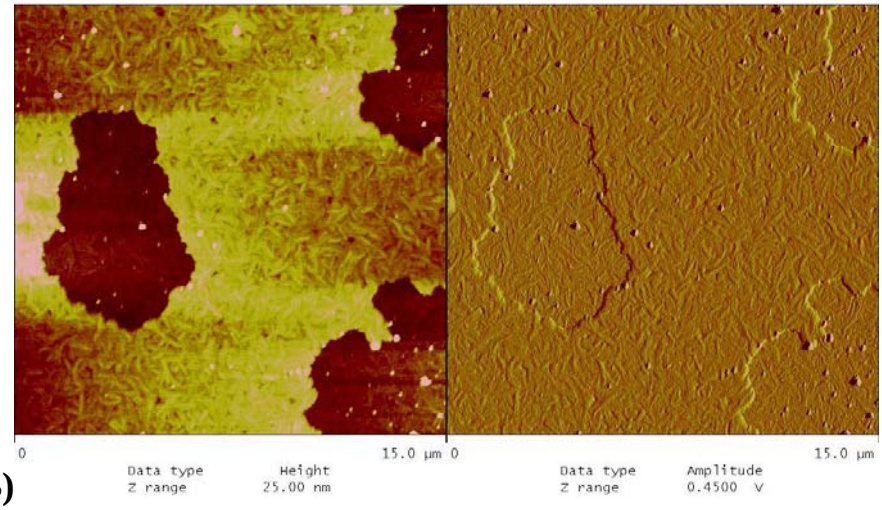

(B)

Figure 2.16. AFM images of **2.1** cast from (**A**) 1 mM and (**B**) 2 mM solution onto OTS-coated silicon. Height differences in the line section of **A**: (red) 8.28 nm, (green) 8.56 nm, (black) 8.17 nm (courtesy of Dorothea Greishaber).

2.4.3 Layer thickness and implied molecular orientation

The thicknesses of 3BPOH layers deposited and annealed on various surfaces are listed in Table 2.2. All observed layer thicknesses are greater than the bulk periodicity obtained by SAXS. Crystallization of the rod segments is known to create some excess free volume around the region of the mushroom stems. It was hypothesized that in the bulk, this free volume is partially filled by a slight interdigitation of the flexible caps between the stems, leading to a lamellar spacing that is less than the full height of a mushroom as shown schematically in Figure 2.17. However, on a substrate, this mechanism is unavailable, so one may be more likely so observe the full height of the mushroom structure. In addition, the excess volume around the stems would likely lead to strain in the film and may be compensated for either by tilting of the rod segments or compression of the coil segments. In the former case, the monolayer thickness is reduced, but it is increased in the latter case. Both tilting of the rods and compression of the coils may occur and compensate for each other, but the results suggest that the latter is more prevalent.

Table 2.2. Thicknesses of layers of **2.1** deposited on various surfaces as measured from AFM of sub-monolayer and sub-bilayer films.

Surface	Layer thickness (nm)	
	First layer	Second layer
HF treated Si (Si-H)	8.28 ± 0.17	8.38 ± 0.12
Piranha treated Si (Si-OH)	9.35 ± 0.12	8.8 ± 0.3
OTS treated Si	7.78 ± 0.13	8.07 ± 0.16

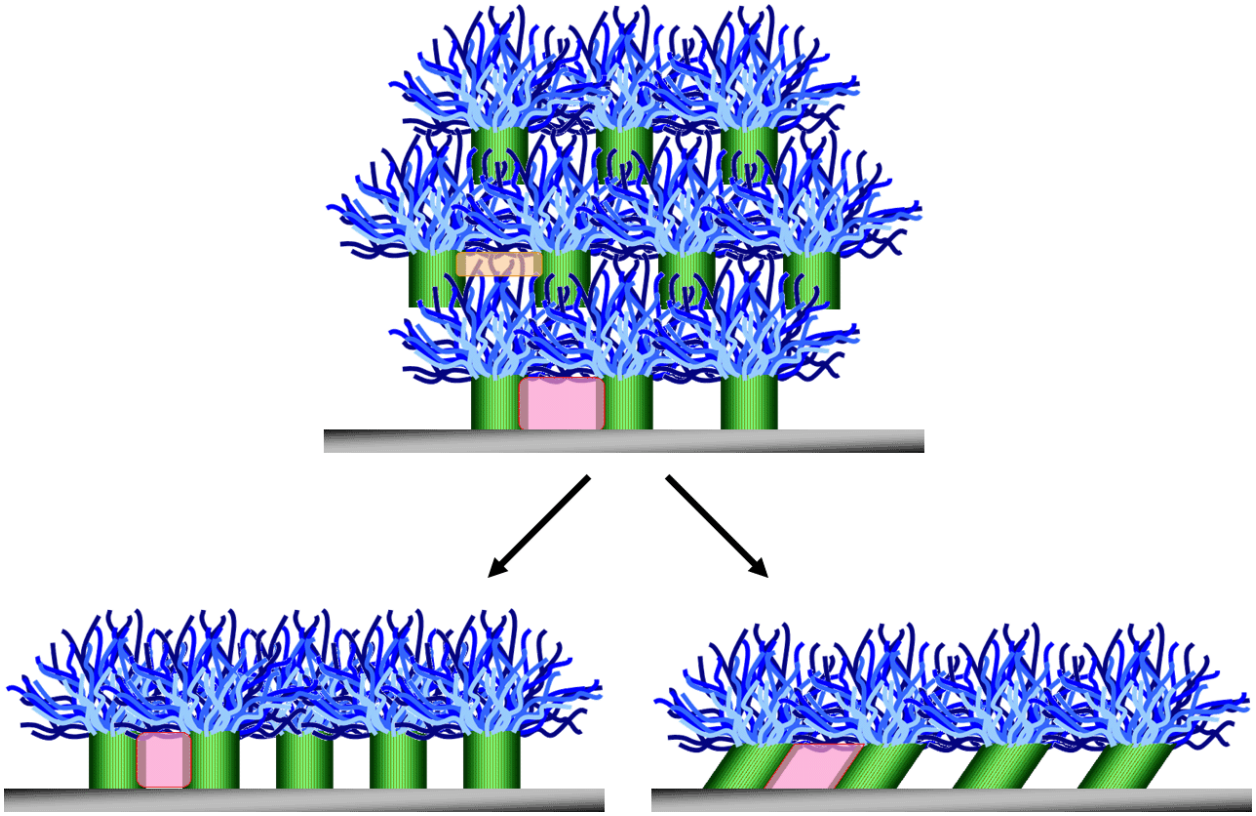

Figure 2.17. Schematic representation of the packing of supramolecular mushroom-shaped aggregates near a surface. In the bulk, free space (orange) between the "stems" can be partially filled by interdigitation of coil segments. However, free space (red) between surface-adsorbed nanostructures must be limited by other mechanisms, such as compression of the "caps" or tilting of the rods.

The thickest monolayers are observed on piranha-cleaned silicon, with the next thickest observed on HF-cleaned silicon and the thinnest on OTS silanized surfaces. This trend may be attributed to a greater affinity for the phenolic end of molecule 2.1 to hydrogen bond to the native oxide. The oxide surface likely exhibits a high density of possible binding sites, favoring a tighter packing of the rod segments and greater compression of the coils, leading to a more extended conformation of the molecule. In addition, the rod segments may prefer to pack more tightly along one axis due to favorable π–π interactions, creating more elongated structures.

This is one possible explanation for the striated textures observed in Figure 2.15c. The subsequent layer deposited on the monolayer also appears to retain some extended molecular conformation, suggesting that the structure of the previous layer affects the structure of the next layer and that the effect of substrate interactions may be felt at least through the second layer.

The thickness of the monolayer may also be used to establish an estimate for the average tilt angle θ of the molecules. This may be done by assuming that the molecules are in a fully extended state but pack together at some angle away from the substrate normal, such that

$$d = l\cos\theta \qquad (2.3)$$

where d is the layer thickness and l is 9.5 nm, the extended length of the molecule. Tilt angles obtained in this manner are plotted in Figure 2.18. The tilt of the rod segment is of particular interest, as it is the portion that is expected to contribute the most to the dipole moment of the

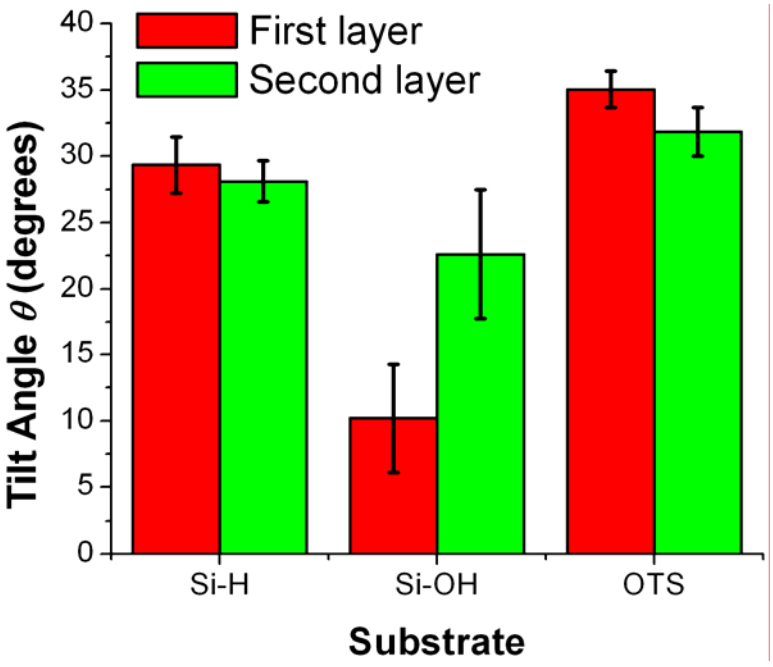

Figure 2.18. Molecular tilt angles calculated from equation 2.3 of layers of **2.1** deposited on various surfaces.

molecule. These values for the tilt angle may underestimate the actual tilt of the rod segment in one way because the molecule can bend and the tail segment may extend at a shallower tilt angle than the rod. However, the tail segment is also likely to coil, which would suggest an overestimation of the tilt angle. Both errors cancel each other to some degree, and the numbers for the tilt angle obtained may not be unreasonable.

2.5 Supramolecular host-guest system

2.5.1 Characterization of the guest molecules

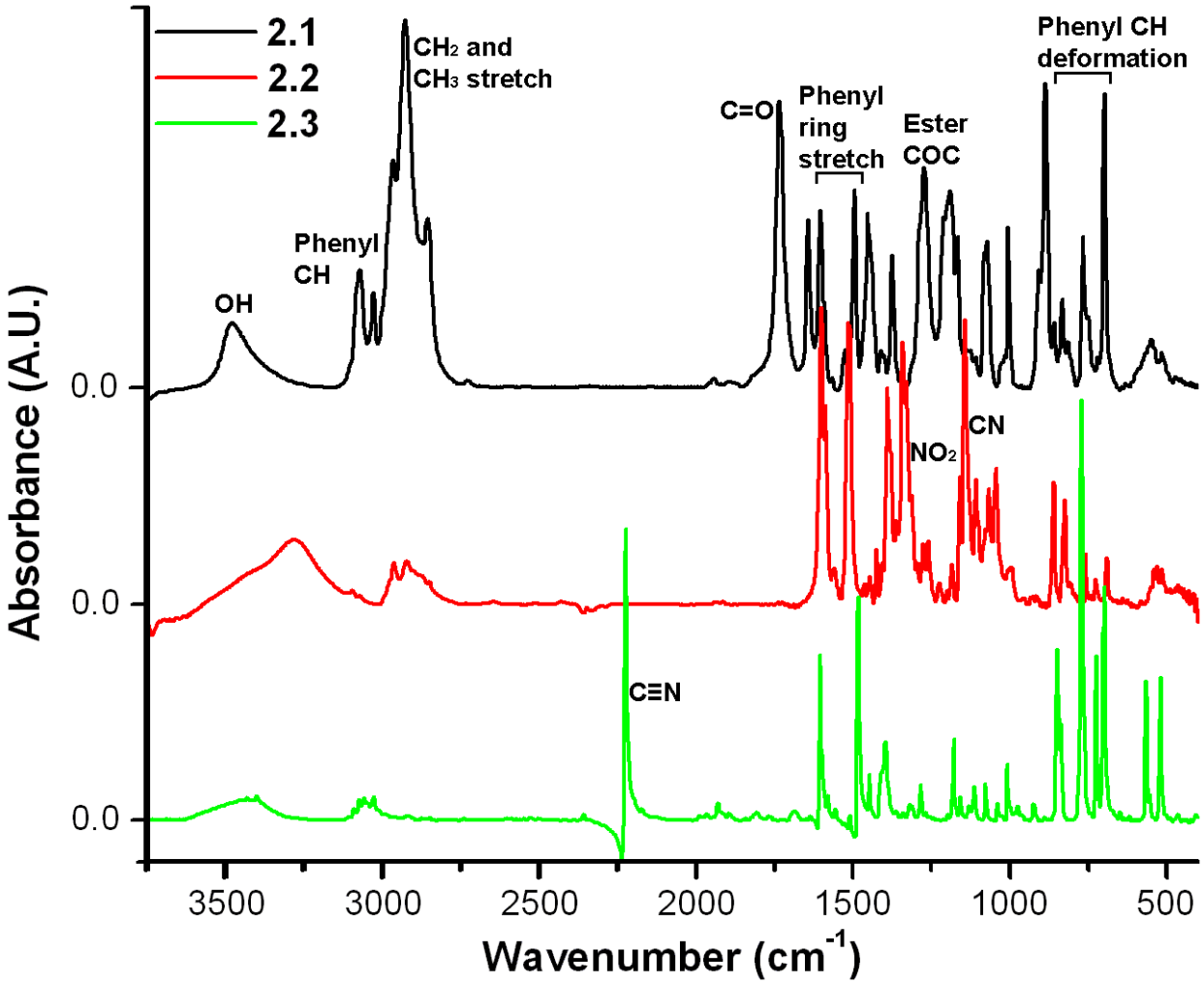

Figure 2.19. FTIR spectra of molecules **2.1** – **2.3** with select peaks of interest labeled.

Table 2.3. IR vibrations of interest and their observed wavenumbers for **2.1** – **2.3**.[246, 247]

Vibration	Wavenumber (cm^{-1})		
	2.1 (3BPOH)	**2.2** (DR1)	**2.3** (CB)
ν(OH)	3475 (aromatic)	3282 (aliphatic)	
Aromatic ν(CH)	3104, 3070, 3026	3100 – 3020	3110 – 3025
$\nu_{as}(CH_3)$ and $\nu_{as}(CH_2)$	2964 and 2926	2966 and 2926	
$\nu_{s}(CH_3)$ and $\nu_{s}(CH_2)$	2872 and 2854	2873 and 2850	
ν(C≡N)			2225
Ester ν(C=O)	1734		
Vinyl ν(C=C)	1643		
Aromatic ring stretch	1603, 1495	1601	1606, 1483
$\nu_{as}(NO_2)$		1516	
CH_2 scissor	1452		
ν(N=N)		1390	
$\delta_{s}(CH_3)$	1375	1378	
$\nu_{s}(NO_2)$		1342	
Ester ν_{as}(COC)	1273		
Phenol ν_{s}(CO)	1190		
Aliphatic amine ν(CN)		1143	
Aliphatic ν_{as}(CCC)	1072	1066	
Aromatic in-plane δ(CC)	1005	1001	1007
Aromatic in-plane δ(CH)	1210 – 1000 (weak)	1200 – 990 (weak)	1180 – 1000 (weak)
Vinyl out-plane wag (CH_2)	887		
Phenyl out-plane δ(CH) near NO_2, COO	858	860	
Para disubstituted phenyl out-plane δ(CH)	833	823	849
Monosubstituted phenyl out-plane δ(CH)	768, 698	755, 690	771, 698
Phenyl in- and out-plane ring deform	550, 517	538, 513	565, 519
Yellow = parallel to axis		*Blue = perpendicular to axis*	

FTIR spectra of molecules **2.1** – **2.3** dispersed in KBr pellets are shown in Figure 2.19. Table 2.3 lists the major vibrations of interest and their observed wavenumbers for each molecule. Molecule **2.2** is a common non-linear optical functionality known as disperse red 1 (DR1) dye. Molecule **2.3** is 4-cyanobiphenyl (CB) and is used as a starting material for the synthesis of some common nematic liquid crystals. DSC measurements give melting points of 161 and 86.5 °C for DR1 and CB, respectively.

2.5.2 Preliminary results with disperse red 1

It was thought that molecule **2.2**, when added to the mushroom system, might align parallel to the liquid crystal director and thus serve as a tool to amplify the SHG signal. SHG intensities of dye-doped films are given in Figure 2.20. DR1 is added in 1:3 molar concentration of dye to 3BPOH (1:21 by weight), dissolved into a 3 wt % solids solution in chloroform, and spin-coated onto clean glass substrates. These films are not annealed as it is found that the dye readily evaporates from the films upon heating. DSC shows no indication of significant phase separation as the melting peak of DR1 is absent. The liquid crystalline transition of **2.1** at 150 °C disappears or shifts to a lower temperature, combining with the transition around 125 °C. A strong SHG signal is seen indicating some orientation normal to the surface. However, equal weight percent mixtures of **2.2** in polymethylmethacrylate (PMMA, M_w=120K, Aldrich) and in polystyrene (PS, M_w=280K, Aldrich) give comparable signals. When **2.2** is diluted to 1:10 molar (1:70 by weight) the 3BPOH film seems to give a stronger signal despite being slightly thinner than the PMMA or PS films, suggesting that the supramolecular structure may influence the molecular orientation of DR1.

Alignment of the dye was found to be due in part to an interaction with the substrate. Thin films of pure DR1 deposited on clean glass give a weak SHG signal, while those deposited on OTS-functionalized (hydrophobic) glass give little or no signal. Transmission FTIR of DR1 both in pellet form and cast onto a clean substrate of undoped silicon is shown in Figure 2.21. It

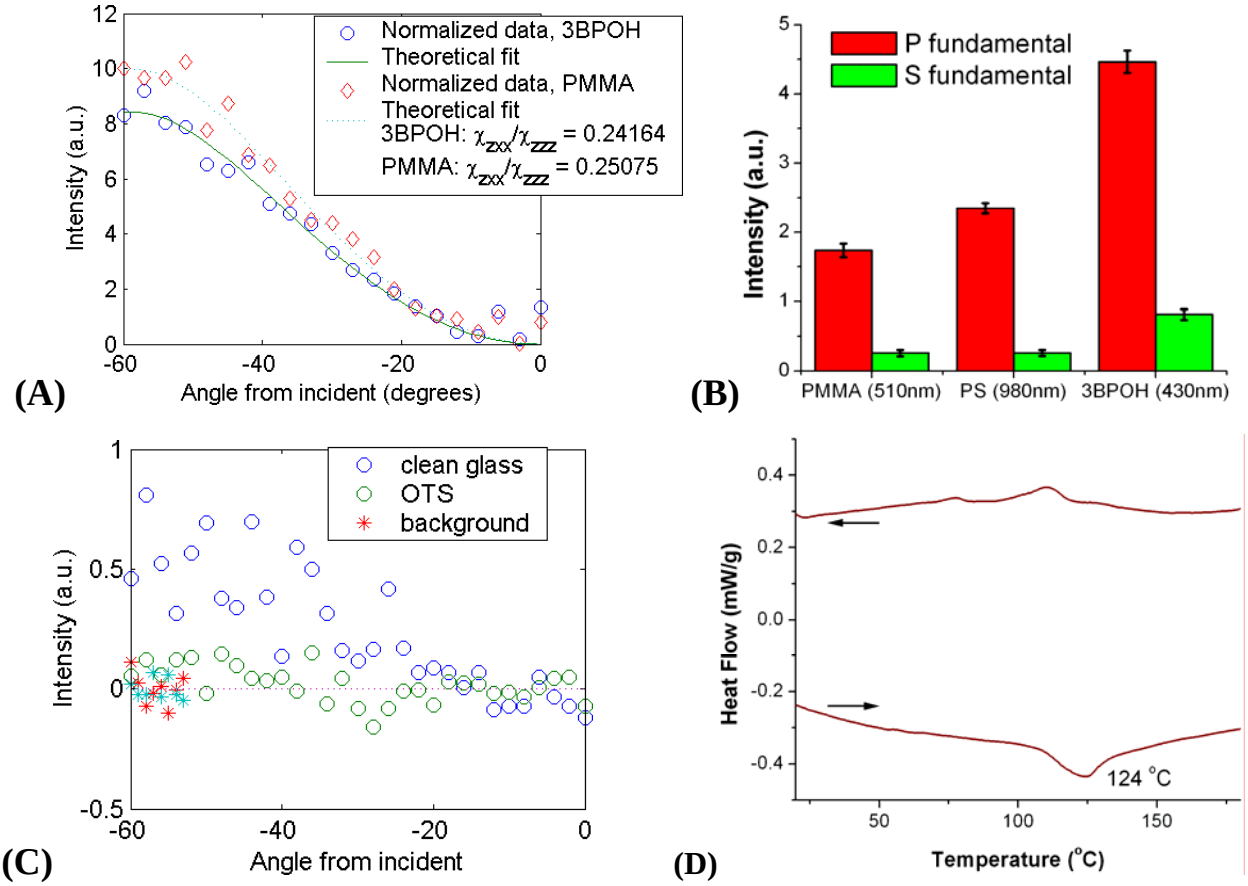

Figure 2.20. (**A**) SHG of spin-coated films doped with DR1 dye (1:21 dye to host by weight) show signals indicative of a net orientation normal to the substrate in all cases ($r^2 > 0.97$ for both fits). (**B**) For 1:70 by weight mixtures, the signal for 3BPOH taken at a fixed angle of 45° over 1000 pulses appears to be slightly larger than for other films (label numbers indicate film thicknesses). (**C**) Thin films of pure disperse red cast from 0.1wt% solution in chloroform onto clean glass show an SHG signal while those cast onto glass treated with OTS show little signal. (**D**) DSC scans of 1:21 DR1:3BPOH mixtures show a slight shift in the liquid crystal transitions of 3BPOH.

is obvious that the hydrophilic oxide surface leads to preferential orientation of the molecule normal to the surface. Results obtained for DR1 are also complicated somewhat by the fact that it undergoes a *trans* to *cis* conformational change upon irradiation with UV light. Because of these factors, it was decided that a simpler small molecule guest, while not as optically active, may be more suitable for studying supramolecular host-guest interactions.

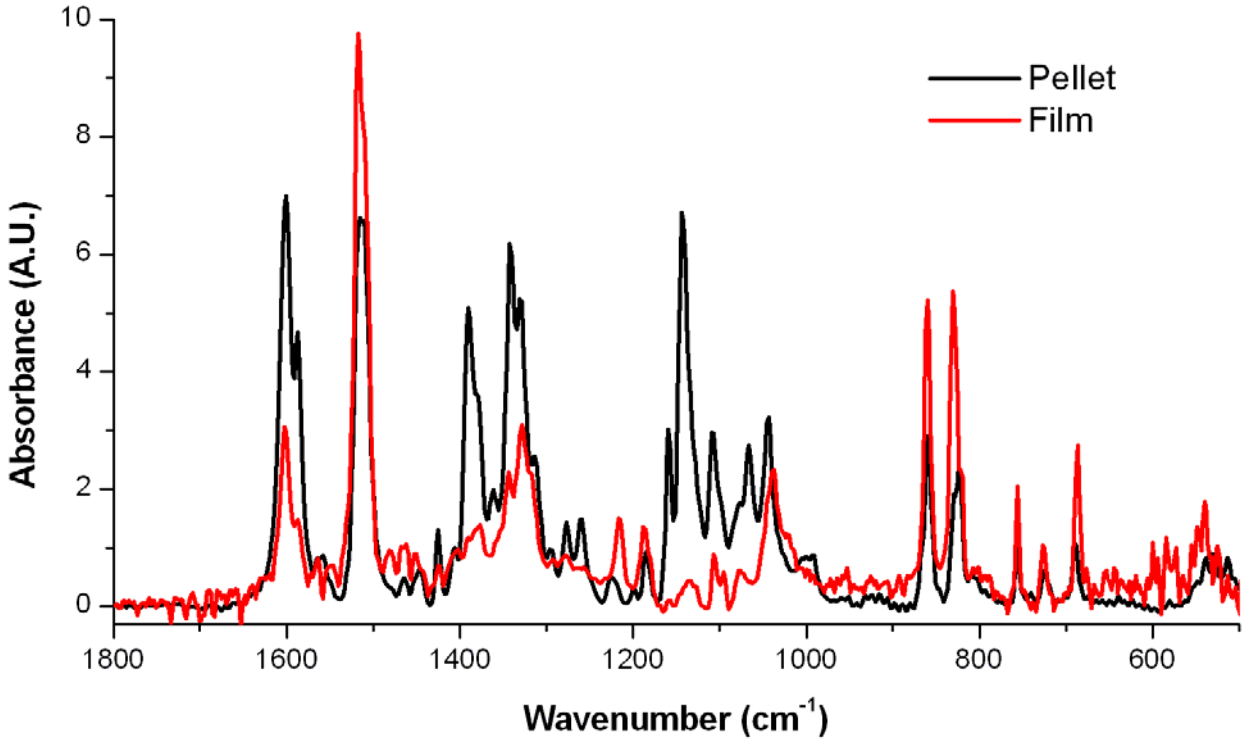

Figure 2.21. Transmission FTIR spectra of a KBr pellet and spin-coated film of DR1. The film shows a molecular orientation normal to the substrate as vibrations parallel to the molecular axis decrease and those perpendicular increase.

2.5.3 Molecular order of 4-cyanobiphenyl mixed in a supramolecular host

4-cyanobiphenyl (CB, molecule **2.3**) was chosen as a suitable model for the study of supramolecular host-guest interactions. It was hypothesized that the biphenyl portion would

interact favorably with the rod segment of molecule **2.1**. In addition, the C≡N stretching vibration, ν(C≡N) absorbs at 2227 cm^{-1}, providing an outstandingly clear handle for probing molecular orientation. Films of **2.1** mixed with CB were studied in molar ratios of 1:1, 3:1, and 10:1 of guest to molecule **2.1**. DSC measurements shown in Figure 2.22 of the mixed material reveal a decrease in temperature of the liquid crystal transitions of molecule **2.1** with increasing CB. The data suggests that the addition of the small molecule at these relatively high concentrations does alter self-assembly behavior slightly, lowering the temperature of the liquid crystal transition. This makes sense as small molecules are often used as polymer plasticizers, and the liquid crystal transition is likely due to melting of the oligomer coils. However, what is telling is that the isotropization temperature related to melting of the rigid rods is not depressed

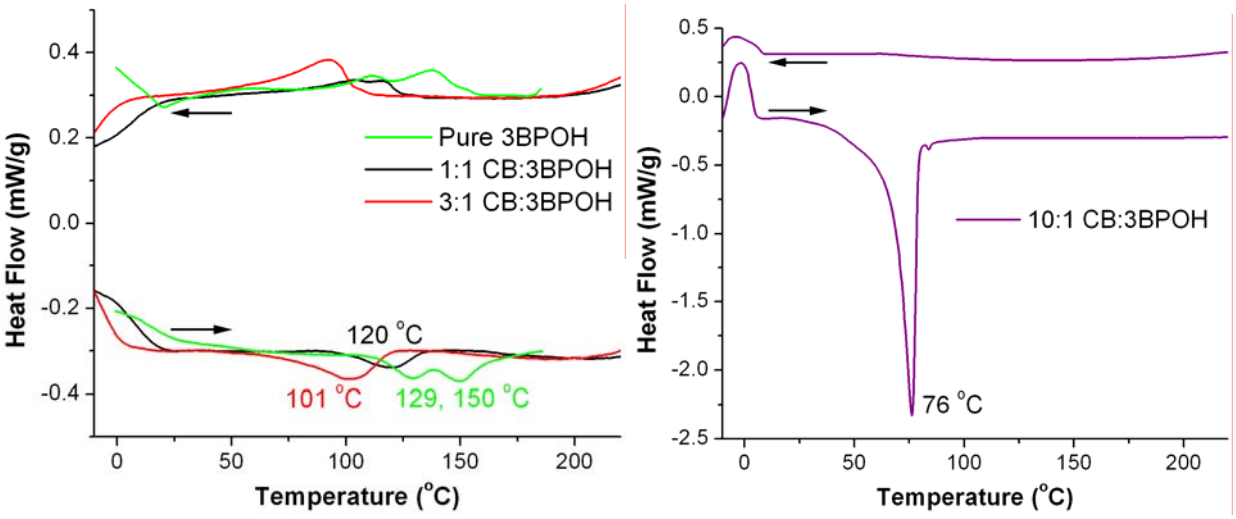

Figure 2.22. DSC scans of 3BPOH and 1:1, 3:1, and 10:1 molar mixtures of CB to 3BPOH (exotherm up). Depression of the liquid crystal transition temperatures of 3BPOH is observed, although the isotropization temperature, originally 250 °C, was never observed to go below 240 °C. The 10:1 mixture shows significant phase separation, although the melting temperature of CB is also depressed.

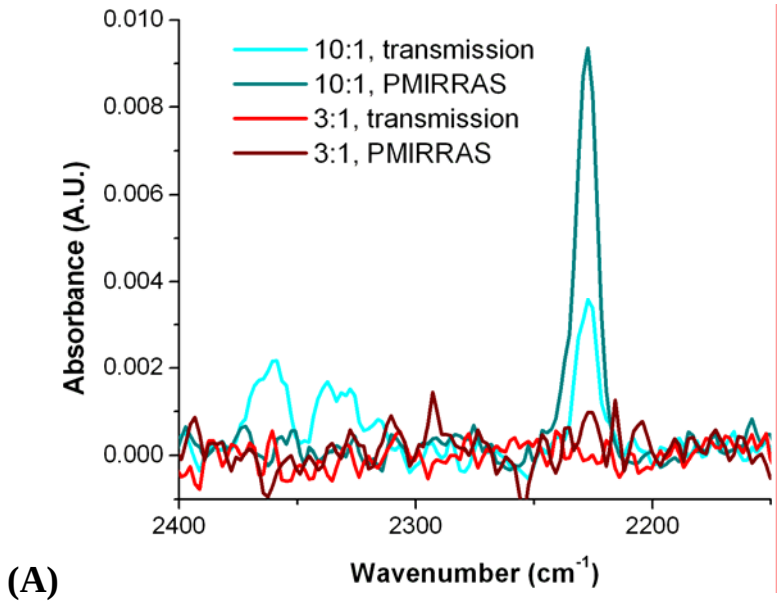

(A)

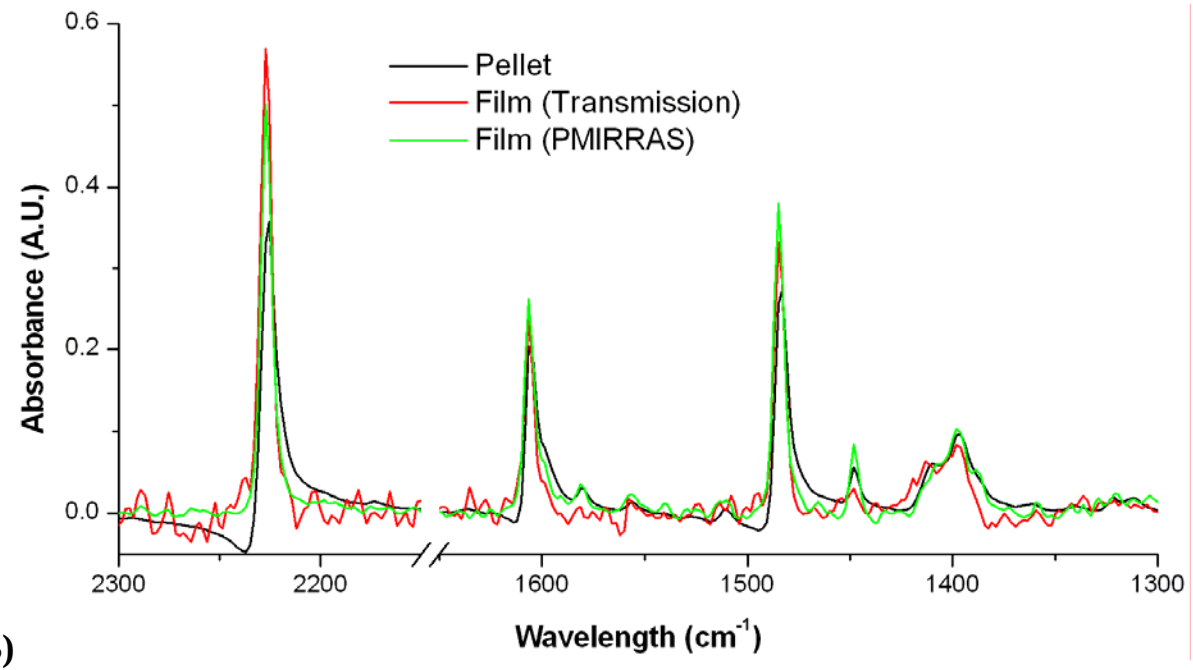

(B)

Figure 2.23. (**A**) Transmission IR and PMIRRAS spectra of films of 3:1 and 10:1 molar mixtures of CB to 3BPOH. The intensity of ν(C≡N) is observed to decrease in transmission, suggesting orientation of the molecule normal to the substrate. No vibrations attributable to CB are observed above noise in the more dilute mixtures. (**B**) Transmission IR and PMIRRAS suggest that films of pure CB alone exhibit minimal net molecular orientation.

(A)

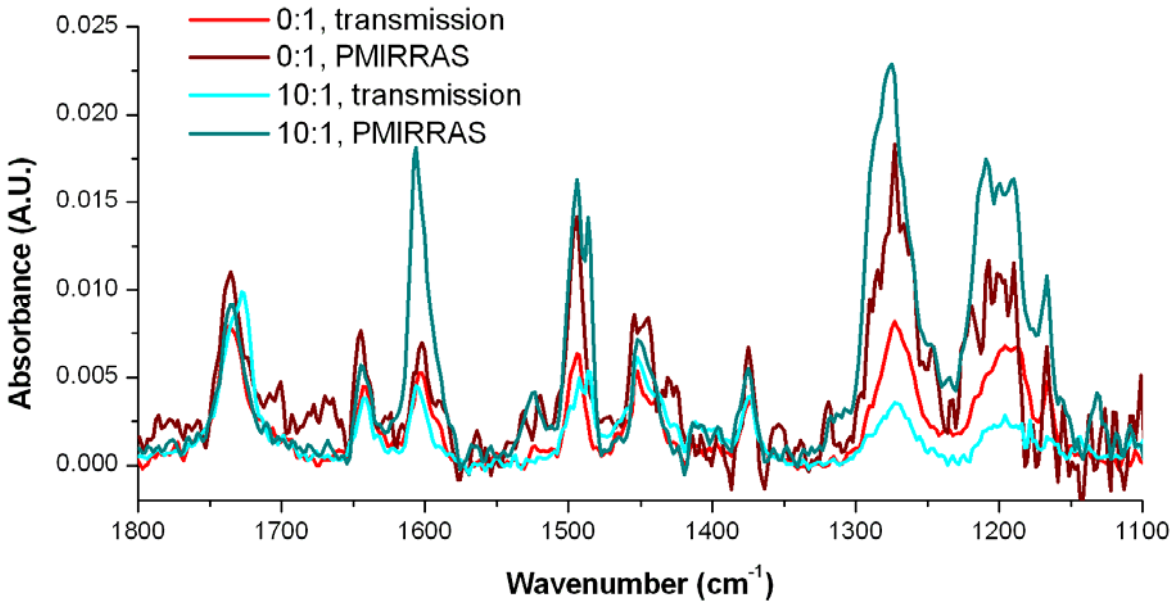

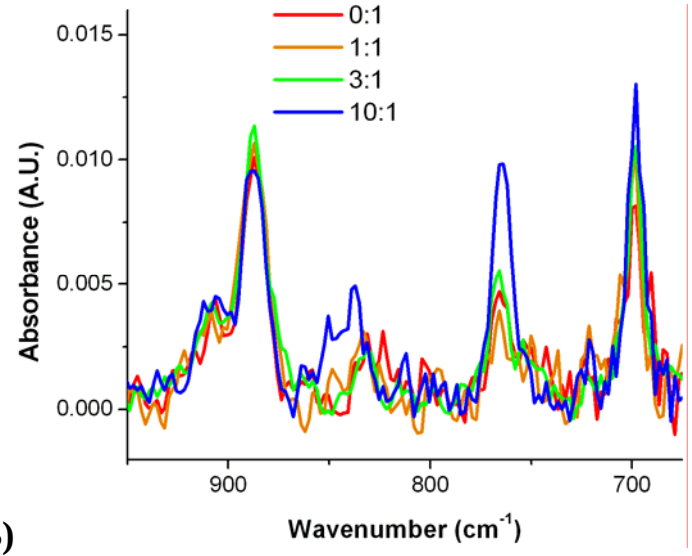

(B)

Figure 2.24. (**A**) Transmission IR and PMIRRAS spectra of films of 0:1 and 10:1 molar mixtures of CB to 3BPOH. The increased intensity in PMIRRAS of the phenyl ring stretching vibrations at 1603 cm^{-1} and 1495 cm^{-1} (note that for CB, the later is shifted to 1483 cm^{-1}), the ester COC antisymmetric stretch at 1273 cm^{-1}, and the phenol CO stretch at 1190 cm^{-1} suggest a more normal orientation not only of the guest but of the host molecule as well. (**B**) The transmission spectra of the mixed films show a slight increase in the intensity of the phenyl CH out-of-plane deformations, also suggestive of a more normal orientation.

into the temperature range of interest. This suggests that the CB is either tightly bound and incorporated intimately within the crystal structure of the stems or, more likely, is excluded entirely from them. At a 10:1 molar ratio there is some phase separation of the excess CB, resulting in the presence of the large melting peak.

Figure 2.23 and Figure 2.24 show representative FTIR spectra mixtures of 2.1 and 2.3 spin-coated into thin films on hydrophilic oxide surfaces. Spectra of (1) are normalized to the sum of the CH_2 and CH_3 symmetric and antisymmetric stretch vibrations between 2970 cm^{-1} and 2850c m^{-1}. In the mixed films of 10:1 molar ratio, ν(C≡N) appears more prominent in the PM-IRRAS spectra than in the transmission spectra. In comparison, films of pure CB showed minor variation between the reflectance and transmission spectra. This result suggests that CB is oriented more normal to the substrate when mixed with **2.1** and cast from solution.

Other characteristic vibrations of CB corroborate this model. The ring stretching vibrations at 1606 cm^{-1} and 1483 cm^{-1} do overlap the same vibrations in **2.1**. However, the relative contribution to the height of those peaks by CB, while quite apparent in PMIRRAS, is not as prominent in transmission. The phenyl CH out-of-plane deformation vibrations are perpendicular to the long axis of CB appear qualitatively to behave in a manner opposite to the ring stretching vibrations, increasing in relative intensity in transmission mode. However, the CH deformations are difficult to compare because they are at wavenumbers where the signal-to-noise ratio is high. Other vibrations perpendicular to the molecular axis are generally too weak to see.

The C≡N peak is only observed in films of the 10:1 molar mixture. This is not only because the concentration of CB in the 3:1 and 1:1 mixtures is more dilute, but because the small molecule is slightly volatile and sublimes from the film. All films are examined by IR

spectroscopy exactly 20 min after spin-coating in order to minimize differences in concentration. This is additional evidence that CB is not assembled within the stem of the mushroom nanostructures or otherwise intimately associated with the host material.

Absorbance values for particular vibrations are obtained from the peak areas and normalized against the total peak area for the CH_2 and CH_3 symmetric and antisymmetric stretching vibrations. The linear dichroic ratio, *d*, is calculated as the ratio of the transmission absorbance to the reflection absorbance. The order parameter[240] quantifying orientation of the molecule relative to the substrate normal may be calculated as

$$f_\theta = \frac{1-d}{2d+1} \qquad (2.4)$$

Based on the ν(C≡N) peak, the small molecule guest aligns normal to the substrate with an order parameter of 0.40 ± 0.13. We hypothesize that preferential orientation of CB in the mixture is a result of favorable π–π stacking interactions with the rigid biphenyl segment of **2.1**. In this case, CB would orient parallel to the rigid segment of **2.1** which is believed to be itself oriented close to normal or slightly tilted relative to the substrate. CB may also be aligned relative to the rod segment of **2.1** through dipole-dipole interactions. Such interactions might result in orientation of CB not only normal to the substrate but antiparallel to the rod segments. The IR data does not give any evidence for or against polar order of the guest molecule, but it could be possible to answer that question with SHG measurements.

The alignment of CB in the host system is not perfect, but the mixture of CB and **2.1** in a 10:1 molar ratio results in an excess of CB that is not mixed homogeneously into the film as evidenced by DSC. This excess quantity is likely not preferentially oriented and would contribute a significant isotropic signal. There is also the likelyhood of some mixing of CB with

the coiled portion of **2.1** where the oligostyrene segment would offer limited π–π stacking. Examining mixtures of CB and **2.1** at molar concentrations between 3:1 and 10:1 may yield films that contain less excess guest molecule and thus show greater orientational order.

2.5.4 Molecular order of supramolecular host mixed with 4-cyanobiphenyl

The spectra in Figure 2.24 also suggest that not only is CB preferentially oriented when incorporated as a guest in films of **2.1**, but that **2.1** is itself oriented more normal to the substrate when mixed with the guest. In pure films of **2.1**, a minimal difference is observed between the PMIRRAS and transmission spectra. However, in mixed films of **2.1** and CB, significant differences in peak intensities are observed at 1190, 1273, 1495 and 1603 cm^{-1}, corresponding to the phenol ν(C-O) stretch, the ester ν_{as}(C-O-C) antisymmetric stretch, and two aromatic ring vibrations, respectively. The peaks in question are enhanced in the PMIRRAS spectra and diminished in the transmission spectra. Those vibrations are generally associated with TDMs on the rigid rod segment that are aligned more parallel to the molecular long axis.

Figure 2.25 outlines the space coordinate system and angles describing orientation of the rod segment of **2.1**. A more detailed description of the equations and assumptions used to calculate the order parameters and orientation angles is given in Appendix A. We begin by calculating a lower bound for the orientational order parameter using equation 2.4 which assumes no tilt of the TDM off the axis of the rod ($\alpha = 0$). Values obtained in this manner based on the ester ν_{as}(COC) of **2.1** are plotted in Figure 2.26. Spin-coated films of **2.1** alone show some degree of orientation normal to the substrate. Surprisingly, annealing the film doesn't appear to improve the orientation, but the addition of CB in molar ratios of 3:1 or greater results in a significant increase in the order parameter.

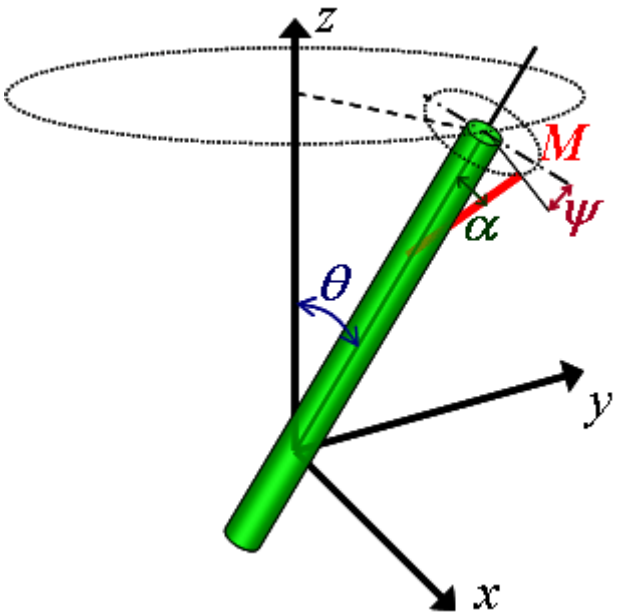

Figure 2.25. Schematic of the space coordinate system and relevant angles describing orientation of the rod segment of molecule **2.1**.

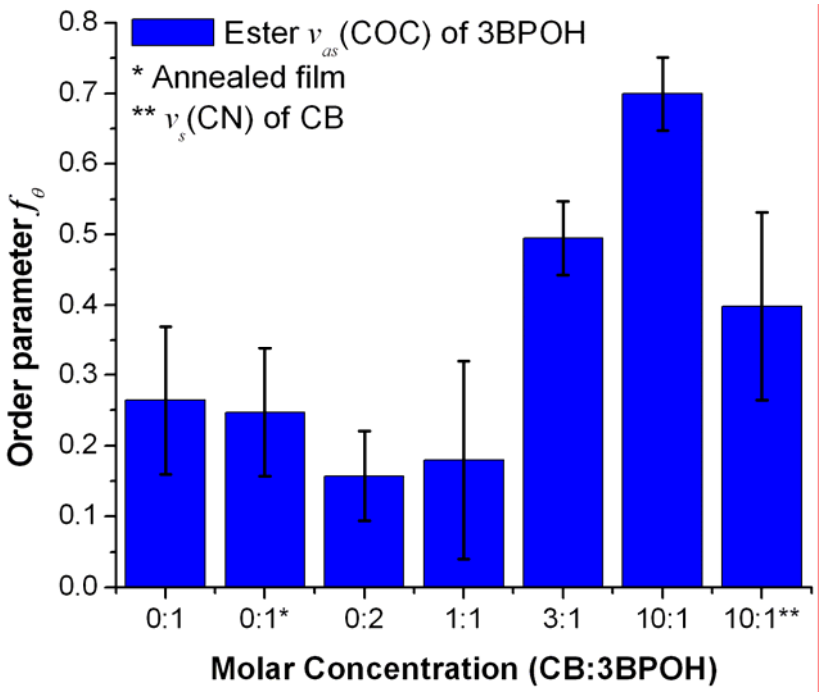

Figure 2.26. Order parameter f_θ of the 3BPOH molecule calculated from the absorption intensities of the ester ν_{as}(COC) using equation 2.4.

A maximum value for the average tilt angle θmax of the rod segments can be calculated from the order parameters. In actuality, $\alpha \neq 0$ and the real order parameter is larger than the values plotted. We may try to obtain more representative values of θ and the order parameter by assuming a value for α. We start by assuming that the condition which exhibits the lowest order parameter (the 10:1 mixture) is in fact perfectly oriented and the observed tilt is due to a non-zero value of a, which would give a value of $\alpha = 27 \pm 2$ °. Maintaining the assumption of a uniform distribution of the molecular twist angle ψ, a "corrected" value of the order parameter f_θ^* is calculated simply from

$$f_\theta^* = f_\theta / f_{\theta,\min} \qquad (2.5)$$

where $f_{\theta,\min}$ is the value of f_θ for the 10:1 mixture. From this value of f_θ^*, a "corrected" value of the tilt angle θ^* can also be calculated.

The assumption of a uniform distribution of the twist angle ψ may also be invalid as it is possible that the rod segments crystallize during self-assembly. We therefore looked at the extreme case in which ψ was not random but fixed at a value of 0. This model results in an upper bound value for the order parameter and a lower bound value of the tilt angle $\theta_{\min} = \theta_{\max} - \alpha$. Calculated values of $\theta_{\max}$, θ^*, and $\theta_{\min}$ are listed in Table 2.4. What is most interesting is the fact that the value of θ obtained earlier from AFM measurements of the thickness of annealed films is still lower than $\theta_{\min}$. This may suggest that the model assuming $\psi = 0$ is valid and that the ester COC bonds in the "stem" of the supramolecular mushroom nanostructures have a specific orientation angled farther from the surface normal than the rest of the rod segment.

Table 2.4. Possible values of the tilt angle θ for the rod segment of **2.1** calculated from spectroscopic data.

Molar concentration of initial solution (CB:3BPOH)	θ from AFM (°)	θ_{max} (°)	θ^{*} (°)	θ_{min} (°)
0:1		44 ± 4	40 ± 6	18 ± 5
0:1*	10 ± 4	45 ± 3	41 ± 5	18 ± 4
0:2		49 ± 2	46 ± 4	22 ± 3
1:1		48 ± 5	45 ± 8	21 ± 6
3:1		35 ± 2	26 ± 4	9 ± 3
10:1		27 ± 2	0	0
10:1**		39 ± 5		

*Film annealed at 155 °C for 4 hrs.

Tilt angle for **2.3

We theorize that the alignment effect of CB on films of **2.1** is due to the ability of the small molecule to fill up free volume and relieve strain at the surface layer as outlined previously in Figure 2.25. At a surface, it is difficult for the mushroom aggregates to pack efficiently, and the strain that results from excess free volume around the stem may be alleviated by compression of the caps, tilting of the rigid rod segment, or both. Introduction of a small molecule guest that preferentially interacts with the rigid segment might be able to take up that free volume and release the strain, allowing **2.1** to adopt a more normal orientation. The normal orientation also allows for the most efficient packing of molecules per unit area over the surface, which is desirable if there is a favorable interaction between the rigid rod terminus and the substrate. In turn, if the guest exhibits a preferred alignment parallel to the rigid segment, then the guest would also be oriented normal to the substrate. This is an exceptional case in which the whole is

greater than the sum of the parts: mixing of a guest into a supramolecular host results in improved ordering of both components.

2.5.5 Discussion of validity and errors in the spectroscopic model

The values of f_θ calculated above are useful as figures of merit by which the effects of different experimental parameters may be compared within the realm of the posited molecular model. The calculated values of θ serve a similar purpose, restating f_θ as a more tangible, physical quantity. However, when judging the accuracy of these values for quantifying molecular order in this self-assembling system, it must be recognized that the model is a simplified one. The IR data alone is insufficient to solve the system of equations exactly, so we attempted to establish a range of possible values for the order parameter by assuming specific molecular structures and TDM orientations. While the range of values may appear quite wide, some structural assumptions often are more likely than others, and one can reasonably focus on a smaller, more probable range of values.

Two major assumptions made in this model are that the material is optically isotropic and that variations in reflectance and refractive index with wavelength are negligible.[248, 249] Dispersion of the real refractive index is known to result in distortion of the spectral line shape for non-normal angles of incidence and is seen most prominent in highly crystalline materials. In our case, no noticeable distortion is observed, and the signal-to-noise ratio appears to be a more significant hindrance to quantitative evaluation. The effect of birefringence in the material on the spectra is also of concern as the effect becomes stronger with increasing molecular order. Neglecting birefringence can lead to over- and underestimation of the absorptions of vibrations oriented perpendicular and parallel, respectively, to the optic axis.[212, 250] For the 3BPOH/CB

system studied, this suggests that the order parameters calculated above underestimate the true order parameter of the material.

2.6 Summary and Outlook

NSOM images show that films of molecule 2.1 exist as a polydomain structure with individual grains on the order of 500 nm in size. Solution embossing was successfully employed to pattern the film into micrometer-scale features, however, NSOM images showed that the domain structure was mostly unaltered, and no improvement in the SHG intensity was observed. It was hypothesized that thinner films would be less likely to show a polydomain structure and would be more responsive to surface treatments. Indeed, monolayer and bilayer films deposited and annealed on hydrophilic oxide surfaces showed greater layer thicknesses than those deposited on hydrophobic surfaces, suggesting that the oxide presents more opportunities for hydrogen bonding of the phenol group, leading to tighter packing of the molecules and a molecular orientation more normal to the substrate. Films deposited on hydrophobic surfaces were also more textured and suggested a greater degree of disorder. Patterning a hydrophilic oxide surface with a regular array of hydrophobic features may be one possible way to control the domain structure of the film, although the features would likely need to be sub-micrometer in size. It remains to be seen whether such surface treatments retain their effect on film morphology beyond the first few layers.

When these films are mixed with a small biphenyl molecule, the supramolecular host appears to align the small molecule guest more normal to the substrate as seen by FTIR. In addition, the supramolecular host appears to be aligned more normal as well by the addition of the guest. It is hypothesized that this effect is due to the small molecule guest taking up excess

free volume around the stems of the mushroom-shaped aggregates, relieving strain within the film and allowing the mushroom-shaped aggregates to adopt a more normal conformation without undue compression of the caps. DSC shows limited mixing of two components and little effect on phase behavior. There is promise that the supramolecular film may be used to align other small-molecule guests that are optically active.

CHAPTER THREE

Microcontact Printing of Self-Assembling Peptide-Amphiphile Nanofibers

Chapter 3: Microcontact Printing of Self-Assembling Peptide-Amphiphile Nanofibers

3.1 Introduction

Controlling the placement and orientation of nanometer-scale objects is essential for many of the technological applications envisioned for supramolecular self-assembly.[8-10] Most self-assembling materials are macroscopically disordered which can limit their bulk properties and potential uses. Patterning on the microscale may extend order in a predictable manner over large areas, dramatically improving performance and enabling new functions.[11, 34, 190, 251-253]

A class of molecules known as peptide-amphiphiles (PAs) that consist of an aliphatic tail linked to an oligopeptide segment have been investigated in recent years and shown to assemble into a wide range of one- and two-dimensional supramolecular structures.[115-117] In our laboratory, PAs have been designed that self-assemble into cylindrical nanofibers from aqueous solution by burying their alkyl segments in the core of a nanofiber and displaying their peptide sequences on the surface.[81] Previous studies suggest that β-sheet formation is a strong determinant of the cylindrical architecture of the supramolecular assemblies.[119, 254-258] The nanofibers intertwine into three-dimensional networks that have been studied in our laboratory for a variety of applications in regenerative medicine, including biomimetic hydroxyapatite mineralization,[81] neural progenitor cell differentiation[120] and blood vessel formation.[123]

One reason we are interested in being able to control the placement and orientation of these nanofibers is that it may offer a handle for controlling templated mineralization or cell behavior over macroscopic distances by tuning interactions at the nanometer scale. Effects of nanofiber alignment on cell behavior in will be discussed in more depth in Chapter 5. Dip-pen

nanolithography (DPN) has shown limited success in patterning PA molecules, but it cannot effectively pattern large areas and has yet to be extended to more than one type of PA.[208] However, it did demonstrate that the PA could be transferred to a substrate and even self-assemble into nanofibers from the confined water meniscus that condenses at the probe tip.

Microcontact printing has proven to be a versatile technique for the low-temperature, parallel patterning of a wide variety of soft matter systems.[177, 200, 259-261] Often, this method is used to indirectly pattern a material system by first patterning a selective surface chemistry on the substrate. However, the application of this technique to directly print systems that self-assemble into discrete, nanometer-scale objects has been limited. Direct patterning of a number of self-organized systems has been reported, including colloidal crystals,[202] polyelectrolytes,[179] layered bionanocomposites,[203] and phase-separating, binary alkanethiol mixtures.[204] Sgarbi and coworkers[207] demonstrated the surface assembly of microcontact printed laminin-1 into physiological polygonal networks. The primary danger in attempting to contact print supramolecular nanostructures is disassembly due to mechanical compression and strong adhesion to the stamp and substrate surfaces. An analogous case is observed in the deformation of some proteins patterned by microcontact printing.[262, 263]

This chapter details research on the direct microcontact printing of two different PA nanofibers. Polydimethylsiloxane (PDMS) stamps cast from anistropically etched silicon masters are used to pattern the nanofibers in arrays of lines or dots with sub-micron resolution. We study what effect the specific PA molecule, the stamping time, and the amount of glycerol added to the solution have on the deposition mechanism and the resolution of the printed features. Disassembly can occur in underneath the contact area, but the nanofibers may reassemble if the volume of water left by the meniscus is sizable enough.

3.2 Materials and Methods

3.2.1 Fabrication of anisotropically etched Si masters.

The masters were fabricated from silicon (100) wafers by conventional contact photolithography followed by anisotropic wet etching in a procedure similar to one previously reported[188, 189] to achieve sharp [011] ridges. The bare silicon substrate was spin-coated with a layer of positive photoresist (AZ-1518, Clariant Corp.) and soft-baked on a hotplate at 90 °C for 2 min. The wafer was mounted onto a Quintel Q-2000 mask aligner and exposed to UV light through a chrome mask with a patterned square array of circles 3 μm in diameter and spaced 3 μm apart. After development in AZ-400K developer (Clariant Corp., 1:5 dilution with deionized water), a square array of circular posts remained. Any photoresist scum was removed by brief exposure to oxygen plasma in an Oxford Instruments PlasmaLab 80 reactive ion etcher (RIE). An etch mask of 15 nm titanium followed by 100 nm gold was evaporated onto the wafers using a BOC Edwards Auto 306 electron-beam evaporator. Ultrasonication in acetone resulted in liftoff, opening the circular holes in the metal etch mask. The silicon was etched in a solution containing 12.5 g of KOH dissolved in 40 mL of Millipore water and 10 mL of isopropanol at 80 °C for *ca.* 1 to 2 hr or until sufficient undercutting of the mask had been achieved, as determined visually by increased bubble evolution and visible lift-off of the gold film. The etched masters were ultrasonicated in deionized water briefly to rinse off the basic solution and remove the bulk of the gold etch mask. The remainder of the gold was removed by dipping in a solution of 1 g I_2, 4 g KI, and 40 mL of Millipore water, followed by dipping in a solution of HNO_3 (69.8 wt %), HF (49 wt %), and Millipore water in a volume ratio of 4:1:50 to remove the titanium.

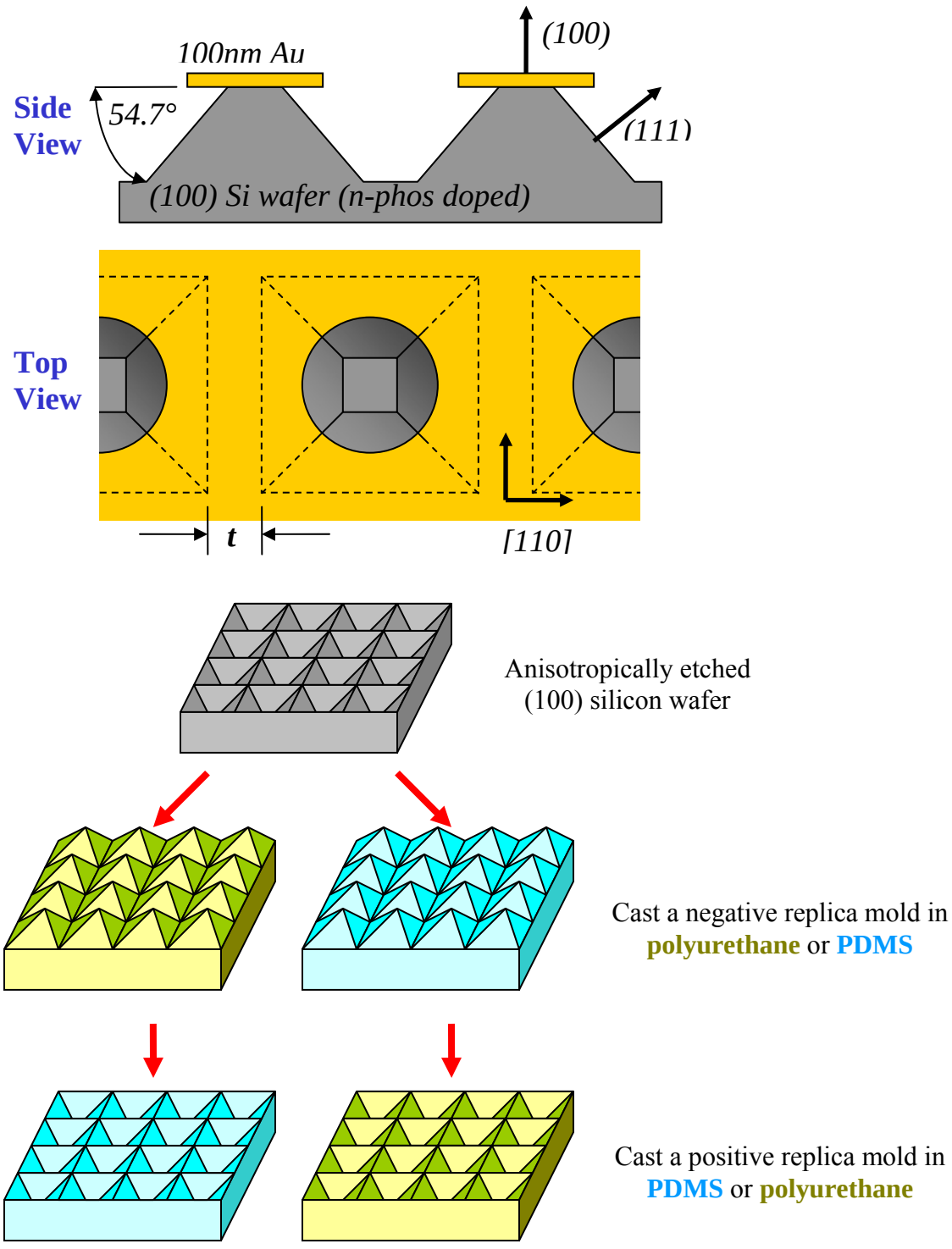

Figure 3.1. Schematic detailing the geometry of the anisotropically etched silicon masters and the fabrication of polymer replica molds.

Silanizing the surface of the master with a hydrocarbon silane aided in the release of the master from the polymer mold during replica molding. If the wafer was not silanized immediately after etching, the wafer was first cleaned in a hot piranha mixture of H_2O_2 (30 wt %) and H_2SO_4 (98 wt %) at 1:3 by volume (caution: strong oxidizer), rinsed in distilled water, briefly immersed in a mixture of H_2O_2 and NH_4OH (29 wt %) at 1:4 by volume, and rinsed in water again. The etched masters were dipped in dry isopropanol and dry toluene before soaking for 15 min in a 1 mM solution of octadecyltrichlorosilane (Aldrich) in toluene. The masters were then rinsed in toluene and isopropanol to remove unreacted silane.

3.2.2 Polymer replica molds

Positive or negative surface relief replica molds of the etched silicon masters could be fabricated from PDMS or UV-curable polyurethane (NOA-61, Norland Products). NOA-61 was first drop cast on to the anisotropically etched Si master, backed with a glass slide separated by spacers, and cured under a 365 nm UV lamp for 20 min. to create a negative relief replica (square pyramids) in polyurethane. A negative relief replica in PDMS could also be cast off the Si master, or a positive relief replica could be cast off the polyurethane negative. To improve the fidelity and mechanical stability of the PDMS replica mold, a composite structure was employed in which the surface features were cast in a stiffer material[264] (h-PDMS) and supported with a thick backing of soft PDMS (Sylgard 184, Dow Corning). The h-PDMS prepolymer was mixed from 2.3 g vinylmethylsiloxane copolymer (VDT-731, Gelest), 6 μL Pt catalyst (SIP-6832.0, Gelest), and 1.0 g hydromethylsiloxane copolymer (HMS-151, Gelest). This mixture was spin-coated onto the appropriate mold at 4000 RPM for 50 sec to yield a film 30 to 40 μm thick. The film was lightly cured in a convection oven at 50 °C for 20 min. until solid but tacky. Sylgard

184 PDMS was then prepared by mixing the prepolymer with crosslinker in a 10:1 w/w ratio, and the mixture was cast over the h-PDMS in a thick layer to form the bulk of the stamp. The ensemble was fully cured at 50 °C for at least 2 hr and removed from the mold. The replicas are trimmed into stamps of 0.25 cm^2 area.

3.2.3 PA molecules and microcontact printing

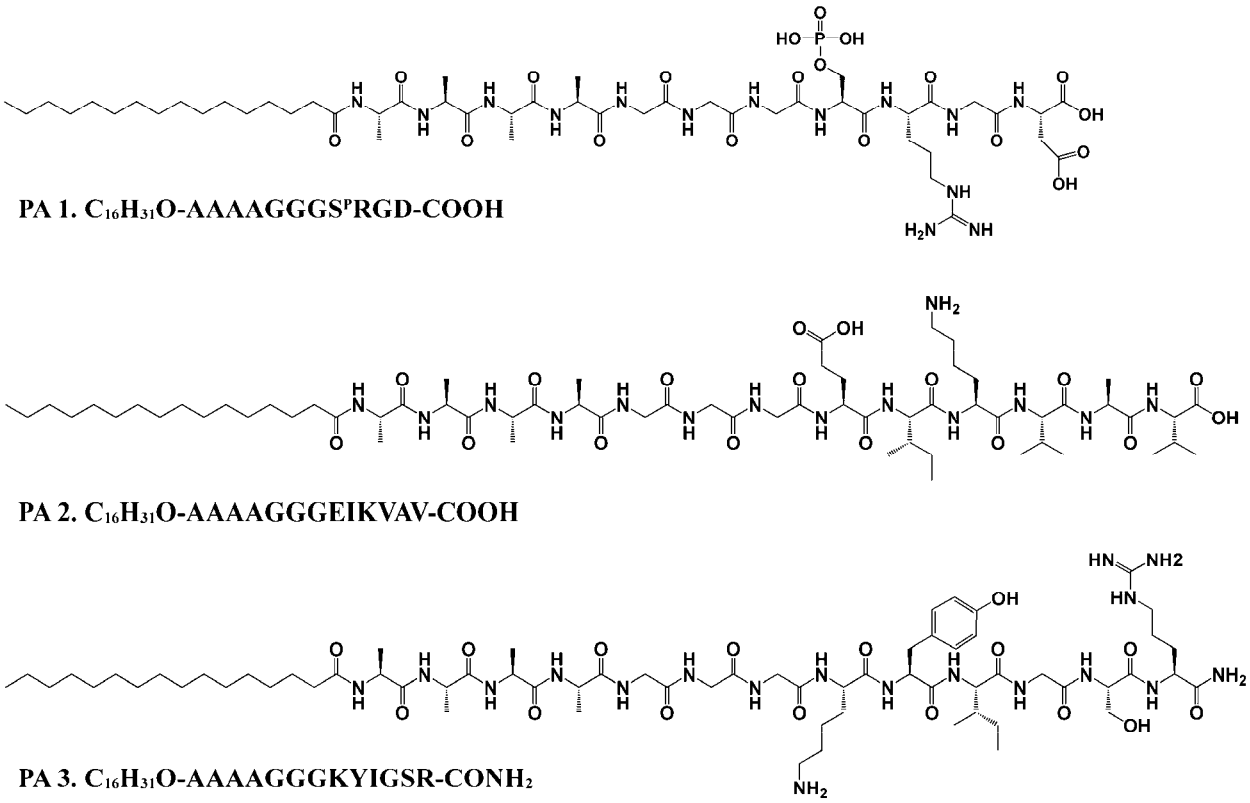

Figure 3.2. Chemical structures of PA molecules **1**, **2**, and **3**.

The PDMS replica molds were used as stamps to micro-contact print two different PA molecules. The chemical structure of PA molecules **1** – **3** employed in this study are given in Figure 3.2. Solid-phase synthesis and cell studies of **1** – **3** have been previously reported.[81, 119, 120] The PA was applied to the stamp as an aqueous inking solution of 0.1 wt % PA with varying

amounts of glycerol added in order to retain some of the moisture upon drying. The stamps were first exposed to oxygen plasma in the RIE very briefly (10 s duration, 50 sccm O_2 flow rate, 150 mtorr throttle pressure, 50 Watts RF power) in order to render the surface hydrophilic and allow for uniform spreading of the ink. 2 μL of the solution was pipetted onto the stamp and allowed to dry for 6 hr at room temperature and relative humidity (22.3 °C and 30 %, respectively). (100) silicon was used as a substrate for the micro-contact printing and was cleaned in piranha and NH_4OH as detailed above. The inked stamp was then brought into contact with the substrate and held in place for 15 to 60 sec while a load of 400 g/cm^2 was applied. The stamps were removed and the samples were imaged by AFM.

3.2.4 SEM and AFM

The etched silicon masters and polymer replica molds were sputter coated with 5 nm of gold-palladium alloy (99.99% Au:Pd, 60/40 ratio) in a Desk III sputter coater (Denton Vacuum) and imaged using a Hitachi S4500 scanning electron microscope. AFM images of the microcontact printed samples were aquired on a JEOL 5200 scanning probe microscope operating in tapping mode. Applied Nanostructures ACT silicon cantilevers (300 kHz resonant frequency, 40 N/m spring constant) were used for AFM imaging.

3.2.5 Force-displacement measurements

Force-displacement measurements were performed using an axisymmetric adhesion apparatus designed by Shull et al.[265] An inchworm stepping motor is coupled to a 100 g load cell (k = 1000 N/m) and drives the PDMS stamp into a rigid glass substrate. A fiberoptic displacement sensor is used to directly measure the displacement due to compression of the elastomer while a light microscope images the deformation in real time.

3.3 Anisotropically etched Si masters and polymer replicas

3.3.1 Resolution of the etched silicon master

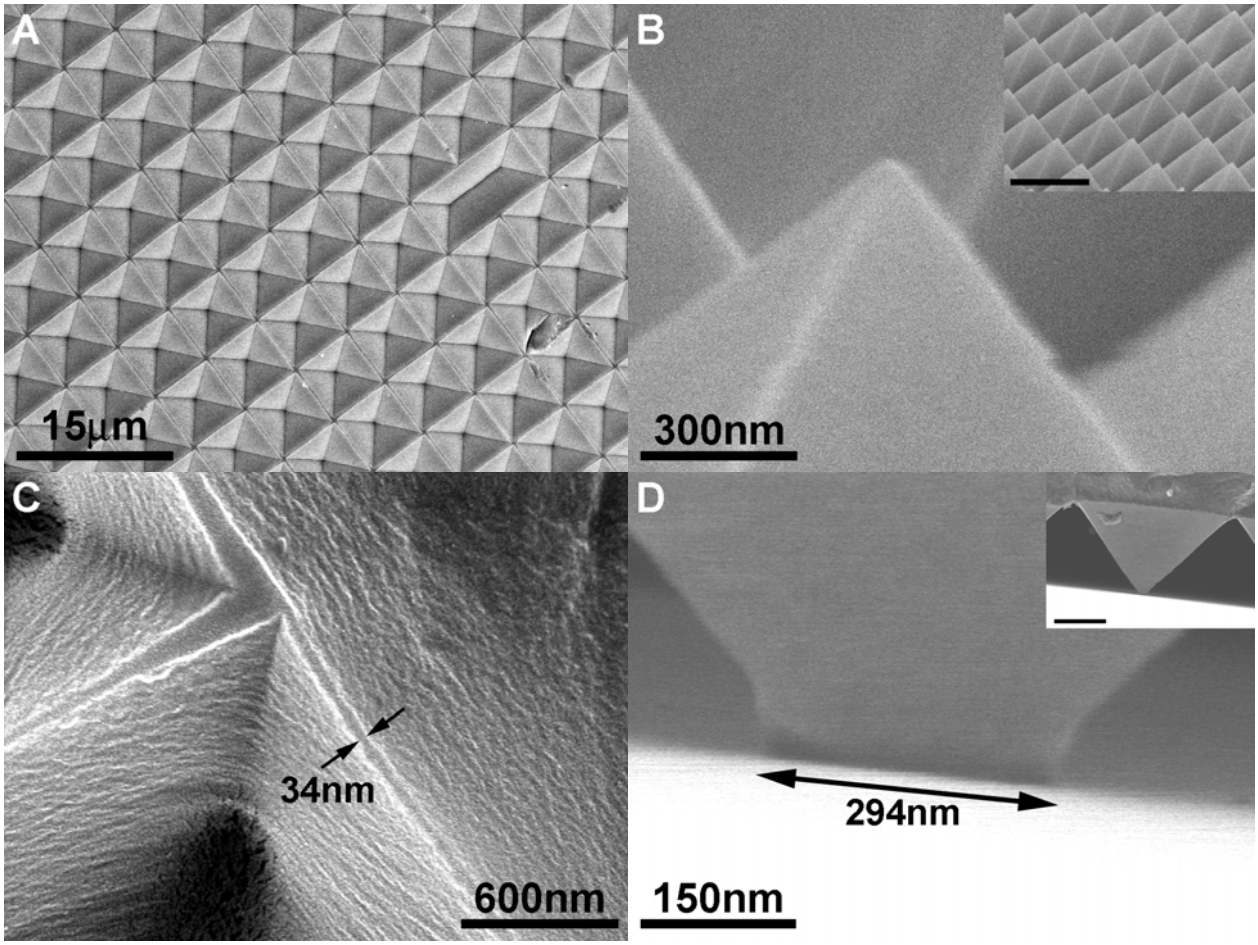

Figure 3.3. SEM images of (**A**) a patterned (100) silicon master anisotropically etched with a grid pattern of sharp ridges, (**B**) a negative relief replica cast in PDMS showing sharp pyramidal tips, and (**C**) a positive relief replica cast in polyurethane off of the PDMS replica demonstrating that the resolution of the features is mostly retained. SEM images (**D**) of a negative PDMS replica loaded against a flat surface shows deformation of the pyramidal tip and gives an idea of the contact area. The inset scale bars for **B** and **D** are 6 μm and 2 μm, respectively.

Figure 3.3 shows SEM images of an anisotropically etched Si master and the polymer replicas molded from it. Anisotropic etching with undercutting of the etch mask can achieve [011] ridge features that are as sharp as 15 nm at the vertex. Being a bench-top method, there is significant variation in the feature width, but tighter controls over the etching conditions and improving the uniformity of the photolithography and metal deposition can reduce that variation greatly. The etch times required are commonly 1 to 2 hr which is an order of magnitude shorter than one might expect if only the bulk (111) face of the Si was being etched in the undercutting process.[242] Most likely, the Ti adhesion layer is being etched at a faster rate, exposing a fresh (100) Si ledge that is rapidly etched down. The benefit of fabricating sharp line features by undercutting the etch mask is that all the line features are guaranteed to be coplanar, a necessary aspect for patterns such as grids and networks that are interconnected.

3.3.2 Elastic contact mechanics and resolution of the polymer replica molds

Figure 3.4 shows schematics of the geometric parameters involved in the indentation of a wedge and a cone against a rigid, flat surface. Starting with the case of very low deformations, we assume fully elastic behavior, frictionless surfaces, and, for the wedge geometry, plane strain. Given an applied load P, the width of the contact area $2a$ for an indenting wedge and cone are expected to vary as:

$$a_{wedge} = \frac{PA}{2\tan\phi} \tag{3.1}$$

$$a_{cone}^2 = \frac{PA}{2\pi\tan\phi} \tag{3.2}$$

$$A = \frac{2\left(1-\nu^2\right)}{E} \tag{3.3}$$

where ϕ is the angle of the indenter, E is the Young's modulus of the PDMS, and v is the Poisson's ratio.[266] The vertical displacement Δ follows the same scaling laws as a. The scaling laws for the deformation of a square pyramid are expected to be the same as those for an axisymmetric cone. At higher loads, lateral deformations will change the shape of the cone or wedge into one that more resembles a vertical punch, for which case a would scale linearly with P.

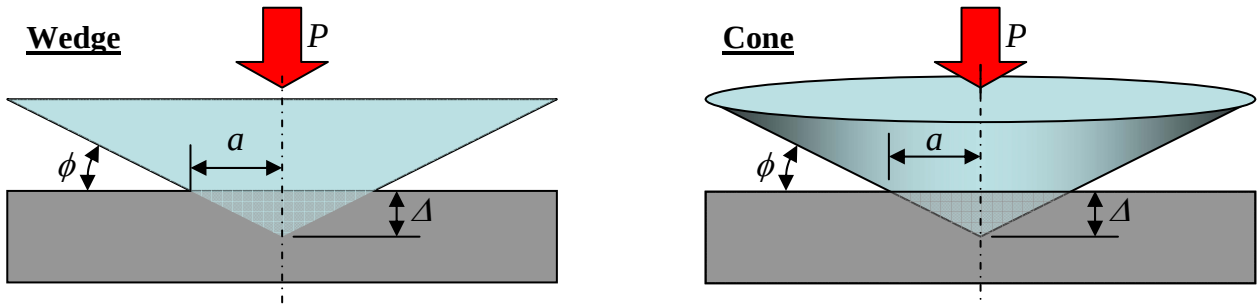

Figure 3.4. Schematic detailing the geometric parameters involved in the indentation of a wedge and an axisymmetric cone.

The negative and positive relief replicas cast from PDMS and polyurethane duplicate the high-resolution features with significant fidelity. The SEM image in Figure 3.3 shows how the square pyramidal PDMS tips deform when loaded against a rigid surface. Equation 3.2 shows that for a pyramidal or conical indenter, the contact width and resulting feature resolution is expected to vary with the square root of the applied pressure.[266] Thus, the contact area is seen to be much wider than the undeformed tip radius. By contrast, the contact width of the wedge-shaped features is expected to vary linearly with applied pressure and should be capable of producing high-resolution features more easily.

Figure 3.5 shows force-displacement curves of stamps with wedge features and pyramid features loaded in compression against a rigid surface. The thickness of the stamps is 2 mm, giving a value of 3 MPa for the Young's modulus of the PDMS. The plot shows that the equations for low deformations given above are applicable out to a load of 0.4 N/cm^2 at most, only one tenth of the load applied during microcontact printing. This is not unexpected as the equations given are best suited for the case of low ϕ and minimal transverse strains. For the experimental conditions of interest, the stamp features are already in a regime of relatively high deformation in which case the width of the contact area in both the wedge and pyramid geometries may be expected to vary only weakly with respect to the applied load. The vertical displacements for the stamps with pyramid-shaped features are quite large, although this may be

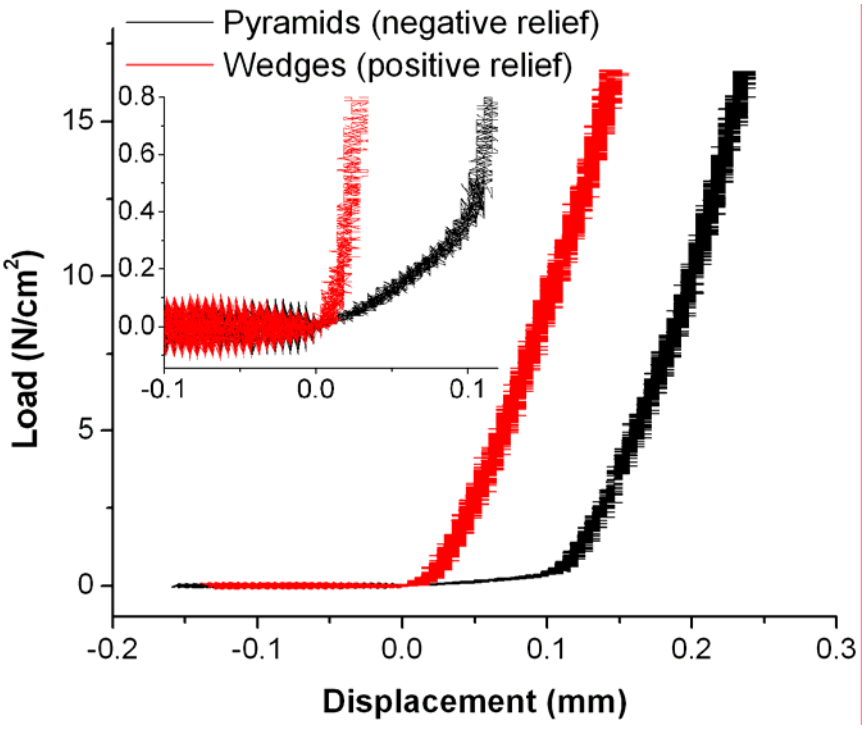

Figure 3.5. Load versus displacement in compression of PDMS stamps with negative (square pyramids) and positive (wedges) surface reliefs.

attributed to asperities and protrusions in the negative-relief pattern that must be compressed first before the majority of the pyramid features can make contact to the substrate. These defects can be limited by fabricating a silicon master with less undercutting of the etch mask and dedicated to replicating only the negative relief.

As seen in Figure 3.6, exposure to oxygen plasma does tend to reduce the feature resolution of the replica molds. For this reason, the exposure time is chosen to be as short as possible. Even so, due to significant deformation of the stamp features upon loading, the slight smoothing of the stamp topology by the oxygen plasma likely has a negligible effect on the resolution of the microcontact printed patterns.

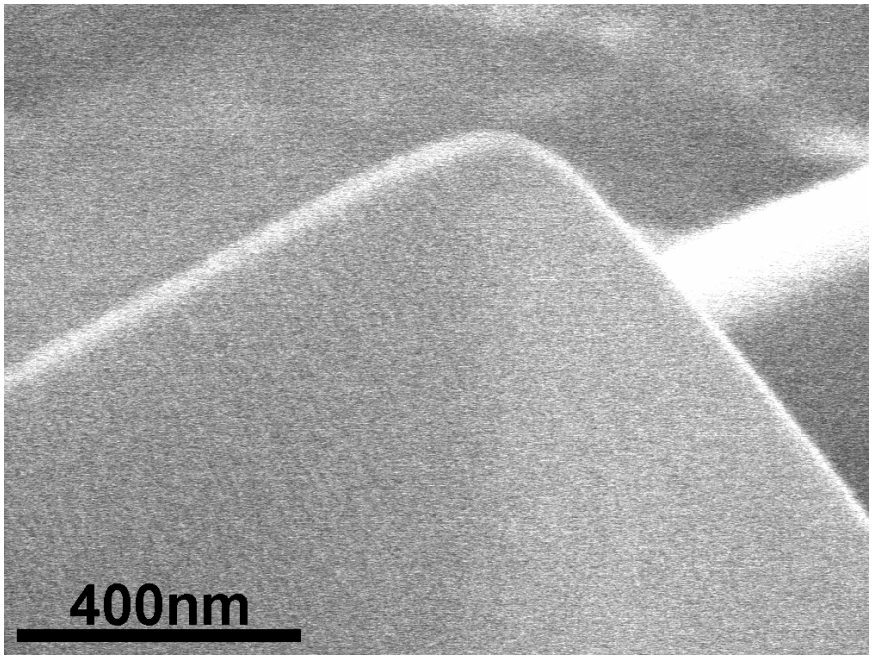

Figure 3.6. SEM of a negative relief PDMS stamp after 10 sec exposure to oxygen plasma in the RIE showing slight rounding of the feature tip.

3.4 Micro-contact printing of PA 1 nanofibers

3.4.1 Dot and line features

Figure 3.7 shows AFM images of PA **1** micro-contact printed using the negative relief stamp of square pyramid tips, demonstrating that the material can be deposited in this manner to yield a square array of dots. The contact area appears to be 600 nm in diameter on average under a load of 40 KPa. With an inking solution of pure PA, the material deposited shows no discernable fiber morphology, and at 2 to 3 nm in height, the deposits are only half the expected thickness of a nanofiber. No material is deposited when there is no ink on the stamp, and SEM images show that there is some fiber formation on the stamp itself, suggesting that disassembly is occurring as result of contact. As glycerol is added to the inking solution in greater quantities, the printed dots of PA increase in diameter, but they remain at 2 to 3 nm in thickness and showing little evidence of nanofiber morphology until we get above a glycerol:PA ratio of 1:1 w/w. At that point, the printed dots expand to 1 μm in diameter and show definite nanofiber morphology with a thickness greater than 5 nm.

AFM images of PA **1** micro-contact printed with a positive relief stamp of linear ridge features are shown in Figure 3.8. A similar sudden transition from minimal deposition to large-scale spreading of the PA ink over the substrate is also observed. In this case, even at low glycerol concentrations there is no significant deposition other than a residual small molecule layer that can only be discerned in the phase contrast image. At a glycerol:PA ratio of 4:5 w/w, we finally see significant fiber deposition along the grid pattern of the stamp used. The line widths are 700 nm, larger than the purported contact area of the stamp, again likely due to the

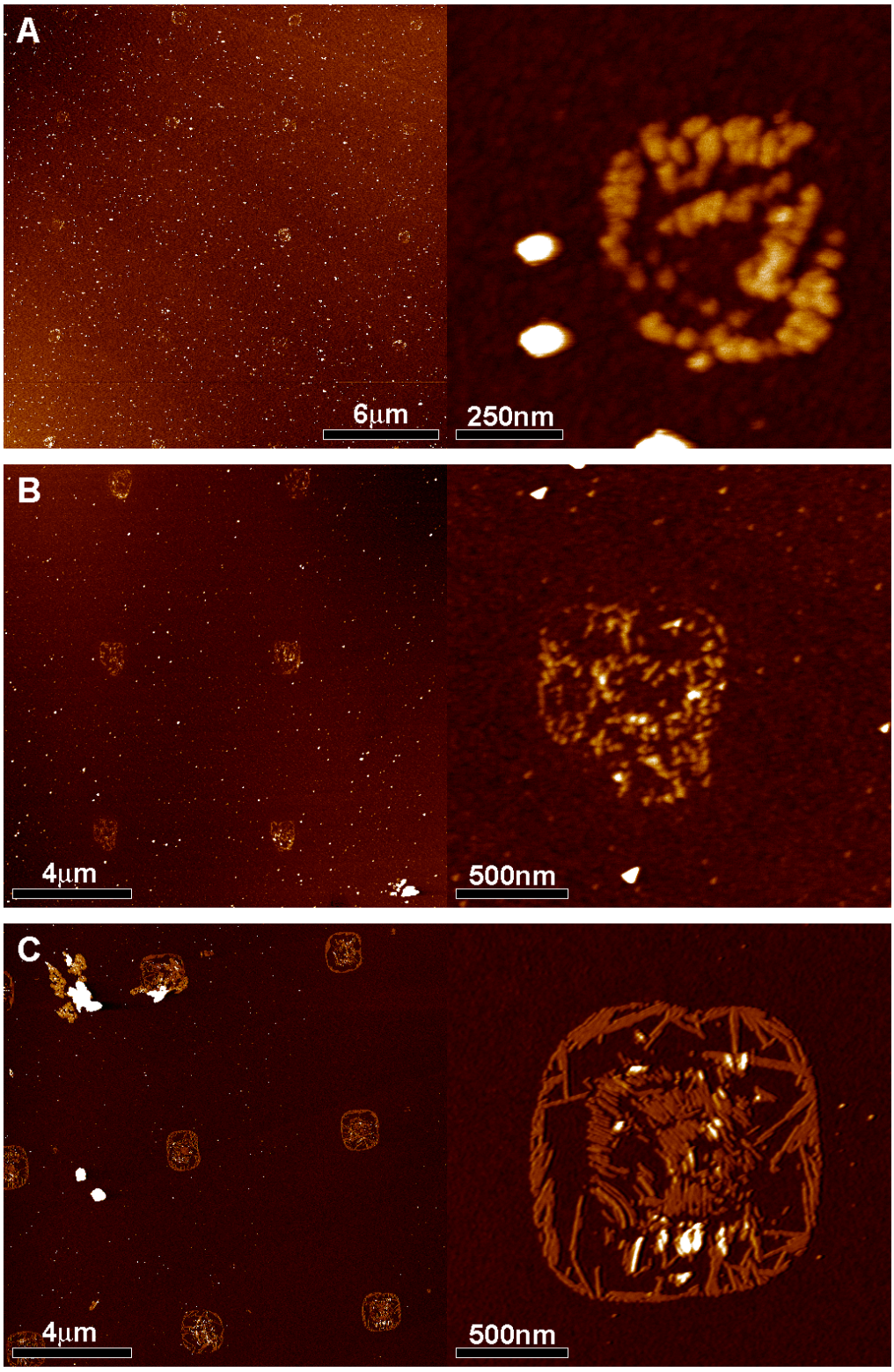

Figure 3.7. AFM height images of micro-contact printed dots of PA **1** using different ratios of glycerol to PA in the inking solution: (**A**) 0:1, (**B**) 1:1, and (**C**) 3:1 by weight, respectively.

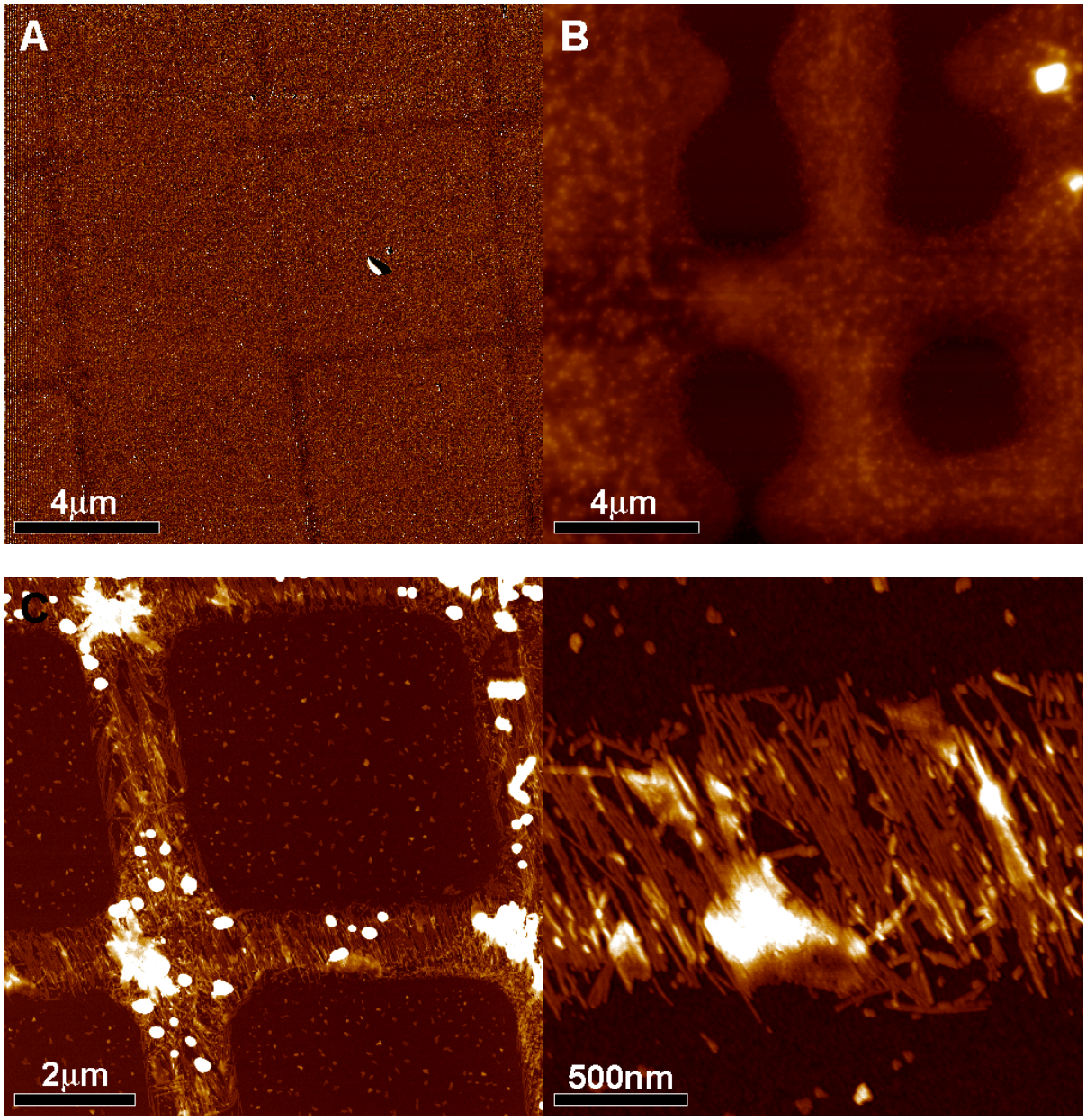

Figure 3.8. AFM images of micro-contact printed lines of PA **1** using different ratios of glycerol to PA in the inking solution: (**A**) 1:5, (**B**) 1:1, and (**C**) 4:5 by weight, respectively. All images are height profiles except for **A** which is a phase image.

formation of a water meniscus on stamping. Increasing the glycerol concentration further results in extensive spreading of the ink over the sample.

3.4.2 Effect of glycerol concentration and stamping time

Figure 3.9 plots the printed dot diameter and height of the material deposited versus the relative glycerol concentration. The fact that at low glycerol concentrations, material is printed by the dot patterns but not the line patterns suggests that the material is transferable by mechanical contact but only if the applied pressure is high enough. The compressive stress underneath each contacting pyramidal tip is estimated to be *ca.* 5 MPa assuming that the contact diameter is 600 nm. By constrast, the contact pressure beneath the wedge features is estimated to

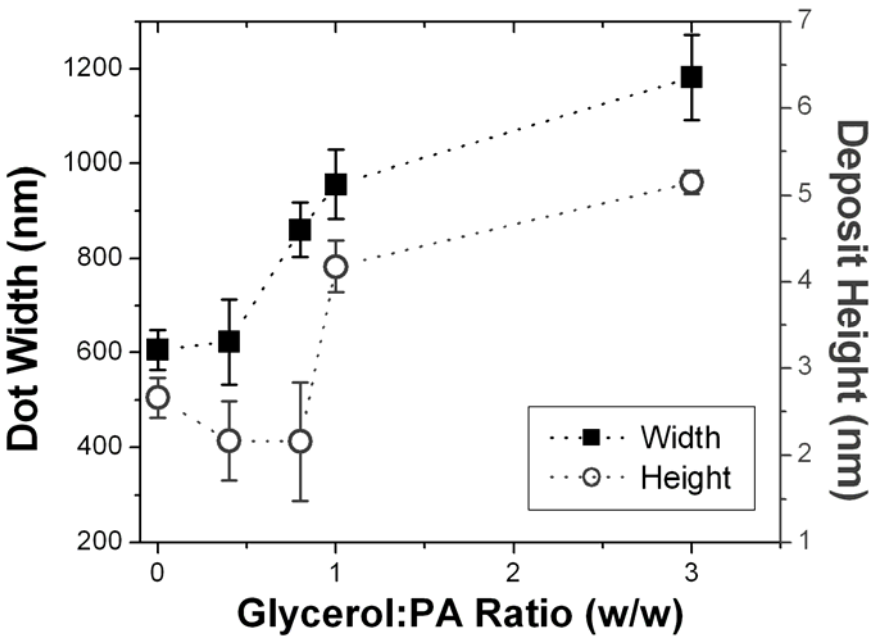

Figure 3.9. Plot of (■) the width of the microcontact printed dots and (○) the height of the deposited material or nanofibers versus the concentration of glycerol in the inking solution of PA **1**. The stamping time was 60 sec.

be less by an order of magnitude. This value may also hint at the order of magnitude of the ultimate compressive strength of the nanofiber assembly.

In addition, there is a kinetic component to the deposition and spreading of the PA ink by micro-contact printing. Figure 3.10 plots the width of the lines printed while varying the duration for which the stamp is held in contact with the substrate. By shortening the contact time from 60 sec to 15 sec, it is seen that the quantity and area of fiber deposition is greatly reduced. This time dependence is likely due to a gradual expansion of the water meniscus that is limited by diffusion of water vapor under the stamp and the viscosity of the ink.

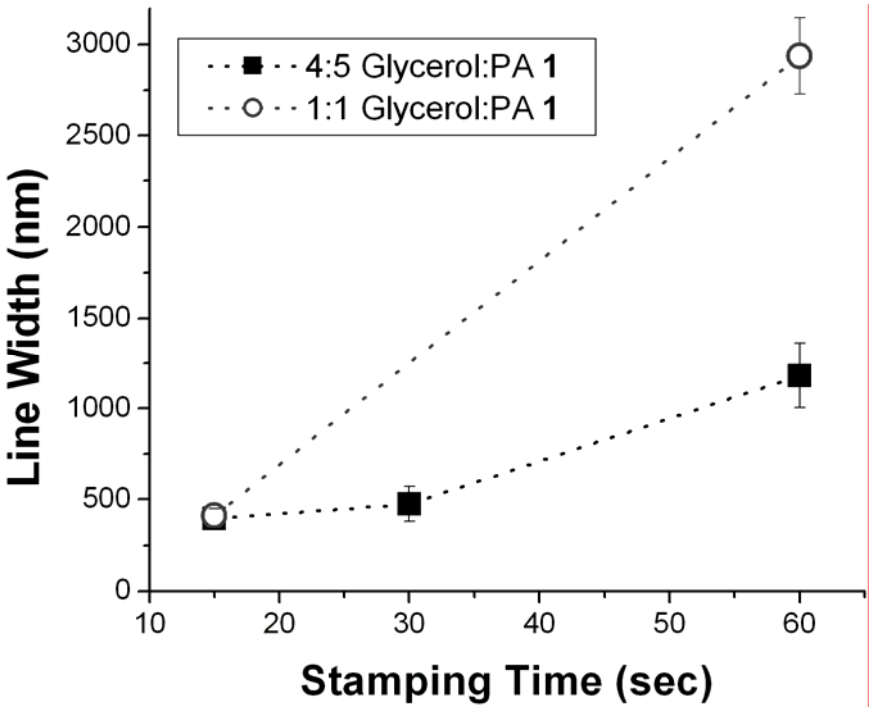

Figure 3.10. Plot of the width of the microcontact printed lines measured at the thinnest point versus stamping time for inking solutions of PA **1** with glycerol:PA ratios (w/w) of (■) 4:5 and (○) 1:1.

The increased water content retained by the glycerol seems to allow for both easier transport of the molecules to the surface and self-assembly of the nanofibers. The perceived transition from a monolayer thickness of 2 to 3 nm to a thickness closer to the diameter of a nanofiber may occur at a point where there is enough water to solubilize the molecule, allowing it to escape the adhesion force on the surface and settle into a more favorable self-assembled structure. Increasing the glycerol content also increases the area of nanofiber deposition, demonstrating that the PA **1** is quite hydrophilic and travels to the very edges of the water meniscus. The AFM images and previous DPN studies[208] show that self-assembly of the nanofibers does occur upon drying out of the water meniscus, but whether the molecule is transported mostly as monomer in solution or as pre-formed aggregates is still under investigation. If the molecules were highly soluble in water, one might expect a more continuous trend of material deposition with respect to glycerol concentration, whereas aggregates may need a large, critical degree of fluidity in the ink to become mobile. The lack of nearly any material deposition along the line patterns at lower glycerol concentrations may be due to the molecule favoring the assembled state, not dissociating fast enough, or being repelled by the negatively charged substrate.

3.4.3 Nanofiber alignment

Although the PA fibers may be micro-contact printed in a line pattern, the fibers do not align along the pattern direction. However, for some samples the nanofibers appear to align in a uniform direction independent of the pattern orientation over a significant area such as in Figure 3.8c. This alignment may be due to either a small amount of lateral shear generated underneath the stamp or the movement of the contact line between the stamp and the substrate. The latter

case is analogous to the molecular combing observed at the receding edge of the water meniscus in the case of DPN and has been exploited before to align contact printed proteins.[267] Any possible shearing would be small given the lack of complete smearing of the original pattern, but we have yet to rule out the possibility. If shear alignment of the PA nanofibers is feasible, it would be attractive as a means of aligning three-dimensional gels.

3.5 Micro-contact printing of PA 2 and PA 3 nanofibers

*3.5.1 Printing of PA **2** nanofibers and the effect of hydrophobicity*

Figure 3.11 and Figure 3.12 show AFM images of PA **2** micro-contact printed in patterns of dots and lines, respectively. While the printed dots of PA **2** also display no discernable nanofiber structure at low glycerol concentrations, the height of the deposits remains closer to the nanofiber diameter of 8 nm or greater. This difference suggests that PA **2** doesn't disassemble as easily as PA **1** which may be due to a difference in mechanical properties of the two nanofibers. A plot of the printed line width versus glycerol concentration comparing PAs **1** and **2** is given in Figure 3.13. While increasing the glycerol content does aid slightly in transferring the nanofibers, PA **2** does not spread to the edges of the water meniscus but remains localized around the contact area. PA **2** is known to be qualitatively more hydrophobic and less soluble in water than PA **1**, so it may be expected that dissolution and transport of PA **2** monomer by the water meniscus would be minimal. Instead, most of the deposition is a result of mechanical contact as pre-assembled nanofibers on the stamp are physically transferred to the substrate, and the resolution of the printed patterns is less dependent on the glycerol concentration.

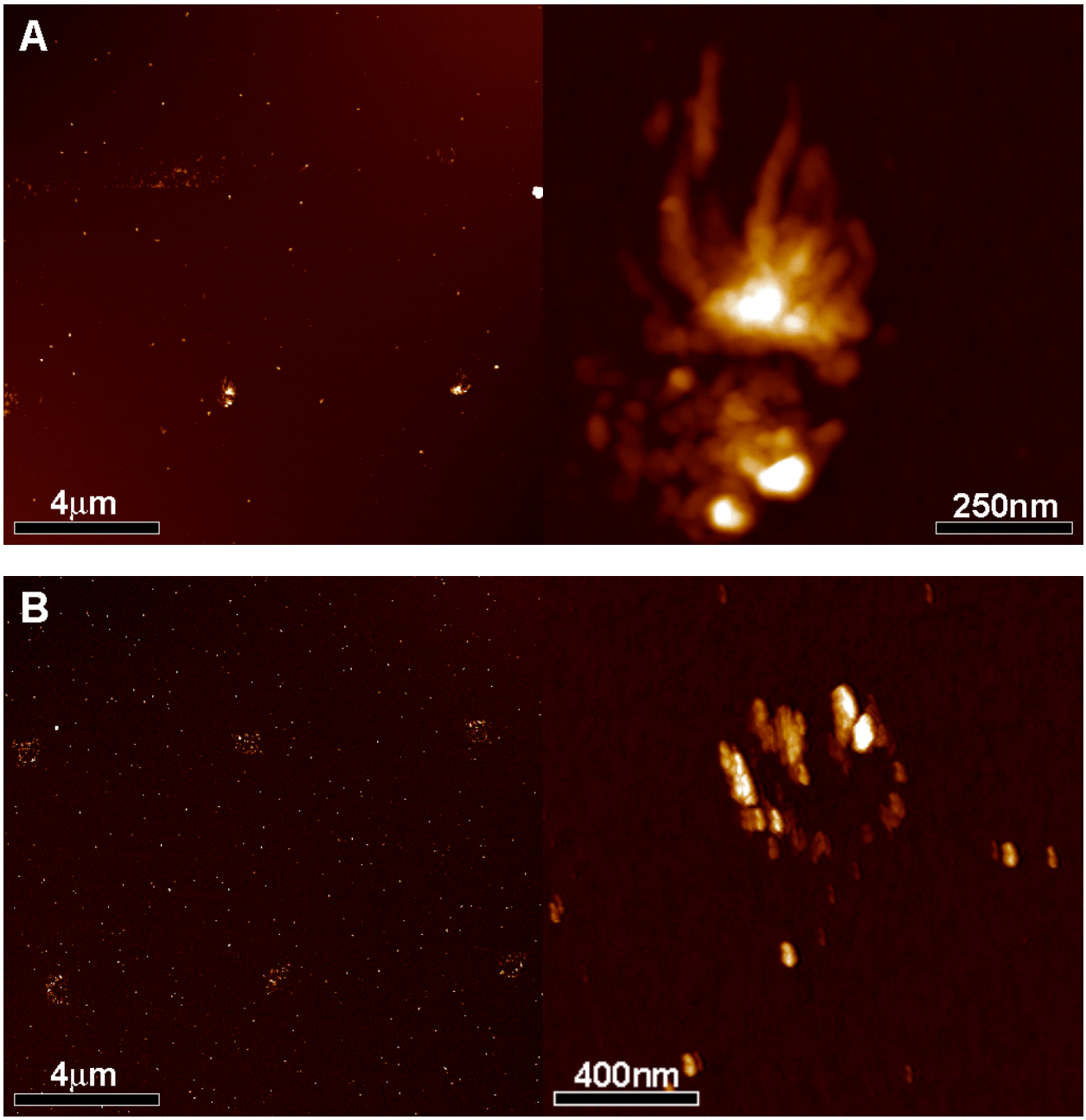

Figure 3.11. AFM height images of micro-contact printed dots of PA **2** using different ratios of glycerol to PA in the inking solution: (**A**) 1:1 and (**B**) 2:5 by weight, respectively.

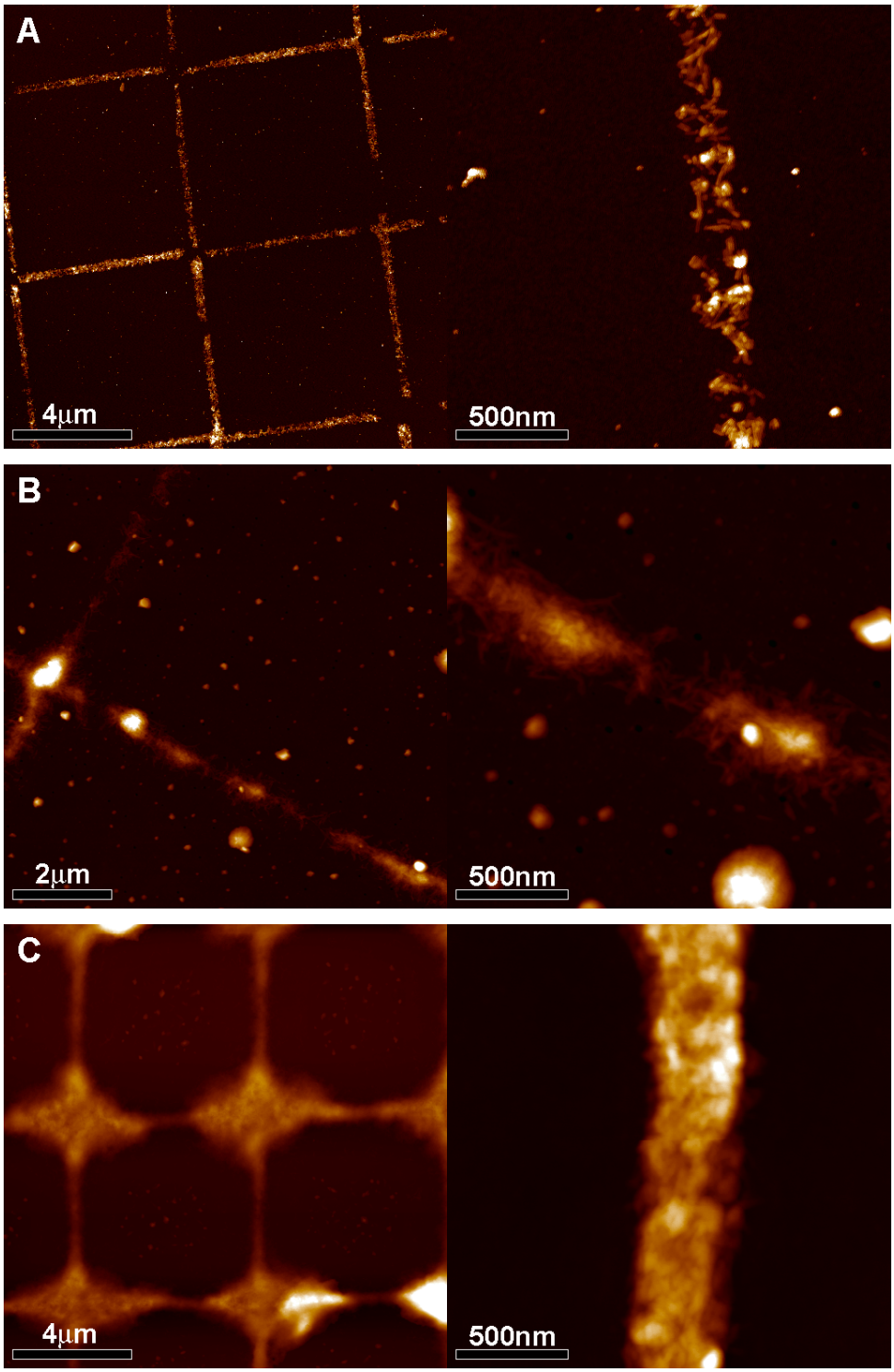

Figure 3.12. AFM height images of micro-contact printed lines of PA **2** using different ratios of glycerol to PA in the inking solution: (**A**) 2:5, (**B**) 4:5, and (**C**) 1:1 by weight, respectively.

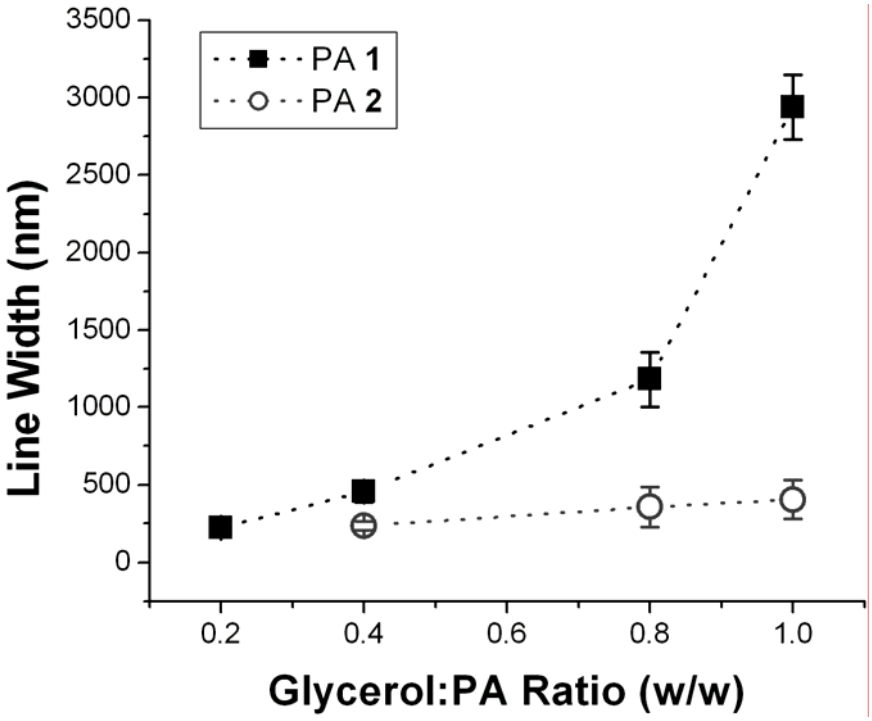

Figure 3.13. Plot of the width of the microcontact printed lines measured at the thinnest point versus glycerol:PA ratios (w/w) for (■) PA **1** and (○) PA **2**.

No uniaxial alignment was observed in any of the patterned samples of PA **2**, however, the nanofibers did tend to deposit in thick mats that increased in thickness with increasing glycerol concentration. In contrast to PA **1**, PA **2** did deposit some material even at low glycerol concentrations. One possible explanation for this observation is that because PA **2** is more hydrophobic and less negatively charged than PA **1**, the electrostatic repulsive force from the silica surface is weaker, and the energetic barrier for physisorption of PA **2** nanofibers is smaller.

*3.5.2 Preliminary results of printing of PA **3** nanofibers*

Figure 3.14 shows AFM images of PA **3** microcontact printed in patterns of lines and dots using an inking solution of 1:1 w/w PA:glycerol. PA **3** may be seen to show some patterning behaviors of both PA **1** and PA **2**, with significant deposition in the middle of the line

pattern but also lines of deposition at the edges of the water meniscus. While the resolution of the printed patterns of PA **3** was not quantified, the images do show that the patterning technique is versatile and can be applied to almost any PA system.

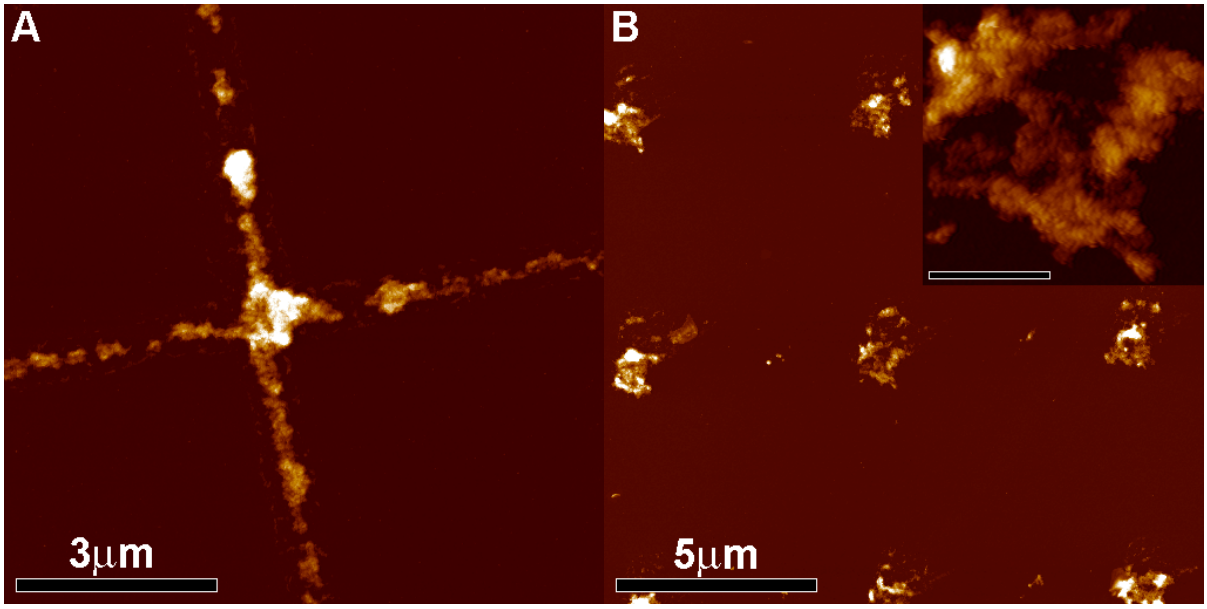

Figure 3.14. AFM height images of micro-contact printed (**A**) lines and (**B**) dots of PA **3** from an aqueous inking solution of 1:1 by weight of glycerol to PA. Scale bar of the inset magnification in (b) is 500 nm.

3.6 Summary and Outlook

We have shown that a PA system that self-assembles into discrete nanofibers can be directly patterned on a substrate by microcontact printing. Anisotropic etching of silicon is a simple and parallel method of fabricating a master mold with sub-100nm features that can be used to cast high-resolution PDMS stamps. PA **1** is easily transported to the substrate through the water meniscus, and the resolution and morphology of the printed features are highly dependent on the glycerol concentration in the solution and the stamping time. In contrast, PA **2**

is transferred primarily by physical contact, and the resolution of the printed features is mostly independent of glycerol concentration. The difference in deposition behavior is hypothesized to result from a difference in hydrophilicity between the two molecules. It may be possible to exploit this difference to print features of two different PAs simultaneously with the more hydrophobic PA segregated to the center of the feature and the more hydrophilic PA around the edges. The nanofibers appear to disassemble with sufficient mechanical compression underneath the contact areas of the stamp, but they can reassemble if a sufficient volume of water is left behind by the meniscus. There is also the possibility of uniaxially aligning PA nanofibers within a microcontact printed pattern by careful control of the contact edge or the application of mild shear.

CHAPTER FOUR

Simultaneous Self-Assembly, Orientation, and Patterning of Peptide-Amphiphile Nanofibers by Soft Lithography

Chapter 4: Simultaneous Self-Assembly, Orientation, and Patterning of Peptide-Amphiphile Nanofibers by Soft Lithography

4.1 Introduction

Self-assembly has proven to be a viable strategy for the bottom-up fabrication of complex and useful nanostructures.[6, 15, 268, 269] However, for their full functionality to be realized, it is often desirable to control the placement and orientation of such nanostructures over macroscopic length scales.[8-10, 270] Toward this end, physical patterning of micrometer and submicrometer features may be a useful strategy. If these features induce a specific orientation locally, repeating the features could extend short range order over large areas. Imitating long range order in this manner may amplify useful anisotropic properties that are commonly not accessible due to local disorder. Increasing the degree of order in self-assembling systems also improves the specificity with which their internal structures can be determined.

Many strategies have been investigated for controlling order in materials, and some of these, including graphoepitaxy[32] and soft lithographic micromolding,[200, 206, 271, 272] rely on the effects that spatial confinement have on the behavior of materials. These techniques take advantage of the strengths of top-down fabrication such as materials generality and facile control of feature shape and pattern and apply them to a bottom-up system. The idea of using spatial confinement to guide micro- or nanoscale ordering has been extensively applied to self-organized systems, including block copolymers,[32, 34, 209, 253, 273] colloidal crystals,[186, 187] and liquid crystals.[133, 185, 212, 213] However, systems that assemble into discrete, nanoscale objects from dilute molecular solution present a unique challenge because they often have poor mobility in the neat phase and therefore must be patterned while solvated. Some of these materials have been

aligned by electric fields,[136, 137, 206] Langmuir-Blodgett techniques,[151, 152] or mixing with liquid crystals,[133, 138-140] but these methods are limited in the patterns and molecular orientations they can produce. To our knowledge, the possibility of patterning such systems by spatial confinement as the molecules self-assemble from solution into supramolecular structures has not been reported.

Our interest in patterning is in its application to self-assembling systems for the development of novel materials that are useful, tunable, and easily processed. In the previous chapter, we introduced a specific class of peptide-amphiphile (PA) molecules synthesized in our laboratory that self-assemble into nanofibers out of aqueous solution upon the evaporation of solvent. These nanofibers have proven to be potentially useful for a variety of target applications in regenerative medicine. We demonstrated the ability to pattern nanofibers of different PAs on a surface with sub-micrometer resolution by a microcontact printing method. This technique is a rapid, parallel process that is also versatile both in terms of the materials it is able to pattern and the features it is able to produce.

Unfortunately, microcontact printing was mostly ineffective in controlling the orientation of the nanofibers. While work on patterning surfaces with proteins and epitopes is extensive,[260, 274-279] the one-dimensional structure of the PA nanofibers adds another level of order that may be exploited to control cell behavior or templated mineralization. Alignment of the PA nanofibers would also enable more detailed investigations of their internal structure. The nanofibers assemble readily upon solvent evaporation but are difficult to manipulate when completely dry. Collagen fibrils have been aligned in arrays created by electron-beam lithography[280] and DPN.[281] Similarly, we have shown that DPN can produce a low degree of orientation of PA nanofibers but only in small areas.[208]

Soft lithography techniques have proven to be inexpensive and versatile methods for low-temperature patterning of soft matter.[200, 206, 260, 271, 272, 279] Micromolding and liquid embossing using grooves cast from diffraction grating masters allows for facile patterning and confinement of material in dense arrays of sub-micron lines.[282-284] In the present work, we achieve long-range order of PA nanofibers starting from solution prior to their self-assembly and using only spatial confinement. We demonstrate the simultaneous self-assembly, alignment and patterning of PA nanofibers over an area approaching 1 cm^2 by a sonication-assisted solution embossing technique. The technique is shown not to be limited to unaxial alignment but can be used to guide the nanofibers around corners.

4.2 Materials and Methods

4.2.1 PA molecules

The chemical structures of PA molecules **1** and **2** employed in this study were shown earlier in Figure 3.2. PA **1** is terminated with the tripeptide RGD, a well-known epitope that among other things can promote cell adhesion.[285, 286] PA **2** displays the pentapeptide IKVAV found in laminin-1 that has been demonstrated to promote process outgrowth in neurons.[287, 288] Solid-phase synthesis and in vitro studies of PA **1** and **2** have been previously reported.[81, 119, 120, 254, 256] PA **2** is of interest for its ability to promote and guide neurite outgrowth in the regeneration of the nervous system or in the creation of *in vitro* assays for neuroscience.

4.2.2 PDMS grating stamps

Optical diffraction gratings (Edmund Industrial Optics) with groove densities of 1200, 2400, and 3600 lines/mm (line periods of 833 nm, 416 nm, and 278 nm, respectively) were used

as master molds to cast patterned PDMS stamps following procedures reported by Roman et al.[283] To improve the fidelity and mechanical stability of the PDMS replica, a composite structure was employed in which the surface features were cast in stiffer PDMS (h-PDMS) and supported with a thick backing of soft PDMS.[264] The h-PDMS prepolymer was mixed from 2.3 g vinylmethylsiloxane copolymer (VDT-731, Gelest), 6 μL Pt catalyst (SIP-6832.0, Gelest), and 1.0 g hydromethylsiloxane copolymer (HMS-151, Gelest). This mixture was spin-coated onto the diffraction gratings at 4000 RPM for 50 sec to yield a film 30 – 40 μm thick. The film was lightly cured in a convection oven at 50°C for 20 min. until solid but tacky. Sylgard 184 PDMS (Dow Corning) was then prepared by mixing the prepolymer with cross-linker in a 10:1 w/w ratio, and the mixture was cast over the h-PDMS in a thick layer to form the bulk of the stamp. The ensemble was fully cured at 50 °C for at least 2 hrs and removed from the mold. Prior to use, the stamps were cleaned of dust and debris by ultrasonication in isopropanol and then in deionized water.

4.2.3 Substrate cleaning

Borosilicate glass or silicon substrates (0.5 mm thick, (111), 1500 Ωcm, University Wafer) were cleaned in a hot piranha mixture to render them hydrophilic. Briefly, the substrates were soaked in a 120 °C piranha mixture of H_2O_2 (30%) and H_2SO_4 (98%) at 1:3 by volume (CAUTION: strong oxidizer) for 1 hr, rinsed in deionized water, immersed for 10 min in a 80 °C mixture of H_2O_2 and NH_4OH (29%) at 1:4 by volume, and finally rinsed again before being stored in 18.2 Ωcm water (Milli-Q A10, Millipore). Before use, the substrates were dried by a nitrogen gun.

4.2.4 Micromolding in capillaries

Micromolding in capillaries (MIMIC) is applied to the PA solutions by a procedure similar to those reported previously. A schematic outlining both MIMIC and solution embossing techniques is given in Figure 4.1a. Briefly, the stamp is placed patterned-side down onto a clean glass substrate so that the grooves in the stamp act as sub-micrometer scale capillaries with two open ends. 2 μL of a 0.1 to 1.0 % by weight aqueous solution of PA is pipetted at one of the open ends of the channels. The solution is allowed to wick into the channels by capillary action and left to dry overnight before the stamp is removed.

4.2.5 Sonication-assisted solution embossing

The stamp was placed patterned-side-up on a piece of glass that served as a rigid backing, and a circular weight was used to apply a load on the stamp of roughly 30 g/cm^2 as shown in Figure 4.1b. The circular weight is affixed to the opposite side of the glass backing with carbon tape. A substrate was placed in the bottom of an empty glass beaker immersed in an ultrasonic bath. The bottom of the beaker is lined with a thin layer of PDMS that is scored in order to hold the sample in place yet allow the sample to be removed with reasonable force. 4 μL of 1-5% by weight PA solution in water was pipetted onto the substrate, and the weighted PDMS stamp brought down on top of the solution. The circular weight was sized to fit snugly within the glass beaker and prevent excessive translational movement of the stamp. Rotational of the weight was hindered by lining the sides of the beaker with Parafilm (American Can Co.). The entire setup was sonicated for 1 hour at 40 kHz in a Branson 1510 ultrasonic cleaner and allowed to dry for a day without any further agitation before the stamp was removed.

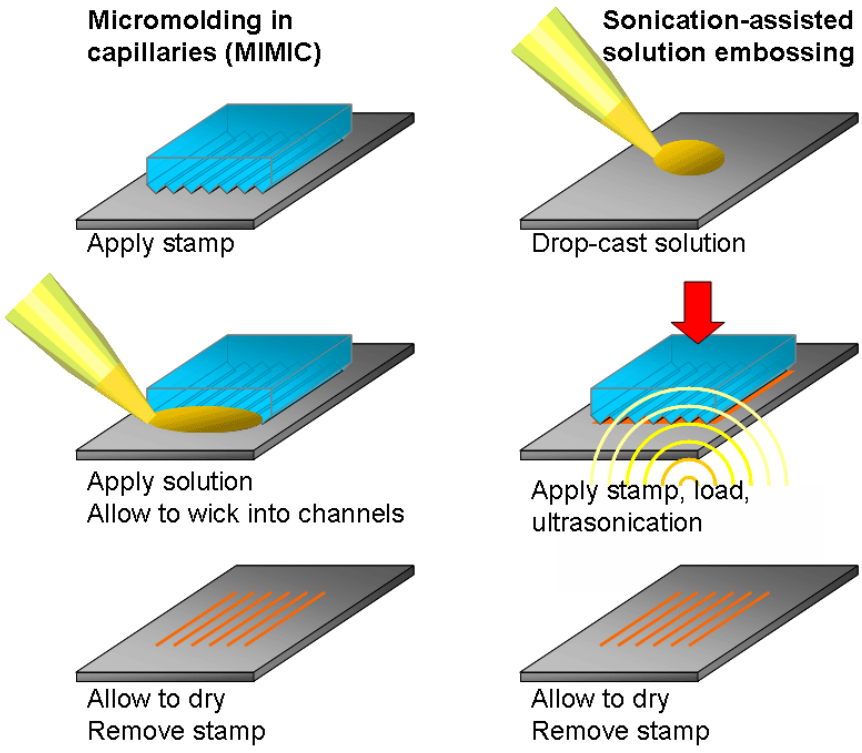

(A)

(B)

Figure 4.1. (**A**) Schematic briefly detailing the two patterning methods employed and (**B**) photographs of the setup used for sonication-assisted solution embossing.

Solution embossing without the aid of sonication is performed by first placing a 4 μL drop of 1-5 % by weight PA solution in water onto a clean glass or silicon substrate. The patterned PDMS stamp is then brought down directly on top of the drop, and a weight of 30 g/cm^2 is placed on the stamp. The solution is allowed to dry overnight before the stamp is removed.

4.2.6 AFM, SEM, and polarized optical microscopy

Samples and stamps were imaged primarily by tapping mode AFM using a JEOL 5200 scanning probe microscope and Applied Nanostructures ACT silicon cantilevers. SEM images of samples and stamps were collected on a Hitachi S4500 scanning electron microscope.

Birefringence photographs were taken on a Minolta X-300 35mm film camera attached to a Leitz Laborlux 12 Pol optical microscope. Concentrated PA gels were mixed and sandwiched between two glass slides separated by Parafilm in order to limit the evaporation of water.

4.2.7 Electron-beam lithography

Microchem A3 950K polymethylmethacrylate (PMMA) resist was spin-coated onto a silicon wafer with a 100 nm thermal oxide layer (University Wafer). Electron-beam lithography was performed with a FEI Quanta ESEM to draw patterns in the PMMA resist film, and the topological pattern was transferred into the oxide layer by dry etching with CF_4 gas in a PlasmaLab 80 reactive ion etcher. The silicon master was silanized by immersion in a 40 mM solution of octadecyltrichlorosilane (Aldrich) in toluene to prevent adhesion to PDMS. It was then employed in a similar manner as the commercially available diffraction gratings to mold PDMS stamps for use in solution embossing.

4.3 Patterning nanofibers by MIMIC

4.3.1 Characterization of the diffraction grating stamps

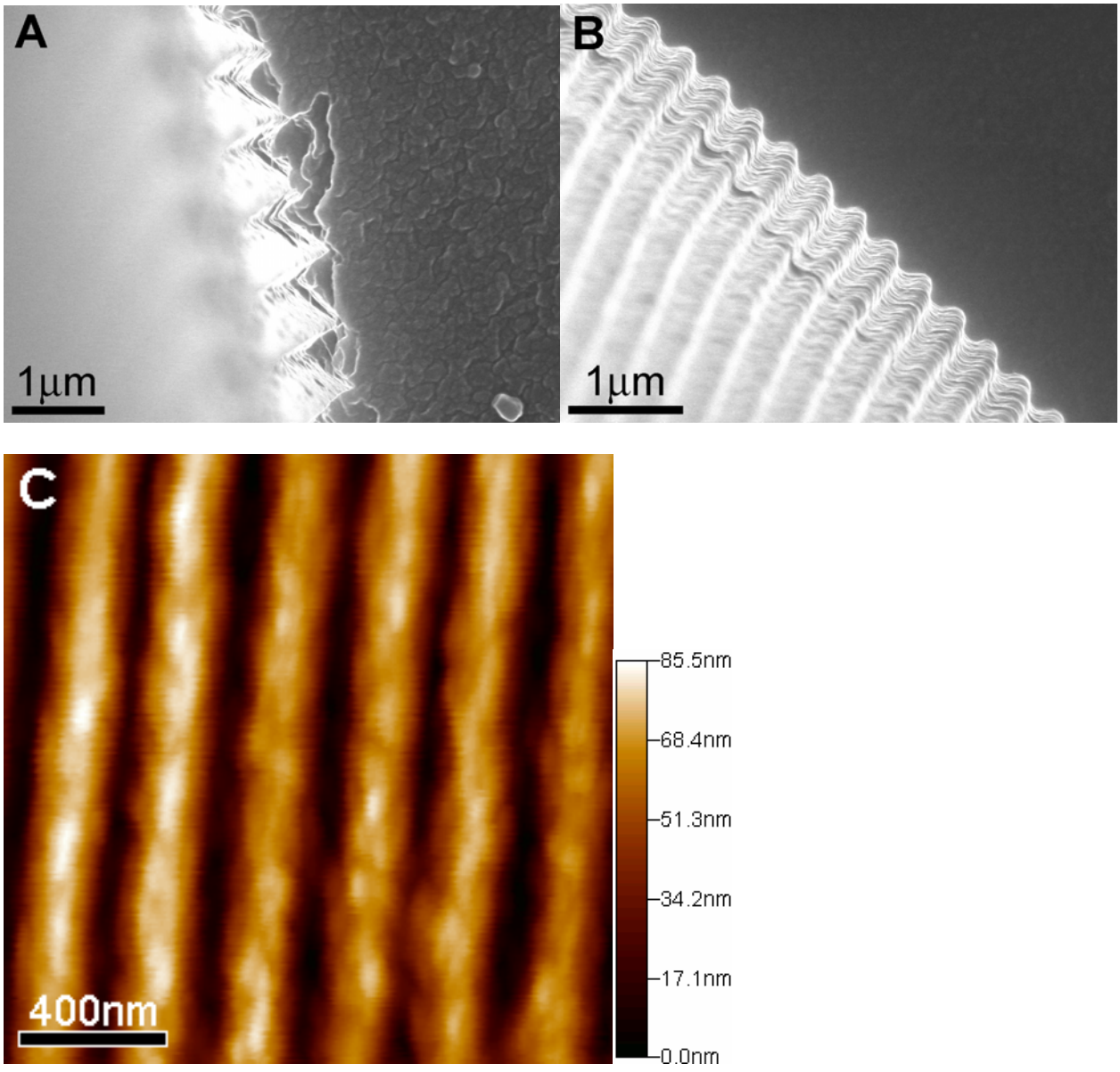

Figure 4.2. SEM micrographs and AFM height contrast image of PDMS stamps molded from diffraction grating of (**A**) 1200 lines/mm, (**B**) 2400 lines/mm, and (**C**) 3600 lines/mm.

Figure 4.2 shows AFM and SEM images of the PDMS stamps molded from the diffraction grating masters. The 1200 lines/mm grating is fabricated by a mechanical blazing method, which yields a triangular groove profile. The 2400 and 3600 lines/mm gratings are fabricated by UV interference lithography in which a resist layer is exposed to the interference pattern of two incident laser beams. This method results in a sinusoidal topology with grooves that are thinner but also much shallower than those made by mechanical blazing. The aspect ratio of the grooves can be seen to decrease with increasing line density, a fact which must be taken into account when considering the mechanism of nanofiber patterning by MIMIC or solution embossing.

Table 4.1. Geometric parameters of diffraction grating masters.

Line density (lines/mm)	Groove period (nm)	Groove Depth (nm)	Aspect ratio	Fabrication method
1200	833	626 ± 17	0.752	Mechanical blazing
2400	417	128 ± 4	0.307	UV interference
3600	278	63 ± 3	0.23	UV interference

Images of the PDMS stamps after being used to pattern PA nanofibers by MIMIC or solution embossing are shown in Figure 4.3. While some PA material does appear to adsorb to the stamp, liftoff of thick bundles of nanofibers by the stamp is very rare. This occurrence is more common for the larger channels of 833 nm periodicity, but it is almost never seen for the two smaller channel sizes. One may safely assume that almost all of the PA material is left on the substrate when the stamp is removed.

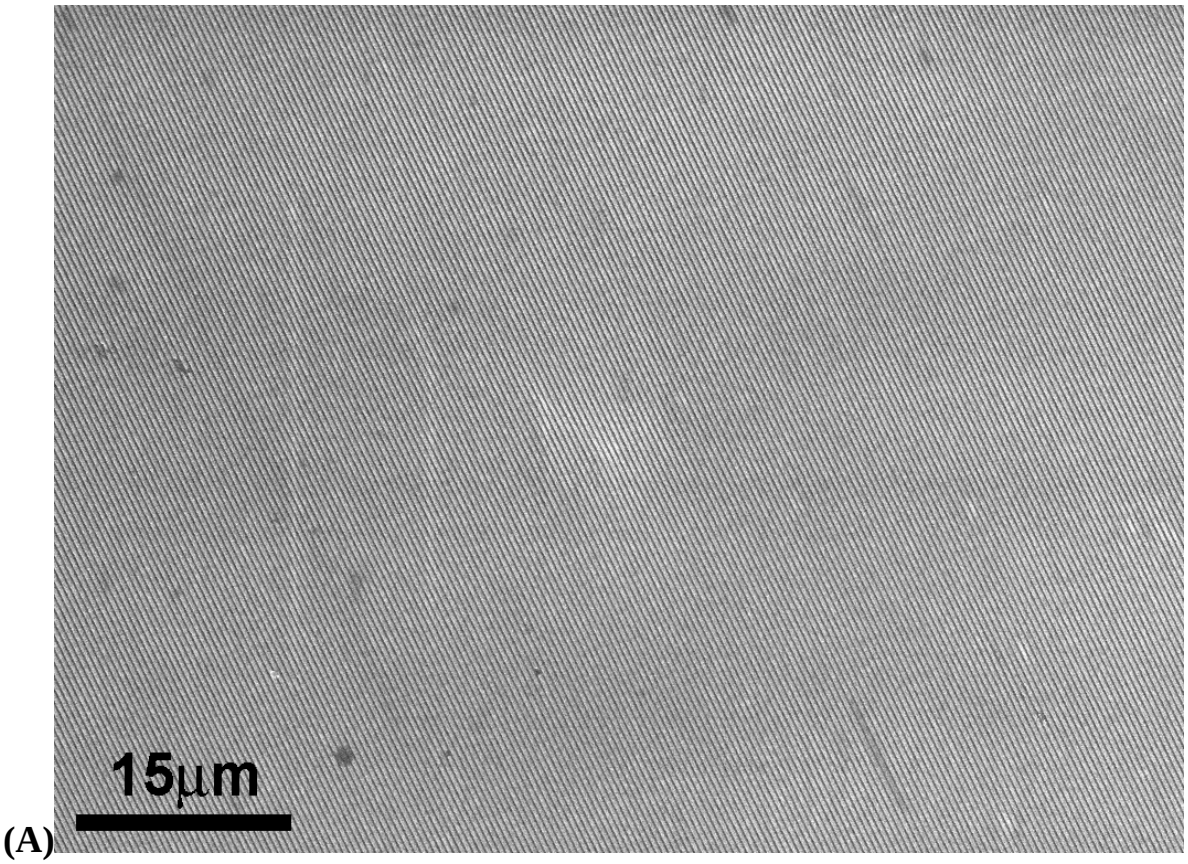

Figure 4.3. (**A**) SEM and (**B**) AFM images of a 2400 lines/mm PDMS stamp after being used for sonication-assisted solution embossing of PA **1**. While the PA did appear to coat the stamp, the grooves were very rarely seen to be filled with nanofibers.

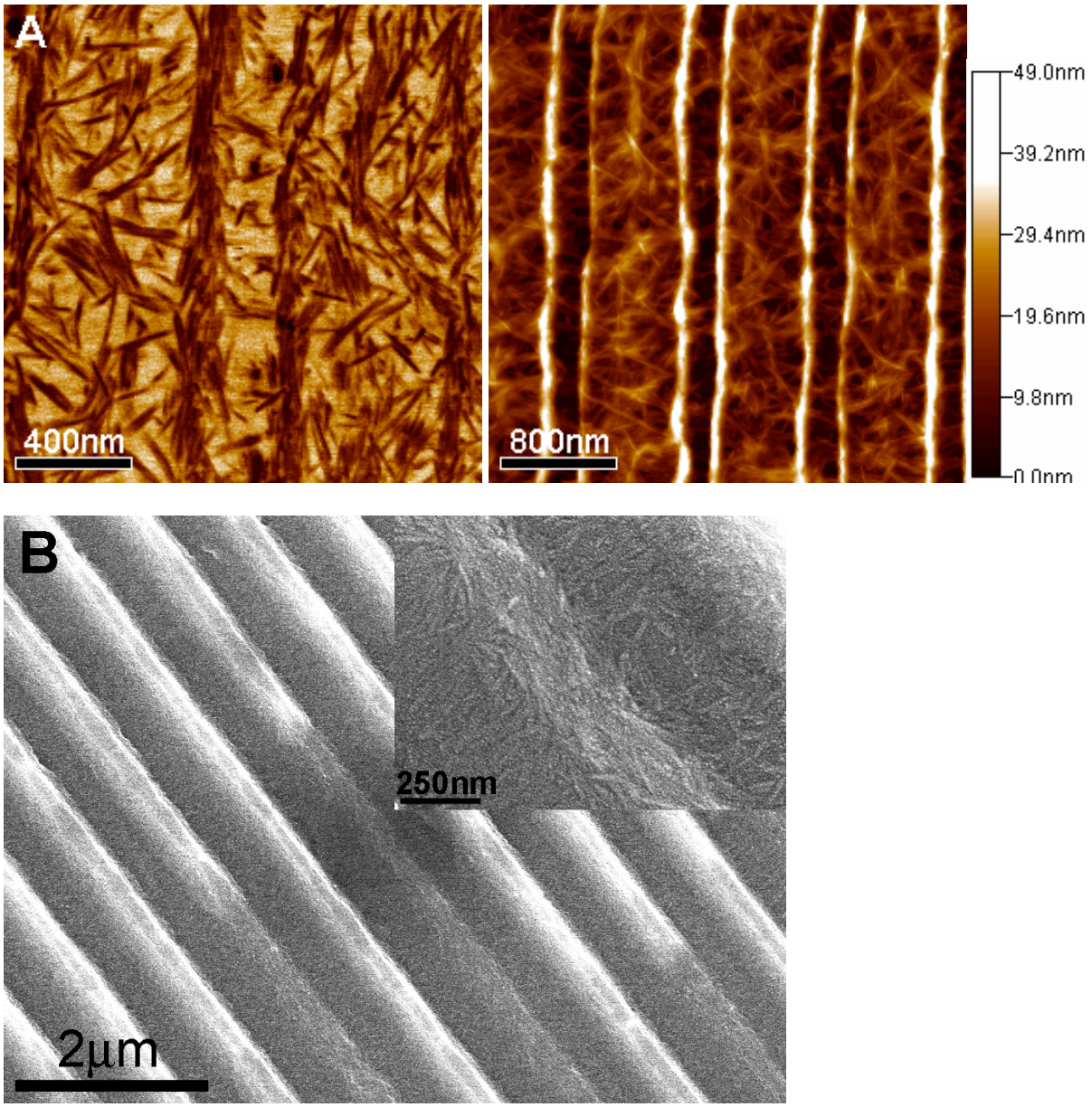

Figure 4.4. (**A**) AFM images (phase and height contrast, respectively) and (**B**) SEM images of nanofibers of PA **1** patterned by MIMIC in capillaries of 833 nm period. Inset in **B** is a magnification of the center of the image.

4.3.2 Effect of channel width

Figure 4.4 shows AFM and SEM images of nanofibers of PA **1** patterned by MIMIC in capillaries of 833 nm periodicity. Qualitatively, the nanofibers appear to deposit in disordered mats within the channels with bundles of nanofibers aligned along the edges of each channel. Alignment in this case is suspected to be due to a drying mechanism. As water evaporates, the remaining solution favors the edges of the channels due to capillary and surface tension forces. At the edges of the channels, the nanofibers are forced to deposit flat against the PDMS sidewalls, making them appear aligned with the groove direction when the stamp is removed.

Despite putting the stamp down first, the solution does appear to get underneath the stamp, and nanofibers are seen bridging the space between the capillaries. The thickest material deposition is observed closest to the open end of the channels where the drop of solution was initially placed. Although the solution travels down the full length of the channels, the nanofibers did not appear to deposit in any significant quantity farther than 1 mm from the open end.

AFM and SEM images of PA **1** nanofibers patterned by MIMIC in capillaries with periods of 278 nm are shown in Figure 4.5. The grooves in this case are much shallower, so the nanofibers don't deposit as thickly or travel as far as they do in the larger channels. The smaller channels do appear to guide nanofiber alignment better than the larger channels, but only in very small, selected areas. The irregular objects seen in Figure 4.5 are suspected to be salt or material deposited by the PDMS stamp.

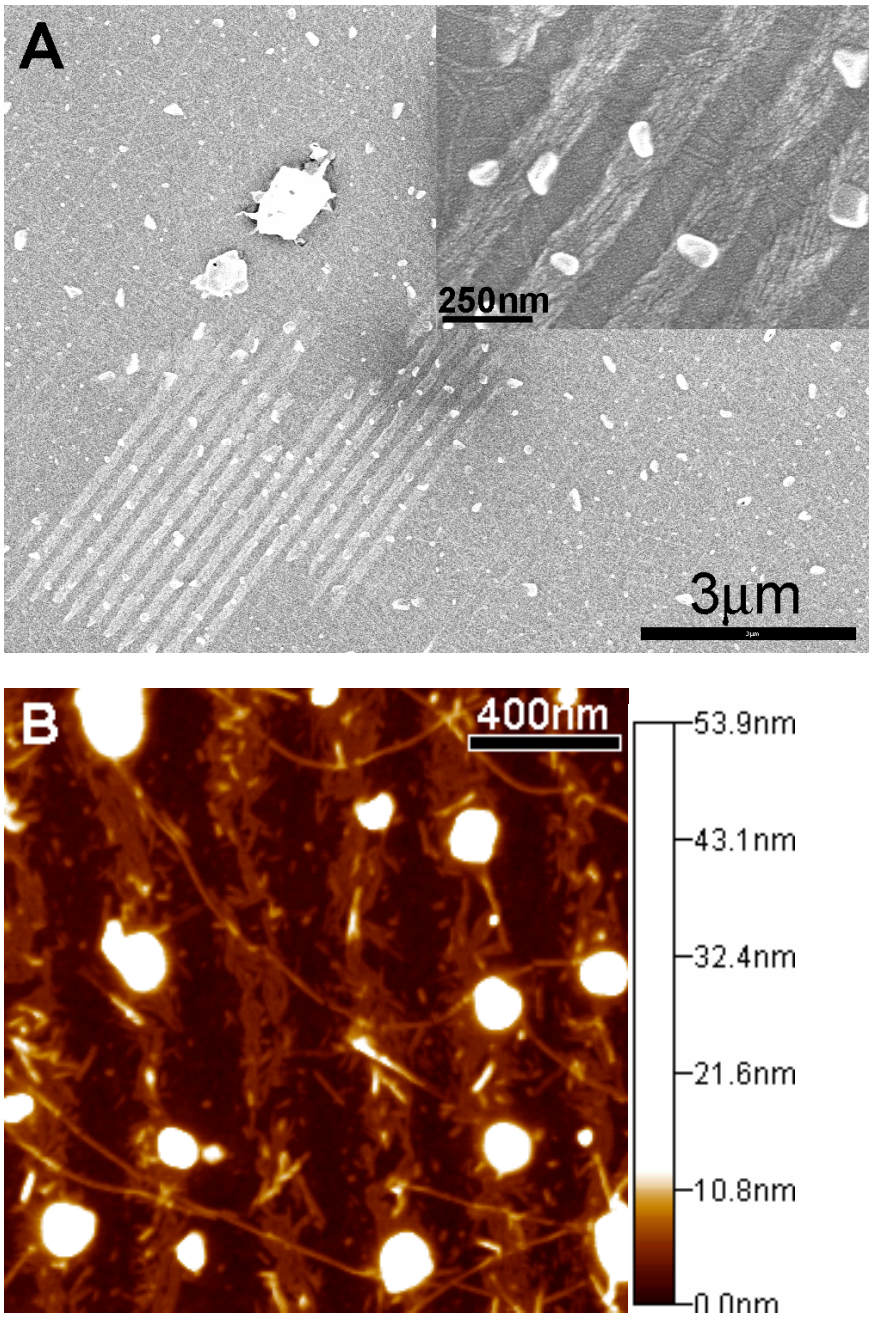

Figure 4.5. (A) SEM and (B) AFM height contrast images of nanofibers of PA 1 patterned by MIMIC in capillaries of 278 nm period. Inset in (A) is a magnification of the center of the image.

4.3.3 Mechanism of patterning

The solution is clearly seen to be drawn down the full length of the channels, at least the larger ones. The PA acts as a surfactant, and if the concentration of the solution is too low, there is not enough surfactant to overcome surface energy forces and the solution doesn't travel down the channels at all. However, while the solution fills the channels, the nanofibers are only deposited in any significant quantity very close to the end where the drop is placed. Attempts to increase the area of nanofiber deposition by reducing the evaporation rate or increasing the solution concentration failed. What we believe occurs is that the initial drop of solution dries first into a concentrated gel while the solution in the channels remains dilute. However, the nanofibers in that concentrated gel become entangled and are extremely slow to diffuse, eventually plugging the open end of the channels and preventing any more material from moving down them. As a result, patterning of the nanofibers by this method is ineffective. For this reason, solution embossing was investigated as an alternate method that might yield more uniform area coverage.

4.4 Patterned, aligned nanofibers by sonication-assisted solution embossing

4.4.1 AFM of patterned, aligned PA nanofibers

Figure 4.6 shows AFM images of nanofibers of PA **1** embossed from a 5 wt % solution in capillaries with periods of 416 nm and 278 nm. Qualitatively, the supramolecular nanofibers conformed to the pattern of the grating and appeared to be very well aligned in long bundles along the direction of the grooves. For the 416 nm lines, most of the bundles were, as in Figure 4.6a, cleanly separated from each other with no residual layer of nanofibers coating the substrate in between. For the 278 nm lines, there was a ubiquitous residual layer of nanofibers between

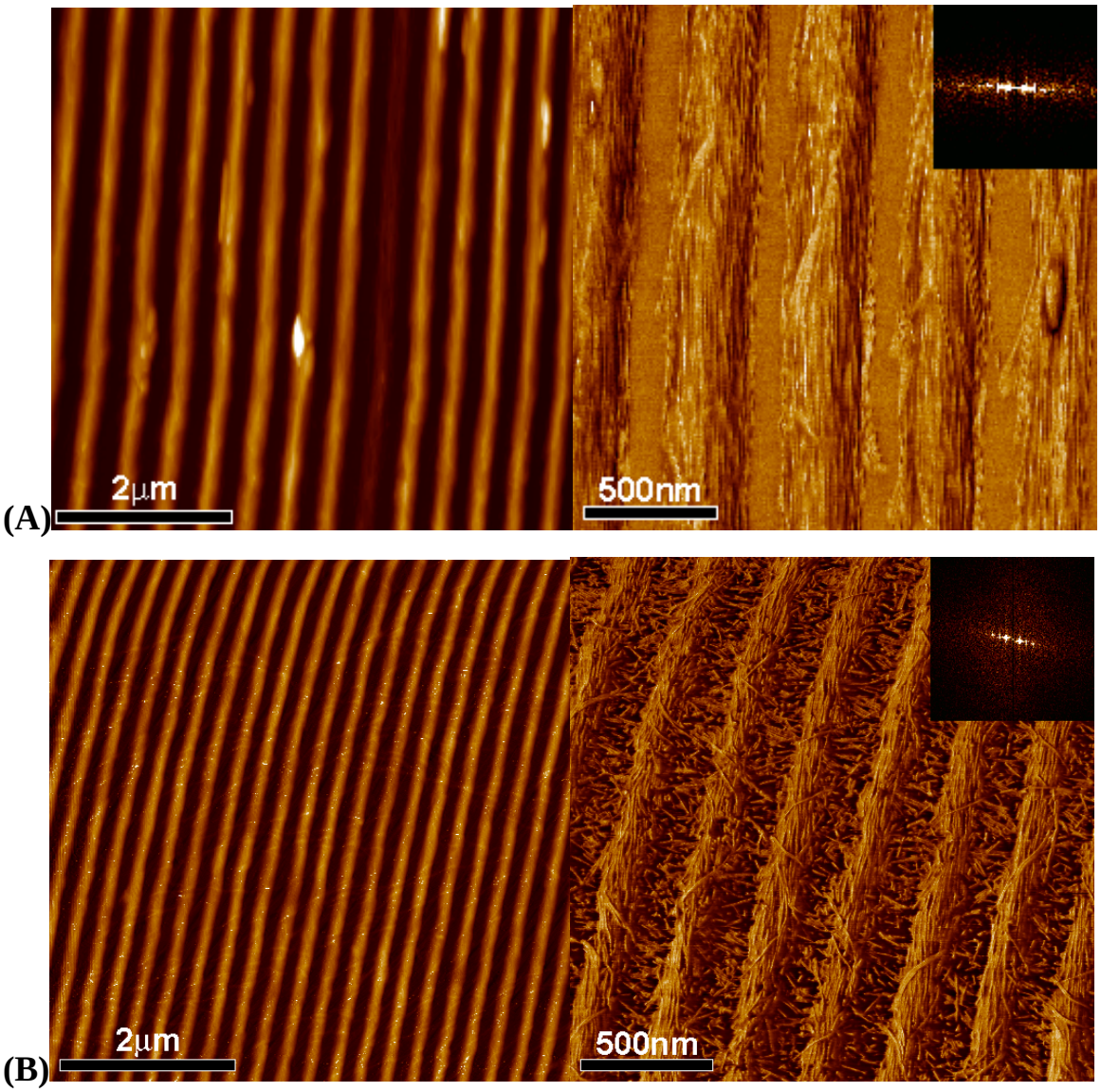

Figure 4.6. AFM height and phase images of aligned supramolecular nanofibers of PA 1. The fibers were embossed from a 5 wt % solution into lines with periods of (**A**) 417 nm and (**B**) 278 nm (height scales 106 nm and 99.8 nm, respectively). In (**A**), the widths of the nanofiber bundles were *ca*. 200–300 nm, and the average height of the lines was 55.1 ± 0.7 nm. The inset shows a fast Fourier transform (FFT) of the phase image, revealing the periodicity of the grating pattern (brightest spots toward the center) and the nanofibers within each line (diffuse bands to the outside). In (**B**), the widths were *ca*. 150 nm, and the average height of the lines was 33.3 ± 1.0 nm. The FFT of the phase image shows similar alignment along the channels as well as some off-axis orientation of the underlying residual layer of nanofibers.

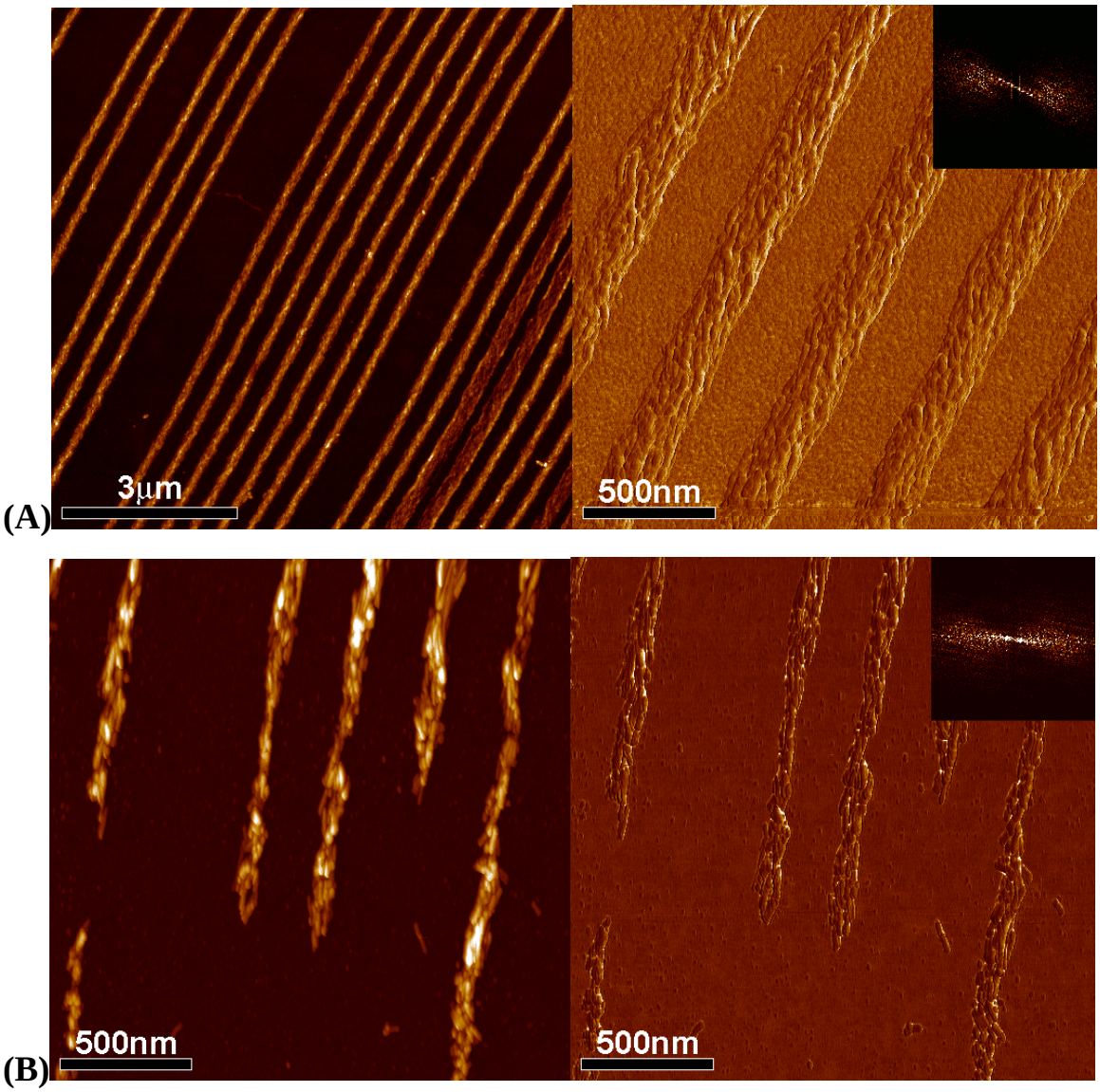

Figure 4.7. AFM height and phase images of aligned supramolecular nanofibers of PA **2**. The fibers were embossed from a 1 wt % solution into lines with periods of (**A**) 417 nm and (**B**) 278 nm (height scales 44.7 nm and 25.4nm, respectively). In **A**, the widths of the nanofiber bundles were *ca*. 150 nm, and the average height of the lines was 23.1 ± 0.7 nm. The inset FFT of the phase image clearly shows the periodicity of the nanofibers within each bundle oriented nearly parallel with that of the overall line pattern. In **B**, the widths were *ca*. 50-100 nm, and the average height of the lines was 13.4 ± 1.2 nm. Overall, the degree of alignment and uniformity of deposition was poorer for the 278 nm lines than for the 416 nm lines.

the nanofiber bundles, but excellent alignment within the bundles was still observed and the uniformity of deposition was very good.

AFM images of PA **2** nanofibers embossed in capillaries with periods of 416 nm and 278 nm from a 1 wt % solution are shown in Figure 4.7. For the 416 nm lines, the degree of order appeared to be comparable to that of PA **1** with nanofibers aligned in neatly spaced bundles. However, the deposition was not as uniform, with some lines completely lacking nanofibers. This characteristic was more pronounced for the finer lines (Figure 4.7b). In some areas, good alignment was observed for cleanly spaced bundles of small numbers of nanofibers, but in other areas the nanofibers were poorly aligned or completely absent. It is possible that in this case, the channels were too shallow and actually hindered the mobility of the nanofibers.

4.4.2 Mechanism of patterning

For the 2400 lines/mm grating, the heights of the lines produced using 5 wt % and 1 wt % solutions were 50 ± 9 nm and 23 ± 6 nm, respectively. The finer grating yielded line heights of 32 ± 2 nm and 17 ± 9nm, respectively. Differences in line height between PAs **1** and **2** were not significant. While the difference in line height due to concentration was not surprising, the overall magnitude of the heights was larger than expected, suggesting that the nanofibers collected within the channels at concentrations of roughly 20% to 50% by volume. If the stamp was in contact with the substrate during the entire process, achieving these concentrations would require extensive mass transport down the length of the channels. This seems unlikely given that PAs **1** and **2** begin to form self-supporting gels at concentrations of 1-2% by weight.

Previous studies that applied capillary micromolding techniques most often involved positioning the stamp onto the substrate first, then placing a drop of solution at one of the open

ends of the channels and allowing the solution to wick in by capillary action.[271, 272, 282-284] This method was initially attempted with PA **1**, but while the solution traveled the full length of the channels, nanofibers were only deposited about one millimeter into the channel, regardless of the initial conditions. This likely occurred because as the size and number of nanofiber aggregates increased with solvent evaporation, their diffusivity decreased. Given this observation, it is improbable that the lines deposited with the current method could result from diffusion down the confining channels. More likely, the stamp does not actually sit in contact with the substrate initially but instead on a thin film of solution several hundreds of nanometers thick. As the water evaporates, this fluid layer decreases in thickness until the stamp finally contacts the substrate, trapping a high concentration of PA nanofibers within each channel.

This mechanism also helps to explain the presence of the residual layer in Figure 4.6b. By AFM and SEM, the depths of the channels were 128 ± 4 nm and 63 ± 3 nm for the 2400 and 3600 lines/mm gratings, respectively. The smaller volume in the 278nm channels meant that less material could be collected in them, and any nanofibers that could not be moved out from under the stamp remained as a residual layer. Furthermore, while the stiffer h-PDMS layer on the patterned surface of the stamp should reduce compression of the channel, some deformation is still expected. As such, the stamp-substrate contact area between each bundle of nanofibers was larger for the 3600 lines/mm grating, which may have decreased the actual pressure underneath the contact area.

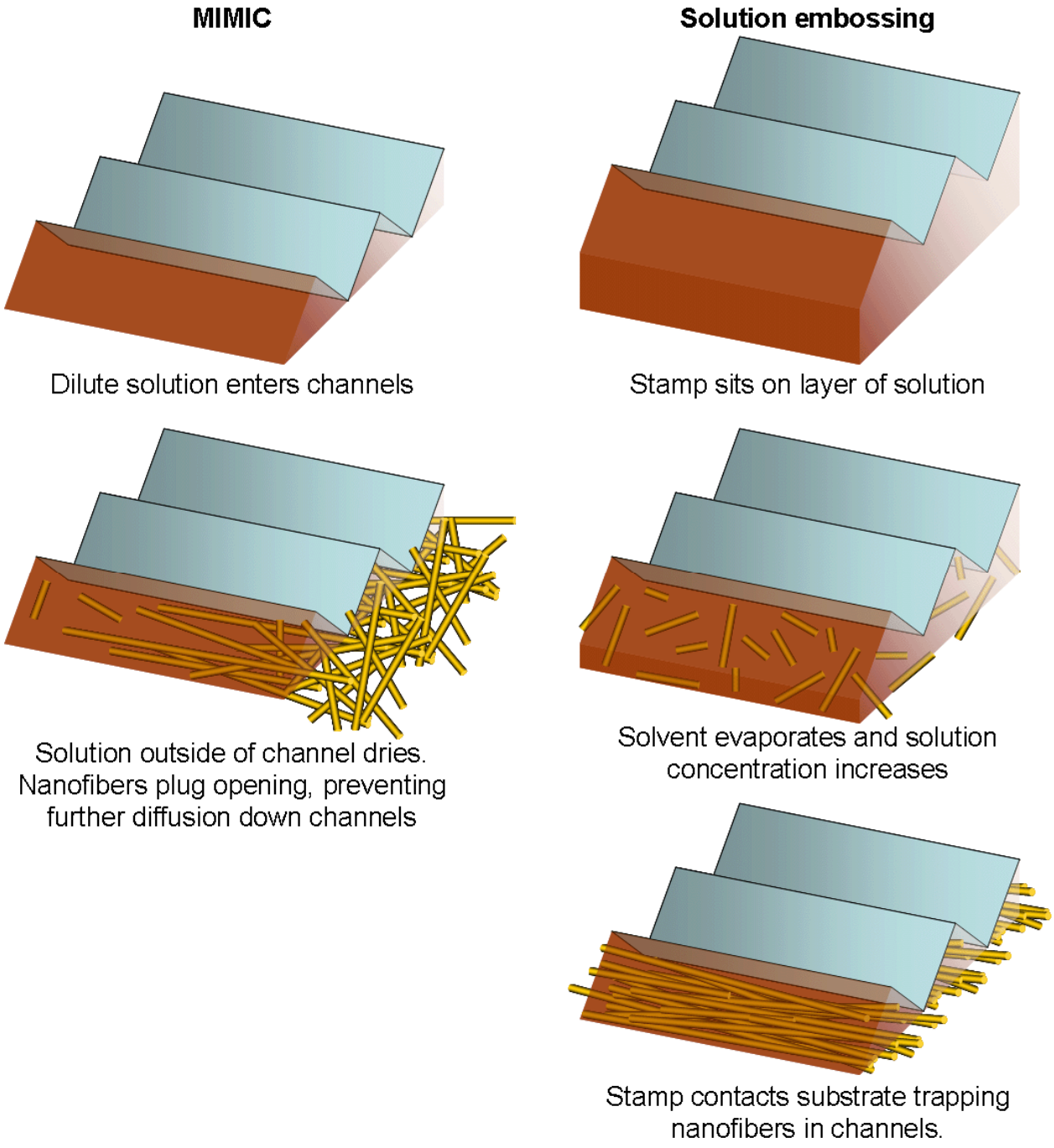

Figure 4.8. Schematic of the proposed mechanisms of nanofiber patterning by MIMIC and by solution embossing.

4.4.3 Effect of ultrasonication and initial solution concentration

Including an ultrasonication step in the procedure improved the overall alignment and uniformity of deposition, especially for nanofibers of PA **2**. Non-sonicated samples tended to have a thicker residual film between the channels and a greater occurrence of defects in line deposition. We suspect that mechanical agitation during the initial stages of drying imparted kinetic energy to the system, enabling the nanofibers to adopt a more equilibrium packing geometry. Ultrasonication could act on large length scales by smoothing out concentration gradients and on smaller length scales by increasing the mobility of both the supramolecular aggregates and the molecules themselves, accelerating the process of dynamic assembly and disassembly of the nanofibers.

Because the sample is not rigidly attached to the beaker during ultrasonication, the higher frequency vibrations are likely damped and not felt by the sample. In further optimizing the process, it may be profitable to explore ways to secure the sample more tightly in order to allow these higher frequency vibrations to be felt. In addition, while ultrasonication was limited to one hour, the samples remain wet for much longer. Given the mechanism of patterning proposed earlier, ultrasonication for longer periods or started at later times may improve nanofiber alignment. The ultrasonic bath does heat up from room temperature to 50 °C after 1 hr of operation, but separate experiments applying thermal energy alone did not appear to benefit nanofiber alignment.

Increasing the concentration of the initial PA solution also appeared to improve the nanofiber alignment and uniformity of deposition. Whether or not a given concentration was "too low" depended on the specific PA molecule and is likely related to solubility. A possible reason for the concentration dependence is discussed in the next section.

4.4.4 Mechanism of alignment and lyotropic liquid crystalline behavior

Nanofibers of both PAs have persistence lengths greater than 600 nm as estimated by TEM, SEM, and AFM images.[81, 208, 256] This length is longer than the dimensions of the confining capillaries, which are 416 nm wide and 128 nm tall at the largest. Because of this fact, steric hindrance likely plays a role in the alignment of the nanofibers within the channels. It is also possible that the system undergoes a phase transition to a lyotropic liquid crystalline phase as the concentration increases. Lyotropic liquid crystal models such as those put forth by Onsager[20] are particularly applicable for high aspect-ratio mesogens with limited interactive forces other than steric repulsion. While more complex models such as those proposed by Khokhlov and Semenov[45] are likely more accurate in predicting the nanofiber concentration and order parameter at the liquid crystal transition, the basic priniciples of both models are the same and may be applied in a general discussion of the mechanism of alignment.

Figure 4.9 shows optical microscopy images of aqueous gels of both PAs **1** and **2** at concentrations of roughly 15% and 7% PA by weight between crossed polarizers. Both gels displayed birefringent textures that suggest self-organization of the nanofibers into nematic phases at higher concentrations. The scattering contrast and coherence length of the concentrated gels appears to be quite low as Figure 4.10 shows SAXS of a gel of 20% PA 1 by weight, with only a weak, broad peak at 7.2nm being visible. Drop cast films of both molecules showed only very limited long-range orientational order, indicating that the liquid crystalline phases are slow to organize. A liquid crystal phase is not necessary to achieve good alignment with adequate spatial confinement, however, in our systems the cooperative effect of both phenomena would improve the degree of order.

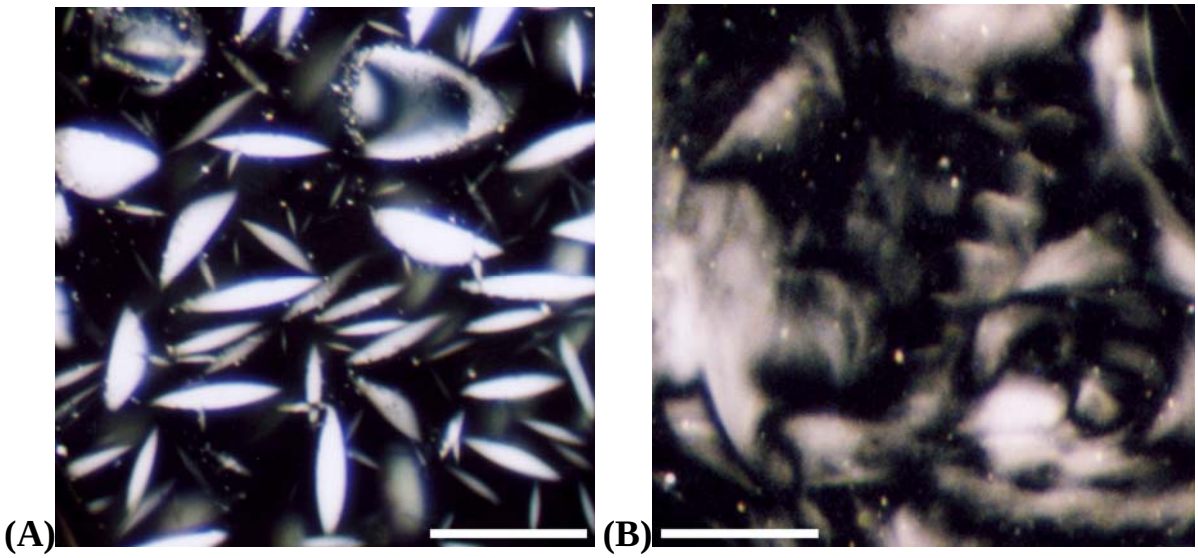

Figure 4.9. Polarized optical microscopy images of concentrated aqueous gels of PA nanofibers. Both scale bars are 100 μm. (**A**) PA **1** at roughly 15 wt % shows bright birefringence suggestive of a hexagonal liquid crystalline phase and possible phase separation from an isotropic phase. At higher concentrations, fingerprint textures indicative of a cholesteric phase can be seen, similar to those reported previously.[24] (**B**) PA **2** at roughly 7 wt % is more weakly birefringent but does display a texture that suggests the formation of a nematic phase.

If the system indeed entered a lyotropic phase, it might be possible to observe a difference in behavior depending on solution concentration. At an Onsager transition, the material would be expected to phase separate into a dilute isotropic phase and a more concentrated nematic phase.[20] This behavior can be seen in concentrated gels of PA **1** (Figure 4.9a) where strongly birefringent needle-like domains on the order of tens of micrometers precipitate from a disordered medium. The "empty" lines such as those in Figure 4.7a and observed in samples of patterned nanofibers of both PA **1** and **2** may be due to phase separation during patterning, resulting in lines of nematic and isotropic phases. Alignment in the former would be dominated more by liquid crystalline behavior while alignment in the latter might be

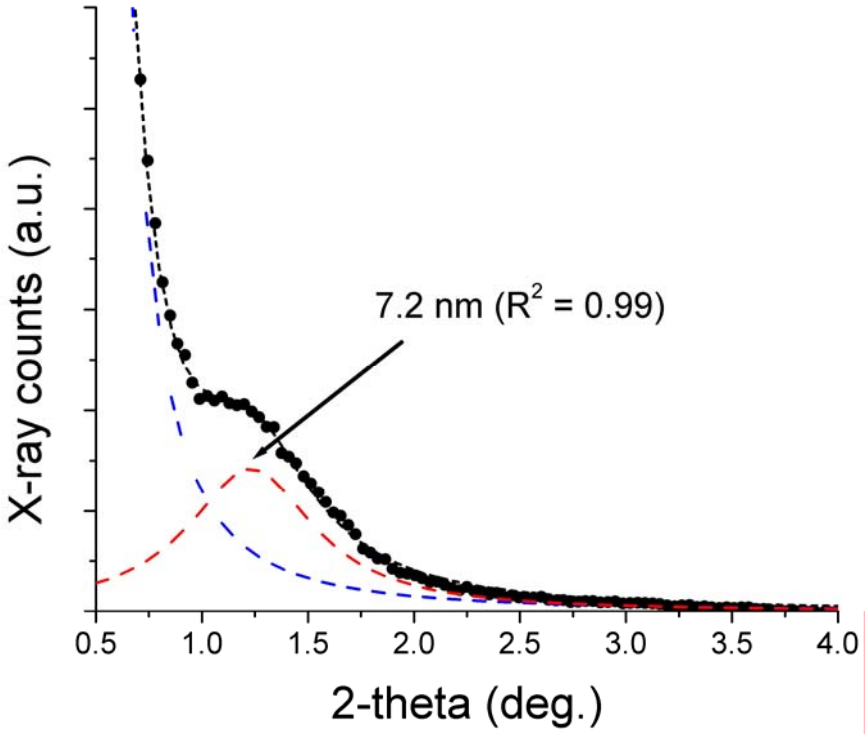

Figure 4.10. SAXS of a 20 wt % aqueous gel of PA **1** with peaks fit to a mixed Gaussian-Lorentzian form (courtesy of James Hulvat).

affected more by drying effects. When the initial solution concentration is increased from 1 wt % to 5 wt % as shown for PA **1** in Figure 4.6, very few "empty" lines were seen, presumably because all of the material in solution collapsed into the condensed phase within the channels. AFM and SEM of used stamps revealed that liftoff of entire lines of nanofibers with the stamp was extremely rare, and even so, liftoff would not explain the concentration dependence.

The effectiveness of this method depends not only on the degree of order of any liquid crystalline intermediate but the dynamics of self-assembly as well. Instead of being a detriment, self-assembly during the patterning process may in fact improve the degree of order. Alignment of a covalently cross-linked fiber requires the full rotation of the whole fiber, whereas self-assembled nanofibers can break and reform, effecting alignment with a minimum of mass

transport. Differences in the degree of orientation between PA **1** and PA **2** may reflect differences in self-assembly kinetics. Despite these differences, alignment is observed in both PAs, demonstrating the promise of this method for the alignment of other self-assembling one-dimensional nanostructures.

4.4.5 Guiding PA nanofibers through complex paths

Having found that it is possible to align PA nanofibers within parallel channels, we were interested in determining whether we could arrange the nanofibers in more complex patterns. Toward this end, we fabricated a rigid master with a topological pattern of channels by electron-beam lithography. While electron-beam lithography was time-consuming, it was required

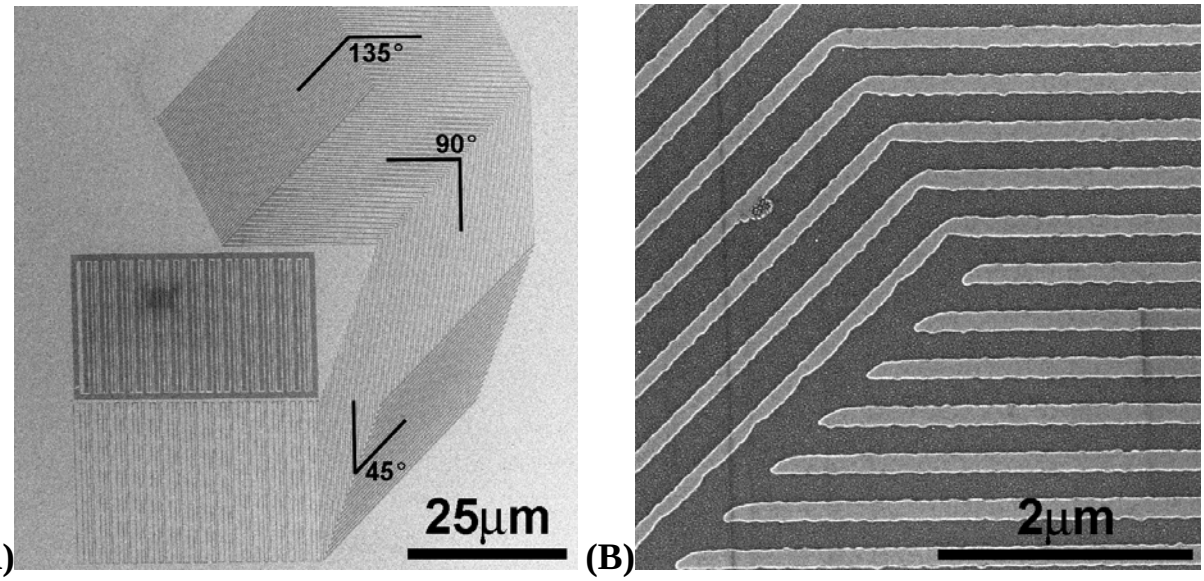

Figure 4.11. (**A**) SEM image of the complex grating pattern master used in the present study. The master was fabricated by electron-beam lithography and dry etching a 100 nm oxide layer on a silicon wafer. The pattern consists of lines *ca* 200 nm wide with a periodicity of 400 nm. The lines turn corners of angles 135º, 90º, and 45º. A magnified image of the 135º corner is shown in (**B**).

only once to create the rigid master from which the pattern could be replicated multiple times by soft lithography. SEM images are shown in Figure 4.11 of a custom-drawn channel pattern etched into a 100nm thermal oxide layer on silicon. The pattern consisted of parallel lines 200 nm wide and spaced 200 nm apart similar to a diffraction grating, except the lines turned sharp corners periodically at angles varying from 45º to 135º.

Figure 4.12 shows SEM images of nanofibers of PA **1** embossed in the electron-beam defined capillaries. The nanofibers aligned along these channels just as they did in the diffraction grating-molded channels. When the nanofibers reached a corner, they would either bend or break and then continue traveling parallel to the new channel direction. At a 135 º turn in the channel, the nanofibers appeared to bend but remain intact as they round the corner. At sharper angles of 90 º or 45 º, the nanofibers usually terminated before taking up the new channel

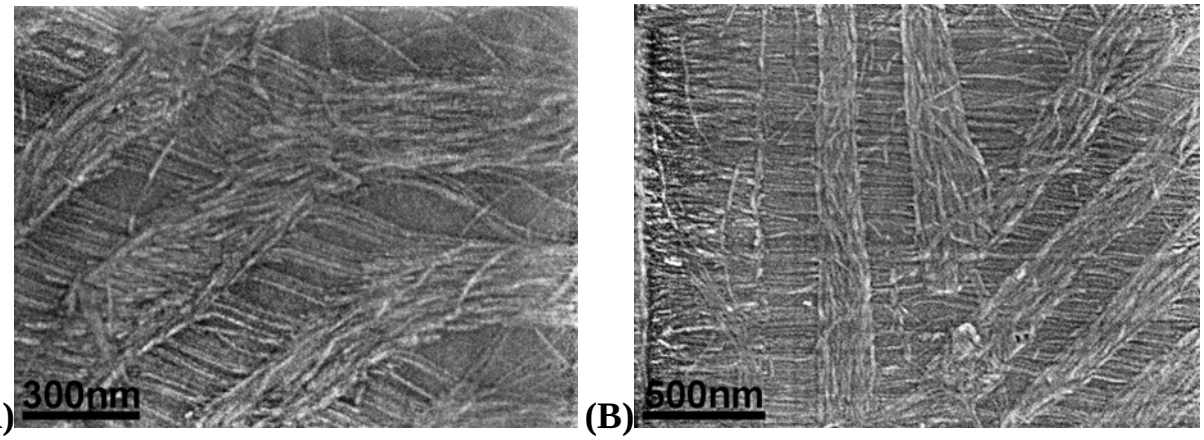

Figure 4.12. SEM images of nanofibers of PA **1** aligned in capillaries defined by electron-beam lithography. (**A**) At a 135º corner, the nanofibers were able to turn the corner without breaking. (**B**) At a 45º corner, most nanofibers broke before continuing in the new direction but otherwise remained aligned within the channels.

direction. The minimum radius of curvature of the nanofibers was generally observed to be about 400 nm. This is perhaps the most definitive proof that alignment in these sub-micron capillaries is due to spatial confinement and not due to any shear force generated between the stamp and the substrate. Such shear forces would likely have resulted in uniaxial alignment of the nanofibers over the substrate regardless of channel orientation.

4.5 Summary and outlook

Self-assembled nanofibers of peptide-amphiphile molecules have been of great interest because of their bioactivity both in vitro and in vivo. These nanofibers can be patterned on a substrate by micromolding in capillaries or solution embossing. We demonstrate the controlled alignment of these nanofibers over large areas within arrays of submicron channels by a novel technique termed sonication-assisted solution embossing. In this soft lithographic technique, the nanostructures self-assemble by solvent evaporation while under the influence of ultrasonic agitation and confinement within the topographical features of an elastomeric stamp. The nanofibers orient parallel to the channels as they assemble out of disordered solution, yielding bundles of aligned nanofibers on the substrate after the stamp is removed. Alignment is likely a result of steric confinement and possibly a transition to a lyotropic liquid crystalline phase as solvent evaporates. This technique is not limited to uniaxial alignment and is shown to be able to guide nanofibers around turns. It is also versatile enough to be used in the alignment of other self-assembling supramolecular systems starting from solutions of small molecules. The ability to align nanostructures by this method introduces the possibility of controlling macroscopic cellular behavior or material properties by tuning the directionality of interactions at the nanometer scale.

CHAPTER FIVE

Infrared Spectroscopy and Preliminary Cell Studies on Peptide-Amphiphile Nanofibers Patterned and Aligned by Solution Embossing

Chapter 5: Infrared Spectroscopy and Preliminary Cell Studies on Peptide-Amphiphile Nanofibers Patterned and Aligned by Solution Embossing

5.1 Introduction

Discrete, one-dimensional supramolecular nanostructures are particularly interesting for the anisotropic properties inherent in their shape. The ability to control the orientation of such structures would be useful but is difficult given their poor mobility in non-solvated states as a result of their large mass. The previous chapter described work on creating large-area, aligned patterns of self-assembled nanofibers of PA molecules by sonication-assisted solution embossing.[289] This soft lithographic technique involved assembling the nanofibers from aqueous solution within confining sub-micron channels while under the influence of ultrasonic agitation. Self-assembly was triggered by solvent evaporation, and the nanofibers were forced by steric repulsion to orient parallel to the channel direction. Unlike previous alignment techniques,[136, 137, 139, 151, 152, 208] sonication-assisted solution embossing is a parallel process that is not limited to creating uniaxially aligned patterns but can be employed to guide nanofibers around turns and through complex paths. This method may also be applicable to a wider range of supramolecular systems.

Alignment of PA nanofibers enables more in-depth studies of the self-assembled structure and its interaction with ions, molecules, and cells. Electron microscopy shows that the molecules assemble with their peptide sequences on the periphery of the nanofiber exposed to water and their alkyl segments sequestered in the core.[81] Circular dichroism (CD)[254, 257, 290, 291] and Fourier transform infrared (FTIR) spectroscopy[120, 255, 257, 291] show the formation of β-sheet secondary structure among peptide segments in these assemblies, and molecular dynamics

simulations suggest that these β-sheets orient along the long axis of the nanofiber and may be critical to the formation of the cylindrical structure.[121, 122] However, the outermost peptide shell of the nanofibers remains highly solvated as demonstrated by fluorescence quenching experiments.[258]

Recent investigations of neat nanofiber films by transmission and reflectance IR spectroscopy support the model of internal β-sheet structures aligned along the nanofiber axis. Paramonov et al showed previously that the innermost amino acid residues in the peptide sequence of PA molecules most strongly influence β-sheet formation and nanofiber self-assembly.[257] Jiang et al also showed that the outer peptide sequence influences the degree of internal order in the nanostructure which may in turn strongly affect the nanofiber's bioactivity.[255] This work reported molecular order within the alkyl core of the nanofibers, which seems to be linked to order in their peptide shell. However, neither analysis can identify vibrations that are perpendicular to the nanofiber axis, and the possibility that the observed structure is a result of adsorption to the substrate is only briefly addressed.

All previous studies of the PA nanofibers were performed on disordered films or aqueous solutions. Alignment of the nanofibers now makes polarized transmission FTIR a useful tool for obtaining higher order information. Polarized IR spectroscopy is frequently used to determine the orientation state and degree of alignment in peptides[292-294] and other materials,[240] but transmission IR can only excite vibrations oriented within the plane of the film. Polarization modulation-infrared reflection-absorption spectroscopy (PM-IRRAS) is thus useful as a complementary tool because of surface selection rules that allow it to discriminate between transition dipole moments (TDMs) oriented normal and parallel to the substrate surface.[241] In the first part of this chapter, we study the aligned nanofiber samples by both polarized

transmission FTIR and PM-IRRAS in order to generate a three-dimensional picture of average TDM orientations. The measurements prove the effectiveness of the soft lithographic technique in aligning the nanofibers over macroscopic areas, and the effects of ultrasonication and size of the confining channels on nanofiber alignment are quantitatively compared. The previously proposed structural model is confirmed, and because the nanofibers are aligned, we are able to identify vibrations oriented perpendicular to the nanofiber. We also see an increased degree of β-sheet ordering within the patterned nanofibers, possibly due to the slower solvent evaporation rate.

Alignment of the PA nanofibers also enables studies on the nature of cell-substrate interactions at the nanometer scale and their influence on cell behavior. The ability to align cells is not only useful for controlling and studying cellular behavior and processes, it is necessary for the morphologically correct regeneration of many tissue types.[295-297] Patterned topologies and surface chemistries on the micrometer scale have shown some success in controlling cell shape, orientation, and limited functions.[298-301] However, more recent work suggests that patterns with nanometer-scale features may be more effective because they more closely mimic the extracellular matrix and can influence a wider range of behaviors beyond cell morphology and adhesion.[277, 302-310] Self-assembly can easily access this length scale, and it may be possible to direct cell behavior through the controlled placement and orientation of self-assembled nanostructures. In the second part of this chapter, we show preferential orientation of cell bodies and processes of primary mouse neural progenitor cells (NPCs) cultured on substrates of patterned, aligned PA nanofibers. Cell alignment is not observed on any of the control substrates and is hypothesized to result from a mediation of integrin clustering by the nanofiber, leading to a restructuring of the cytoskeleton.

5.2 Materials and Methods

5.2.1 PA molecules

The chemical structure of PA molecules **1** and **2** employed in this study are given in Figure 5.1 along with a schematic of the hypothesized structure of the nanofiber in which the molecules form β-sheet "fins" (pink) with the direction of hydrogen bonding aligned parallel to the long axis of the nanofiber. Solid-phase synthesis and cell studies of **1** and **2** have been reported previously.[81, 119, 120] The pentapeptide IKVAV displayed on PA **2** is found in laminin-1 and has been demonstrated to promote process outgrowth in neurons.[287, 288] PA **1** displays the tripeptide RGD, a well-known epitope that among other things can promote cell adhesion.[285, 286]

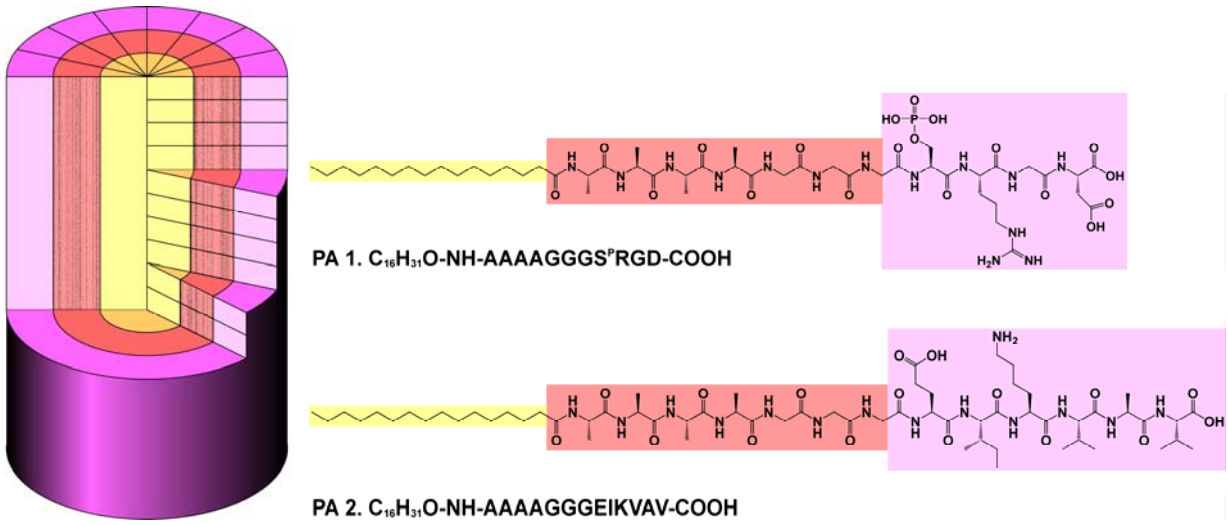

Figure 5.1. Chemical structures of PA **1** and PA **2** including a schematic of the molecular structure of the nanofibers into which they assemble.

5.2.2 Soft lithography

Optical diffraction gratings (Edmund Industrial Optics) with groove densities of 1200, 2400 and 3600 lines/mm (833 nm, 416 nm, and 278 nm period, respectively) were used as master molds for casting line patterned PDMS stamps. These stamps were employed to create uniaxially aligned patterns of nanofibers of **1** and **2** by sonication-assisted solution embossing. The procedure for casting the stamps, cleaning the substrates in piranha solution, and patterning the nanofibers was detailed previously.[289] Samples prepared for polarized transmission FTIR were patterned on piranha-cleaned undoped (111) silicon (n-type, resistivity: 1500 Ωcm, University Wafer). Samples for PM-IRRAS measurements were required to be on conductive metal substrates. For this purpose, a thin metal film was evaporated on slide glass in a BOC Edwards Auto 306 electron-beam evaporator. An adhesion layer of 5 nm of titanium was evaporated first, followed by 30 nm of gold capped with a 1 nm layer of titanium on top of the gold to produce a hydrophilic oxide surface. Evaporated metal substrates were cleaned in oxygen plasma in a PlasmaLab 80 reactive ion etcher (Oxford Instruments) prior to use.

5.2.3 FTIR and determination of direction cosines and orientation parameters

Samples made on undoped silicon substrates were characterized by polarized transmission FTIR. A Thermo Nicolet Nexus 870 FTIR spectrometer was set up in transmission mode with a polarizer in the beam path ahead of the sample. FTIR spectra of the samples were collected for polarization angles ranging from 0° to 90° relative to the grating line direction. Samples made on thin film metal substrates were studied by PM-IRRAS using the same instrument in grazing-incidence reflection mode with an attached tabletop optics module.

Selected peaks in the spectra were fit to Lorentzian forms so that the peak areas could be obtained and the quality of alignment between samples could be quantitatively compared. In the amide I region (1700-1620 cm^{-1}), a rigorous deconvolution of each of the non-β-sheet peaks was not attempted, rather, the peak fitting was performed to the extent to which we were able to reliably determine the area of the β-sheet peak at 1630 cm^{-1}. The amide A band (3310 – 3270 cm^{-1}) is much less sensitive to secondary structure[311, 312] and even more difficult to deconvolute, so orientation parameters obtained for the amide A band were used only to qualitatively confirm observed trends.

The peak areas were used to calculate the direction cosines for select TDMs, and the direction cosines were used to calculate order parameters and tilt angles. A derivation of the equations involved is given in Appendix A.

For comparison, AFM images of aligned nanofibers were analyzed to yield estimates of the orientation parameter. One method to do this is to record the length and orientation angle with respect to the grating angle of as many fibers as convenient in each image in order to calculate a length-weighted average value of $\cos^2\theta$. Another, method to determine the distribution of $\cos\theta$ is to take the FFT of the image and integrate the intensity for several orientation angles over a range of spatial frequencies from 0.02 to 0.2 nm^{-1}.

5.2.4 Cell studies

To probe the effect of nanofiber alignment on cell behavior, three types of samples were prepared as outlined in Figure 5.2 on piranha-cleaned glass substrates. In treatment **A**, 4 uL of PA **1** was dropped onto the glass substrate and allowed to dry with no further intervention. In **B**, the stamping procedure was followed with the omission of the ultrasonication step. This resulted

in nanofibers that were molded into a grating pattern of 2400 lines/mm but not aligned as in ultrasonicated samples. In **C**, the full stamping procedure was used, resulting in patterns nearly identical to **B** samples except the nanofibers are aligned with an orientation factor of roughly 0.25.[240, 289] Samples of PA **2** and laminin-1 were also prepared under treatments **A** and **C**. Duplicate samples were prepared for each case. Samples were encoded so that the experimenter was blind to which treatment had been used and to the direction of patterning.

Murine neural progenitor cells were harvested and prepared as described previously.[120, 313] Briefly, second-passage cells were grown for four days as neurospheres, after which the cells were dissociated and diluted to a concentration of 10^4 cells/mL in DMEM/F12 medium supplemented with bFGF. Samples were placed in separate wells of a six-well plate and 3 mL of cell suspension was added to each well. After incubation for three days at 37 °C and 95% humidity, samples were viewed using a Nikon microscope.

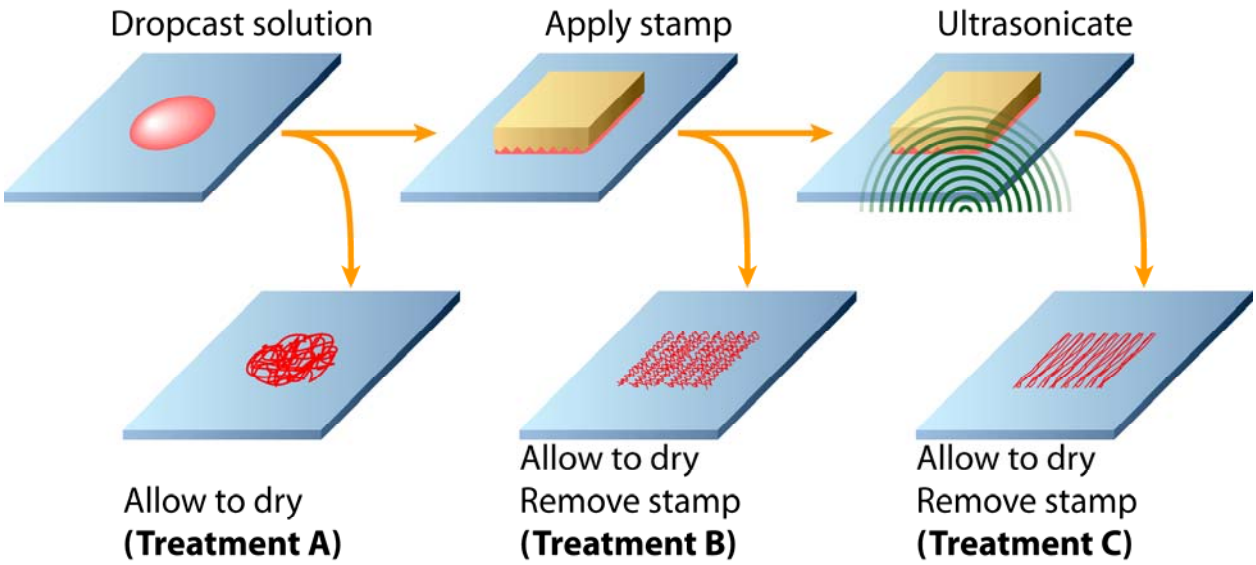

Figure 5.2. Schematic of the three treatments used to pattern the nanofibers.

5.3 Characterization of Nanofiber Structure

5.3.1 Comparison to the previously proposed structure

Figure 5.3 shows polarized transmission FTIR spectra of **1** well aligned along capillaries of 278 nm period. Table 5.1 lists the peaks of interest and their vibrational assignments. The intensities of the amide I β-sheet (1629 cm^{-1}), amide A (3292 cm^{-1}), and CH_2 symmetric stretch (2849 cm^{-1}) peaks all decreased relative to the intensity of the amide I random coil, β-turn, or alpha helix peak (1660 cm^{-1}) as the polarization of the incident beam was rotated from 0° to 90° relative to the fiber alignment direction. In some cases, the amide II (1544 cm^{-1}) and CH_2 antisymmetric stretch (2920 cm^{-1}) peaks also increased in intensity relative to the random coil peak.

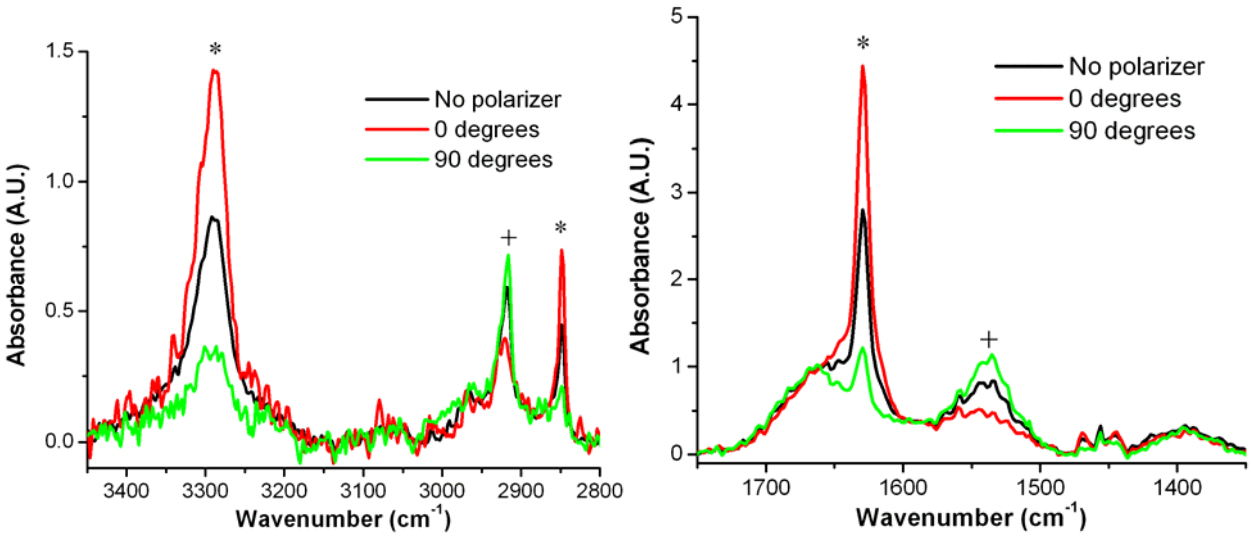

Figure 5.3. Polarized transmission FTIR spectra of nanofibers of **1** aligned in gratings of 278 nm period. Spectra are normalized to the intensity of the residual silane Si-CH_3 peak at 1261 cm^{-1}. Transition dipole moments oriented parallel (*) and perpendicular (+) to the fiber structure can be readily identified as the incident polarization is rotated from 0° to 90° relative to the alignment direction.

Polarized transmission FTIR spectra of **2** well aligned along capillaries of 416 nm are shown in Figure 5.4. The intensities of the β-sheet and amide A peaks also decrease as the incident polarization was rotated from parallel to perpendicular to the fiber alignment direction, although the difference was less pronounced than in **1**. The higher number of CH_3 groups in **2** was evident from the more intense CH_3 antisymmetric stretching peak (2964 cm^{-1}), but orientation of the CH_2 groups was minimal or non-existent as any change in the symmetric and antisymmetric stretch intensities could not be discerned from noise. Structurally, the β-sheet character of **2** appears to be greater than for **1**.

The spectroscopic data are consistent with the hypothesis that the peptide portion of the molecules assemble in β-sheet "fins" oriented mostly parallel to the long axis of the fiber. In

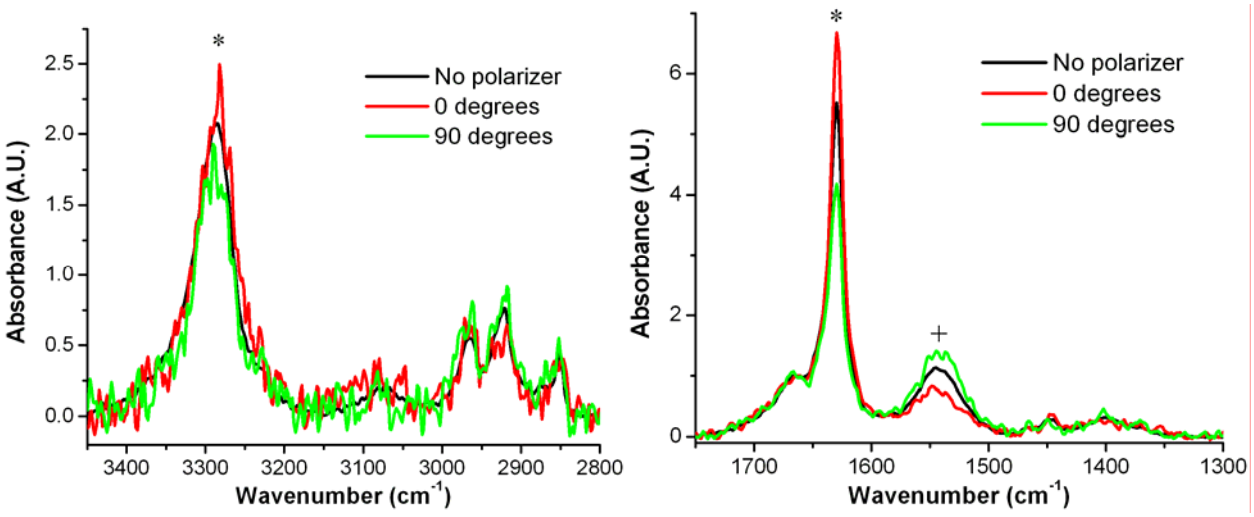

Figure 5.4. Polarized transmission FTIR spectra of nanofibers of **2** aligned in gratings of 416 nm period. Spectra are normalized to the intensity of the residual silane peak at 1261 cm^{-1}. Transition dipole moments oriented parallel (*) and perpendicular (+) to the fiber structure can be readily identified as the incident polarization is rotated from 0° to 90° relative to the alignment direction.

Table 5.1. Absorption peaks analyzed and their assignments.[311, 312]

Assignment	Description	Observed Wavenumber (cm^{-1}) for **1**	Observed Wavenumber (cm^{-1}) for **2**
Amide A	Amide N-H stretch	3292	3289
Amide B	Fermi resonance of amide A and amide II	3071	3074
$\nu_{as}(CH_3)$	CH_3 antisymmetric stretch	2963	2964
$\nu_{as}(CH_2)$	CH_2 antisymmetric stretch	2920	2923
$\nu_{s}(CH_3)$	CH_3 symmetric stretch	2866	2872
$\nu_{s}(CH_2)$	CH_2 symmetric stretch	2849	2850
Amide I	Non-β-sheet C=O stretch	~1660	1670
	β-sheet C=O stretch	1629	1630
Amide II	Amide C-N stretch and N-H bend	1544	1543

such a structure, the TDMs of both the C=O and N-H stretching bands that comprise the bulk of the amide I β-sheet and amide A peaks, respectively, would orient mostly parallel to the fiber.[255, 257, 311, 312] The intensity of the random coil peak demonstrates that much of the peptide segment, likely the head group, does not participate in this β-sheet structure. Based on this model and previously reported AFM studies,[289] we attribute the observed difference in the polarized spectra to nanofibers that have been uniaxially aligned by sonication-assisted solution embossing.

Figure 5.5 shows PM-IRRAS spectra of nanofibers of **1** and **2** patterned in grating channels of 416 nm period. There is little difference in PM-IRRAS spectra of nanofibers patterned in difference channel sizes. The sharp decrease in the β-sheet peak relative to the transmission spectra is consistent with the proposed structural model. The possibility that the β-sheets are not perfectly parallel with the nanofiber but twist instead around the nanofiber axis is difficult to rule out entirely. However, the reflectance data shows that if this twist is present it is

small and may vary with the specific peptide sequence. The fact that the TDM of the parallel β-sheet amide I vibration does not lie parallel to the plane of the β-sheet but at an angle tilted out of the plane will also contribute to the intensity of the band in the reflectance spectra and must be taken in to account.[293, 314]

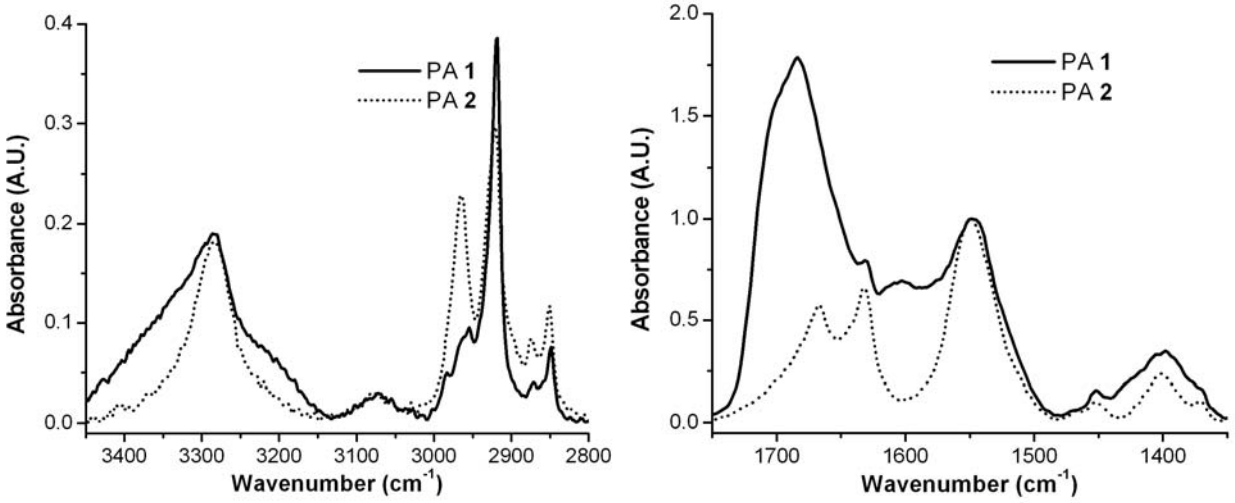

Figure 5.5. PM-IRRAS spectra of PAs **1** and **2** patterned in gratings of 416 nm period.

These spectra are consistent with previously reported data on nanofiber monolayers[255] except for the seemingly larger β-sheet peak for **2**. While the thicker multilayer films make it more likely for nanofibers of **2** to be oriented at an angle out of the plane of the substrate, that angle is expected to be very small. Also, PM-IRRAS of unpatterned films of comparable thickness do not show as large a β-sheet peak, so the difference in intensities cannot be solely due to this factor. Another possibility is that the slower evaporation rate during patterning leads to greater β-sheet character and less random coil structure. This hypothesis is supported by the fact that the random coil peak is shorter than is observed for drop cast films, making the peak at 1630 cm^{-1} seem more intense. One final possibility is that patterned nanofibers of **2** are shorter

than drop-cast ones as observed qualitatively by AFM, giving rise to a greater number of end-caps that may have some randomly oriented β-sheet structure. Consistent with this hypothesis is the fact that patterned nanofibers of **1** are longer than nanofibers of **2** and do not show as large a difference in PM-IRRAS spectra when compared to monolayer films.

Previous FTIR studies of PA fibers do not completely exclude the possibility that the perceived nanofiber substructure is due to reconstruction of the nanofiber when adsorbed to a surface.[255, 257] This data is addition evidence that the molecular structure observed is not solely a product of rearrangement on the substrate surface. Both the PM-IRRAS spectra and the polarized transmission spectra are consistent with the proposed model that the β-sheet hydrogen bonds are oriented primarily along the axis of the nanofiber. The films studied are at least 30 nm thick, the equivalent of five or more nanofiber layers, suggesting that this architecture is a property of the bulk condensed phase.

5.3.2 Vibrations perpendicular to the nanofiber

The amide II peak arises primarily from the C-N stretch and N-H bend vibrations.[311, 312] In a β-sheet structure, dipole coupling results in the TDM being oriented parallel to the axis of the peptide backbone and perpendicular to the nanofiber axis.[293, 314] Indeed, some spectra show an increase in the amide II peak as the incident polarization is rotated from parallel to perpendicular to the fiber alignment direction. This effect is not consistently seen because the peak is insensitive to secondary structure, so the polarization effect is diluted by randomly oriented vibrations of non-β-sheet structures. However, the ability to identify potential vibrations oriented perpendicular to the nanofiber is a novel aspect of this analysis.

For **1**, the $\nu_s(CH_2)$ peak is observed to decrease in intensity in both the PM-IRRAS spectra and the transmission spectra in which the beam is polarized perpendicular to the grating lines. The data are consistent with previously reported data[255] and suggest that the plane the carbon backbone of the aliphatic tail is oriented mostly parallel to the fiber axis. Ordering of the aliphatic tail is thought to be a result of both the compression of the nanofiber core under Laplace pressure and the structural constrains imposed by β-sheet ordering of the peptide segment. Arrangement of the CH_2 groups of the four glycine residues in a β-sheet configuration is not enough to generate the polarization effect observed. Orientation alone does not translate to crystallinity, however the peak location of the stretching vibration is slightly red-shifted from values reported for amorphous chains, suggesting that the aliphatic groups are tightly packed. This model also predicts that $\nu_{as}(CH_2)$ is perpendicular to the nanofiber axis. Similar to the amide II vibration, the asymmetric vibration is sometimes seen to increase in intensity when the incident beam is polarized perpendicular to the nanofiber. This polarization effect is not regularly observed because both the peak intensity and the degree of order of the CH_2 groups are weaker than the amide groups, but it would not be seen at all without alignment of the nanofibers.

5.4 Determination of Order Parameters and α_{max}

*5.4.1 Orientation parameter f_{φ} and quantifying the alignment of PA **1** nanofibers*

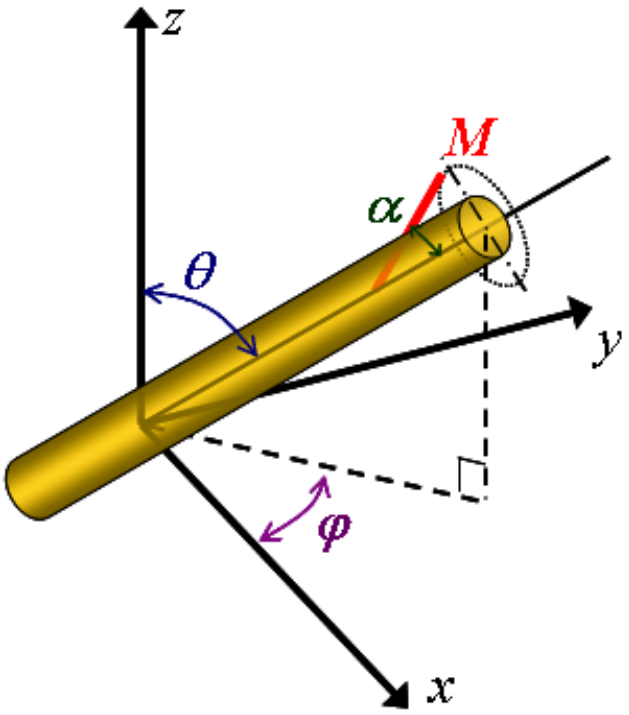

Figure 5.6. Schematic of the space coordinate system and relevant angles describing nanofiber orientation.

The tilt angle θ denotes the angle between the nanofiber long axis and the surface normal or the *z* axis. Taking the projection of the nanofiber long axis into the plane of the substrate, the azimuthal angle φ is the angle of the projection relative to the channel direction or the *x* axis. A third angle α is required to describe the orientation of the TDM relative to the nanofiber long axis. A more thorough description of the space coordinate system employed and derivation of

the equations for the orientation parameters is given in Appendix A. Briefly, Stein[315, 316] introduced two orientation parameters, f_θ and f_φ, to describe alignment in biaxially oriented films:

$$f_\theta = \frac{3\langle \cos^2 \theta \rangle - 1}{2} \tag{5.1}$$

$$f_\varphi = 2\langle \cos^2 \varphi \rangle - 1 \tag{5.2}$$

where $<\cos^2\theta>$ and $<\cos^2\varphi>$ are the mean values of $\cos^2\theta$ and $\cos^2\varphi$ for a distribution of TDMs in the film. f_φ can be thought of as a two-dimensional order parameter quantifying the in-plane alignment of directors along the channel direction. While it cannot be calculated exactly, upper and lower bounds to f_φ can be obtained from the values of the direction cosines:

$$f_{\varphi,\min} = \frac{K_x - K_y}{K_x + K_y} \tag{5.3}$$

$$f_{\varphi,\max} = \frac{K_x - K_y}{K_x + K_y - 2K_z} \tag{5.4}$$

The upper bound value is closer to the real value because it assumes that the nanofibers are lying perfectly flat against the substrate, which is not unreasonable. Additional insight into the structure of the nanofibers is also gained by calculating the maximum value of α for a given TDM from the smallest value of K_z:

$$\alpha_{\max} = \arcsin\left(\sqrt{2K_z}\right) \tag{5.5}$$

This value of α is due to a combination of tilt of the nanofiber out of the plane of the substrate, inherent tilt of the TDM out of the plane of the parallel β-sheet, twist of the β-sheet about the nanofiber axis, and disorder in the self-assembled structure.

The upper and lower bound values of the orientation parameter f_φ of the nanofibers with respect to PA, channel size, and vibration band are plotted in Figure 5.7. Table 2 lists the values obtained for the direction cosines and the value of α_{max} calculated for the amide I and $\nu_s(CH_2)$ band. Based on the β-sheet amide I vibration, fibers of **1** align well in confining channels of 833 nm, 416 nm and 278 nm period, with values of f_φ approaching 0.4 for the amide I and amide A bands. This is equivalent to having 40% of the nanofibers perfectly aligned along the *x* axis with the remainder oriented randomly in the *xy* plane. The $\nu_s(CH_2)$ band also gives sizable values of f_φ around 0.3. The maximum value of α obtained for the β-sheet amide I band is 19º, which is very close to the value calculated for a monolayer of nanofibers.[255] This observation suggests that nanofibers of **1** do not tilt far out of the plane of the substrate, at least in the 278 nm period channels. It is also more evidence that the reported self-assembled structure is a property of the bulk material.

*5.4.2 Effect of patterning on the alignment and structure of PA **2** nanofibers*

Nanofibers of **2** do not align as well as those of **1**, but do show some degree of order, yielding values of $f_\varphi > 0.14$ within channels of 416 nm period and a maximum of 30% alignment of the nanofibers. These data support qualitative observations derived from AFM images. One explanation for the observed difference is that **2** is more hydrophobic than **1,** leading to stronger interactions between fibers and kinetic trapping. While **2** appears to have greater β-sheet character than **1**, the speed of nanofiber reorientation and β-sheet formation rather than the degree of β-sheet formation is more critical for alignment. The difference in self-assembly character between **1** and **2** is highlighted by the value of $\alpha_{max} = 25º$ calculated for the β-sheet amide I vibration of nanofibers of **2**, which is significantly lower than that reported for a

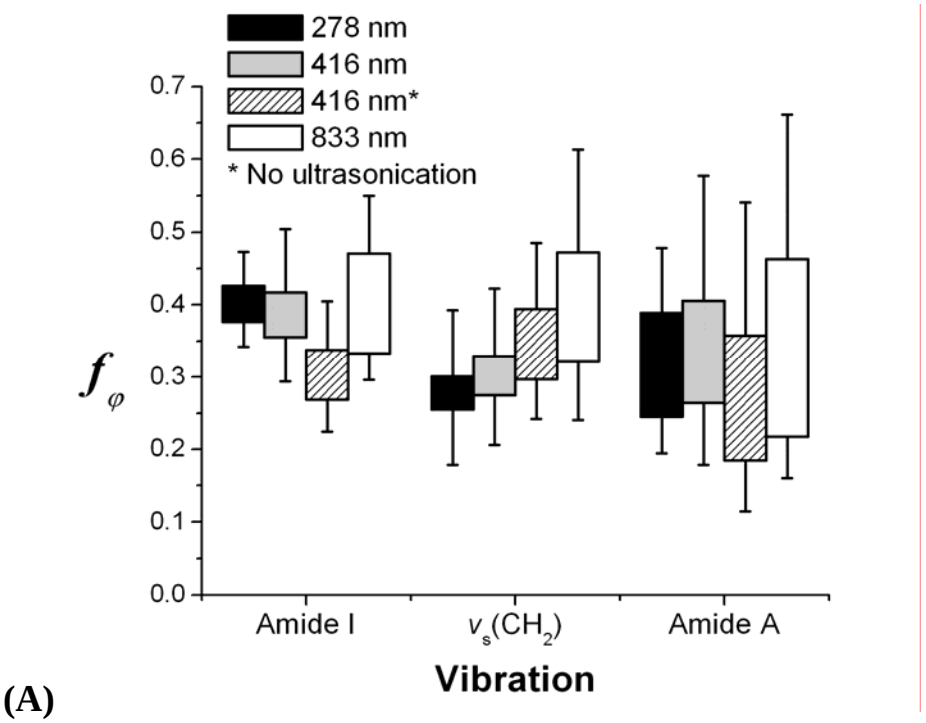

(A)

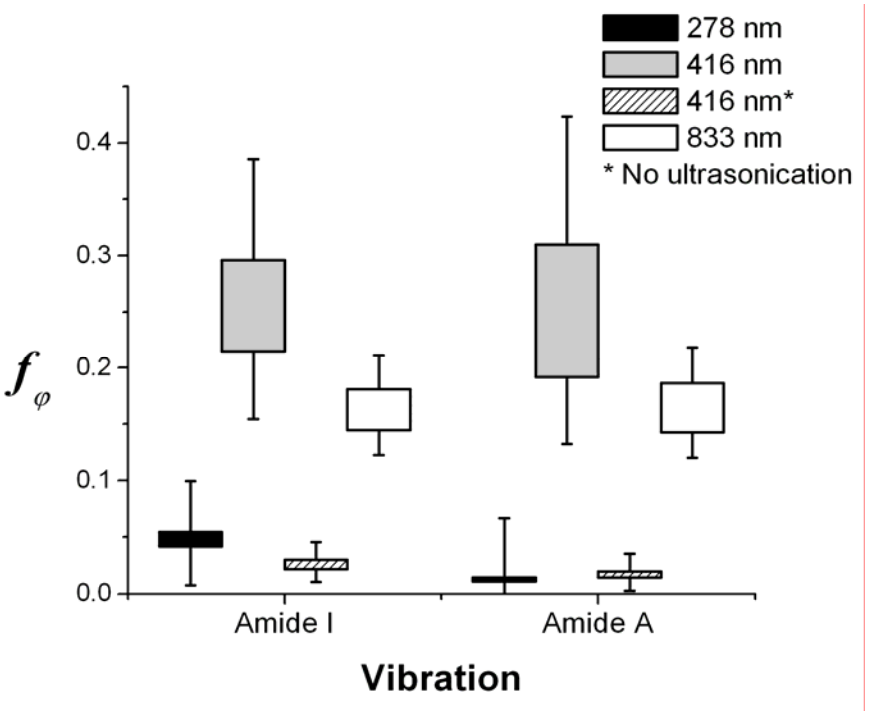

(B)

Figure 5.7. Upper and lower bound values of the orientational order parameter f_φ calculated from selected IR bands for nanofibers of (**A**) PA **1** and (**B**) PA **2** aligned in grating channels of different periodicities.

Table 5.2. Calculated direction cosines and α_{max} for TDMs of **1** in different channel sizes.

IR band	Channel period (nm)	K_x	K_y	K_z	α_{max}	α_{max} (ref 255)
Amide I	278	0.65 ± 0.03	0.29 ± 0.02	0.06 ± 0.02	19º ± 4º	20º
	416	0.63 ± 0.05	0.30 ± 0.04	0.07 ± 0.05		
	416*	0.58 ± 0.03	0.33 ± 0.03	0.09 ± 0.04		
	833	0.58 ± 0.03	0.291 ± 0.019	0.13 ± 0.04		
$\nu_s(CH_2)$	278	0.58 ± 0.05	0.35 ± 0.05	0.071 ± 0.017	22º ± 3º	25º
	416	0.59 ± 0.05	0.34 ± 0.04	0.08 ± 0.05		
	416*	0.58 ± 0.04	0.31 ± 0.03	0.11 ± 0.04		
	833	0.57 ± 0.05	0.29 ± 0.05	0.14 ± 0.04		
Amide A	278	0.53 ± 0.03	0.32 ± 0.03	0.16 ± 0.03		
	416	0.54 ± 0.06	0.31 ± 0.05	0.15 ± 0.08		
	416*	0.48 ± 0.05	0.33 ± 0.04	0.19 ± 0.07		
	833	0.48 ± 0.04	0.31 ± 0.03	0.21 ± 0.06		

* No ultrasonication

nanofiber monolayer.[255] One explanation for this discrepancy is that the slower evaporation rate due to the patterning method results in nanofibers of **2** with greater β-sheet character and more ordered β-sheets than those deposited by Langmuir-Blodgett techniques. This argument was also put forth earlier when attempting to explain the difference in PM-IRRAS spectra.

The values of α_{max} offer an indication of the degree of β-sheet twist in the nanofibers. The twist angle cannot exceed α_{max} and is likely much lower. That is because the calculated value of α_{max} is due to a combination of four factors: disorder in the β-sheet arrangment, tilt of

Table 5.3. Calculated direction cosines and α_{max} for TDMs of **2** in different channel sizes.

IR band	Channel period (nm)	K_x	K_y	K_z	α_{max}	α_{max} (ref 255)
Amide I	278	0.47 ± 0.02	0.43 ± 0.02	0.10 ± 0.04		
	416	0.53 ± 0.04	0.35 ± 0.04	0.12 ± 0.03		
	416*	0.450 ± 0.007	0.430 ± 0.007	0.120 ± 0.010		
	833	0.521 ± 0.016	0.389 ± 0.013	0.09 ± 0.02	25º ± 4º	34º
Amide A	278	0.45 ± 0.03	0.44 ± 0.02	0.11 ± 0.04		
	416	0.50 ± 0.04	0.34 ± 0.03	0.16 ± 0.05		
	416*	0.450 ± 0.008	0.437 ± 0.007	0.112 ± 0.009		
	833	0.512 ± 0.016	0.384 ± 0.013	0.10 ± 0.02		

* No ultrasonication

the nanofiber out of the *xy* plane, twist of the β-sheet, and tilt of the TDM out of the plane of the β-sheet. The average tilt of the nanofiber is not expected to be much more than a few degrees, a minimal contribution to α_{max}. Assuming cylindrical symmetry, disorder in the β-sheet arrangement cannot be distinguished from a regular twist, but it is also speculated to be minimal given the slower evaporation rate. Tilt of the TDM out of the β-sheet plane varies slightly depending on the peptide sequence but is generally 5 ° to 10 °. If there is limited disorder in the b-sheet arrangement, the twist angle would thus be 10 ° to 15 °. For antiparallel β-sheet structures, dipole coupling results in splitting of the amide I band into in-plane and out-of-plane components, eliminating the tilt of the TDM at 1630cm^{-1}.[293, 314] Addition of "reverse" PAs[116, 254] may convert the parallel β-sheet to an antiparallel β-sheet and allow for a more precise determination of the degree of twist.

5.4.3 Effect of channel width and ultrasonication on alignment

Spectral data show no significant difference in alignment between nanofibers of **1** aligned in any of the three channel widths. Conversely, spectral data of **2** show the best alignment of the nanofibers in the 416 nm period channels, but almost negligible alignment in the smaller channels. This observation is corroborated by AFM images[289] and suggests a lower bound to the length scale in which the supramolecular assemblies prefer to align under confinement while yet having the mobility to do so. **2** is more hydrophobic than **1** and may thus interact more strongly with the PDMS surface of the stamp, hindering the ability of nanofibers of **2** to reorient at high degrees of confinement. The alignment in the 833 nm channels appears to be less than in the 416 nm channels, although not to a significant degree. The order parameter is expected to drop continuously as the size of the channels is increased further. However, this point cannot be definitively proven within the range of channel widths studied here. The fact that alignment of both **1** and **2** can be observed within channels approaching 833 nm in period and *ca*. 700 nm in width suggests that the method may be effective even for micron scale channels. Achieving alignment in larger channels is desirable because the pattern masters can then be made by photolithography rather than electron-beam lithography or interference lithography.

Inclusion of the ultrasonication step during patterning appears to have minimal impact on the degree of order in nanofibers of **1**. There is only a small improvement in the absorption anisotropy when the ultrasonication step is added. In contrast, without ultrasonication there is effectively no alignment of nanofibers of **2**. The extra energy imparted by mechanical agitation appears to drive the nanofibers of **2** to find a more stable aligned state. PA **1** readily finds the ordered state without the aid of ultrasonication possibly because it is more water soluble and tends to organize in a more ordered liquid crystalline phase. Ultrasonication can speed up

reorganization of the nanofibers, but it cannot force them to align more than is energetically favorable. The insignificant difference with and without the extra patterning step may mean that nanofibers of **1** are already near their optimal degree of alignment at this temperature. However, there is a chance that nanofibers of **2** have yet to reach an energy minimum in these samples, and alignment may be improved further by adjusting the parameters of the patterning method. Ideally, if the alignment can be optimized and the scattering contrast in the material increased, this technique could be used to make aligned samples suitable for study by x-ray diffraction.

5.4.4 f_φ derived from AFM images and discussion of the validity of the calculated values

Some limitations of using such a simplified spectroscopic model to determine molecular structure was briefly discussed in Section 2.5.5. With respect to the PA nanofibers, no dispersion of the spectral line shape is observed likely due to the lack of significant crystallinity. The birefringence of the oriented films will affect the spectra, possibly resulting in a reduction of the measured orientation parameter assuming that the optic axis is aligned parallel to the nanofiber axis. There is also the potential for scattering of the incident radiation by the topological grating pattern, however, this effect appears to be negligible as unpolaraized spectra of unpatterned and patterned films are almost identical.

Given the concerns regarding the validity of the spectroscopic model, it might be useful to compare the values of the orientation parameter calculated from the IR data with those that may be collected from analysis of AFM images. Values of f_φ obtained from selected AFM images of aligned PA nanofibers are listed in Table 5.4. The two analysis methods outlined in Section 5.2.3, tracing of individual nanofibers and integration of the FFT, were each performed on the same images in order to compare their respective merits. FFT integration was

implemented on a total image area of 8 μm^2. Manual tracing of individual fibers was limited to 2 μm^2 of that image area due to time constraints. Even within that limited area, the values of f_φ obtained by this method are comparable to those calculated from the IR spectra. While faster, integration of the FFT is not as accurate because scanning artifacts in the AFM images severely impact the calculated numbers.

Table 5.4. Values of f_φ obtained by two methods of image analysis.

PA	Channel period (nm)	f_φ by line tracing	f_φ from FFT
1	278	0.75	0.42
	416	0.50	0.19
2	278	0.04	0.11
	416	0.27	0.33
	416*	0.05	0.13

* No ultrasonication

While the accuracy of the tracing method is limited by the minimal sampling area, the inability to count nanofibers buried underneather other nanofibers, and the possibility of systematic error, the values given in Table 5.4 do suggest that the spectroscopic analysis is not invalid. At the very least, the trends suggested by the IR data are confirmed, including the differences between PAs **1** and **2** and the positive impact of ultrasonication.

5.5 Effect of nanofiber alignment on cellular morphology

5.5.1 Results with murine neural progenitor cells

Alignment of cells and processes was observed in treatment **C** of PA **2** and not in any other condition. Representative optical micrographs are shown in Figure 5.8. In addition, the blinded experimenter correctly deduced the orientation of the nanofibers along the direction of the grating lines based on the orientation of the cells. The cells adhered and survived but displayed no noticeable alignment on **A** and **B** samples of PA **2** and on all samples of laminin-1. The fact that no cellular alignment was seen on patterned but non-aligned substrates of PA **2** rules out the larger surface topology as a significant factor. This result also suggests that the cells can detect and respond to even modest alignment of the nanofibers. Cell survival was poor on plain glass and all samples of PA **1**, whereas on samples of laminin-1 and PA **2** the cells adhered to the surface and survived. This observation demonstrates that the sequence of the peptide coating the surface is important for cell adhesion and viability.

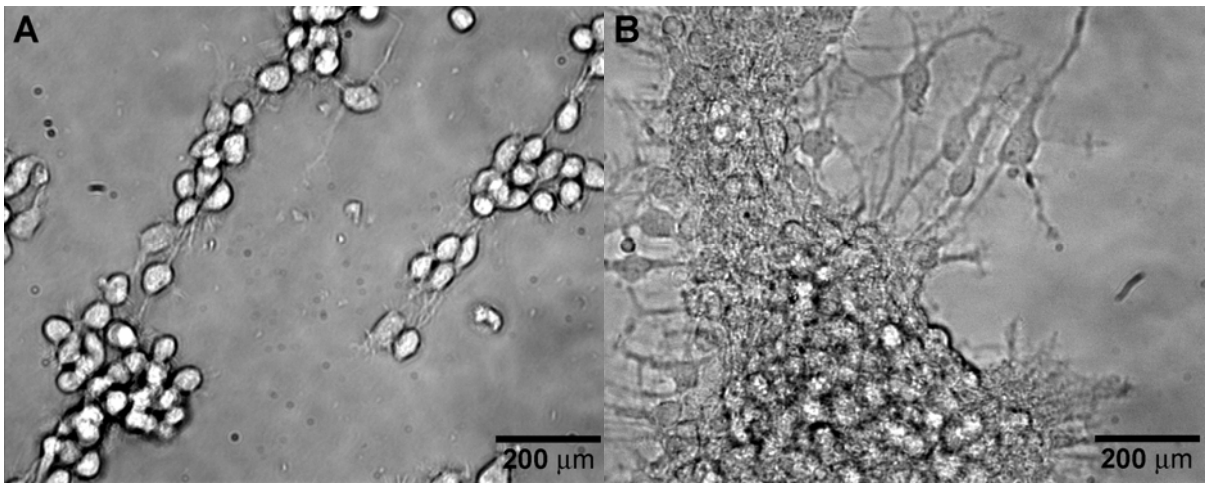

Figure 5.8. Optical micrographs of NPCs cultured on substrates of (**A**) aligned and (**B**) non-aligned nanofibers of PA **1**.

Perhaps more importantly, the fact that no cellular alignment was seen on control substrates patterned with laminin-1 protein suggests that nanofiber structure itself is not only seen by the cell but can exert significant influence on cell behavior. Clustering and patterning of receptors on the cell surface have been shown to be important in determining aspects of cell adhesion, structure, and mobility.[317, 318] We hypothesize that the IKVAV epitopes displayed on the nanofiber surfaces bind to receptors on the cell surface, and the nanofiber structure forces the receptors to cluster and arrange themselves in a specific manner. Receptor clustering in turn affects neurite outgrowth and leads to changes in the shape of the cytoskeleton.

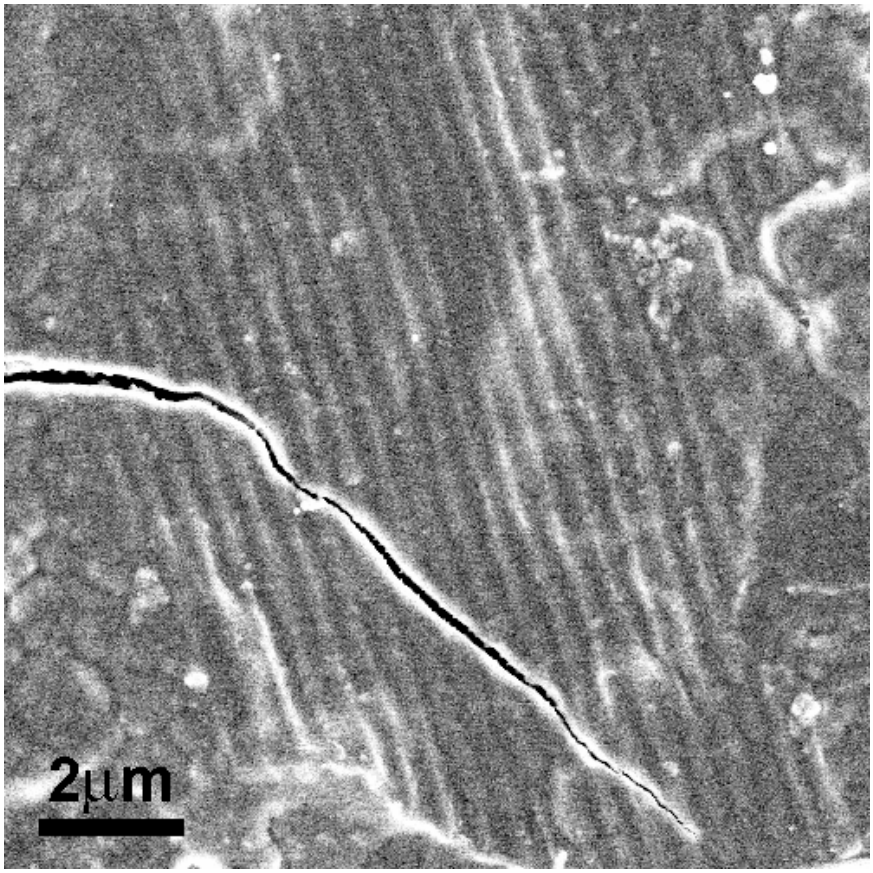

Figure 5.9. SEM micrograph of a patterned sample of PA **1** recovered and lyophilized after 7 days in cell culture showing persistence of the topographical grating pattern.

5.5.2 Resilience of the substrate pattern and the alignment effect

While it is possible that the nanofibers reorganize slightly when immersed in media, the previous results suggest that some semblance of both the nanofiber structure and alignment are retained. In fact, the patterns are surprisingly robust in physiological media. Figure 5.9 shows SEM images of samples that were recovered and lyophilized after seven days of cell culture. The patterned topology is seen to persist for the duration of the experiment. Whether the nanofibers remain or are replaced by cellular proteins is still under investigation.

As might be expected, the positive effect of the aligned nanofiber substrates is very sensitive. No cell alignment was observed on samples that were not dipped briefly in ethanol. Gently rinsing the patterned nanofiber substrates in ethanol generally leads to sharper AFM images as shown in Figure 5.10. This step is thought to remove much of the silane and siloxane residue deposited by the PDMS stamp. While the cells still adhere to the non-rinsed samples, the PDMS residue likely interferes with the ability of the cells to sense the nanofiber structure.

5.6 Summary and Outlook

FTIR spectroscopy proves that the orientation of one-dimensional supramolecular assemblies can be controlled by sonication-assisted solution embossing, extending molecular order to macroscopic length scales. PA nanofibers were aligned within microchannels approaching ca. 700 nm in width, suggesting that this technique might be effective up to the micrometer length scale where patterned masters could be easily fabricated by photolithography. In the cases where nanofiber mobility is hindered by strong interfiber interactions, ultrasonic agitation helps drive the system to a more equilibrium aligned configuration, making this a viable technique for aligning a wide range of different PA systems. The spectroscopic data also

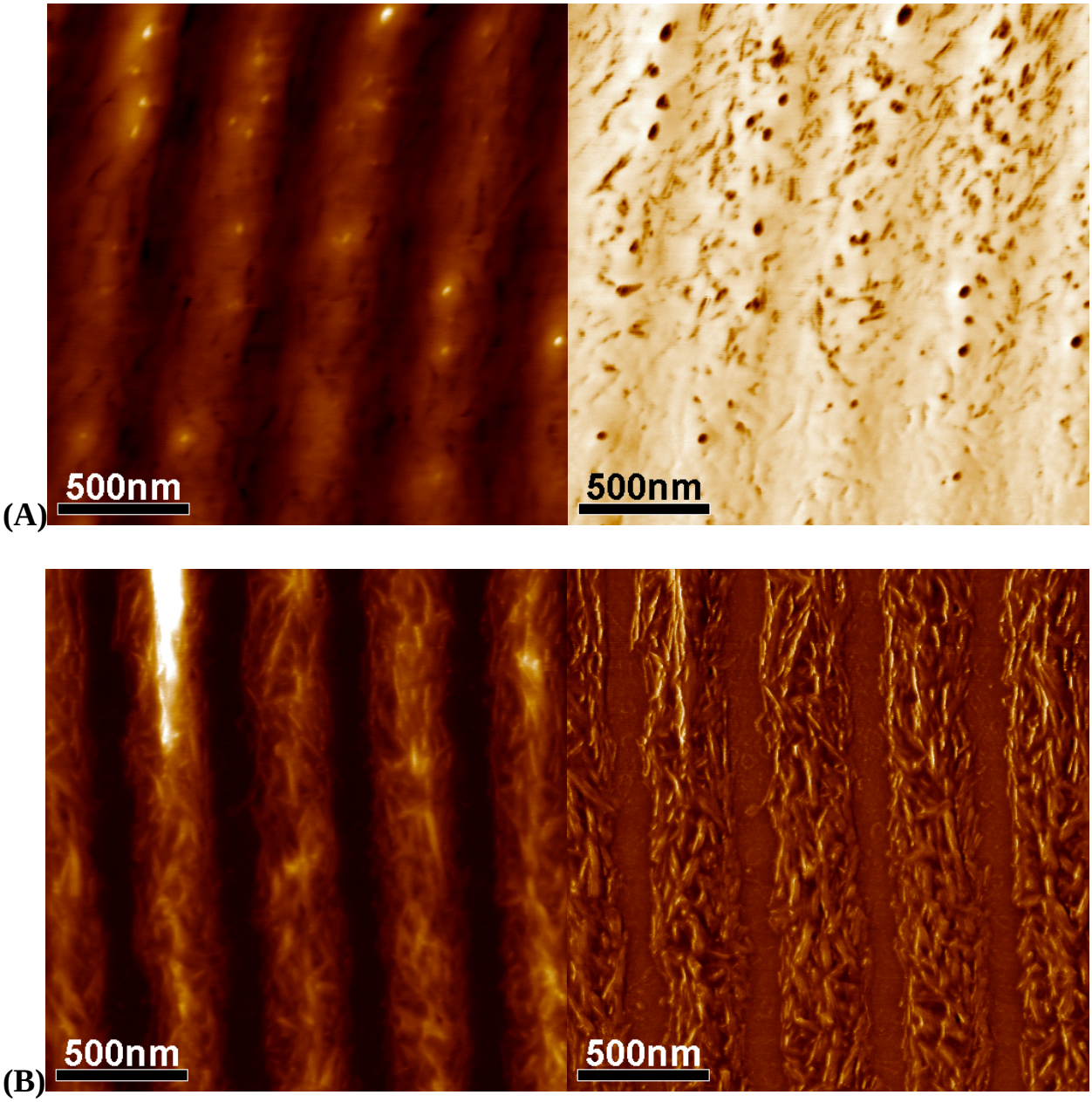

Figure 5.10. AFM height and phase images of PA nanofibers patterned by sonication-assisted solution embossing, (**A**) before and (**B**) after brief immersion in ethanol.

support the structural model of the nanofibers being composed of β-sheet fins oriented mostly parallel to the nanofiber. Reducing the rate of solvent evaporation may increase the degree of internal β-sheet ordering in the nanofibers. The proposed structure is a property of the bulk condensed phase and not simply a result of reconstruction on the substrate surface.

We demonstrate preferential orientation of the cell bodies and processes of murine NPC cultures on substrates of aligned, patterned IKVAV-bearing nanofibers and present preliminary evidence that suggests the nanoscale orientation of the fibers may play a role as well as the epitope itself. The effect is noticeable even if the alignment of the nanofibers is modest, and the patterned substrate topology persists through seven days of cell culture. These results are also an important demonstration of how nanometer-scale structure can influence cell behavior and may have significant implications for biomedical applications including spinal cord injury repair.

CHAPTER SIX

Morphological Study of Thin Films of Thiophene-Based Amphiphiles

Chapter 6: Morphological Study of Thin Films of Thiophene-Based Amphiphiles

6.1 Introduction

In recent years, environmental and political concerns have fueled intense interest in the development of alternative sources of energy, including solar power.[319] However, in order to make solar energy economically viable, significant gains must be made in terms of efficiency or affordability. Organic and hybrid photovoltaic materials are of interest in this regard because they are often easily processed, tunable to specific wavelengths, and can be deposited on a variety of substrates.[320-322] Unfortunately, their efficiencies as of yet are too low to warrant widespread adoption.[323] Self-assembly offers one possible strategy for improving the energy conversion properties in these systems. Ideally, the material would self-assemble on the nanometer scale into an ordered mesostructure of separate *p*- and *n*-type phases. Such a structure would exhibit an extraordinary amount of available interface for exciton splitting, and that interface would be within the exciton diffusion length, 5 to 10nm, of most of the bulk material.[324]

On their own, most conjugated polymers are insoluble and must be functionalized with solubilizing groups in order for them to be processed. However, functionalization results in a disruption of conjugation and a reduction in conductivity.[325, 326] Another strategy is to synthesize amphiphilic molecules consisting of blocks of conjugated oligomers with solubilizing groups at either end.[99, 105, 109, 327, 328] The conjugated blocks preferentially associate with each other through π–π interactions, creating a path for charge conduction and resulting in self-assembly of the molecules into a variety of nanostructures. Our group recently reported the synthesis and self-assembly of amphiphilic molecules based on oligo(*p*-phenylene vinylene).[113, 114] These molecules could be used to template the mineralization of mesoporous silica and exhibited

remarkable energy transfer properties. While self-assembly strategies can lead to the discovery of novel materials that spontaneously form nanostructured phases, there remains no guarantee that the phase will exhibit structural order or a net orientation at macroscopic scales. With respect to photovoltaic systems, photoexcited charge pairs must not only be separated, but the individual charges must be able to travel to opposite electrodes to be collected. Optimal charge conduction requires continuous pathways that connect to either electrode.[217, 320] This condition is automatically satisfied if the system self-assembles into a bicontinuous phase, but such phases are rare and often difficult to realize. Cylindrical and lamellar phases are more common, but the order and orientation of these phases must be controlled in order to generate continuous charge-conduction pathways to either electrode.

Micrometer- and nanometer-scale patterning of surface interactions or of the active material itself is one possible method for controlling the orientation and order of mesostructured photovoltaic materials. It is conceivable that the morphology of the active material immediately adjacent to a surface could be altered by careful control of the chemical nature or topology of the surface, and the alteration of structure may extend to some degree into the bulk. Spatial confinement may also induce a preferred orientation in the mesophase and is most often achieved by physical patterning of the active material itself. Patterning on the length scales similar to the wavelengths of the incident radiation can also lead to coherent scattering of an enhancement of absorption through photon trapping.[283, 329]

Our laboratory has since synthesized a number of variants on the original phenylene vinylene molecule. One particular variant replaces the phenylene vinylene block with an oligo-thiophene block and uses a long poly(ethylene glycol) (PEG) chain to make the molecule amphiphilic and water-soluble. X-ray studies suggest that the molecule assembles upon

evaporation of solvent into a lamellar phase with the hydrophilic PEG segments segregated from the hydrophobic blocks. This molecule is also of interest for the development of hybrid photovoltaic systems where inorganic, semiconducting materials could be infiltrated or mineralized within the PEG phase. While thick films of this material are birefringent, suggesting orientation of the lamellae perpendicular to the substrate, the lamellae nearest the surface are likely oriented parallel, forming a barrier to direct charge transport to the electrode. Thus, it is desirable to find a method of coaxing the molecules to orient themselves parallel to the surface thereby nucleating lamellae aligned normal to the substrate.

One possible strategy for achieving normal orientation of the lamellae is to pattern the surface with alternating lines of hydrophobic and hydrophilic chemical functionalities. Similar strategies have been successfully applied to align block copolymer phases. A very simple method for creating such surface patterns is through friction transfer of polytetrafluoroethylene (PTFE).[176] Briefly, a solid PTFE rod or block is dragged across a heated substrate, resulting in deposition of aligned, nanometer-scale polymer fibers. These substrates have been previously used to control molecular orientation in films of liquid crystals[330] and conjugated oligomers.[331, 332] While the spacing between the fibers is not regular, lithographically defining a periodic pattern on similar length scales requires significantly greater effort and resources.

In this chapter, we study the morphology of substrate-supported thin films of the thiophene-PEG amphiphilic molecule. Periodic surface textures are observed when the thickness of the film is reduced below the equilibrium bilayer spacing. We hypothesize that the textures are a result of incomplete surface coverage disrupting the association of the hydrophobic blocks. The periodicity of the textures is very consistent, suggesting that they are metastable states of assembly. Preliminary experiments on deposition of thiophene-PEG films on friction-transferred

PTFE show displacement of the PTFE fibers and no noticeable effect on the orientation of whole lamellae. However, the method does show some promise in being able to control order of the sub-bilayer film textures.

6.2 Materials and Methods

6.2.1 Synthesis

The chemical structure of molecule **6.1** and a schematic of the reaction steps required are given in Figure 6.1. Low temperature synthesis of anatase TiO_2 nanorods was accomplished following a procedure reported by Cozzoli et al.[333]

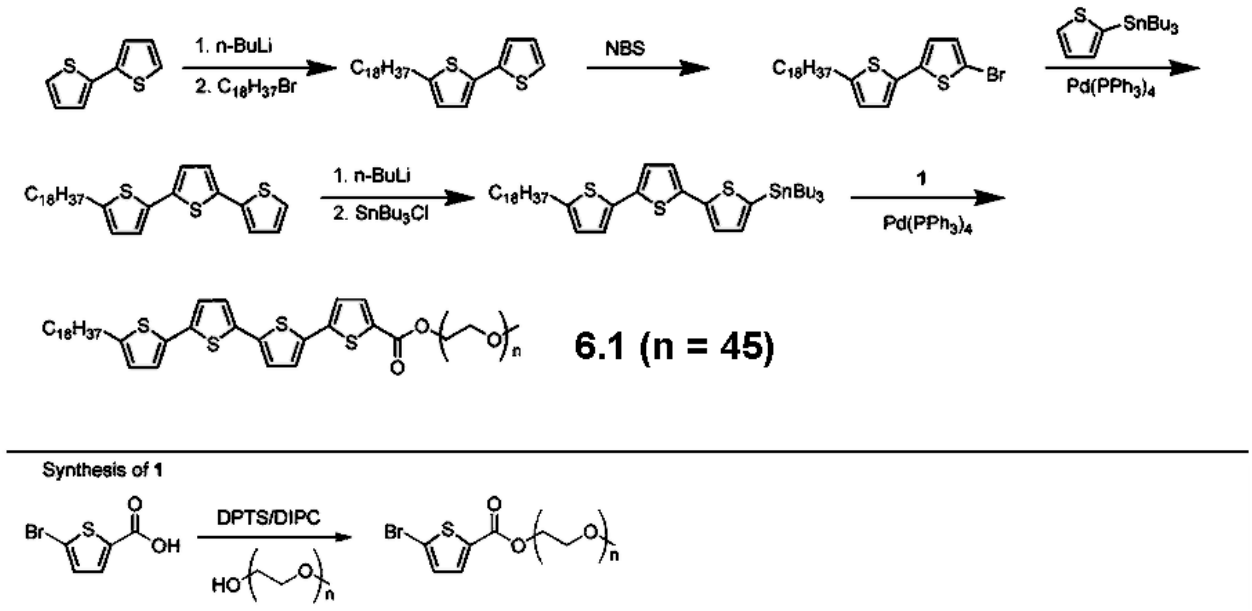

Figure 6.1. Synthetic scheme for molecule 6.1 (courtesy of David Stone).

6.2.2 Material characterization

SAXS spectra were collected on small amounts of **6.1** in dry form and concentrated aqueous gels. The material is contained in a polycarbonate holder and diffraction was performed in transmission geometry using a Rigaku CuKa source (λ = 1.542 Å, 30 kV, 17 mA) and a 2D Bruker CCD detector. The 2θ scale was calibrated with silver behenate, and the spectra were collected for 2000 sec. The baseline was substracted and the peaks fit using a mixed Gaussian-Lorentzian fitting algorithm. DSC was performed to determine phase transitions of the material. At least 5 mg of **6.1** was hermetically sealed in aluminum pans, and samples were cycled at 5 °C/min using a TA Instruments 2920 DSC. Transition temperatures were determined from the second heating cycle. Films of 6.1 deposited on glass substrates were examined between crossed polarizers on a Leitz Laborlux 12POL polarizing microscope. POM images were captured on a 35mm film camera. The samples were imaged while heated on a Linkam THM 600 thermostatic heating stage to confirm the liquid crystalline phase transitions suggested by DSC.

6.2.3 Film patterning

Parallel fibers of PTFE were deposited on piranha-cleaned glass by a friction-transfer method.[176] A piece of microscope slide glass wrapped in Teflon tape was used as a source. The substrate was placed on a hotplate at 200 °C and the Teflon source was hand-drawn across the the surface with a force of *ca.* 10 N and speed of ca. 1 mm/sec. Thin films of **6.1** were deposited by spin-coating from a 0.3 wt % solution at 3000 rpm. The samples were annealed at room temperature in a saturated chloroform atmosphere for 4 to 12 hrs by suspending them above a pool of solvent within a covered crystallization dish.

Solution embossing was performed following a procedure similar to that given in section 4.2.5. Briefly, a 4 uL drop of 1.5 wt % **6.1** in ethanol solution is dropped onto a piranha-cleaned glass substrate. A PDMS stamp with a 2400 lines/mm diffraction grating relief is brought down on the drop of solution. The sample is allowed to dry for a day before the stamp is removed.

Thick films of **6.1** could also be patterned by a related technique termed hot embossing. In this case, a 170 nm thick film is spin-coated onto a substrate from 1.5 wt % solution in ethanol at 750 rpm. The diffraction grating-patterned PDMS stamp is brought in contact with the film and a load of 20 g/cm2 is applied. The film is then softened by heating to 60 °C under nitrogen atmosphere, and the film is imprinted with the PDMS stamp topology.

6.2.4 Characterization of film thickness and morphology

AFM images were aquired on a JEOL 5200 scanning probe microscope operating in tapping mode. Applied Nanostructures ACT silicon cantilevers (300 kHz, 40 N/m) were used for AFM imaging. Heights of thicker films were determined using a Tencor P10 profilometer with a 2 μm tip radius to measure the depth of scratches made in the film.

6.2.5 Characterization of optical properties

Absorption spectra of films and solutions of **6.1** were collected using a Cary 500 UV/VIS/NIR spectrophotometer (Varian, Inc.) operating in double beam mode allowing for simultaneous subtraction of the absorption of a reference sample. Fluorescence spectra of films of **6.1** were measured using a Horiba Jobin-Yvon Nanolog-3 fluorimeter with a double excitation-side and a single emission-side monochromator and a liquid nitrogen cooled InGaAs detector.

6.3 Characterization of thiophene-PEG films

6.3.1 Material characterization

SAXS of molecule **6.1** in the dry form suggests that the molecule organizes into a lamellar phase with a bilayer spacing of 13.0 nm. The fully extended length of the molecule is 21 nm with the PEG block being 17 nm. The d-spacing suggests that the molecule is in a partially extended state with significant interdigitation or folding of the PEG segment. DSC shows transitions at 50 °C and 85 °C with a loss of birefringence of the film at the lower transition temperature. It is believed that this transition originates from the melting of the PEG block and results in a phase that is either homeotropically aligned or mostly disordered with some aggregation of the thiophene blocks. The higher transition temperature is likely due to dissociation into a completely isotropic phase. POM of thick films of **6.1** are given in Figure 6.2 and show birefringent patterns indicative of spherulites, which suggests that the long PEG segment dominates the film morphology. The material is seen by UV-vis measurements to

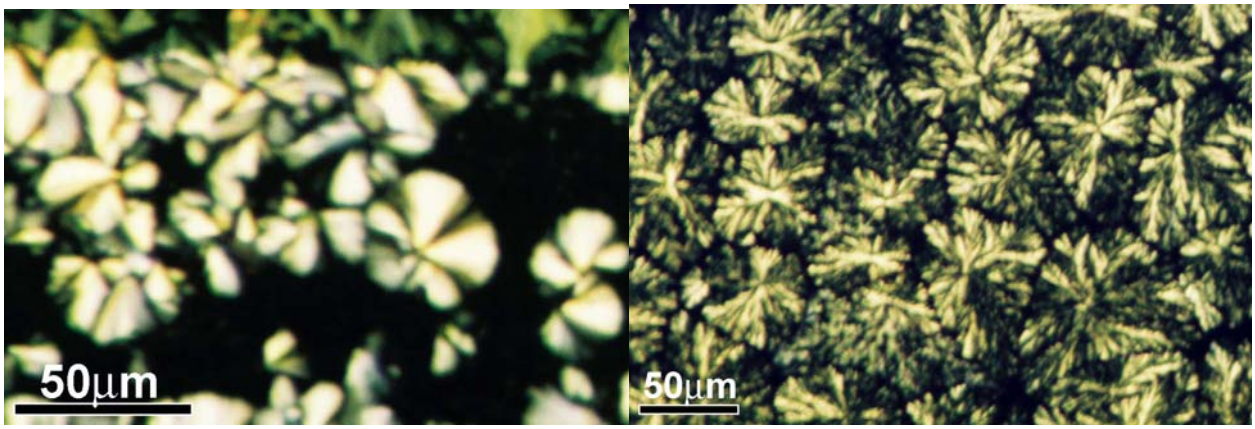

Figure 6.2. POM images of thick films of **6.1** showing radial patterns of birefringence suggestive of spherulitic structures. These structures grow larger and more disordered upon annealing at room temperature under saturated solvent atmosphere (right image).

exhibit a broad absorption peak around 377 nm as a gel in water, and 415 nm dissolved in THF. The corresponding fluorescence emission peaks in water and THF are 545 and 510 nm, respectively. The blue shift in absorbance and red shift in emission indicate that the thiophenes form H-aggregates (stacks) in water.[334]

6.3.2 Thin film morphology

Thin films of molecule 6.1 spin-coated from 1.5 wt% solution out of ethanol at 3000 rpm appear to be mostly featureless. Layer steps are observed that are 12.4 ± 1.4 nm in height, close to the *d*-spacing observed in SAXS. In some cases, a faint texture may be seen on the surface of the layers, but it is difficult to deconvolute from imaging artifacts. This is especially true given that the films are very soft and can be indented by the cantilever tip if the reference amplitude is set too low.

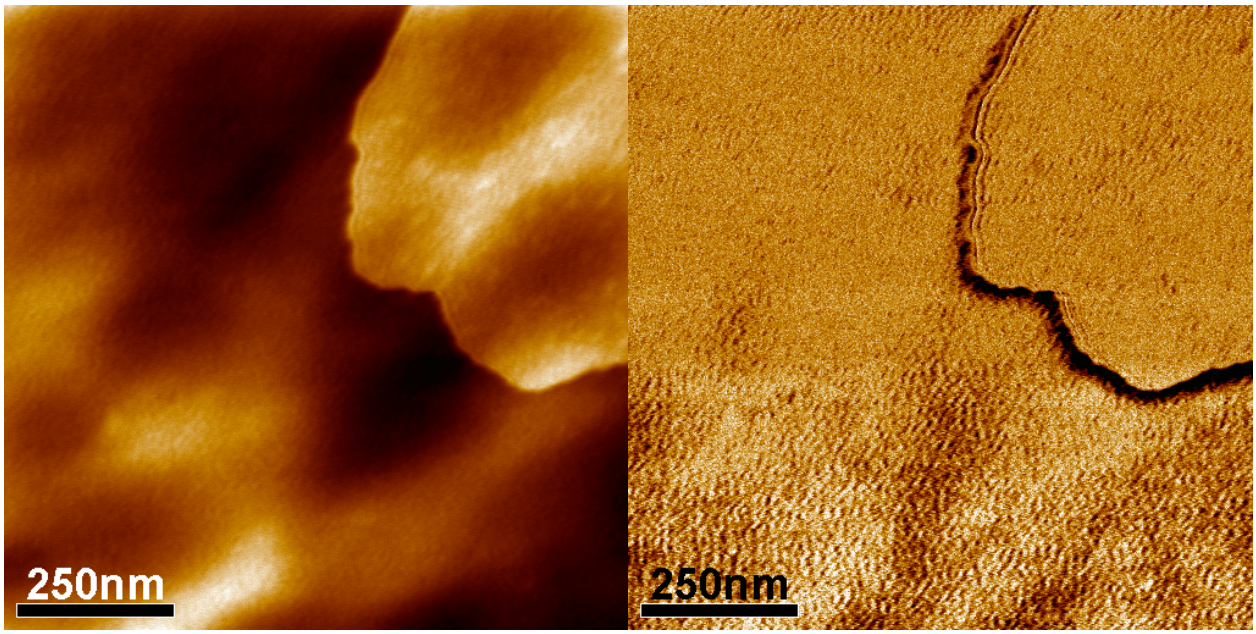

Figure 6.3. AFM height and phase contrast images of a film of **6.1** showing a lamellar step of 12.4 ± 1.4 nm and a surface texture possibly indicative of an underlying molecular structure.

When the material is spin-coated at lower concentrations of 0.3 to 0.5 wt % at 3000 rpm, the films obtained are ca. 10 nm thick on average. After annealing the films at room temperature in a saturated chloroform atmosphere, a variety of different surface textures are visible. The dotted textures shown in Figure 6.4 appear to have a height contrast of 1 nm and a lateral periodicity of 18 nm. While mostly disordered, there does appear to be some very short range hexagonal order in the placement of the dot structures with domain sizes on the order of 100 nm. In some areas, the dotted texture appears to evolve into a more striped morphology shown in Figure 6.5. Indeed, some AFM images show the elongation and fusion of dots while others show strip structures breaking into shorter segments. The striped textures have a similar height contrast and periodicity as the dotted textures. In all samples, some areas with little or

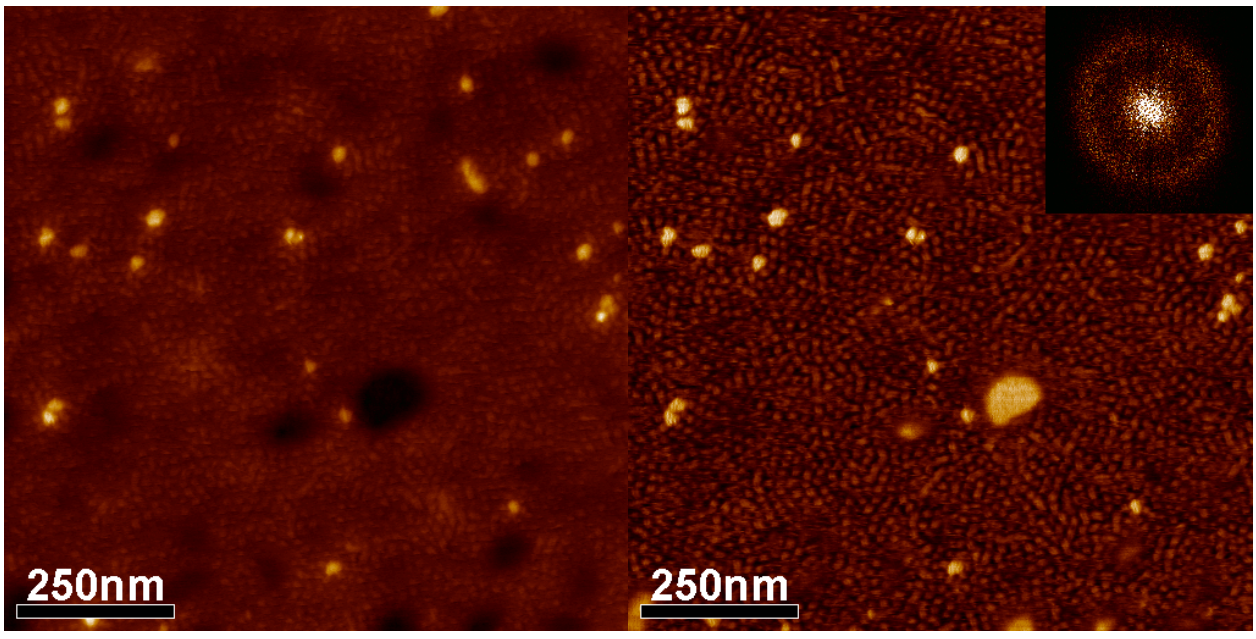

Figure 6.4. AFM height and phase images of a thin film of **6.1** showing a dotted surface texture. Assuming the "hole" in the middle of the height image reaches the underlying substrate, the thickness of the film is *ca.* 5 nm. FFT (inset) of the phase image shows that the pattern is periodic with a characteristic period of 18 nm.

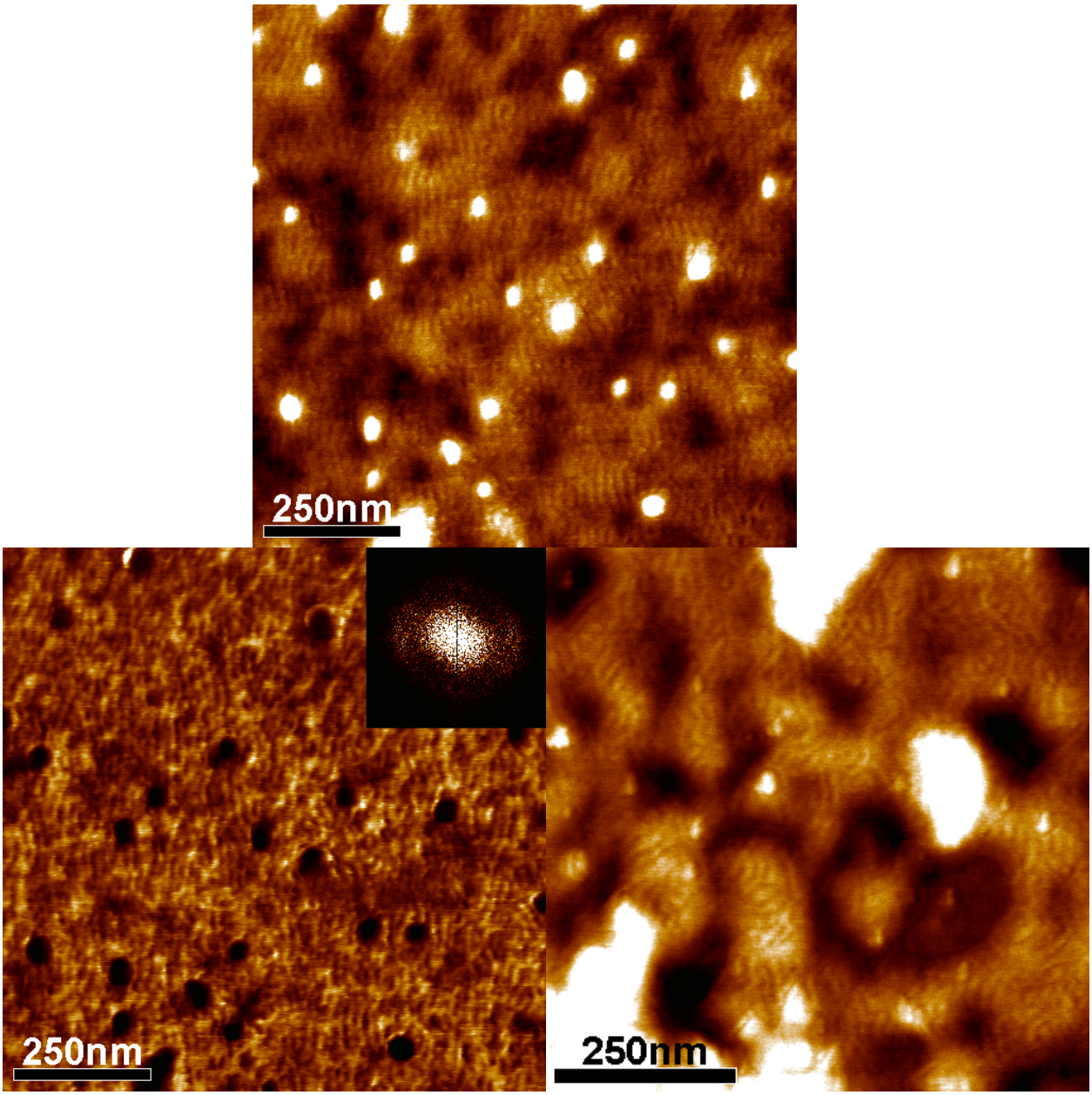

Figure 6.5. AFM height and phase images of thin films of **6.1** showing a striped surface texture. The film thickness is *ca.* 8 nm. The striped texture appears to evolve from a coalescence of the dotted texture observed earlier. FFT (inset) of the phase image shows that the 18 nm periodicity in the texture remains.

no surface structure are also observed. The film thickness in these areas is often greater than that in the textured areas.

Partial dewetting of the film from the substrate occasionally allows us to determine the localized film thickness. Areas with the hexagonal texture are also areas where the film is the thinnest, *ca.* 4 – 5 nm. The striped textures are usually observed with film heights of *ca.* 7 – 8 nm. Areas the film with little or no texture are *ca.* 10 – 14 nm thick, closest to the original *d*-spacing. This observation leads us to believe that the textures are a result of differences in film thickness and area density of molecules that arise upon solvent annealing. Effects of thin film confinement on block copolymer structure have been observed before by Knoll and coworkers.[216] Confinement of compound **6.1** into a film 10 nm thick is likely to be unstable given its equilibrium *d*-spacing of 13 nm. Upon annealing by solvent vapor, the material is allowed to migrate and partially dewets from some areas, resulting in portions of the film that are closer to the equilibrium thickness of 13 nm. This mass transport also results in some areas of the substrate that are not coated or covered with only a thin layer of molecules. In these areas, there are not enough molecules to assemble into a complete lamellar bilayer. The thiophene and alkyl segements still prefer to associate together, so they aggregate into smaller, individual structures. In the thinnest areas, the structures they may form are limited to zero-dimensional islands, but as the area density of molecules increases, the aggregate structures become larger, evolving first into stripes and then complete layers.

6.3.3 Theory of thin film structure

The periodicity and thickness of the textures is very consistent between samples, suggesting that this may be a metastable state. As a first approximation, we may imagine the PEG segments as polymer brushes end-grafted to a thiophene "substrate." In the condensed

phase at lower grafting densities, the polymer brush behaves as ideal chains, giving a brush thickness of

$$d_{ideal} = l_k N_k^{1/2} \qquad (6.1)$$

where l_k is the Kuhn length (the length of the chain that may be modeled as being a single, freely-jointed segment) and N_k is the number of Kuhn segments in the chain.[335] The Kuhn length is equal to twice the persistence length in semiflexible polymers, and using 0.38 nm as the persistence length of PEG[336] gives a value for d_{ideal} of 3.6 nm. This value matches reasonably to the observed thickness of the films that display the dotted textures. While the conformation of the PEG segment is unknown in these textured films, it is suspected that the chains are amorphous and not crystallized, at least in the case of the dotted patterns, due to a low area density of molecules and disruption of the structure by interactions with the substrate and assembly of the thiophenes. What may happen is that ideal chain statistics of the PEG segment first determines the thickness of the monolayer as well as the area density of molecules. Fixing of the latter the value thus limits the size and structure of the assemblies of the hydrophobic blocks, yielding a periodic texture that is consistent between different samples.

The observation of the striped textures is suggestive of another stable or metastable monolayer structure at higher area densities of molecules. Returning to the grafted polymer analogy, as the grafting density increases, the brush transitions into a "dry brush" regime where the chains become more extended due to excluded volume interactions. In this model, the brush thickness scales as

$$d_{dry} = l_k N_k \sigma \qquad (6.2)$$

where σ is the grafting number density normalized to the cross-sectional area of the chain (l_k^2).[335] This transition is expected to occur at a value of $\sigma \approx N^{-1/2}$, corresponding to an area density of

molecules of 0.38 nm^{-2}. With respect to the dotted textures, this is equal to 160 molecules per "dot." The thickness of the stripe films are close to half the bulk *d*-spacing and suggest that, in this case, the conformation of the molecule is more akin to that seen in the bulk where the PEG chains are slightly extended and possibly crystallized.

6.3.4 Preliminary examination of hybrid mixtures

When mixed with TiO_2 nanorods, the nanorods are not visible through thick layers of organic. In some areas, the film appears thinner, and the nanorods are visible by AFM, but they appear not to be evenly dispersed. This is not necessarily a detriment as it is preferable that the TiO_2 nanorods be in close enough contact to allow percolation of charge carriers. However, it is apparent that a higher concentration of nanorods is necessary in order to increase degree of percolation and the chances of an exciton generated in the organic being able to diffuse to a TiO_2

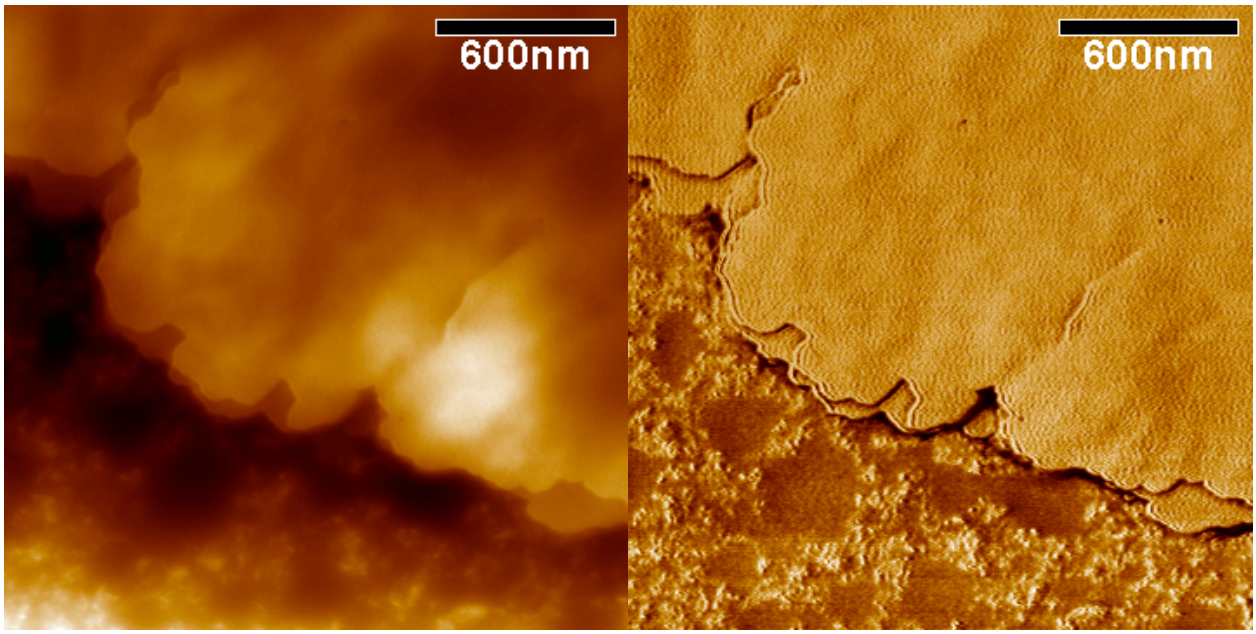

Figure 6.6. AFM height and phase images of films of **6.1** mixed with TiO_2 nanorods.

interface. At the moment, AFM cannot determine if the TiO_2 nanorods prefer to associate with any particular block of compound **6.1**.

6.4 Patterning of thiophene-PEG films

6.4.1 Deposition on friction-transferred PTFE

AFM images of friction-transferred PTFE on a silicon substrate are shown in Figure 6.7. The well-aligned strips of PTFE are small as 10 nm in width and 3 to 10 nm in height. Polarized transmission FTIR spectra given in Figure 6.8 show that the CF_2 antisymmetric (1207 cm^{-1}) and symmetric (1151 cm^{-1}) stretching modes orient perpendicular to the stripes while the CF_2 wagging mode (625 cm^{-1}) orients parallel. This is consistent with previously reported data showing that the PTFE chains are aligned along the length of the strips.[337, 338]

Figure 6.9 shows AFM images of molecule **6.1** spin-coated or drop-cast onto a substrate of friction-transferred PTFE on glass. After annealing at room temperature in a saturated chloroform atmosphere, the film is seen to adopt a morphology to that shown previously in which most of the substrate is covered with a thin monolayer of material with scattered large islands of full bilayers. Yet, the PTFE strips are highly visible, even over thicker portions of the film, and they appear less well aligned than they are in Figure 6.7, often curving around larger obstacles. These observations suggest that the PTFE strips lift off the substrate either during spin-coating or solvent annealing and are displaced slightly by migration of the material. The film actually seems to get underneath the PTFE, possibly to decrease surface energies by allowing the PEG groups to associate with the glass and exposing the fluorine groups to the air interface.

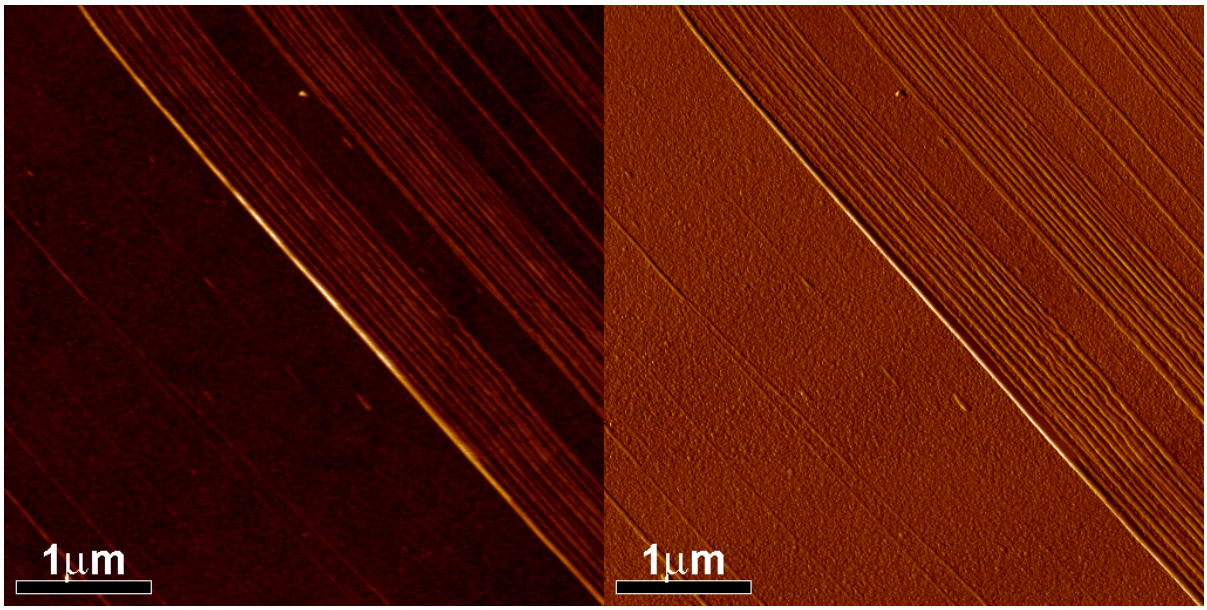

Figure 6.7. AFM height and phase images of friction-transferred PTFE fibers on glass.

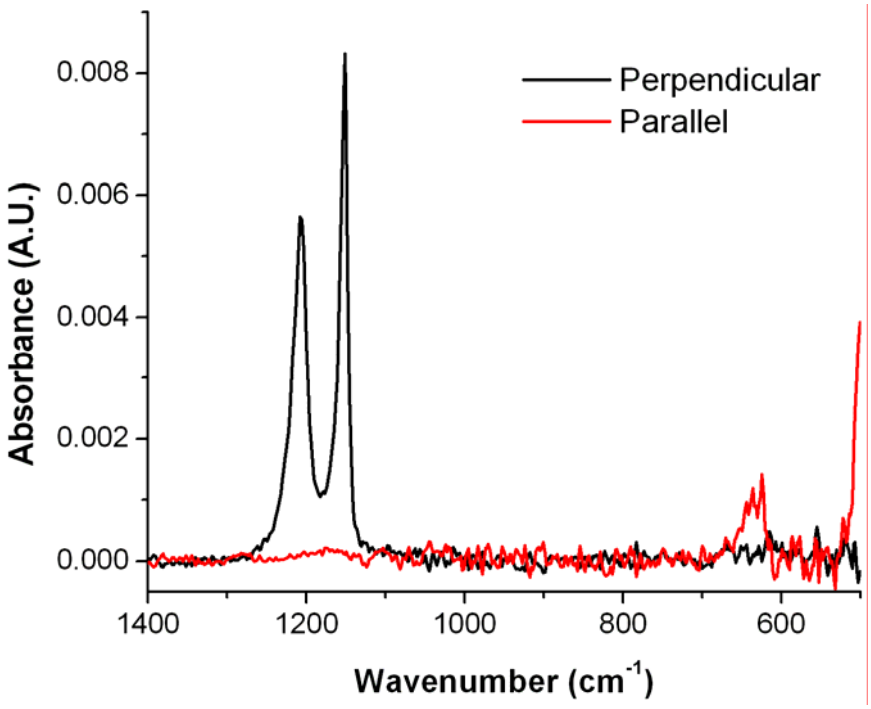

Figure 6.8. Polarized transmission FTIR spectra of friction-transferred PTFE on silicon shows molecular alignment of the polymer chains parallel to the direction of drawing.

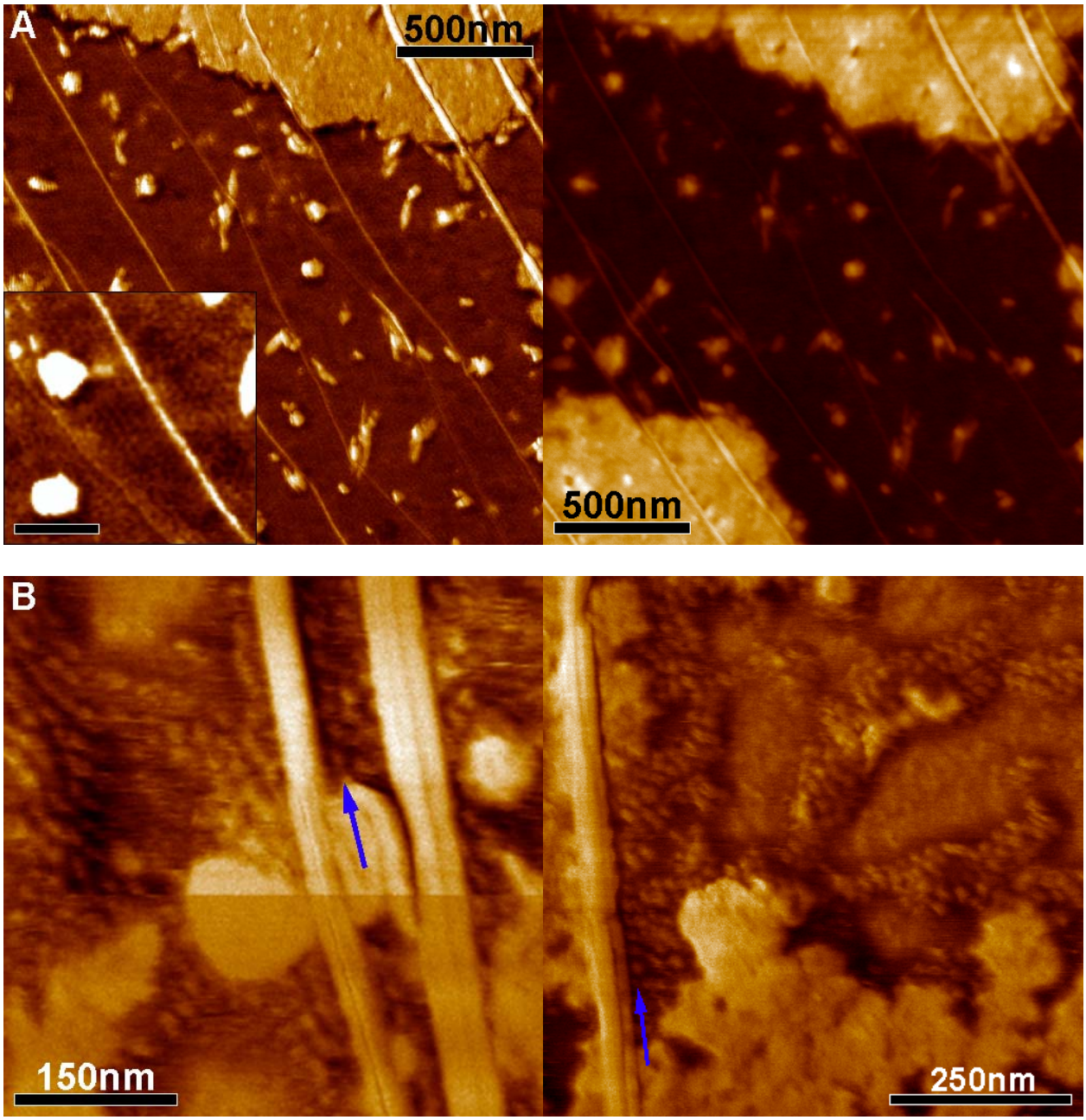

Figure 6.9. AFM images of **6.1** (**A**) spin-coated or (**B**) drop cast on friction-transferred PTFE on glass and annealed under saturated solvent atmosphere. Phase contrast images (all except image on right in **A**) show weak ordering of the dot texture adjacent to the PTFE fibers. The scale bar in the inset in **A** is 150 nm.

The dotted texture of the monolayer is very faint in Figure 6.9a due to the poor quality of the scanning probe tip, but the same periodicity as before is observed. In some locations, the PTFE fibers do seem to influence the ordering of the dotted texture with lines of dots running parallel to the fibers. However, the sizes of the ordered domains appear to vary widely from hundreds of nanometers to only the line of dots immediately adjacent to a PTFE fiber. The weak contrast of the texture as well as disorder in the alignment of the PTFE strips makes it difficult to draw definitive conclusions. However, controlling the order of nanostructured thin films of these thiophene-based amphiphiles through the use of friction-transferred PTFE is promising, particularly because there is significant room for improvement. The AFM images show that the area density of the transferred PTFE fibers is low and may not be enough to adequately improve the order of the film, especially since the intrinsic order of the nanostructured film is low to begin with. The quantity of PTFE deposited can be increased by increasing the temperature of the hotplate or the pressure applied during transfer. Reducing the concentration of the solution used to cast the film may reduce the occurrence of thicker islands and material migration that can displace the PTFE strips At the same time, uniform deposition of a very thin film of material by spin-coating becomes difficult due to the dewetting of the solution from the PTFE surface. Thus the deposition procedure needs to be altered, either by switching to a dip-coating method or by exposing the friction-transferred PTFE surface very briefly to oxygen plasma to render it hydrophilic enough to be wetted by the solution. Displacement of the PTFE fibers from the substrate surface is troublesome primarily because the alignment of the fibers is disrupted. The mechanism of this displacement is still under investigation, but it requires desorption of relatively large objects and is therefore suspected to be slower than the evolution of the dotted film texture. If so, displacement of the PTFE strips may

be limited by shortening the time given for annealing the film in saturated solvent atmosphere. The original time of 4 hrs was chosen arbitrarily and can likely be shortened while at the same time still yield the dotted texture. The striped textures, however, are more often observed after longer annealing times, so a different strategy would be required in order to limit PTFE displacement in that case.

6.4.2 Preliminary work on soft lithographic embossing of thick films

AFM images of solution embossed films of compound **6.1** are shown in Figure 6.10. The lines of material do mimic the grating periodicity, but are shallower than the grooves in the original stamp, indicating that the presence of solvent doesn't allow the material to completely fill the channels. The patterned lines do exhibit a layered surface texture indicative of a lamellar

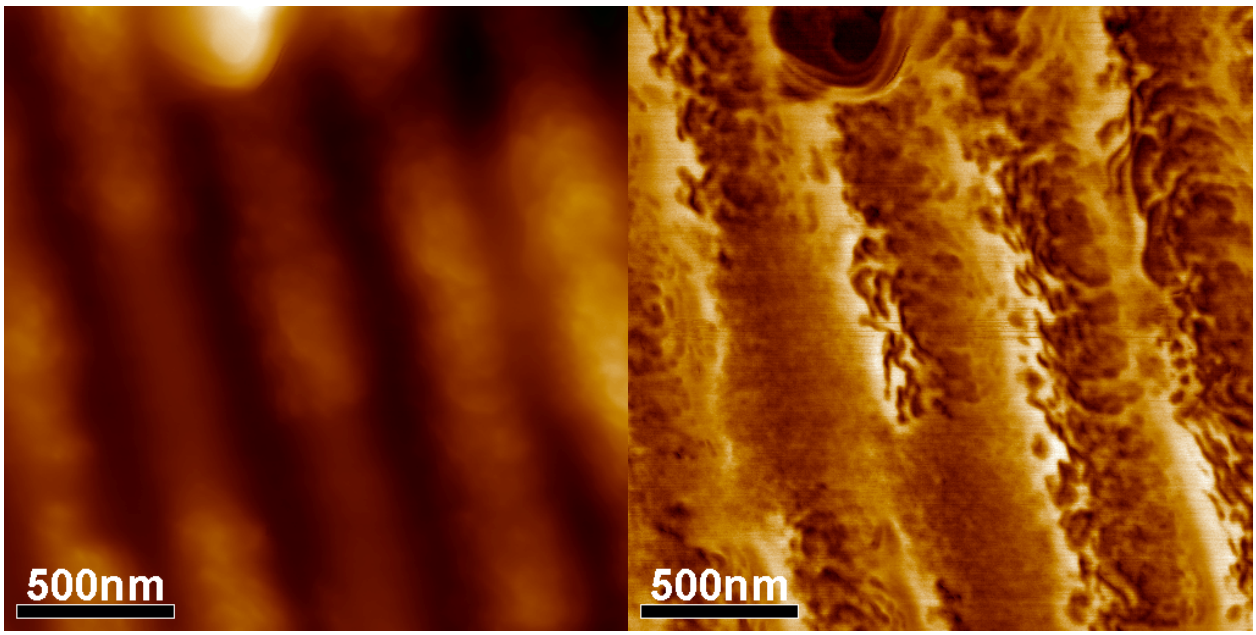

Figure 6.10. AFM height and phase contrast images of **6.1** patterned by solution embossing into diffraction grating lines of 416 nm period. The ridge heights are 74 ± 10 nm.

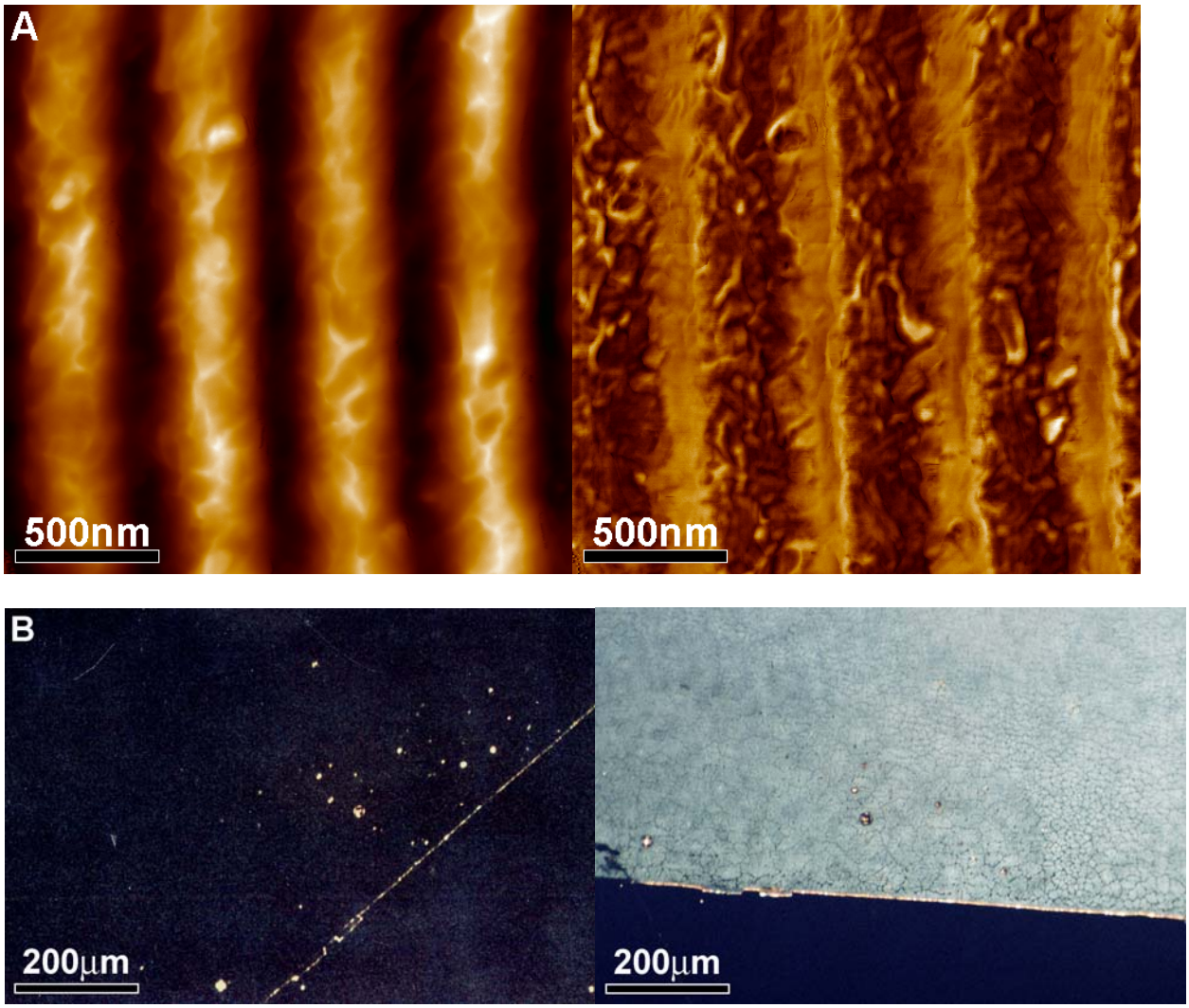

Figure 6.11. (**A**) AFM height and phase contrast images of **6.1** patterned by hot embossing a 170 nm thick film into diffraction grating lines of 416 nm period. The ridge heights are 105 ± 3 nm. (**B**) POM of the edge of the embossed area showing that the grating pattern polarizes light, as the transmitted illumation is extinguished when the sample is rotated 45 °.

phase, but no controlled orientation of the layered structure is evident. Breaks in the lines are believed to be due to drying effects as very little material is observed to lift off with the stamp.

AFM and POM images of thick films of molecule **6.1** molded into diffraction grating patterns by hot embossing are shown in Figure 6.11. The heights of the lines are closer to the

depth of the original grooves, and the fact that the patterned film effectively polarizes light indicates that the grating topology is replicated very well. Unlike with solution embossing, no breaks in the lines are observed, but definitive indications of a lamellar structure are also largely absent as the film more closely adopts the surface texture of the PDMS stamp itself.

UV-vis absorption spectra shown in Figure 6.12 of the patterned and non-patterned films display a higher overall absorption by the patterned films. If photon trapping does occur, a peak in absorption is expected to be seen when the waveguide mode, k, of the incident radiation for a given material and incident angle matches the wave vector of the diffraction grating, k_g. The wavelength, λ, of this scattering peak is given by[329]

$$k_g = \pm 2\pi/\Lambda \tag{6.3}$$

$$k = 2\pi n_{eff}/\lambda \tag{6.4}$$

$$\lambda = \frac{2\pi \sin\theta}{|k - k_g|} = \Lambda(n_{eff} \pm \sin\theta) \tag{6.5}$$

where Λ is the grating wavelength, θ is the incident angle, and n_{eff} is the effective refractive index. For the solution embossed films, no peak is observed, and the increase in absorption extends over all wavelengths, indicating that the perceived absorption is due to incoherent scattering by the noticeably rough film. By comparison, the film patterned by hot embossing also shows increased absorption over a wide wavelength range, but an additional shallow peak is observed around 594 nm.

Fluorescence measurements may be used to determine if the patterning actually increases absorption by the film. Figure 6.13 shows emission spectra of non-patterned and hot embossed films of 6.1 excited at 545 nm. The embossed films show photoluminescence intensity similar to

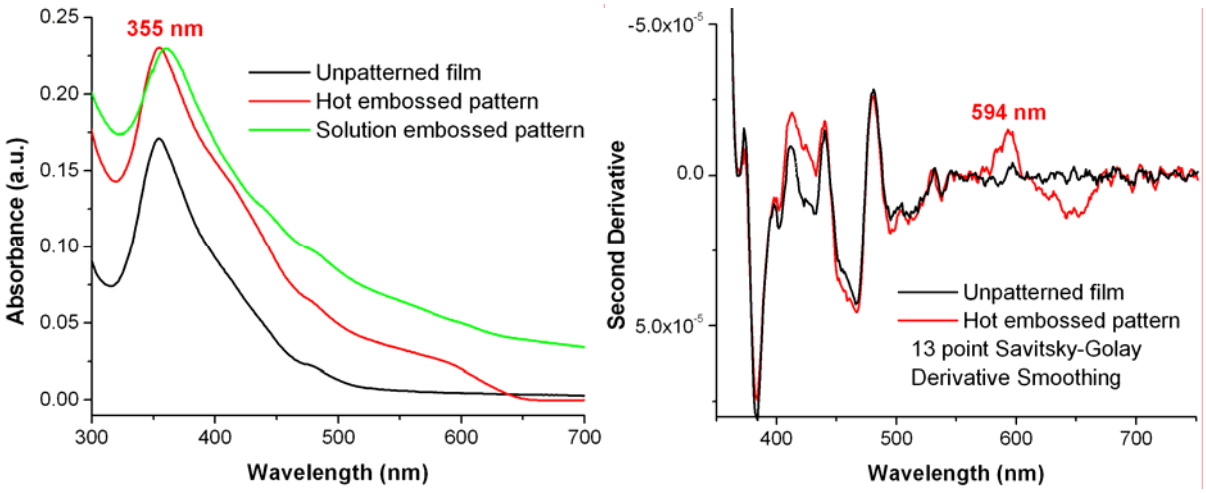

Figure 6.12. Absorption spectra of 170 nm thick films of **6.1** either unpatterned or patterned with a 2400 lines/mm grating topology. The solution embossed pattern shows an increase in signal due to incoherent scattering over the entire wavelength range. Second derivative fine structure enhancement shows an extra peak in the spectra of the hot embossed sample at 594 nm.

that of unpatterned films, indicating that the pattern scatters incoherently or the coherently scattered radiation is not absorbed by the material before it escapes. Both cases are possible given that λ appears to be significantly displaced from the absorbance peak of the material. This issue can be resolved simply by decreasing Λ. More importantly, however, it has yet to be shown that the goal of controlling structural orientation can be achieved. The former issue may be addressed by increasing the aspect ratio of the patterned features, resulting in a more prominent pattern that scatters more effectively. The latter issue may simply be due to the limitations of using AFM to probe bulk mesoscale order, in which case X-ray diffraction techniques would offer more insight. Altering the procedure to limit the use of PDMS or employing a more rigid form of spatial confinement such as topologically patterned substrates are other options for controlling and observing orientational order in these systems.

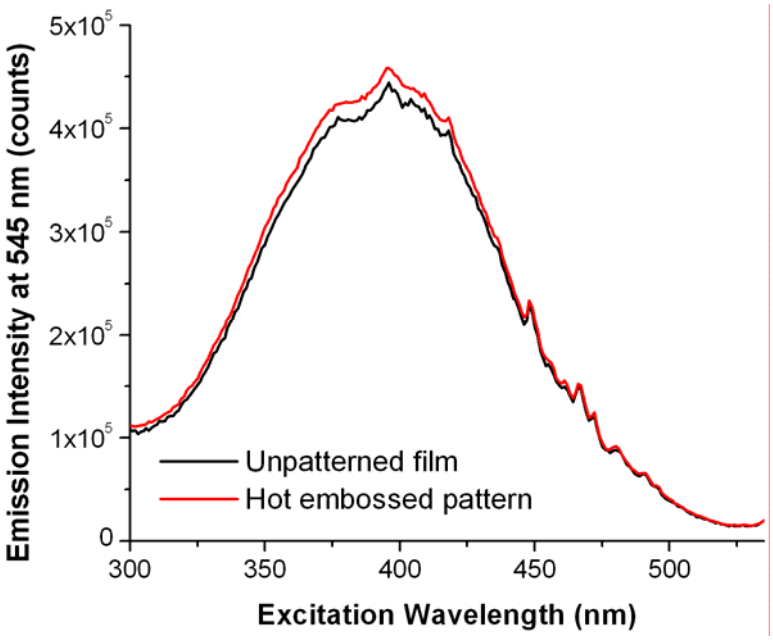

Figure 6.13. Fluorescence excitation spectra of unpatterned and grating patterned films of **6.1**. The emission intensity at 545 nm differs little between the two samples.

6.5 Summary and outlook

We have studied the morphology of thin films of a self-assembling, thiophene-based amphiphile by AFM. As thick films, the material self-assembles into a lamellar phase dominated by crystallization of the PEG block. However, as the average film thickness goes below the equilibrium *d*-spacing of 13 nm, striped and hexagonal dotted textures can be observed. It is hypothesized that the dotted texture is a result of assembly of the thiophene and alkyl units in the monolayer regime in which ideal chain statistics determine the morphology of the PEG segment and the area density of molecules. The striped textures are observed in films whose thicknesses are close to half the bulk *d*-spacing. In this case, it is thought that the PEG segments are more extended and possibly crystallized, and the area density of molecules is greater, so the thiophenes are capable of packing into larger structures. Deposition of thin films of **6.1** on friction-

transferred PTFE shows promise for controlling the degree of order of the surface textures. Demonstrating control over the morphology of the monolayer is a desirable first step toward controlling the bulk film morphology and achieving direct charge conduction pathways to an electrode surface. In addition, hot embossing of thicker films of **6.1** into diffraction grating topologies shows promise for improving absorption properties by photon trapping. Pattering of the bulk may be a complementary strategy for controlling the orientation and order of the self-assembled structure.

APPENDIX A

Determination of molecular orientation by polarized IR spectroscopy

Appendix A Determination of molecular orientation by polarized IR spectroscopy

A.1 Quantifying alignement and structure of PA nanofibers

The orientation of a TDM (*M*) of a single molecule may be described with respect to a fixed space coordinate system (*x, y, z*) by using the Euler angles as shown in Figure A.1. The molecular coordinate system is described by the *u*, *v*, and *w* axes, where *w* denotes the main axis of the molecule or supramolecular structure. The *z* axis is chosen to be normal to the substrate while the *x* and *y* axes are chosen to lie in the substrate plane. In the case of the PA nanofibers, *w* denotes the long axis of the nanofiber structure, and the *x* axis is chosen to be parallel to the direction of the patterned channels. The tilt (θ) and azimuthal (φ) angles describe the orientation

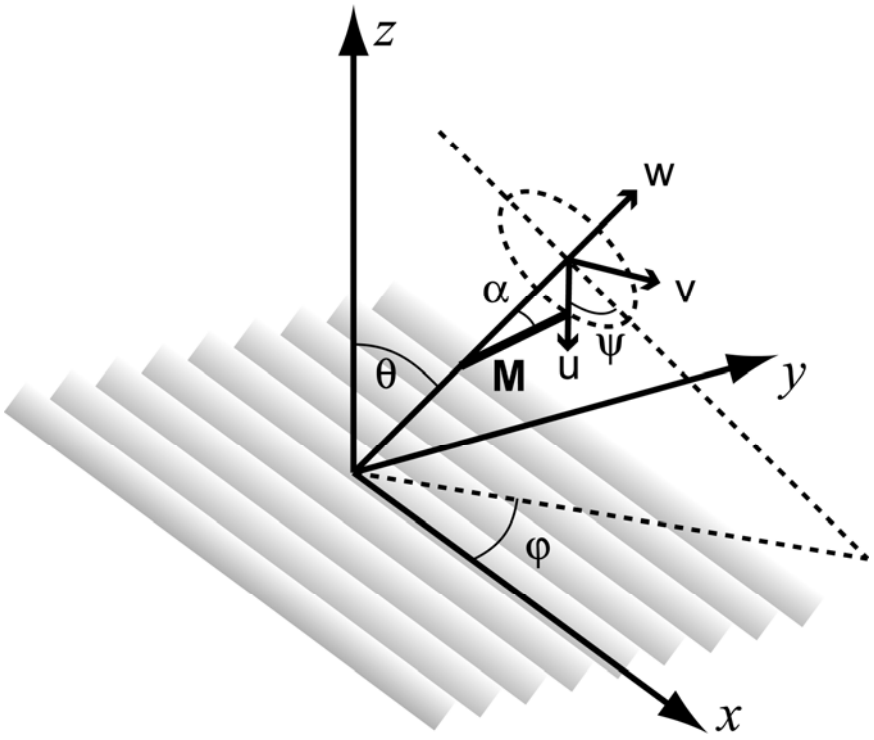

Figure A.1. Fixed space coordinate system (*x, y, z*), nanofiber or molecular coordinate system (*u, v, w*), and the angles (θ, φ, ψ, α) used to describe the orientation of the nanofiber and TDMs (*M*).

of *w* with respect to the space coordinate system. The orientation of the TDM with respect to the nanofiber coordinate system is described by a tilt (α) and a twist (ψ) angle.

The direction cosines K_x, K_y, and K_z are the square of the components of the unit vector of the TDM along each axis of the spatial coordinate system and are related to their respective extinction coefficients by a constant of proportionality.[240] Given the absorption intensities E_x, E_y, and E_z for a given vibration obtained experimentally from spectra polarized along each fixed space axis, the direction cosines can be calculated from $K_i = E_i/\Sigma E$, where $\Sigma E = E_x + E_y + E_z$. The function of K_i with respect to α and the three Euler angles θ, φ, and ψ is determined by straightforward geometric arguments as shown by Zbinden.[339] The components of the TDM along each axis of the space coordinate system (M_x, M_y, and M_z) are related to the components of the TDM along each axis of the molecular coordinate system (M_u, M_v, and M_w) as follows:

$$\begin{pmatrix} M_x \\ M_y \\ M_z \end{pmatrix} = \begin{pmatrix} \cos\psi\cos\theta\cos\varphi + \sin\psi\sin\varphi & \sin\psi\cos\theta\cos\varphi - \cos\psi\sin\varphi & \cos\varphi\sin\theta \\ \cos\psi\cos\theta\sin\varphi - \sin\psi\cos\varphi & \sin\psi\cos\theta\sin\varphi + \cos\psi\cos\varphi & \sin\varphi\sin\theta \\ -\sin\theta\cos\psi & -\sin\theta\sin\psi & \cos\theta \end{pmatrix} \begin{pmatrix} M_u \\ M_v \\ M_w \end{pmatrix} \quad \text{(A.1)}$$

The components of the TDM with respect to the molecular coordinate system are related to the absolute magnitude of the TDM *M* and the angle α by simple relations:

$$\begin{pmatrix} M_u \\ M_v \\ M_w \end{pmatrix} = \begin{pmatrix} M\sin\alpha \\ 0 \\ M\cos\alpha \end{pmatrix} \quad \text{(A.2)}$$

Inserting equations A.2 into A.1 yields expressions for M_x, M_y, and M_z in terms of α, θ, φ, and ψ. Knowing that the direction cosines are proportional to the square of the components of the TDM as $K_i = (M_i/M)^2$, we obtain:

$$K_x = \left(\cos\psi\cos\theta\cos\varphi\sin\alpha + \sin\psi\sin\varphi\sin\alpha + \cos\varphi\sin\theta\cos\alpha\right)^2 \quad \text{(A.3)}$$

$$K_y = \left(\cos\psi\cos\theta\sin\varphi\sin\alpha - \sin\psi\cos\varphi\sin\alpha + \sin\varphi\sin\theta\cos\alpha\right)^2 \quad \text{(A.4)}$$

$$K_z = \left(-\sin\theta\cos\psi\sin\alpha + \cos\theta\cos\alpha\right)^2 \quad \text{(A.5)}$$

The nanofibers are assumed to have cylindrical symmetry about their long axis, so the distribution of ψ is taken to be uniform. Cylindrical symmetry allows us to integrate the expressions for the direction cosines over the angle ψ to yield:

$$K_x = \frac{1}{2}\cos^2\theta\cos^2\varphi\sin^2\alpha + \frac{1}{2}\sin^2\varphi\sin^2\alpha + \cos^2\varphi\sin^2\theta\cos^2\alpha \quad \text{(A.6)}$$

$$K_y = \frac{1}{2}\cos^2\theta\sin^2\varphi\sin^2\alpha + \frac{1}{2}\cos^2\varphi\sin^2\alpha + \sin^2\varphi\sin^2\theta\cos^2\alpha \quad \text{(A.7)}$$

$$K_z = \frac{1}{2}\sin^2\theta\sin^2\alpha + \cos^2\theta\cos^2\alpha \quad \text{(A.8)}$$

The patterned nanofibers can be thought of as a biaxially oriented film where the nanofibers preferentially align perpendicular to the *z* axis and parallel to the *x* axis within the *xy* plane. Stein[315, 316] introduced two orientation parameters, f_θ and f_φ, to describe alignment in biaxially oriented films:

$$f_\theta = \frac{3\left\langle\cos^2\theta\right\rangle - 1}{2} \quad \text{(A.9)}$$

$$f_\varphi = 2\left\langle\cos^2\varphi\right\rangle - 1 \quad \text{(A.10)}$$

where $\langle\cos^2\theta\rangle$ and $\langle\cos^2\varphi\rangle$ are the mean values of $\cos^2\theta$ and $\cos^2\varphi$ for a distribution of TDMs in the film. f_θ is equal to the space-averaged second order Legendre polynomial P_2 or Saupe order parameter S_{zz} describing alignment along the *z* axis out of the substrate plane.[42, 340] f_φ can be thought of as a two-dimensional order parameter quantifying the in-plane alignment of directors along the *x* axis. Pelletier and coworkers[341] rewrote the expressions for K_i given by

Zbinden in terms of these two parameters assuming cylindrical symmetry about the *w* axis, resulting in the following:

$$K_x = \left[\left(\frac{1}{2}\sin^2\alpha - \frac{1}{3}\right)\left(f_\theta + f_\theta f_\varphi - f_\varphi\right) + \frac{1}{3}\right] \quad \text{(A.11)}$$

$$K_y = \left[\left(\frac{1}{2}\sin^2\alpha - \frac{1}{3}\right)\left(f_\theta - f_\theta f_\varphi + f_\varphi\right) + \frac{1}{3}\right] \quad \text{(A.12)}$$

$$K_z = \left[\left(\cos^2\alpha - \frac{1}{3}\right) f_\theta + \frac{1}{3}\right] \quad \text{(A.13)}$$

For the patterned nanofibers, θ is close to 90º and f_θ approachs -0.5. We choose to concentrate our quantitative evaluations on the amide I and amide A vibrations known to be aligned mostly parallel to the nanofiber long axis (α approaching 0). While the orientation parameters cannot be determined exactly from the three polarized spectra alone, upper and lower bound values of f_φ can be calculated assuming specific values of α and θ. The lower bound is obtained assuming that the TDM is oriented parallel to the nanofiber long axis ($\alpha = 0$) and that the non-zero value of K_z is due to tilt of the nanofiber out of the *xy* plane ($f_\theta > -0.5$). Solving for f_φ from equations A.11 – A.13 gives

$$f_{\varphi,\min} = \frac{K_x - K_y}{K_x + K_y} \quad \text{(A.14)}$$

Considering a different idealized case in which all of the nanofibers are lying perfectly parallel to the substrate ($f_\theta = -0.5$), any observed non-zero value of K_z is attributable to an average tilt of the TDM off the axis of the nanofiber ($\alpha > 0$). This scenario yields an upper bound value for f_φ given by

$$f_{\varphi,\max} = \frac{K_x - K_y}{K_x + K_y - 2K_z} \quad \text{(A.15)}$$

Assuming cylindrical symmetry, it is impossible to distinguish whether this value of α is due to inherent tilt of the TDM out of the plane of the parallel β-sheet, twist of the β-sheet about the nanofiber axis, or disorder in the self-assembled structure. We can at least obtain a maximum value of α by selecting the smallest value of K_z for each molecule and each vibration and solving for f_θ = -0.5:

$$\alpha_{\max} = \arcsin\left(\sqrt{2K_z}\right) \quad \text{(A.16)}$$

Selected peaks in the spectra were fit to Lorentzian forms so that the peak areas could be obtained and the quality of alignment between samples could be quantitatively compared. In the amide I region (1700-1620 cm^{-1}), a rigorous deconvolution of each of the non-β-sheet peaks was not attempted, rather, the peak fitting was performed to the extent to which we were able to reliably determine the area of the β-sheet peak at 1630 cm^{-1}. The amide A band (3310-3270 cm^{-1}) is much less sensitive to secondary structure[311, 312] and even more difficult to deconvolute, so orientation parameters obtained for the amide A band were used only to qualitatively confirm observed trends.

A.2 Quantifying order in films of supramolecular mushroom-shaped nanostructures

In the case of the mushroom nanostructures, *w* is chosen to represent the long axis of the rod segment of each molecule. If it is assumed that there is no preferred orientation to the twist of the molecule, the distribution of the twist angle ψ may be taken to be uniform and equations A.6 through A.13 remain applicable. Although this may not necessarily be the case for the mushroom molecule, the assumption of cylindrical symmetry can still be instructive as a first

approximation. Films of the supramolecular mushroom nanostructures are believed to have uniaxial order relative to the surface normal which may be quantified by the order parameter f_θ given in equation A.9. The value of f_φ is taken to be 0, and solving for f_θ in terms of α, K_y, and K_z gives:

$$f_\theta = \left(\frac{2}{3\cos^2\alpha - 1}\right)\left(\frac{1-d}{2d+1}\right) = \frac{1-d}{2d+1} \text{ assuming } \alpha = 0 \qquad \text{(A.17)}$$

$$d = \frac{K_y}{K_z} \qquad \text{(A.18)}$$

where d is the dichroic ratio. If the value of α is not known exactly, it can be taken to be 0, and the value of f_θ calculated would be a lower bound. Corresponding values of the tilt angle θ calculated from these values of f_θ can be taken as upper bound values, $\theta_{\max}$. The assumptions listed may be overly simplistic for the molecule **2.1** but are not unreasonable for the guest molecule **2.3**. Thus, values for the order parameter of the guest molecules calculated using equation A.17 are considered valid estimates.

An upper bound for the value of α can be obtained by assuming that the condition that yields the lowest value of d is perfectly aligned ($f_\theta = 1$), and that the non-zero value of d is entirely due to tilt of the TDM off the main axis of the molecule.

$$\alpha_{\max} = \arctan\left(\sqrt{2d_{\min}}\right) \qquad \text{(A.19)}$$

The original value of f_θ obtained for this particular condition from equation A.17 is denoted $f_{\theta,\min}$, and "corrected" values of f_θ taking into account $\alpha_{\max}$ can be calculated for each other condition:

$$f_\theta^* = f_\theta \Big/ f_{\theta,\min} \qquad \text{(A.20)}$$

$$\theta^* = \cos^{-1}\sqrt{\frac{2f_\theta^* + 1}{3}} \tag{A.21}$$

Removing the assumption of cylindrical symmetry entirely would complicate the model by adding another variable into the equations. Instead, we chose to examine a different idealized case where the twist angle ψ is fixed at a value of 0. In this case, the angle α tilts the TDM farther from the surface normal and the value of f_θ given by equation A.17 would be a severe underestimation. Returning to equations A.3 – A.5, we implement this idealized case by setting $\psi = 0$ and integrating over a uniform distribution of the angle φ to yield:

$$K_x = K_y = \frac{1}{2}\sin^2(\theta + \alpha) \tag{A.22}$$

$$K_z = \cos^2(\theta + \alpha) \tag{A.23}$$

In essence, α becomes indistinguishable from the molecular tilt angle θ. We can again correct for the value of α_{max} obtained from equation A.19 by calculating a reduced value of the molecular tilt angle θ:

$$\theta_{min} = \arccos\left(\sqrt{\frac{2f_\theta + 1}{3}}\right) - \alpha_{max} \tag{A.24}$$

$$f_\theta^{**} = \frac{3\cos^2\theta_{min} - 1}{2} \tag{A.25}$$

Because α_{max} overestimates the value of α, values of f_θ^{**} obtained in this manner overestimate the order parameter and should be considered upper bounds. The corresponding value for the tilt angle θ_{min} can be considered a lower bound. By comparing these values to the values for the order parameter and tilt angle gathered by other techniques, we can formulate a better picture of the orientation and packing of the molecules within the film.

REFERENCES AND NOTES

References and Notes

1. Feynman, R. P., There's plenty of room at the bottom. *California Institute of Technology Journal of Engineering and Science* **1960,** 4, (2), 23-36.

2. Bhushan, B., *Springer Handbook of Nanotechnology*. 2nd ed.; Springer Science: London, 2007.

3. Lehn, J. M., *Supramolecular Chemistry*. VCH Press: New York, 1995.

4. Lehn, J. M., Toward self-organization and complex matter. *Science* **2002,** 295, (5564), 2400-2403.

5. Schneider, H. J.; Yatsimirsky, A. K., *Principles and Methods in Supramolecular Chemistry*. John Wiley & Sons: New York, 2000.

6. Stupp, S. I.; LeBonheur, V.; Walker, K.; Li, L. S.; Huggins, K. E.; Keser, M.; Amstutz, A., Supramolecular materials: Self-organized nanostructures. *Science* **1997,** 276, (5311), 384-389.

7. Whitesides, G. M.; Mathias, J. P.; Seto, C. T., Molecular Self-Assembly and Nanochemistry - a Chemical Strategy for the Synthesis of Nanostructures. *Science* **1991,** 254, (5036), 1312-1319.

8. Alivisatos, A. P.; Barbara, P. F.; Castleman, A. W.; Chang, J.; Dixon, D. A.; Klein, M. L.; McLendon, G. L.; Miller, J. S.; Ratner, M. A.; Rossky, P. J.; Stupp, S. I.; Thompson, M. E., From molecules to materials: Current trends and future directions. *Advanced Materials* **1998,** 10, (16), 1297-1336.

9. Hoeben, F. J. M.; Jonkheijm, P.; Meijer, E. W.; Schenning, A., About supramolecular assemblies of pi-conjugated systems. *Chemical Reviews* **2005,** 105, (4), 1491-1546.

10. Whitesides, G. M.; Grzybowski, B., Self-assembly at all scales. *Science* **2002,** 295, (5564), 2418-2421.

11. Muthukumar, M.; Ober, C. K.; Thomas, E. L., Competing interactions and levels of ordering in self-organizing polymeric materials. *Science* **1997,** 277, (5330), 1225-1232.

12. Lee, H. N.; Christen, H. M.; Chisholm, M. F.; Rouleau, C. M.; Lowndes, D. H., Strong polarization enhancement in asymmetric three-component ferroelectric superlattices. *Nature* **2005,** 433, (7024), 395-399.

13. Zeng, H.; Li, J.; Liu, J. P.; Wang, Z. L.; Sun, S. H., Exchange-coupled nanocomposite magnets by nanoparticle self-assembly. *Nature* **2002,** 420, (6914), 395-398.

14. Crespo-Biel, O.; Ravoo, B. J.; Reinhoudt, D. N.; Huskens, J., Noncovalent nanoarchitectures on surfaces: from 2D to 3D nanostructures. *Journal of Materials Chemistry* **2006,** 16, (41), 3997-4021.

15. Lehn, J. M., Supramolecular Chemistry - Scope and Perspectives Molecules, Supermolecules, and Molecular Devices. *Angewandte Chemie-International Edition in English* **1988,** 27, (1), 89-112.

16. Israelachivili, J. N., *Intermolecular and Surface Forces*. 2nd ed.; Academic Press: London, 1992.

17. Tsuzuki, S.; Honda, K.; Uchimaru, T.; Mikami, M.; Tanabe, K., Origin of attraction and directionality of the x/x interaction: Model chemistry calculations of benzene dimer interaction. *Journal of the American Chemical Society* **2002,** 124, (1), 104-112.

18. Ma, J. C.; Dougherty, D. A., The cation-pi interaction. *Chemical Reviews* **1997,** 97, (5), 1303-1324.

19. Dill, K. A., Dominant Forces in Protein Folding. *Biochemistry* **1990,** 29, (31), 7133-7155.

20. De Gennes, P. G.; Prost, J., *The Physics of Liquid Crystals*. 2 ed.; Oxford University Press: Oxford, 1993.

21. Eldridge, M. D.; Madden, P. A.; Frenkel, D., Entropy-Driven Formation of a Superlattice in a Hard-Sphere Binary Mixture. *Nature* **1993,** 365, (6441), 35-37.

22. Hadjichristidis, N.; Pispas, S.; Floudas, G. A., *Block Copolymers: Synthetic strategies, physical properties, and applications*. Wiley Interscience: Hoboken, N.J., 2003.

23. Shchukin, E. D.; Pertsov, A. V.; Amelina, E. A.; Zelenev, A. S., *Colloid and Surface Chemistry*. Elsevier Science: New York, 2001.

24. Leibler, L., Theory of Microphase Separation in Block Co-Polymers. *Macromolecules* **1980,** 13, (6), 1602-1617.

25. Ziherl, P.; Kamien, R. D., Maximizing entropy by minimizing area: Towards a new principle of self-organization. *Journal of Physical Chemistry B* **2001,** 105, (42), 10147-10158.

26. Velichko, Y. S.; de la Cruz, M. O., Pattern formation on the surface of cationic-anionic cylindrical aggregates. *Physical Review E* **2005,** 72, (4).

27. Solis, F. J.; Stupp, S. I.; de la Cruz, M. O., Charge induced pattern formation on surfaces: Segregation in cylindrical micelles of cationic-anionic peptide-amphiphiles. *Journal of Chemical Physics* **2005,** 122, (5).

28. Dubois, M.; Lizunov, V.; Meister, A.; Gulik-Krzywicki, T.; Verbavatz, J. M.; Perez, E.; Zimmerberg, J.; Zemb, T., Shape control through molecular segregation in giant surfactant aggregates. *Proceedings of the National Academy of Sciences of the United States of America* **2004,** 101, (42), 15082-15087.

29. Borue, V. Y.; Erukhimovich, I. Y., A Statistical-Theory of Weakly Charged Poly-Electrolytes - Fluctuations, Equation of State, and Microphase Separation. *Macromolecules* **1988,** 21, (11), 3240-3249.

30. Barmentlo, M.; Vanaerle, N.; Hollering, R. W. J.; Damen, J. P. M., Surface Induced Liquid-Crystal Alignment Studied by Optical 2nd-Harmonic Generation. *Journal of Applied Physics* **1992,** 71, (10), 4799-4804.

31. Segalman, R. A.; Hexemer, A.; Kramer, E. J., Effects of lateral confinement on order in spherical domain block copolymer thin films. *Macromolecules* **2003,** 36, (18), 6831-6839.

32. Segalman, R. A.; Yokoyama, H.; Kramer, E. J., Graphoepitaxy of spherical domain block copolymer films. *Advanced Materials* **2001,** 13, (15), 1152-1155.

33. Lazzari, M.; Liu, G.; Lecommandoux, S., *Block Copolymers in Nanoscience*. Wiley-VCH: Weinheim, 2006.

34. Fasolka, M. J.; Mayes, A. M., Block copolymer thin films: Physics and applications. *Annual Review of Materials Research* **2001,** 31, 323-355.

35. Bates, F. S.; Fredrickson, G. H., Block copolymers - Designer soft materials. *Physics Today* **1999,** 52, (2), 32-38.

36. Khandpur, A. K.; Forster, S.; Bates, F. S.; Hamley, I. W.; Ryan, A. J.; Bras, W.; Almdal, K.; Mortensen, K., Polyisoprene-polystyrene diblock copolymer phase diagram near the order-disorder transition. *Macromolecules* **1995,** 28, (26), 8796-8806.

37. Shefelbine, T. A.; Vigild, M. E.; Matsen, M. W.; Hajduk, D. A.; Hillmyer, M. A.; Cussler, E. L.; Bates, F. S., Core-shell gyroid morphology in a poly(isoprene-block-styrene-block-dimethylsiloxane) triblock copolymer. *Journal of the American Chemical Society* **1999,** 121, (37), 8457-8465.

38. Breiner, U.; Krappe, U.; Thomas, E. L.; Stadler, R., Structural characterization of the "knitting pattern" in polystyrene-block-poly(ethylene-co-butylene)-block-poly(methylmethacryla te) triblock copolymers. *Macromolecules* **1998,** 31, (1), 135-141.

39. Stadler, R.; Auschra, C.; Beckmann, J.; Krappe, U.; Voigtmartin, I.; Leibler, L., Morphology and Thermodynamics of Symmetrical Poly(a-Block-B-Bloch-C) Triblock Copolymers. *Macromolecules* **1995,** 28, (9), 3080-3097.

40. Collins, P. J., *Liquid Crystals*. 1 ed.; Princeton University Press: Princeton, NJ, 1990.

41. Wang, X. J.; Zhou, Q. F., *Liquid Crystalline Polymers*. World Scientific: River Edge, NJ, 2004.

42. Onsager, L., *Annals of the New York Academy of Sciences* **1949,** 51, 627-632.

43. Flory, P. J., Molecular Theory of Liquid-Crystals. *Advances in Polymer Science* **1984,** 59, 1-36.

44. Flory, P. J., Phase Equilibria in Solutions of Rod-Like Particles. *Proceedings of the Royal Society of London Series a-Mathematical and Physical Sciences* **1956,** 234, (1196), 73-89.

45. Khokhlov, A. R.; Semenov, A. N., Liquid-Crystalline Ordering in the Solution of Partially Flexible Macromolecules. *Physica A* **1982,** 112, (3), 605-614.

46. Cosgrove, T., *Colloid Science: Principles, methods, and applications*. Blackwell Publishing: Ames, IA, 2005.

47. Denkov, N. D.; Velev, O. D.; Kralchevsky, P. A.; Ivanov, I. B.; Yoshimura, H.; Nagayama, K., Mechanism of Formation of 2-Dimensional Crystals from Latex-Particles on Substrates. *Langmuir* **1992,** 8, (12), 3183-3190.

48. Li, L. S.; Walda, J.; Manna, L.; Alivisatos, A. P., Semiconductor nanorod liquid crystals. *Nano Letters* **2002,** 2, (6), 557-560.

49. Shevchenko, E. V.; Talapin, D. V.; Kotov, N. A.; O'Brien, S.; Murray, C. B., Structural diversity in binary nanoparticle superlattices. *Nature* **2006,** 439, (7072), 55-59.

50. Kiely, C. J.; Fink, J.; Brust, M.; Bethell, D.; Schiffrin, D. J., Spontaneous ordering of bimodal ensembles of nanoscopic gold clusters. *Nature* **1998,** 396, (6710), 444-446.

51. Sanders, J. V.; Murray, M. J., Ordered Arrangements of Spheres of 2 Different Sizes in Opal. *Nature* **1978,** 275, (5677), 201-203.

52. Kalsin, A. M.; Fialkowski, M.; Paszewski, M.; Smoukov, S. K.; Bishop, K. J. M.; Grzybowski, B. A., Electrostatic self-assembly of binary nanoparticle crystals with a diamond-like lattice. *Science* **2006,** 312, (5772), 420-424.

53. Shevchenko, E. V.; Talapin, D. V.; Murray, C. B.; O'Brien, S., Structural characterization of self-assembled multifunctional binary nanoparticle superlattices. *Journal of the American Chemical Society* **2006,** 128, (11), 3620-3637.

54. Park, M.; Harrison, C.; Chaikin, P. M.; Register, R. A.; Adamson, D. H., Block copolymer lithography: Periodic arrays of similar to 10(11) holes in 1 square centimeter. *Science* **1997,** 276, (5317), 1401-1404.

55. Li, R. R.; Dapkus, P. D.; Thompson, M. E.; Jeong, W. G.; Harrison, C.; Chaikin, P. M.; Register, R. A.; Adamson, D. H., Dense arrays of ordered GaAs nanostructures by selective area growth on substrates patterned by block copolymer lithography. *Applied Physics Letters* **2000,** 76, (13), 1689-1691.

56. Thurn-Albrecht, T.; Schotter, J.; Kastle, C. A.; Emley, N.; Shibauchi, T.; Krusin-Elbaum, L.; Guarini, K.; Black, C. T.; Tuominen, M. T.; Russell, T. P., Ultrahigh-density nanowire arrays grown in self-assembled diblock copolymer templates. *Science* **2000,** 290, (5499), 2126-2129.

57. Goltner, C. G.; Antonietti, M., Mesoporous materials by templating of liquid crystalline phases. *Advanced Materials* **1997,** 9, (5), 431-&.

58. Kresge, C. T.; Leonowicz, M. E.; Roth, W. J.; Vartuli, J. C.; Beck, J. S., Ordered Mesoporous Molecular-Sieves Synthesized by a Liquid-Crystal Template Mechanism. *Nature* **1992,** 359, (6397), 710-712.

59. Braun, P. V.; Osenar, P.; Stupp, S. I., Semiconducting superlattices templated by molecular assemblies. *Nature* **1996,** 380, (6572), 325-328.

60. Hulvat, J. F.; Stupp, S. I., Liquid-crystal templating of conducting polymers. *Angewandte Chemie-International Edition* **2003,** 42, (7), 778-781.

61. Huang, L. M.; Wang, Z. B.; Wang, H. T.; Cheng, X. L.; Mitra, A.; Yan, Y. S., Polyaniline nanowires by electropolymerization from liquid crystalline phases. *Journal of Materials Chemistry* **2002,** 12, (2), 388-391.

62. Lagerwall, J.; Scalia, G.; Haluska, M.; Dettlaff-Weglikowska, U.; Roth, S.; Giesselmann, F., Nanotube alignment using lyotropic liquid crystals. *Advanced Materials* **2007,** 19, (3), 359-+.

63. Deckman, H. W.; Dunsmuir, J. H., Natural Lithography. *Applied Physics Letters* **1982,** 41, (4), 377-379.

64. Hulteen, J. C.; Vanduyne, R. P., Nanosphere Lithography - a Materials General Fabrication Process for Periodic Particle Array Surfaces. *Journal of Vacuum Science & Technology a-Vacuum Surfaces and Films* **1995,** 13, (3), 1553-1558.

65. Joannopoulos, J. D.; Meade, R. D.; Winn, J. N., *Photonic Crystals: Molding the flow of light*. Princeton University Press: Princeton, N.J., 1995.

66. Courty, A.; Mermet, A.; Albouy, P. A.; Duval, E.; Pileni, M. P., Vibrational coherence of self-organized silver nanocrystals in f.c.c. supra-crystals. *Nature Materials* **2005,** 4, (5), 395-398.

67. Kagan, C. R.; Murray, C. B.; Bawendi, M. G., Long-range resonance transfer of electronic excitations in close-packed CdSe quantum-dot solids. *Physical Review B* **1996,** 54, (12), 8633-8643.

68. Skomski, R.; Coey, J. M. D., Giant Energy Product in Nanostructured 2-Phase Magnets. *Physical Review B* **1993,** 48, (21), 15812-15816.

69. Thurmond, K. B.; Kowalewski, T.; Wooley, K. L., Shell cross-linked knedels: A synthetic study of the factors affecting the dimensions and properties of amphiphilic core-shell nanospheres. *Journal of the American Chemical Society* **1997,** 119, (28), 6656-6665.

70. Kato, T.; Kihara, H.; Kumar, U.; Uryu, T.; Frechet, J. M. J., A Liquid-Crystalline Polymer Network Built by Molecular Self-Assembly through Intermolecular Hydrogen-Bonding. *Angewandte Chemie-International Edition in English* **1994,** 33, (15-16), 1644-1645.

71. Kato, T.; Frechet, J. M. J., New Approach to Mesophase Stabilization through Hydrogen-Bonding Molecular-Interactions in Binary-Mixtures. *Journal of the American Chemical Society* **1989,** 111, (22), 8533-8534.

72. Michl, J.; Magnera, T. F., Two-dimensional supramolecular chemistry with molecular Tinkertoys. *Proceedings of the National Academy of Sciences of the United States of America* **2002,** 99, (8), 4788-4792.

73. Winfree, E.; Liu, F. R.; Wenzler, L. A.; Seeman, N. C., Design and self-assembly of two-dimensional DNA crystals. *Nature* **1998,** 394, (6693), 539-544.

74. Bowden, N.; Terfort, A.; Carbeck, J.; Whitesides, G. M., Self-assembly of mesoscale objects into ordered two-dimensional arrays. *Science* **1997,** 276, (5310), 233-235.

75. Stupp, S. I.; Son, S.; Lin, H. C.; Li, L. S., Synthesis of 2-Dimensional Polymers. *Science* **1993,** 259, (5091), 59-63.

76. van Hameren, R.; Schon, P.; van Buul, A. M.; Hoogboom, J.; Lazarenko, S. V.; Gerritsen, J. W.; Engelkamp, H.; Christianen, P. C. M.; Heus, H. A.; Maan, J. C.; Rasing, T.; Speller, S.; Rowan, A. E.; Elemans, J.; Nolte, R. J. M., Macroscopic hierarchical surface patterning of porphyrin trimers via self-assembly and dewetting. *Science* **2006,** 314, (5804), 1433-1436.

77. Yan, D. Y.; Zhou, Y. F.; Hou, J., Supramolecular self-assembly of macroscopic tubes. *Science* **2004,** 303, (5654), 65-67.

78. Sijbesma, R. P.; Beijer, F. H.; Brunsveld, L.; Folmer, B. J. B.; Hirschberg, J.; Lange, R. F. M.; Lowe, J. K. L.; Meijer, E. W., Reversible polymers formed from self-complementary monomers using quadruple hydrogen bonding. *Science* **1997,** 278, (5343), 1601-1604.

79. Schnur, J. M., Lipid Tubules - a Paradigm for Molecularly Engineered Structures. *Science* **1993,** 262, (5140), 1669-1676.

80. Lehn, J. M.; Rigault, A.; Siegel, J.; Harrowfield, J.; Chevrier, B.; Moras, D., Spontaneous Assembly of Double-Stranded Helicates from Oligobipyridine Ligands and Copper(I) Cations - Structure of an Inorganic Double Helix. *Proceedings of the National Academy of Sciences of the United States of America* **1987,** 84, (9), 2565-2569.

81. Hartgerink, J. D.; Beniash, E.; Stupp, S. I., Self-assembly and mineralization of peptide-amphiphile nanofibers. *Science* **2001,** 294, (5547), 1684-1688.

82. Zubarev, E. R.; Pralle, M. U.; Sone, E. D.; Stupp, S. I., Self-assembly of dendron rodcoil molecules into nanoribbons. *Journal of the American Chemical Society* **2001,** 123, (17), 4105-4106.

83. Yamada, K.; Ihara, H.; Ide, T.; Fukumoto, T.; Hirayama, C., Formation of Helical Super Structure from Single-Walled Bilayers by Amphiphiles with Oligo-L-Glutamic Acid-Head Group. *Chemistry Letters* **1984**, (10), 1713-1716.

84. Prins, L. J.; Huskens, J.; de Jong, F.; Timmerman, P.; Reinhoudt, D. N., Complete asymmetric induction of supramolecular chirality in a hydrogen-bonded assembly. *Nature* **1999,** 398, (6727), 498-502.

85. Percec, V.; Ahn, C. H.; Ungar, G.; Yeardley, D. J. P.; Moller, M.; Sheiko, S. S., Controlling polymer shape through the self-assembly of dendritic side-groups. *Nature* **1998,** 391, (6663), 161-164.

86. Zimmerman, S. C.; Zeng, F. W.; Reichert, D. E. C.; Kolotuchin, S. V., Self-assembling dendrimers. *Science* **1996,** 271, (5252), 1095-1098.

87. Seto, C. T.; Mathias, J. P.; Whitesides, G. M., Molecular Self-Assembly through Hydrogen-Bonding - Aggregation of 5 Molecules to Form a Discrete Supramolecular Structure. *Journal of the American Chemical Society* **1993,** 115, (4), 1321-1329.

88. Corbellini, F.; Mulder, A.; Sartori, A.; Ludden, M. J. W.; Casnati, A.; Ungaro, R.; Huskens, J.; Crego-Calama, M.; Reinhoudt, D. N., Assembly of a supramolecular capsule on a molecular printboard. *Journal of the American Chemical Society* **2004,** 126, (51), 17050-17058.

89. Ratner, B. D., *Biomaterials Science: An introduction to materials in medicine*. Elsevier Academic Press: San Diego, 2004.

90. Leclere, P.; Surin, M.; Viville, P.; Lazzaroni, R.; Kilbinger, A. F. M.; Henze, O.; Feast, W. J.; Cavallini, M.; Biscarini, F.; Schenning, A.; Meijer, E. W., About oligothiophene self-assembly: From aggregation in solution to solid-state nanostructures. *Chemistry of Materials* **2004,** 16, (23), 4452-4466.

91. Radzilowski, L. H.; Carragher, B. O.; Stupp, S. I., Three-dimensional self-assembly of rodcoil copolymer nanostructures. *Macromolecules* **1997,** 30, (7), 2110-2119.

92. Radzilowski, L. H.; Stupp, S. I., Nanophase Separation in Monodisperse Rodcoil Diblock Polymers. *Macromolecules* **1994,** 27, (26), 7747-7753.

93. Stupp, S. I.; Pralle, M. U.; Tew, G. N.; Li, L. M.; Sayar, M.; Zubarev, E. R., Self-assembly of organic nano-objects into functional materials. *Mrs Bulletin* **2000,** 25, (4), 42-48.

94. Pralle, M. U.; Whitaker, C. M.; Braun, P. V.; Stupp, S. I., Molecular variables in the self-assembly of supramolecular nanostructures. *Macromolecules* **2000,** 33, (10), 3550-3556.

95. Sayar, M.; de la Cruz, M. O.; Stupp, S. I., Polar order in nanostructured organic materials. *Europhysics Letters* **2003,** 61, (3), 334-340.

96. Sayar, M.; Solis, F. J.; de la Cruz, M. O.; Stupp, S. I., Competing interactions among supramolecular structures on surfaces. *Macromolecules* **2000,** 33, (20), 7226-7228.

97. Li, L. M.; Zubarev, E. R.; Acker, B. A.; Stupp, S. I., Chemical structure and nonlinear optical properties of polar self-assembling films. *Macromolecules* **2002,** 35, (7), 2560-2565.

98. Pralle, M. U.; Urayama, K.; Tew, G. N.; Neher, D.; Wegner, G.; Stupp, S. I., Piezoelectricity in polar supramolecular materials. *Angewandte Chemie-International Edition* **2000,** 39, (8), 1486-+.

99. Schenning, A.; Kilbinger, A. F. M.; Biscarini, F.; Cavallini, M.; Cooper, H. J.; Derrick, P. J.; Feast, W. J.; Lazzaroni, R.; Leclere, P.; McDonell, L. A.; Meijer, E. W.; Meskers, S. C. J., Supramolecular organization of alpha,alpha '-disubstituted sexithiophenes. *Journal of the American Chemical Society* **2002,** 124, (7), 1269-1275.

100. Peters, L.; Sano, T.; Morrison, J. J.; Feeder, N.; Holmes, A. B.; Kraft, A., Supramolecular assemblies with dithieno[3,2-b;2 ',3 '-d]thiophenes and other conjugated thiophene-containing pi-systems. *Synthetic Metals* **2001,** 119, (1-3), 175-176.

101. Schenning, A.; Jonkheijm, P.; Peeters, E.; Meijer, E. W., Hierarchical order in supramolecular assemblies of hydrogen-bonded oligo(p-phenylene vinylene)s. *Journal of the American Chemical Society* **2001,** 123, (3), 409-416.

102. Berlin, A.; Zotti, G., Self-assembly of mono- and multilayers of polyconjugated conducting polymers. *Macromolecular Rapid Communications* **2000,** 21, (7), 301-318.

103. Michalitsch, R.; Nogues, C.; Najari, A.; El Kassmi, A.; Yassar, A.; Lang, P.; Garnier, F., beta-functionalized oligothiophenes for molecular self-assembly. *Synthetic Metals* **1999,** 101, (1-3), 5-6.

104. Lagrost, C.; Lacroix, J. C.; Chane-Ching, K. I.; Jouini, M.; Aeiyach, S.; Lacaze, P. C., Host-guest complexation: A strategy to form sexithiophene exhibiting self-assembly properties. *Advanced Materials* **1999,** 11, (8), 664-+.

105. Bjornholm, T.; Greve, D. R.; Reitzel, N.; Hassenkam, T.; Kjaer, K.; Howes, P. B.; Larsen, N. B.; Bogelund, J.; Jayaraman, M.; Ewbank, P. C.; McCullough, R. D., Self-assembly of regioregular, amphiphilic polythiophenes into highly ordered pi-stacked conjugated polymer thin films and nanocircuits. *Journal of the American Chemical Society* **1998,** 120, (30), 7643-7644.

106. Ashton, P. R.; Preece, J. A.; Stoddart, J. F.; Tolley, M. S.; White, A. J. P.; Williams, D. J., The Self-Assembly and Dynamic Properties of Thiophene-Containing [2]Catenanes. *Synthesis-Stuttgart* **1994**, 1344-1352.

107. Tew, G. N.; Pralle, M. U.; Stupp, S. I., Supramolecular materials from triblock rodcoil molecules containing phenylene vinylene. *Journal of the American Chemical Society* **1999,** 121, (42), 9852-9866.

108. Herz, L. M.; Daniel, C.; Silva, C.; Hoeben, F. J. M.; Schenning, A.; Meijer, E. W.; Friend, R. H.; Phillips, R. T., Fast exciton diffusion in chiral stacks of conjugated p-phenylene vinylene oligomers. *Physical Review B* **2003,** 68, (4).

109. Ajayaghosh, A.; George, S. J.; Praveen, V. K., Gelation-assisted light harvesting by selective energy transfer from an oligo(p-phenylenevinylene)-based self-assembly to an organic dye. *Angewandte Chemie-International Edition* **2003,** 42, (3), 332-+.

110. Schenning, A.; Peeters, E.; Meijer, E. W., Energy transfer in supramolecular assemblies of oligo(p-phenylene vinylene)s terminated poly(propylene imine) dendrimers. *Journal of the American Chemical Society* **2000,** 122, (18), 4489-4495.

111. Ghosh, S.; Inganas, O., Self-assembly of a conducting polymer nanostructure by physical crosslinking: applications to conducting blends and modified electrodes. *Synthetic Metals* **1999,** 101, (1-3), 413-416.

112. Tew, G. N.; Pralle, M. U.; Stupp, S. I., Supramolecular materials with electroactive chemical functions. *Angewandte Chemie-International Edition* **2000,** 39, (3), 517-+.

113. Hulvat, J. F.; Sofos, M.; Tajima, K.; Stupp, S. I., Self-assembly and luminescence of oligo(p-phenylene vinylene) amphiphiles. *Journal of the American Chemical Society* **2005,** 127, (1), 366-372.

114. Tajima, K.; Li, L. S.; Stupp, S. I., Nanostructured oligo(p-phenylene vinylene)/silicate hybrid films: One-step fabrication and energy transfer studies. *Journal of the American Chemical Society* **2006,** 128, (16), 5488-5495.

115. Lee, K. C.; Carlson, P. A.; Goldstein, A. S.; Yager, P.; Gelb, M. H., Protection of a decapeptide from proteolytic cleavage by lipidation and self-assembly into high-axial-

ratio microstructures: A kinetic and structural study. *Langmuir* **1999,** 15, (17), 5500-5508.

116. Yamada, N.; Koyama, E.; Imai, T.; Matsubara, K.; Ishida, S., Reversed micellar fibres in organic media as a new model of the parallel-chain beta-sheet structure of peptides. *Chemical Communications* **1996**, (19), 2297-2298.

117. Yu, Y. C.; Berndt, P.; Tirrell, M.; Fields, G. B., Self-assembling amphiphiles for construction of protein molecular architecture. *Journal of the American Chemical Society* **1996,** 118, (50), 12515-12520.

118. Kogiso, M.; Ohnishi, S.; Yase, K.; Masuda, M.; Shimizu, T., Dicarboxylic oligopeptide bolaamphiphiles: Proton-triggered self-assembly of microtubes with loose solid surfaces. *Langmuir* **1998,** 14, (18), 4978-4986.

119. Hartgerink, J. D.; Beniash, E.; Stupp, S. I., Peptide-amphiphile nanofibers: A versatile scaffold for the preparation of self-assembling materials. *Proceedings of the National Academy of Sciences of the United States of America* **2002,** 99, (8), 5133-5138.

120. Silva, G. A.; Czeisler, C.; Niece, K. L.; Beniash, E.; Harrington, D. A.; Kessler, J. A.; Stupp, S. I., Selective differentiation of neural progenitor cells by high-epitope density nanofibers. *Science* **2004,** 303, (5662), 1352-1355.

121. Tsonchev, S.; Schatz, G. C.; Ratner, M. A., Electrostatically-directed self-assembly of cylindrical peptide amphiphile nanostructures. *Journal of Physical Chemistry B* **2004,** 108, (26), 8817-8822.

122. Tsonchev, S.; Troisi, A.; Schatz, G. C.; Ratner, M. A., On the structure and stability of self-assembled zwitterionic peptide amphiphiles: A theoretical study. *Nano Letters* **2004,** 4, (3), 427-431.

123. Rajangam, K.; Behanna, H. A.; Hui, M. J.; Han, X. Q.; Hulvat, J. F.; Lomasney, J. W.; Stupp, S. I., Heparin binding nanostructures to promote growth of blood vessels. *Nano Letters* **2006,** 6, (9), 2086-2090.

124. van der Gucht, J.; Lemmers, M.; Knoben, W.; Besseling, N. A. M.; Lettinga, M. P., Multiple shear-banding transitions in a supramolecular polymer solution. *Physical Review Letters* **2006,** 97, (10).

125. Thurn-Albrecht, T.; DeRouchey, J.; Russell, T. P.; Kolb, R., Pathways toward electric field induced alignment of block copolymers. *Macromolecules* **2002,** 35, (21), 8106-8110.

126. Thurn-Albrecht, T.; DeRouchey, J.; Russell, T. P.; Jaeger, H. M., Overcoming interfacial interactions with electric fields. *Macromolecules* **2000,** 33, (9), 3250-3253.

127. Xu, T.; Zhu, Y. Q.; Gido, S. P.; Russell, T. P., Electric field alignment of symmetric diblock copolymer thin films. *Macromolecules* **2004,** 37, (7), 2625-2629.

128. Osuji, C.; Ferreira, P. J.; Mao, G. P.; Ober, C. K.; Vander Sande, J. B.; Thomas, E. L., Alignment of self-assembled hierarchical microstructure in liquid crystalline diblock copolymers using high magnetic fields. *Macromolecules* **2004,** 37, (26), 9903-9908.

129. Chen, Z. R.; Kornfield, J. A.; Smith, S. D.; Grothaus, J. T.; Satkowski, M. M., Pathways to macroscale order in nanostructured block copolymers. *Science* **1997,** 277, (5330), 1248-1253.

130. Morrison, F. A.; Winter, H. H., Effect of Unidirectional Shear on the Structure of Triblock Copolymers .1. Polystyrene Polybutadiene Polystyrene. *Macromolecules* **1989,** 22, (9), 3533-3540.

131. Keller, A.; Pedemont.E; Willmout.Fm, Macro-Lattice from Segregated Amorphous Phases of a 3 Block Copolymer. *Nature* **1970,** 225, (5232), 538-&.

132. Makinen, R.; Ruokolainen, J.; Ikkala, O.; de Moel, K.; ten Brinke, G.; De Odorico, W.; Stamm, M., Orientation of supramolecular self-organized polymeric nanostructures by oscillatory shear flow. *Macromolecules* **2000,** 33, (9), 3441-3446.

133. Kato, T.; Mizoshita, N.; Kishimoto, K., Functional liquid-crystalline assemblies: Self-organized soft materials. *Angewandte Chemie-International Edition* **2006,** 45, (1), 38-68.

134. Yoshio, M.; Kagata, T.; Hoshino, K.; Mukai, T.; Ohno, H.; Kato, T., One-dimensional ion-conductive polymer films: Alignment and fixation of ionic channels formed by self-organization of polymerizable columnar liquid crystals. *Journal of the American Chemical Society* **2006,** 128, (16), 5570-5577.

135. Yeardley, D. J. P.; Ungar, G.; Percec, V.; Holerca, M. N.; Johansson, G., Spherical supramolecular minidendrimers self-organized in an "inverse micellar"-like thermotropic body-centered cubic liquid crystalline phase. *Journal of the American Chemical Society* **2000,** 122, (8), 1684-1689.

136. Messmore, B. W.; Hulvat, J. F.; Sone, E. D.; Stupp, S. I., Synthesis, self-assembly, and characterization of supramolecular polymers from electroactive dendron rodcoil molecules. *Journal of the American Chemical Society* **2004,** 126, (44), 14452-14458.

137. Sardone, L.; Palermo, V.; Devaux, E.; Credgington, D.; De Loos, M.; Marletta, G.; Cacialli, F.; Van Esch, J.; Samori, P., Electric-field-assisted alignment of supramolecular fibers. *Advanced Materials* **2006,** 18, (10), 1276-1280.

138. Kato, T.; Kutsuna, T.; Hanabusa, K.; Ukon, M., Gelation of room-temperature liquid crystals by the association of a trans-1,2-bis(amino)cyclohexane derivative. *Advanced Materials* **1998,** 10, (8), 606-+.

139. Kato, T.; Kutsuna, T.; Yabuuchi, K.; Mizoshita, N., Anisotropic self-aggregation of an anthracene derivative: Formation of liquid-crystalline physical gels in oriented states. *Langmuir* **2002,** 18, (18), 7086-7088.

140. Kitamura, T.; Nakaso, S.; Mizoshita, N.; Tochigi, Y.; Shimomura, T.; Moriyama, M.; Ito, K.; Kato, T., Electroactive supramolecular self-assembled fibers comprised of doped tetrathiafulvalene-based gelators. *Journal of the American Chemical Society* **2005,** 127, (42), 14769-14775.

141. Lagerwall, S. T., *Ferroelectric and Antiferroelectric Liquid Crystals*. Wiley-VCH: New York, 1999.

142. Blodgett, K. B., Films Built by Depositing Successive Monomolecular Layers on a Solid Surface. *Journal of the American Chemical Society* **1935,** 57, 1007.

143. Dai, L. M.; Patil, A.; Gong, X. Y.; Guo, Z. X.; Liu, L. Q.; Liu, Y.; Zhu, D. B., Aligned nanotubes. *Chemphyschem* **2003,** 4, (11), 1150-1169.

144. Huang, Y.; Duan, X. F.; Wei, Q. Q.; Lieber, C. M., Directed assembly of one-dimensional nanostructures into functional networks. *Science* **2001,** 291, (5504), 630-633.

145. Shimoda, H.; Oh, S. J.; Geng, H. Z.; Walker, R. J.; Zhang, X. B.; McNeil, L. E.; Zhou, O., Self-assembly of carbon nanotubes. *Advanced Materials* **2002,** 14, (12), 899-901.

146. Kim, F.; Kwan, S.; Akana, J.; Yang, P. D., Langmuir-Blodgett nanorod assembly. *Journal of the American Chemical Society* **2001,** 123, (18), 4360-4361.

147. Michalet, X.; Ekong, R.; Fougerousse, F.; Rousseaux, S.; Schurra, C.; Hornigold, N.; vanSlegtenhorst, M.; Wolfe, J.; Povey, S.; Beckmann, J. S.; Bensimon, A., Dynamic molecular combing: Stretching the whole human genome for high-resolution studies. *Science* **1997,** 277, (5331), 1518-1523.

148. Tang, C. B.; Tracz, A.; Kruk, M.; Zhang, R.; Smilgies, D. M.; Matyjaszewski, K.; Kowalewski, T., Long-range ordered thin films of block copolymers prepared by zone-casting and their thermal conversion into ordered nanostructured carbon. *Journal of the American Chemical Society* **2005,** 127, (19), 6918-6919.

149. Huang, J. X.; Kim, F.; Tao, A. R.; Connor, S.; Yang, P. D., Spontaneous formation of nanoparticle stripe patterns through dewetting. *Nature Materials* **2005,** 4, (12), 896-900.

150. Micheletto, R.; Fukuda, H.; Ohtsu, M., A Simple Method for the Production of a 2-Dimensional, Ordered Array of Small Latex-Particles. *Langmuir* **1995,** 11, (9), 3333-3336.

151. Kim, J. S.; McHugh, S. K.; Swager, T. M., Nanoscale fibrils and grids: Aggregated structures from rigid-rod conjugated polymers. *Macromolecules* **1999,** 32, (5), 1500-1507.

152. Zhao, Y.; Fang, J. Y., Positioning and alignment of lipid tubules on patterned Au substrates. *Langmuir* **2006,** 22, (4), 1891-1895.

153. Breiby, D. W.; Bunk, O.; Pisula, W.; Solling, T. I.; Tracz, A.; Pakula, T.; Mullen, K.; Nielsen, M. M., Structure of zone-cast HBC-C12H25 films. *Journal of the American Chemical Society* **2005,** 127, (32), 11288-11293.

154. Tracz, A.; Jeszka, J. K.; Watson, M. D.; Pisula, W.; Mullen, K.; Pakula, T., Uniaxial alignment of the columnar super-structure of a hexa (alkyl) hexa-peri-hexabenzocoronene on untreated glass by simple solution processing. *Journal of the American Chemical Society* **2003,** 125, (7), 1682-1683.

155. Kuncicky, D. M.; Naik, R. R.; Velev, O. D., Rapid deposition and long-range alignment of nanocoatings and arrays of electrically conductive wires from tobacco mosaic virus. *Small* **2006,** 2, (12), 1462-1466.

156. De Rosa, C.; Park, C.; Thomas, E. L.; Lotz, B., Microdomain patterns from directional eutectic solidification and epitaxy. *Nature* **2000,** 405, (6785), 433-437.

157. Park, C.; De Rosa, C.; Thomas, E. L., Large area orientation of block copolymer microdomains in thin films via directional crystallization of a solvent. *Macromolecules* **2001,** 34, (8), 2602-2606.

158. Burghardt, W. R., Molecular orientation and rheology in sheared lyotropic liquid crystalline polymers. *Macromolecular Chemistry and Physics* **1998,** 199, (4), 471-488.

159. Schuddeboom, P. C.; Meister, R.; Cecchetto, E.; Jerome, B., Poling of liquid crystals in thin films. *European Physical Journal E* **2003,** 11, (1), 37-52.

160. Kim, S. O.; Solak, H. H.; Stoykovich, M. P.; Ferrier, N. J.; de Pablo, J. J.; Nealey, P. F., Epitaxial self-assembly of block copolymers on lithographically defined nanopatterned substrates. *Nature* **2003,** 424, (6947), 411-414.

161. Yang, X. M.; Peters, R. D.; Nealey, P. F.; Solak, H. H.; Cerrina, F., Guided self-assembly of symmetric diblock copolymer films on chemically nanopatterned substrates. *Macromolecules* **2000,** 33, (26), 9575-9582.

162. Fasolka, M. J.; Harris, D. J.; Mayes, A. M.; Yoon, M.; Mochrie, S. G. J., Observed substrate topography-mediated lateral patterning of diblock copolymer films. *Physical Review Letters* **1997,** 79, (16), 3018-3021.

163. Rockford, L.; Liu, Y.; Mansky, P.; Russell, T. P.; Yoon, M.; Mochrie, S. G. J., Polymers on nanoperiodic, heterogeneous surfaces. *Physical Review Letters* **1999,** 82, (12), 2602-2605.

164. Sundrani, D.; Sibener, S. J., Spontaneous spatial alignment of polymer cylindrical nanodomains on silicon nitride gratings. *Macromolecules* **2002,** 35, (22), 8531-8539.

165. Delrio, E. M.; Dagama, M. M. T.; Demiguel, E.; Rull, L. F., Surface-Induced Alignment at Model Nematic Interfaces. *Physical Review E* **1995,** 52, (5), 5028-5039.

166. Jerome, B.; Shen, Y. R., Anchoring of Nematic Liquid-Crystals on Mica in the Presence of Volatile Molecules. *Physical Review E* **1993,** 48, (6), 4556-4574.

167. Smela, E.; Martinezmiranda, L. J., Effect of Substrate Preparation on Smectic Liquid-Crystal Alignment - a Structural Study. *Journal of Applied Physics* **1993,** 73, (7), 3299-3304.

168. Kim, J. H.; Yoneya, M.; Yokoyama, H., Tristable nematic liquid-crystal device using micropatterned surface alignment. *Nature* **2002,** 420, (6912), 159-162.

169. Lee, S. W.; Chae, B.; Kim, H. C.; Lee, B.; Choi, W.; Kim, S. B.; Chang, T. H.; Ree, M., New clues to the factors governing the perpendicular alignment of liquid crystals on rubbed polystyrene film surfaces. *Langmuir* **2003,** 19, (21), 8735-8743.

170. Rastegar, A.; Skarabot, M.; Blij, B.; Rasing, T., Mechanism of liquid crystal alignment on submicron patterned surfaces. *Journal of Applied Physics* **2001,** 89, (2), 960-964.

171. Berreman, D. W., Alignment of Liquid-Crystals by Grooved Surfaces. *Molecular Crystals and Liquid Crystals* **1973,** 23, (3-4), 215-231.

172. Martinez-Miranda, L. J., Smectic ordering in confined liquid crystal films: A depth study. *Journal of Applied Physics* **2002,** 91, (10), 6452-6456.

173. Lee, B. W.; Clark, N. A., Alignment of liquid crystals with patterned isotropic surfaces. *Science* **2001,** 291, (5513), 2576-2580.

174. Wittmann, J. C.; Lotz, B., Epitaxial Crystallization of Aliphatic Polyesters on Trioxane and Various Aromatic-Hydrocarbons. *Journal of Polymer Science Part B-Polymer Physics* **1981,** 19, (12), 1853-1864.

175. Wittmann, J. C.; Lotz, B., Epitaxial Crystallization of Monoclinic and Orthorhombic Polyethylene Phases. *Polymer* **1989,** 30, (1), 27-34.

176. Wittmann, J. C.; Smith, P., Highly Oriented Thin-Films of Poly(Tetrafluoroethylene) as a Substrate for Oriented Growth of Materials. *Nature* **1991,** 352, (6334), 414-417.

177. Kumar, A.; Biebuyck, H. A.; Whitesides, G. M., Patterning Self-Assembled Monolayers - Applications in Materials Science. *Langmuir* **1994,** 10, (5), 1498-1511.

178. Yan, L.; Huck, W. T. S.; Whitesides, G. M., Self-assembled monolayers (SAMS) and synthesis of planar micro- and nanostructures. *Journal of Macromolecular Science-Polymer Reviews* **2004,** C44, (2), 175-206.

179. Lee, I.; Ahn, J. S.; Hendricks, T. R.; Rubner, M. F.; Hammond, P. T., Patterned and controlled polyelectrolyte fractal growth and aggregations. *Langmuir* **2004,** 20, (6), 2478-2483.

180. Zheng, H. P.; Rubner, M. F.; Hammond, P. T., Particle assembly on patterned "plus/minus" polyelectrolyte surfaces via polymer-on-polymer stamping. *Langmuir* **2002,** 18, (11), 4505-4510.

181. Aizenberg, J.; Braun, P. V.; Wiltzius, P., Patterned colloidal deposition controlled by electrostatic and capillary forces. *Physical Review Letters* **2000,** 84, (13), 2997-3000.

182. Gupta, V. K.; Abbott, N. L., Design of surfaces for patterned alignment of liquid crystals on planar and curved substrates. *Science* **1997,** 276, (5318), 1533-1536.

183. Gunther, J.; Stupp, S. I., Surface patterns of supramolecular materials. *Langmuir* **2001,** 17, (21), 6530-6539.

184. Ludden, M. J. W.; Reinhoudt, D. N.; Huskens, J., Molecular printboards: versatile platforms for the creation and positioning of supramolecular assemblies and materials. *Chemical Society Reviews* **2006,** 35, (11), 1122-1134.

185. Stutzmann, N.; Tervoort, T. A.; Broer, D. J.; Sirringhaus, H.; Friend, R. H.; Smith, P., Microcutting materials on polymer substrates. *Advanced Functional Materials* **2002,** 12, (2), 105-109.

186. Dziomkina, N. V.; Vancso, G. J., Colloidal crystal assembly on topologically patterned templates. *Soft Matter* **2005,** 1, (4), 265-279.

187. vanBlaaderen, A.; Ruel, R.; Wiltzius, P., Template-directed colloidal crystallization. *Nature* **1997,** 385, (6614), 321-324.

188. Yin, Y.; Li, Z. Y.; Xia, Y., Template-directed growth of (100)-oriented colloidal crystals. *Langmuir* **2003,** 19, (3), 622-631.

189. Yin, Y. D.; Xia, Y. N., Growth of large colloidal crystals with their (100) planes orientated parallel to the surfaces of supporting substrates. *Advanced Materials* **2002,** 14, (8), 605-608.

190. Xia, Y. N.; Rogers, J. A.; Paul, K. E.; Whitesides, G. M., Unconventional methods for fabricating and patterning nanostructures. *Chemical Reviews* **1999,** 99, (7), 1823-1848.

191. Geissler, M.; Xia, Y. N., Patterning: Principles and some new developments. *Advanced Materials* **2004,** 16, (15), 1249-1269.

192. Kramer, S.; Fuierer, R. R.; Gorman, C. B., Scanning probe lithography using self-assembled monolayers. *Chemical Reviews* **2003,** 103, (11), 4367-4418.

193. Bruckbauer, A.; Zhou, D. J.; Ying, L. M.; Korchev, Y. E.; Abell, C.; Klenerman, D., Multicomponent submicron features of biomolecules created by voltage controlled deposition from a nanopipet. *Journal of the American Chemical Society* **2003,** 125, (32), 9834-9839.

194. Piner, R. D.; Zhu, J.; Xu, F.; Hong, S. H.; Mirkin, C. A., "Dip-pen" nanolithography. *Science* **1999,** 283, (5402), 661-663.

195. Maoz, R.; Cohen, S. R.; Sagiv, J., Nanoelectrochemical patterning of monolayer surfaces: Toward spatially defined self-assembly of nanostructures. *Advanced Materials* **1999,** 11, (1), 55-61.

196. Leggett, G. J., Scanning near-field photolithography-surface photochemistry with nanoscale spatial resolution. *Chemical Society Reviews* **2006,** 35, (11), 1150-1161.

197. Sun, S.; Leggett, G. J., Matching the resolution of electron beam lithography by scanning near-field photolithography. *Nano Letters* **2004,** 4, (8), 1381-1384.

198. Yatziv, Y.; Turyan, I.; Mandler, D., A new approach to micropatterning: Application of potential-assisted ion transfer at the liquid-liquid interface for the local metal deposition. *Journal of the American Chemical Society* **2002,** 124, (20), 5618-5619.

199. Snow, E. S.; Campbell, P. M., Afm Fabrication of Sub-10-Nanometer Metal-Oxide Devices with in-Situ Control of Electrical-Properties. *Science* **1995,** 270, (5242), 1639-1641.

200. Xia, Y. N.; Whitesides, G. M., Soft lithography. *Angewandte Chemie-International Edition* **1998,** 37, (5), 551-575.

201. Xia, Y. N.; Kim, E.; Zhao, X. M.; Rogers, J. A.; Prentiss, M.; Whitesides, G. M., Complex optical surfaces formed by replica molding against elastomeric masters. *Science* **1996,** 273, (5273), 347-349.

202. Yan, X.; Yao, J. M.; Lu, G. A.; Chen, X.; Zhang, K.; Yang, B., Microcontact printing of colloidal crystals. *Journal of the American Chemical Society* **2004,** 126, (34), 10510-10511.

203. Kohli, N.; Worden, R. M.; Lee, I., Intact transfer of layered, bionanocomposite arrays by microcontact printing. *Chemical Communications* **2005**, (3), 316-318.

204. Salaita, K.; Amarnath, A.; Maspoch, D.; Higgins, T. B.; Mirkin, C. A., Spontaneous "phase separation" of patterned binary alkanethiol mixtures. *Journal of the American Chemical Society* **2005,** 127, (32), 11283-11287.

205. Kim, E.; Xia, Y. N.; Whitesides, G. M., Two- and three-dimensional crystallization of polymeric microspheres by micromolding in capillaries. *Advanced Materials* **1996,** 8, (3), 245-&.

206. Trau, M.; Yao, N.; Kim, E.; Xia, Y.; Whitesides, G. M.; Aksay, I. A., Microscopic patterning of orientated mesoscopic silica through guided growth. *Nature* **1997,** 390, (6661), 674-676.

207. Sgarbi, N.; Pisignano, D.; Di Benedetto, F.; Gigli, G.; Cingolani, R.; Rinaldi, R., Self-assembled extracellular matrix protein networks by microcontact printing. *Biomaterials* **2004,** 25, (7-8), 1349-1353.

208. Jiang, H. Z.; Stupp, S. I., Dip-pen patterning and surface assembly of peptide amphiphiles. *Langmuir* **2005,** 21, (12), 5242-5246.

209. Arsenault, A. C.; Rider, D. A.; Tetreault, N.; Chen, J. I. L.; Coombs, N.; Ozin, G. A.; Manners, I., Block copolymers under periodic, strong three-dimensional confinement. *Journal of the American Chemical Society* **2005,** 127, (28), 9954-9955.

210. Wu, Y. Y.; Cheng, G. S.; Katsov, K.; Sides, S. W.; Wang, J. F.; Tang, J.; Fredrickson, G. H.; Moskovits, M.; Stucky, G. D., Composite mesostructures by nano-confinement. *Nature Materials* **2004,** 3, (11), 816-822.

211. Xiang, H. Q.; Shin, K.; Kim, T.; Moon, S. I.; McCarthy, T. J.; Russell, T. P., Block copolymers under cylindrical confinement. *Macromolecules* **2004,** 37, (15), 5660-5664.

212. Binder, H.; Schmiedel, H.; Lantzsch, G.; Cramer, C.; Klose, G., Molecular ordering in microconfined liquid crystals: An infrared linear dichroism study. *Liquid Crystals* **1996,** 21, (3), 415-426.

213. Crawford, G. P.; Yang, D. K.; Zumer, S.; Finotello, D.; Doane, J. W., Ordering and Self-Diffusion in the 1st Molecular Layer at a Liquid-Crystal Polymer Interface. *Physical Review Letters* **1991,** 66, (6), 723-726.

214. Steinhart, M.; Zimmermann, S.; Goring, P.; Schaper, A. K.; Gosele, U.; Weder, C.; Wendorff, J. H., Liquid crystalline nanowires in porous alumina: Geometric confinement versus influence of pore walls. *Nano Letters* **2005,** 5, (3), 429-434.

215. Rudhardt, D.; Fernandez-Nieves, A.; Link, D. R.; Weitz, D. A., Phase switching of ordered arrays of liquid crystal emulsions. *Applied Physics Letters* **2003,** 82, (16), 2610-2612.

216. Knoll, A.; Horvat, A.; Lyakhova, K. S.; Krausch, G.; Sevink, G. J. A.; Zvelindovsky, A. V.; Magerle, R., Phase behavior in thin films of cylinder-forming block copolymers. *Physical Review Letters* **2002,** 89, (3).

217. Sirringhaus, H.; Brown, P. J.; Friend, R. H.; Nielsen, M. M.; Bechgaard, K.; Langeveld-Voss, B. M. W.; Spiering, A. J. H.; Janssen, R. A. J.; Meijer, E. W.; Herwig, P.; de Leeuw, D. M., Two-dimensional charge transport in self-organized, high-mobility conjugated polymers. *Nature* **1999,** 401, (6754), 685-688.

218. Sirringhaus, H.; Wilson, R. J.; Friend, R. H.; Inbasekaran, M.; Wu, W.; Woo, E. P.; Grell, M.; Bradley, D. D. C., Mobility enhancement in conjugated polymer field-effect transistors through chain alignment in a liquid-crystalline phase. *Applied Physics Letters* **2000,** 77, (3), 406-408.

219. Verbiest, T.; Van Elshocht, S.; Kauranen, M.; Hellemans, L.; Snauwaert, J.; Nuckolls, C.; Katz, T. J.; Persoons, A., Strong enhancement of nonlinear optical properties through supramolecular chirality. *Science* **1998,** 282, (5390), 913-915.

220. Blinov, L. M., On the way to polar achiral liquid crystals. *Liquid Crystals* **1998,** 24, (1), 143-152.

221. Niori, T.; Sekine, T.; Watanabe, J.; Furukawa, T.; Takezoe, H., Distinct ferroelectric smectic liquid crystals consisting of banana shaped achiral molecules. *Journal of Materials Chemistry* **1996,** 6, (7), 1231-1233.

222. Li, L. M.; Stupp, S. I., Effects of substrate micropatterning on nonlinear optical properties of polar self-assembling films. *Applied Physics Letters* **2001,** 78, (26), 4127-4129.

223. Hecht, B.; Sick, B.; Wild, U. P.; Deckert, V.; Zenobi, R.; Martin, O. J. F.; Pohl, D. W., Scanning near-field optical microscopy with aperture probes: Fundamentals and applications. *Journal of Chemical Physics* **2000,** 112, (18), 7761-7774.

224. Betzig, E.; Trautman, J. K., Near-Field Optics - Microscopy, Spectroscopy, and Surface Modification Beyond the Diffraction Limit. *Science* **1992,** 257, (5067), 189-195.

225. Shen, Y. R., Surface-Properties Probed by 2nd-Harmonic and Sum-Frequency Generation. *Nature* **1989,** 337, (6207), 519-525.

226. Prasad, P. N.; Williams, D. J., *Introduction to Nonlinear Optical Effects in Molecules and Polymers*. John Wiley & Sons: New York, 1991.

227. Williams, D. J., Organic Polymeric and Non-Polymeric Materials with Large Optical Nonlinearities. *Angewandte Chemie-International Edition in English* **1984,** 23, (9), 690-703.

228. Bauer, S.; Bauer-Gogonea, S.; Ploss, B.; Ploss, B., Nonlinear dielectric response of poled amorphous polymer dipole glasses. *Journal of Non-Crystalline Solids* **2005,** 351, (33-36), 2759-2763.

229. Burland, D. M.; Miller, R. D.; Walsh, C. A., 2nd-Order Nonlinearity in Poled-Polymer Systems. *Chemical Reviews* **1994,** 94, (1), 31-75.

230. Lei, D.; Runt, J.; Safari, A.; Newnham, R. E., Dielectric-Properties of Azo Dye Poly(Methyl Methacrylate) Mixtures. *Macromolecules* **1987,** 20, (8), 1797-1801.

231. Singer, K. D.; Sohn, J. E.; Lalama, S. J., 2nd Harmonic-Generation in Poled Polymer-Films. *Applied Physics Letters* **1986,** 49, (5), 248-250.

232. Wang, Y. J.; Carlisle, G. O., Optical properties of disperse-red-1-doped nematic liquid crystal. *Journal of Materials Science-Materials in Electronics* **2002,** 13, (3), 173-178.

233. Walba, D. M.; Dyer, D. J.; Sierra, T.; Cobben, P. L.; Shao, R. F.; Clark, N. A., Ferroelectric liquid crystals for nonlinear optics: Orientation of the disperse red 1 chromophore along the ferroelectric liquid crystal polar axis. *Journal of the American Chemical Society* **1996,** 118, (5), 1211-1212.

234. Chen, W.; Feller, M. B.; Shen, Y. R., Investigation of Anisotropic Molecular Orientational Distributions of Liquid-Crystal Monolayers by Optical 2nd-Harmonic Generation. *Physical Review Letters* **1989,** 63, (24), 2665-2668.

235. Lin, W. B.; Lin, W. P.; Wong, G. K.; Marks, T. J., Supramolecular approaches to second-order nonlinear optical materials. Self-assembly and microstructural characterization of intrinsically acentric [(aminophenyl)azo]pyridinium superlattices. *Journal of the American Chemical Society* **1996,** 118, (34), 8034-8042.

236. Kauranen, M.; Verbiest, T.; Boutton, C.; Teerenstra, M. N.; Clays, K.; Schouten, A. J.; Nolte, R. J. M.; Persoons, A., Supramolecular 2nd-Order Nonlinearity of Polymers with Orientationally Correlated Chromophores. *Science* **1995,** 270, (5238), 966-969.

237. Khan, R. U. A.; Kwon, O. P.; Tapponnier, A.; Rashid, A. N.; Gunter, P., Supramolecular ordered organic thin films for nonlinear optical and optoelectronic applications. *Advanced Functional Materials* **2006,** 16, (2), 180-188.

238. Hulliger, J.; Konig, O.; Hoss, R., Polar Inclusion-Compounds of Perhydrotriphenylene (Phtp) and Efficient Nonlinear-Optical Molecules. *Advanced Materials* **1995,** 7, (8), 719-721.

239. Hoss, R.; Konig, O.; KramerHoss, V.; Berger, U.; Rogin, P.; Hulliger, J., Crystallization of supramolecular materials: Perhydrotriphenylene (PHTP) inclusion compounds with nonlinear optical properties. *Angewandte Chemie-International Edition in English* **1996,** 35, (15), 1664-1666.

240. Thulstrup, E. W.; Michl, J., *Elementary Polarization Spectroscopy*. VCH: New York, 1989.

241. Buffeteau, T.; Desbat, B.; Turlet, J. M., Polarization Modulation Ft-Ir Spectroscopy of Surfaces and Ultra-Thin Films - Experimental Procedure and Quantitative-Analysis. *Applied Spectroscopy* **1991,** 45, (3), 380-389.

242. Madou, M. J., *Fundamentals of Microfabrication: the Science of Miniturization*. 2nd ed.; CRC Press: New York, 2002.

243. Huggins, K. E. Photonic properties of organic molecular assemblies. University of Illinois at Urbana-Champaign, Urbana, IL, 1997.

244. Carminati, R.; Madrazo, A.; NietoVesperinas, M.; Greffet, J. J., Optical content and resolution of near-field optical images: Influence of the operating mode. *Journal of Applied Physics* **1997,** 82, (2), 501-509.

245. Hecht, B.; Bielefeldt, H.; Inouye, Y.; Pohl, D. W.; Novotny, L., Facts and artifacts in near-field optical microscopy. *Journal of Applied Physics* **1997,** 81, (6), 2492-2498.

246. Lambert, J. B.; Shurvell, H. F.; Lightner, D. A.; Cooks, R. G., *Organic Structural Spectroscopy*. Prentice Hall: Upper Saddle River, NJ, 1998.

247. Merkel, K.; Kocot, A.; Vij, J. K.; Mehl, G. H.; Meyer, T., The orientational order parameters of a dendritic liquid crystal organo-siloxane tetrapode oligomer, determined using polarized infrared spectroscopy. *Journal of Chemical Physics* **2004,** 121, (10), 5012-5021.

248. Axelsen, P. H.; Citra, M. J., Orientational order determination by internal reflection infrared spectroscopy. *Progress in Biophysics & Molecular Biology* **1996,** 66, (3), 227-253.

249. Parikh, A. N.; Allara, D. L., Quantitative-Determination of Molecular-Structure in Multilayered Thin-Films of Biaxial and Lower Symmetry from Photon Spectroscopies .1. Reflection Infrared Vibrational Spectroscopy. *Journal of Chemical Physics* **1992,** 96, (2), 927-945.

250. Binder, H.; Schmiedel, H., Infrared dichroism investigations on the acyl chain ordering in lamellar structures: I. Order parameter formalism and its application to polycrystalline stearic acid. *Vibrational Spectroscopy* **1999,** 21, (1-2), 51-73.

251. Aizenberg, J.; Black, A. J.; Whitesides, G. M., Control of crystal nucleation by patterned self-assembled monolayers. *Nature* **1999,** 398, (6727), 495-498.

252. Bao, Z. N.; Rogers, J. A.; Katz, H. E., Printable organic and polymeric semiconducting materials and devices. *Journal of Materials Chemistry* **1999,** 9, (9), 1895-1904.

253. Park, C.; Yoon, J.; Thomas, E. L., Enabling nanotechnology with self assembled block copolymer patterns. *Polymer* **2003,** 44, (22), 6725-6760.

254. Behanna, H. A.; Donners, J.; Gordon, A. C.; Stupp, S. I., Coassembly of amphiphiles with opposite peptide polarities into nanofibers. *Journal of the American Chemical Society* **2005,** 127, (4), 1193-1200.

255. Jiang, H. Z.; Guler, M. O.; Stupp, S. I., The internal structure of self-assembled peptide amphiphile nanofibers. *Soft Matter* **2007,** 3, (4), 454-462.

256. Niece, K. L.; Hartgerink, J. D.; Donners, J.; Stupp, S. I., Self-assembly combining two bioactive peptide-amphiphile molecules into nanofibers by electrostatic attraction. *Journal of the American Chemical Society* **2003,** 125, (24), 7146-7147.

257. Paramonov, S. E.; Jun, H. W.; Hartgerink, J. D., Self-assembly of peptide-amphiphile nanofibers: The roles of hydrogen bonding and amphiphilic packing. *Journal of the American Chemical Society* **2006,** 128, (22), 7291-7298.

258. Tovar, J. D.; Claussen, R. C.; Stupp, S. I., Probing the interior of peptide amphiphile supramolecular aggregates. *Journal of the American Chemical Society* **2005,** 127, (20), 7337-7345.

259. Jiang, X. P.; Zheng, H. P.; Gourdin, S.; Hammond, P. T., Polymer-on-polymer stamping: Universal approaches to chemically patterned surfaces. *Langmuir* **2002,** 18, (7), 2607-2615.

260. Kane, R. S.; Takayama, S.; Ostuni, E.; Ingber, D. E.; Whitesides, G. M., Patterning proteins and cells using soft lithography. *Biomaterials* **1999,** 20, (23-24), 2363-2376.

261. Quist, A. P.; Pavlovic, E.; Oscarsson, S., Recent advances in microcontact printing. *Analytical and Bioanalytical Chemistry* **2005,** 381, (3), 591-600.

262. Biasco, A.; Pisignano, D.; Krebs, B.; Pompa, P. P.; Persano, L.; Cingolani, R.; Rinaldi, R., Conformation of microcontact-printed proteins by atomic force miroscopy molecular sizing. *Langmuir* **2005,** 21, (11), 5154-5158.

263. Cho, Y.; Ivanisevic, A., Peptides on GaAs surfaces: Comparison between features generated by microcontact printing and dip-pen nanolithography. *Langmuir* **2006,** 22, (21), 8670-8674.

264. Odom, T. W.; Love, J. C.; Wolfe, D. B.; Paul, K. E.; Whitesides, G. M., Improved pattern transfer in soft lithography using composite stamps. *Langmuir* **2002,** 18, (13), 5314-5320.

265. Shull, K. R.; Martin, E. F.; Drzal, P. L.; Hersam, M. C.; Markowitz, A. R.; McSwain, R. L., Adhesive transfer of thin viscoelastic films. *Langmuir* **2005,** 21, (1), 178-186.

266. Hills, D. A.; Nowell, D.; Sackfield, A., *Mechanics of Elastic Contacts*. Butterworth-Heinemann: Oxford, 1993.

267. Tingey, M. L.; Snodgrass, E. J.; Abbott, N. L., Patterned orientations of liquid crystals on affinity microcontact printed proteins. *Advanced Materials* **2004,** 16, (15), 1331-+.

268. Philp, D.; Stoddart, J. F., Self-assembly in natural and unnatural systems. *Angewandte Chemie-International Edition in English* **1996,** 35, (11), 1155-1196.

269. Reinhoudt, D. N.; Crego-Calama, M., Synthesis beyond the molecule. *Science* **2002,** 295, (5564), 2403-2407.

270. Hamley, I. W., Nanotechnology with soft materials. *Angewandte Chemie-International Edition* **2003,** 42, (15), 1692-1712.

271. Kim, E.; Xia, Y. N.; Whitesides, G. M., Polymer Microstructures Formed by Molding in Capillaries. *Nature* **1995,** 376, (6541), 581-584.

272. Rogers, J. A.; Meier, M.; Dodabalapur, A., Using printing and molding techniques to produce distributed feedback and Bragg reflector resonators for plastic lasers. *Applied Physics Letters* **1998,** 73, (13), 1766-1768.

273. Cheng, J. Y.; Mayes, A. M.; Ross, C. A., Nanostructure engineering by templated self-assembly of block copolymers. *Nature Materials* **2004,** 3, (11), 823-828.

274. Agheli, H.; Malmstrom, J.; Larsson, E. M.; Textor, M.; Sutherland, D. S., Large area protein nanopatterning for biological applications. *Nano Letters* **2006,** 6, (6), 1165-1171.

275. Falconnet, D.; Csucs, G.; Grandin, H. M.; Textor, M., Surface engineering approaches to micropattern surfaces for cell-based assays. *Biomaterials* **2006,** 27, (16), 3044-3063.

276. Lee, K. B.; Park, S. J.; Mirkin, C. A.; Smith, J. C.; Mrksich, M., Protein nanoarrays generated by dip-pen nanolithography. *Science* **2002,** 295, (5560), 1702-1705.

277. Stevens, M. M.; George, J. H., Exploring and engineering the cell surface interface. *Science* **2005,** 310, (5751), 1135-1138.

278. Sullivan, T. P.; van Poll, M. L.; Dankers, P. Y. W.; Huck, W. T. S., Forced peptide synthesis in nanoscale confinement under elastomeric stamps. *Angewandte Chemie-International Edition* **2004,** 43, (32), 4190-4193.

279. Whitesides, G. M.; Ostuni, E.; Takayama, S.; Jiang, X. Y.; Ingber, D. E., Soft lithography in biology and biochemistry. *Annual Review of Biomedical Engineering* **2001,** 3, 335-373.

280. Denis, F. A.; Pallandre, A.; Nysten, B.; Jonas, A. M.; Dupont-Gillain, C. C., Alignment and assembly of adsorbed collagen molecules induced by anisotropic chemical nanopatterns. *Small* **2005,** 1, (10), 984-991.

281. Wilson, D. L.; Martin, R.; Hong, S.; Cronin-Golomb, M.; Mirkin, C. A.; Kaplan, D. L., Surface organization and nanopatterning of collagen by dip-pen nanolithography. *Proceedings of the National Academy of Sciences of the United States of America* **2001,** 98, (24), 13660-13664.

282. Donthu, S. K.; Pan, Z.; Shekhawat, G. S.; Dravid, V. P.; Balakrisnan, B.; Tripathy, S., Near-field scanning optical microscopy of ZnO nanopatterns fabricated by micromolding in capillaries. *Journal of Applied Physics* **2005,** 98, (2), 024304.

283. Roman, L. S.; Inganas, O.; Granlund, T.; Nyberg, T.; Svensson, M.; Andersson, M. R.; Hummelen, J. C., Trapping light in polymer photodiodes with soft embossed gratings. *Advanced Materials* **2000,** 12, (3), 189-+.

284. Zhang, F. L.; Nyberg, T.; Inganas, O., Conducting polymer nanowires and nanodots made with soft lithography. *Nano Letters* **2002,** 2, (12), 1373-1377.

285. Pierschbacher, M. D.; Ruoslahti, E., Variants of the Cell Recognition Site of Fibronectin That Retain Attachment-Promoting Activity. *Proceedings of the National Academy of Sciences of the United States of America-Biological Sciences* **1984,** 81, (19), 5985-5988.

286. Pierschbacher, M. D.; Ruoslahti, E., Cell Attachment Activity of Fibronectin Can Be Duplicated by Small Synthetic Fragments of the Molecule. *Nature* **1984,** 309, (5963), 30-33.

287. Sephel, G. C.; Tashiro, K. I.; Sasaki, M.; Greatorex, D.; Martin, G. R.; Yamada, Y.; Kleinman, H. K., Laminin-a Chain Synthetic Peptide Which Supports Neurite Outgrowth. *Biochemical and Biophysical Research Communications* **1989,** 162, (2), 821-829.

288. Tashiro, K.; Sephel, G. C.; Weeks, B.; Sasaki, M.; Martin, G. R.; Kleinman, H. K.; Yamada, Y., A Synthetic Peptide Containing the Ikvav Sequence from the a-Chain of Laminin Mediates Cell Attachment, Migration, and Neurite Outgrowth. *Journal of Biological Chemistry* **1989,** 264, (27), 16174-16182.

289. Hung, A. M.; Stupp, S. I., *Nano Letters* accepted.

290. Guler, M. O.; Hsu, L.; Soukasene, S.; Harrington, D. A.; Hulvat, J. F.; Stupp, S. I., Presentation of RGDS epitopes on self-assembled nanofibers of branched peptide amphiphiles. *Biomacromolecules* **2006,** 7, (6), 1855-1863.

291. Stendahl, J. C.; Rao, M. S.; Guler, M. O.; Stupp, S. I., Intermolecular forces in the self-assembly of peptide amphiphile nanofibers. *Advanced Functional Materials* **2006,** 16, (4), 499-508.

292. Kim, H. S.; Hartgerink, J. D.; Ghadiri, M. R., Oriented self-assembly of cyclic peptide nanotubes in lipid membranes. *Journal of the American Chemical Society* **1998,** 120, (18), 4417-4424.

293. Marsh, D., Dichroic ratios in polarized Fourier transform infrared for nonaxial symmetry of beta-sheet structures. *Biophysical Journal* **1997,** 72, (6), 2710-2718.

294. Wang, J.; Chen, X. Y.; Clarke, M. L.; Chen, Z., Vibrational spectroscopic studies on fibrinogen adsorption at polystyrene/protein solution interfaces: Hydrophobic side chain and secondary structure changes. *Journal of Physical Chemistry B* **2006,** 110, (10), 5017-5024.

295. Boyan, B. D.; Hummert, T. W.; Dean, D. D.; Schwartz, Z., Role of material surfaces in regulating bone and cartilage cell response. *Biomaterials* **1996,** 17, (2), 137-146.

296. Cima, L. G.; Vacanti, J. P.; Vacanti, C.; Ingber, D.; Mooney, D.; Langer, R., Tissue Engineering by Cell Transplantation Using Degradable Polymer Substrates. *Journal of Biomechanical Engineering-Transactions of the Asme* **1991,** 113, (2), 143-151.

297. Schmidt, C. E.; Leach, J. B., Neural tissue engineering: Strategies for repair and regeneration. *Annual Review of Biomedical Engineering* **2003,** 5, 293-347.

298. Chen, C. S.; Mrksich, M.; Huang, S.; Whitesides, G. M.; Ingber, D. E., Geometric control of cell life and death. *Science* **1997,** 276, (5317), 1425-1428.

299. Curtis, A.; Wilkinson, C., Topographical control of cells. *Biomaterials* **1997,** 18, (24), 1573-1583.

300. Folch, A.; Toner, M., Microengineering of cellular interactions. *Annual Review of Biomedical Engineering* **2000,** 2, 227-+.

301. Mrksich, M.; Whitesides, G. M., Using self-assembled monolayers to understand the interactions of man-made surfaces with proteins and cells. *Annual Review of Biophysics and Biomolecular Structure* **1996,** 25, 55-78.

302. Andersson, A. S.; Backhed, F.; von Euler, A.; Richter-Dahlfors, A.; Sutherland, D.; Kasemo, B., Nanoscale features influence epithelial cell morphology and cytokine production. *Biomaterials* **2003,** 24, (20), 3427-3436.

303. Curtis, A. S. G.; Gadegaard, N.; Dalby, M. J.; Riehle, M. O.; Wilkinson, C. D. W.; Aitchison, G., Cells react to nanoscale order and symmetry in their surroundings. *Ieee Transactions on Nanobioscience* **2004,** 3, (1), 61-65.

304. Dalby, M. J.; McCloy, D.; Robertson, M.; Wilkinson, C. D. W.; Oreffo, R. O. C., Osteoprogenitor response to defined topographies with nanoscale depths. *Biomaterials* **2006,** 27, (8), 1306-1315.

305. Kong, H. J.; Hsiong, S.; Mooney, D. J., Nanoscale cell adhesion ligand presentation regulates nonviral gene delivery and expression. *Nano Letters* **2007,** 7, (1), 161-166.

306. Kriparamanan, R.; Aswath, P.; Zhou, A.; Tang, L. P.; Nguyen, K. T., Nanotopography: Cellular responses to nanostructured materials. *Journal of Nanoscience and Nanotechnology* **2006,** 6, (7), 1905-1919.

307. Price, R. L.; Haberstroh, K. M.; Webster, T. J., Enhanced functions of osteoblasts on nanostructured surfaces of carbon and alumina. *Medical & Biological Engineering & Computing* **2003,** 41, (3), 372-375.

308. Teixeira, A. I.; Nealey, P. F.; Murphy, C. J., Responses of human keratocytes to micro- and nanostructured substrates. *Journal of Biomedical Materials Research Part A* **2004,** 71A, (3), 369-376.

309. Yim, E. K. F.; Reano, R. M.; Pang, S. W.; Yee, A. F.; Chen, C. S.; Leong, K. W., Nanopattern-induced changes in morphology and motility of smooth muscle cells. *Biomaterials* **2005,** 26, (26), 5405-5413.

310. Zinger, O.; Zhao, G.; Schwartz, Z.; Simpson, J.; Wieland, M.; Landolt, D.; Boyan, B., Differential regulation of osteoblasts by substrate microstructural features. *Biomaterials* **2005,** 26, (14), 1837-1847.

311. Barth, A.; Zscherp, C., What vibrations tell us about proteins. *Quarterly Reviews of Biophysics* **2002,** 35, (4), 369-430.

312. Krimm, S.; Bandekar, J., Vibrational Spectroscopy and Conformation of Peptides, Polypeptides, and Proteins. *Advances in Protein Chemistry* **1986,** 38, 181-364.

313. Zhu, G.; Mehler, M. F.; Mabie, P. C.; Kessler, J. A., Developmental changes in neural progenitor cell lineage commitment do not depend on epidermal growth factor receptor signaling. *Journal of Neuroscience Research* **2000,** 59, (3), 312-320.

314. Miyazawa, T., Perturbation treatment of the characteristic vibrations of polypeptide chains in various configurations. *Journal of Chemical Physics* **1960,** 32, 1647-1652.

315. Stein, R. S., The X-ray diffraction, birefringence, and infrared dichroism of stretched polyethylene: 2. Generalized uniaxial crystal orientation. *Journal of Polymer Science* **1958,** 31, (123), 327-334.

316. Stein, R. S., The X-ray diffraction, birefringence, and infrared dichroism of stretched polyethylene: 3. Biaxial orientation. *Journal of Polymer Science* **1958,** 31, (123), 335-343.

317. Bokel, C.; Brown, N. H., Integrins in development: Moving on, responding to, and sticking to the extracellular matrix. *Developmental Cell* **2002,** 3, (3), 311-321.

318. Maheshwari, G.; Brown, G.; Lauffenburger, D. A.; Wells, A.; Griffith, L. G., Cell adhesion and motility depend on nanoscale RGD clustering. *Journal of Cell Science* **2000,** 113, (10), 1677-1686.

319. Lewis, N. S.; Crabtree, G.; Nozik, A. J.; Wasielewski, M. R.; Alivisatos, A. P. *Basic Needs for Solar Energy Utilization: Report on the Basic Energy Sciences Workshop on Solar Energy Utilization, April 18 - 21, 2005*; U.S. Department of Energy, Office of Science: Washington, D.C., 2005.

320. Brabec, C. J.; Dyakonov, V.; Parisi, J.; Sariciftci, N. S., *Organic Photovoltaics: Concepts and Realization*. Springer: New York, 2003; p xii, 297.

321. Brabec, C. J.; Sariciftci, N. S.; Hummelen, J. C., Plastic solar cells. *Advanced Functional Materials* **2001,** 11, (1), 15-26.

322. Hoppe, H.; Sariciftci, N. S., Organic solar cells: An overview. *Journal of Materials Research* **2004,** 19, (7), 1924-1945.

323. Xue, J. G.; Uchida, S.; Rand, B. P.; Forrest, S. R., Asymmetric tandem organic photovoltaic cells with hybrid planar-mixed molecular heterojunctions. *Applied Physics Letters* **2004,** 85, (23), 5757-5759.

324. Scholes, G. D.; Rumbles, G., Excitons in nanoscale systems. *Nature Materials* **2006,** 5, (9), 683-696.

325. Assadi, A.; Svensson, C.; Willander, M.; Inganas, O., Field-Effect Mobility of Poly(3-Hexylthiophene). *Applied Physics Letters* **1988,** 53, (3), 195-197.

326. Kwong, C. Y.; Djurisic, A. B.; Chui, P. C.; Cheng, K. W.; Chan, W. K., Influence of solvent on film morphology and device performance of poly(3-hexylthiophene): TiO2 nanocomposite solar cells. *Chemical Physics Letters* **2004,** 384, (4-6), 372-375.

327. Tao, Y.; Donat-Bouillud, A.; D'Iorio, M.; Lam, J.; Gorjanc, T. C.; Py, C.; Wong, M. S., Luminescence properties of end-substituted oligo (phenylenevinylene)s. *Synthetic Metals* **2000,** 111, 417-420.

328. Funahashi, M.; Hanna, J. I., High carrier mobility up to 0.1 cm(2)V(-1)s(-1) at ambient temperatures in thiophene-based smectic liquid crystals. *Advanced Materials* **2005,** 17, (5), 594-+.

329. Lawrence, J. R.; Andrew, P.; Barnes, W. L.; Buck, M.; Turnbull, G. A.; Samuel, I. D. W., Optical properties of a light-emitting polymer directly patterned by soft lithography. *Applied Physics Letters* **2002,** 81, (11), 1955-1957.

330. Zimmermann, S.; Wendorff, J. H.; Weder, C., Uniaxial orientation of columnar discotic liquid crystals. *Chemistry of Materials* **2002,** 14, (5), 2218-2223.

331. Wittmann, J. C.; Straupe, C.; Meyer, S.; Lotz, B.; Lang, P.; Horowitz, G.; Garnier, F., Sexithiophene thin films epitaxially oriented on polytetrafluoroethylene substrates: Structure and morphology (vol 303, pg 207, 1997). *Thin Solid Films* **1997,** 311, (1-2), 317-322.

332. Gill, R. E.; Hadziioannou, G.; Lang, P.; Garnier, F.; Wittmann, J. C., Highly oriented thin films of a substituted oligo(para-phenylenevinylene) on friction-transferred PTFE substrates. *Advanced Materials* **1997,** 9, (4), 331-&.

333. Cozzoli, P. D.; Kornowski, A.; Weller, H., Low-temperature synthesis of soluble and processable organic-capped anatase TiO2 nanorods. *Journal of the American Chemical Society* **2003,** 125, (47), 14539-14548.

334. Whitten, D. G., Photochemistry and Photophysics of Trans-Stilbene and Related Alkenes in Surfactant Assemblies. *Accounts of Chemical Research* **1993,** 26, (9), 502-509.

335. Jones, R. A. L.; Richards, R. W., *Polymers at Surfaces and Interfaces*. Cambridge University Press: New York, 1999.

336. Kienberger, F.; Pastushenko, V. P.; Kada, G.; Gruber, H. J.; Riener, C.; Schindler, H.; Hinterdorfer, P., Static and Dynamical Properties of Single Poly(Ethylene Glycol) Molecules Investigated by Force Spectroscopy. *Single Molecules* **2000,** 1, (2), 123-128.

337. Breiby, D. W.; Solling, T. I.; Bunk, O.; Nyberg, R. B.; Norrman, K.; Nielsen, M. M., Structural surprises in friction-deposited films of poly(tetrafluoroethylene). *Macromolecules* **2005,** 38, (6), 2383-2390.

338. Tanigaki, N.; Yoshida, Y.; Kaito, A.; Yase, K., Total-reflection X-ray diffraction study of friction-tranferred poly(tetrafluoroethylene) film. *Journal of Polymer Science Part B-Polymer Physics* **2001,** 39, (4), 432-438.

339. Zbinden, R., *Infrared Spectroscopy of High Polymers*. Academic Press: New York, 1964.

340. Saupe, A., Recent results in field of liquid crystals. *Angewandte Chemie-International Edition* **1968,** 7, (2), 97.

341. Pelletier, I.; Laurin, I.; Buffeteau, T.; Pezolet, M., Determination of molecular orientation in biaxially oriented ultrathin films. *Journal of Physical Chemistry B* **2004,** 108, (22), 7162-7169.

VITA

Albert Melvin Hung was born January 9, 1980 in Sunnyvale, California, the youngest of three children, to Ching-mao and Pei-jean Hung. After graduating from Henry M. Gunn High School (Palo Alto, California) in 1997, he enrolled at the Massachsetts Institute of Technology (Cambridge, Massachusetts), following in the footsteps of his older siblings, Jeffrey and Emilie, who both earned masters degrees at MIT. He pursued a course of study in materials science and engineering with a minor in mechanical engineering and was named the Oustanding Junior of the Class of 2001 in the Department of Materials Science and Engineering. During the summers of his sophomore and junior years, he worked under Dr. Michael Baskes in the Structure-Properties Relations group at Los Alamos National Laboratories (Los Alamos, New Mexico). Albert would write his senior thesis on the work he performed there, implementing molecular dynamics simulations employing embedded-atom potentials to study the formation of Frenkel defects in metals and the phase separation of binary metal systems. He graduated from MIT with his bachelor's degree in the spring of 2001 and spent the summer of that year working at 3M Corp. (Woodbury, Minnesota) developing metal-matix composites. In the fall, Albert enrolled at Northwestern University (Evanston, Illinois) in the Department of Materials Science and Engineering. He joined the group of Prof. Samuel I. Stupp and initiated research into ways in which patterning and spatial confinement could be employed to influence order in self-assembling systems. During that time, he was awarded a Royal E. Cabell Fellowship from Northwestern University, a National Science Foundation Graduate Research Fellowship, and a National Defense Science and Engineering Graduate Reasearch Fellowship. After completing his graduate studies, Albert is looking forward to continuing research on material behavior at the nanometer scale as well as accomplishing his goal of running 50 marathons in 50 states.